Synthesis, Characterisation and Applications of Zinc-Substituted Zeotypes

IRENE ROSSANA MAZZEI

Synthesis, Characterisation and Applications of Zinc-Substituted Zeotypes

This thesis is submitted in partial fulfilment for the degree of PhD

by Irene Rossana Mazzei

Department of Chemistry, Durham University

February 2022

Supervisor: Dr. Russell A. Taylor

Table of Contents

Statement of Copyright

Part of this thesis is being submitted for publication as:

I. I. R. Mazzei, D. C. Apperley, R. Kerrigan and R. A. Taylor “Analysis of Framework Defect Sites in Zn-substituted MFI Zeotypes by Solid-state NMR and Diffuse Reflectance IR Spectroscopies”, *tbd.*

II. I. R. Mazzei and R. A. Taylor “State of the Art and Future Perspectives in the Synthesis, Characterisation and Applications of Zincosilicate Zeotypes”, *tbd*

Acknowledgements

After reaching the end of the three intense years of my PhD, I would like to dedicate a few words to the people that were - and became - part of it.

First of all, I would like to express my gratitude to my supervisor, Dr. Russell Taylor, for giving me the opportunity of being part of the RAT group, for his constant support and guidance and for pushing me to always give my best and for believing in me. Thanks for always being strong for us and for being there whenever we needed you. Thanks to Meera and Sam R, former members of the group and now amazing scientists, and to Abdul and Sam M, for being there and for their help. A very special thanks to Ryan for being a great friend and colleague, for his support and for trying to teach me some organic chemistry. I couldn't have asked for a better group, through good and bad times, and I will always cherish all the things I've learnt and all the experiences we've shared.

This adventure wouldn't have been the same without having such amazing people by my side, even if they were physically far. My mum and dad have been my anchor, my safe place, and I'm deeply grateful to them for this and for never hesitating to believe in me. I believe my strongest motivation always came from the will to make them and my sister Francesca proud of me. Thank you, Francesca, for being the strongest person I know, without any doubt. This work, my best efforts and my inspiration are dedicated to you.

I'm grateful to all my friends that were there from the start and that joined me along the way. Thanks especially to Rita and Sofia, my "acquired" sisters; to Enza, Mariantonietta, Bruno and Gianfranco. Thanks to my amazing "coinqui" Elena, I can honestly say that this experience was so much better with you by my side, and to all the people that made Durham feel a little bit like home.

I'm grateful to have collected so many good memories, but also to have gone through challenging periods, as these gave me the chance to learn and grow and to say that I'm happy to be the person I am today.

Last - but by no means least - thanks to Matt for sharing with me the end of this experience and the start of my, our, new one.

To Francesca.

1. Chapter 1: Introduction

1.1. Introduction

1.1.1. The Big Picture: Innovative Catalysts for Sustainable Processes

Finding sustainable solutions to the constantly increasing energy and commodity product demand is a crucial challenge in urgent need to be tackled. The majority of industrial processes (90 % of chemical manufacturing processes and more than 20 % of all industrial processes) for the synthesis of chemicals and fuels involve the use of catalysts.[1] Heterogeneous catalysts, including porous materials, provide important benefits not only to efficiency and yield of the process, but also to the reduction of the environmental impact related to longer catalyst lifetime and reduced time and energy-costs.[1]–[3] The advantages of the use of heterogeneous catalysts over homogeneous ones are numerous and range from reusability, simpler preparation methods and application and lower toxicity. Heterogeneous systems can be used as porous supports for homogeneous species or as catalysts themselves. Zeolites mainly belong to the latter category, with a constantly increasing number of applications in several industrial areas (Figure 1(a)).[1] With a large number of available framework structures, well-defined pore architecture, tunable chemical properties (e.g. acidity) and low production costs, zeolites are receiving growing attention as a class of sustainable heterogeneous catalysts and molecular sieves.[4] The cracking of feedstock components in petroleum refining is a major area of industrial interest, as well as the synthesis of chemical products, which benefits by the use of catalysts (especially heterogeneous and porous catalysts) to achieve higher activation and selectivity and lower costs (**Error! Reference source not found.** 1(b)).[2]

a)

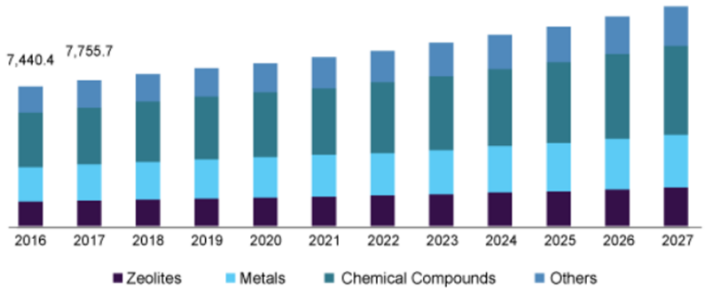

b)

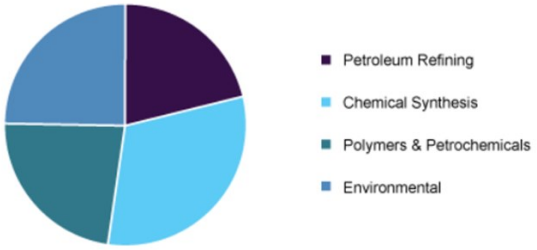

Figure 1: Catalyst market size in the U.S., expressed in US dollars (a) and global catalyst market value share by application in 2019 (b).[2]

The word “sustainability” refers to a situation that involves the continuous use of resources without endangering the stability of the natural systems.[4] It has been estimated that fossil fuels (coal, oil and natural gas) – currently still the main feedstocks for the production of energy, fuels and chemicals – will last for around 40 more years, at the current consumption rate.[5] This is why it is necessary to develop and implement alternative methods to meet the world’s population needs for fuels and commodity products. In addition to issues related to the limited availability of fossil fuels, another major problem is the huge amount of greenhouse emissions that the use of these sources produces. In 2019 the U.S. produced 6,558 million metric tons of CO_2 equivalent greenhouse gas emissions,[6] of which 80 % was due to CO_2 and 10 % to CH_4 emissions (Figure 2). Methane is the main component of natural gas and despite producing a lower amount of CO_2 when burnt compared to other fossil fuels, it is a greenhouse gas 100 times more powerful than CO_2.[7] As a consequence, even small emissions of methane in the atmosphere cause serious damage and substantial contribution to the global warming problem.

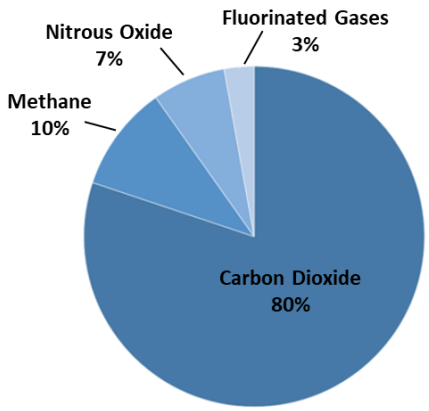

Figure 2: Contribution to the greenhouse gas emissions produced in the U.S. in 2019 by different compounds.[6]

Although the main use of methane is as feedstock for the production of energy, it also represents an important source for the industrial production of commodity chemicals. However, the latter requires the conversion of methane into synthesis gas (or syngas), a mixture of CO and H_2, prior to being converted into higher-value products.[8] Syngas is produced from methane mostly through steam reforming and autothermal reforming, which require extremely harsh conditions of pressure and temperature (> 800 °C and 30 barg).[9] This has a considerable impact on the construction costs of the plant and on the loss of large amounts of methane in order to reach such high temperature conditions.[8] The large scale of syngas plants (paired with at least one chemical manufacturing plant), required in order to limit the impact of these factors, prevents their construction on sites hosting small-sized natural gas deposits (stranded gas), shale gas deposits or gas produced at oil reservoirs (associated gas).[7] Often the transport and

production costs of gas found in these sites overcome the value of the gas itself; therefore, small natural gas deposits are often flared, as the CO_2 emissions produced from flared gas have a lower greenhouse impact than unburned methane (Figure 3).

The direct conversion of methane and other feedstocks to commodity chemicals through the use of catalysts would bring important benefits in terms of energy and cost-cutting. In addition to this, it would help overcome issues related to toxic emissions and to the efficient use of resources, especially if they have limited availability. The main areas of interest for the direct conversion of methane into chemicals are (i) methane to ethylene, (ii) methane to aromatics and (iii) methane to methanol.[10] Research has been achieving important results in all three areas, also reaching the stage of industrial implementation;[11] however, the efficient and profitable direct methane-to-methanol conversion is still considered as the holy grail of catalysis.[12]

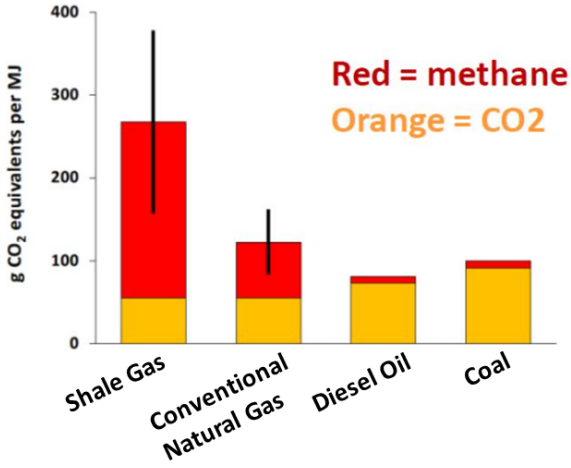

Figure 3: Impact to the greenhouse emissions of various energy sources, expressed in grams of CO_2 equivalents per unit of energy. Adapted with permission from Ref [7].

Another alternative method that can be implemented to mitigate the greenhouse gas problem is the use of biomass-derived sources to replace fossil fuels. Biomass with high sugar content (such as corn, sugar cane or sugar beet) can be easily converted by hydrolysis of starch chains into glucose, which is then transformed into bioethanol.[13] Bioethanol has been recognised as one of the best alternatives to fossil fuels in the transport sector,[14] as well as a great feedstock for the cost-effective production of a wide range of chemicals.[15] Its low price (only 0.027 USD/mol) makes ethanol profitable for its conversion into chemicals such as diethyl ether, ethyl acetate, acetaldehyde and propylene (Figure 4).[15] The conversion of ethanol requires the use of specific catalysts for the production of each chemical. For instance, the dehydration of ethanol into ethylene and diethyl ether takes place over acid catalysts; in this context, Brønsted acid zeolites and especially H/MOR offer higher activity and selectivity compared to alumina-based catalysts, which are commonly used in industrial processes.[15], [16] The production of

butadiene from biomass-derived ethanol, or Lebedev process, is another process of interest.[17] It was found that sugar cane-derived ethanol from Brazil represents a sustainable source of bioethanol for the Lebedev process.[18] The mechanism controlling the conversion of ethanol to butadiene is still under debate; however, a generally accepted pathway involves a first step of dehydrogenation to acetaldehyde, followed by the aldol condensation into acetaldol, dehydration to crotonaldehyde and its reduction to crotyl alcohol and finally, dehydration to butadiene. This pathway is referred to as the Toussaint-Kagan mechanism and is represented in Scheme 1.[18] The key step in the reaction is the dehydrogenation of ethanol to acetaldehyde, a highly reactive compound, that takes place over Lewis acid sites.[17] This occurs through selective O–H and C–H bond cleavage, producing acetaldehyde and H_2.[19] Homogeneous systems involving Ru and Os have shown outstanding results in the dehydrogenation of ethanol to acetaldehyde; however, they rely on the use of expensive noble metals and ligands.[19] Heterogeneous catalysts represent valid alternative systems, providing all the advantages related to the use of solid catalysts, reusability and lower costs. Although a number of promising heterogeneous catalysts containing metals such as Cu, Ag, Ni and Zn have been identified, more research is needed in order to develop more competitive systems.[19]

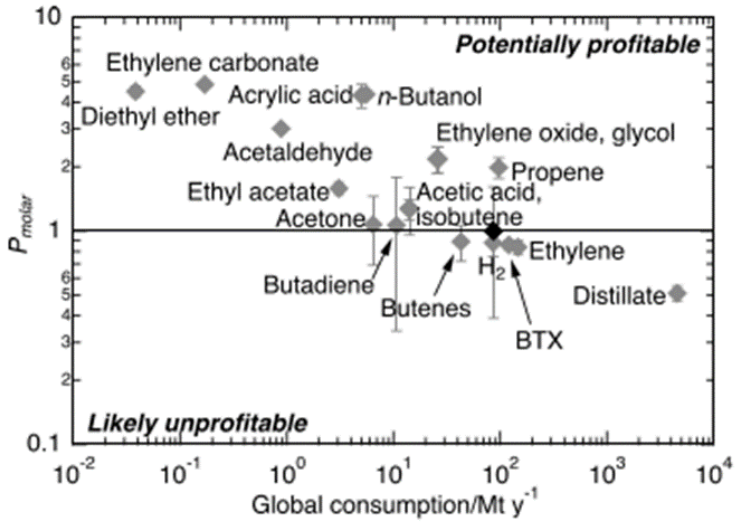

Figure 4: Profitability of the production of various chemicals from ethanol, evaluated considering their costs divided by the cost of ethanol. P_{molar} indicates the ratio of the price of a product divided by the cost of the quantity of ethanol required to produce it; the global consumption is indicated in Mt per year. Adapted with permission from ref [15].

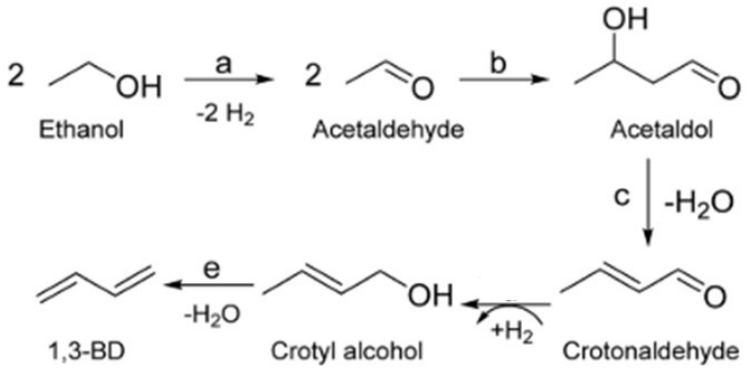

Scheme 1: The Toussaint-Kagan mechanism, generally accepted as the reaction pathway for the conversion of ethanol to 1,3-butadiene. Adapted with permission from ref [18]. The process starts with the dehydrogenation of ethanol to acetaldehyde (a), then an aldol process takes place between two molecules of acetaldehyde to form acetaldol (b), which undergo a dehydration reaction to crotonaldehyde (c). Subsequently, a Meerwein-Ponndorf-Verley-Oppenauer (MPVO) reduction takes place to form crotyl alcohol which further dehydrates to 1,3-butadiene (e).

1.1.2. Introduction to Zeolites

Zeolites are a family of tectosilicates with an open crystalline structure composed of interconnected cavities and channels. The term “zeolite” was introduced by the Swedish mineralogist A. Cronstedt in 1756 when he discovered the first natural zeolite.[20] The name zeolite, from the Greek ζέω (zéō), meaning "to boil" and λίθος (líthos), meaning "stone", refers to the ability of these rocks to produce large amounts of steam when heated up, due to the water adsorbed in their pores. Currently, 235 different zeolite structures have been discovered, among which over 40 have natural origin.[21] These materials are conventionally identified by a name followed by a three-letter code that indicates their framework type.

After the pioneering work of R. Barrer, who for the first time reported the preparation of zeolite mordenite (MOR) in the laboratory,[22] these materials started to receive increasing interest and were first used commercially as adsorbents during the mid-1950s.[23] However, their superior chemical and physical properties (strong acidity, tunable properties, resistance to high pressure and temperature) made zeolites suitable materials to be employed as catalysts in the hydrocarbon cracking industry.[24]–[27] To date, zeolites are used in several different areas, such as waste-water treatment,[28] green chemistry and catalysis,[29] sustainable agriculture,[30] gas adsorption[31] and many others.[32]

One major application area for zeolites is still the conversion of hydrocarbons from the petrochemical industry, where 5 of the 20 different zeolite frameworks employed in industry exhibit excellent performances: BEA, FAU, FER, MOR and MFI (the “Big Five”, Table 1).[32], [33]

Table 1: Framework size and dimensionality of the most important zeolites used in industrial applications.

Framework type	Channel system	Description
BEA	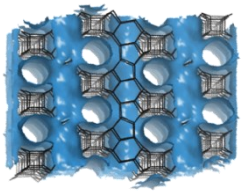	Ring size: 12, 6, 5, 4 3D Intersection of 12 MR channels.
FAU	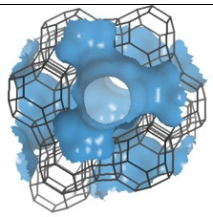	Ring size: 12, 6, 4 3D Intersection of 12 MR channels.
MOR	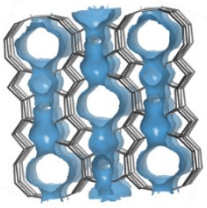	Ring size: 12, 8, 5, 4 2D 8MR channels intersecting 12MR channels.
FER	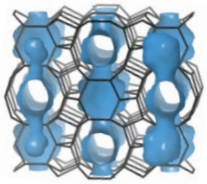	Ring size: 10, 8, 6, 5 2D 8MR channels intersecting 10MR channels.
MFI	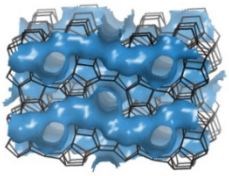	Ring size: 10, 6, 5, 4 3D Sinusoidal intersection of 10 MR channels.

The structure of zeolites is made up of corner-sharing $[SiO_4]$ and $[AlO_4]^-$ tetrahedra with extra-framework cations balancing negative framework charges. An empirical formula of a zeolite framework is the following:

$$M_{x/n}{}^{n+}\,[(SiO_2)(AlO_2)_x]\cdot w\,H_2O$$

Where M is a cation with a positive charge equal to n. According to Loewenstein's rule,[34] Al^{III} atoms can only be connected to Si^{IV} atoms through oxygen bridges, therefore the Si:Al ratios in zeolites is always bigger than 1. Variations in the SiO_2 content tailor the thermal stability, acidity, ion-exchange capacity and polar molecule adsorption capacity.[23] Pure SiO_2 materials have neutral frameworks, whilst the substitution of Al^{III} species introduces monovalent negative charges into the framework. When these are balanced by H^+ species, the zeolite exhibits

Brønsted acid character. Brønsted acid zeolites are mainly used in fluid catalytic cracking (FCC), isomerisation and synthesis of hydrocarbons.[35], [36] The incorporation of different heteroatoms, replacing Al^{III}, introduces new acid properties in the zeolite materials. This can be achieved during the synthesis stage, with the isomorphous substitution of different species in tetrahedral framework positions, or through post-synthetic modifications (e.g. ion exchange or incipient wetness impregnation). The materials obtained from these procedures possess a certain degree of Lewis acid character; Lewis-acid sites in zeolites (or zeotypes) catalyse reactions such as the epoxidation of olefins, aldol condensation and biomass conversion reactions.[27], [37] A representation of Brønsted and Lewis acid sites is given in Figure 5.

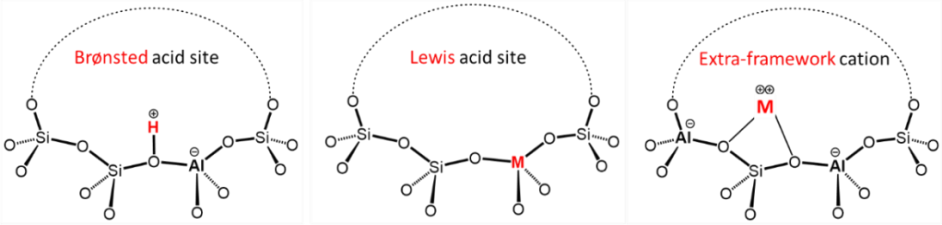

Figure 5: Representation of Brønsted and Lewis acid sites and extra-framework cations species with charge-balancing role.

1.1.3. Zeolites for Methane Upgrade

Attempts to upgrade methane to higher-value products, such as methanol, date back to 1902,[38] and the introduction and optimisation of homogeneous and heterogeneous systems continued throughout the 20th century.[39]–[41] In more recent years, the use of transition metal oxides has been emerging for the partial oxidation of methane to methanol, with materials such as MoO_3, V_2O_5 and Fe_2O_3.[42]–[44] Zeolites, and in particular metal-modified zeolites, have also been considered as catalysts for the direct oxidation of methane to methanol.

The first promising results were reported by Panov in 1995, who showed that it was possible to extract liquid methanol from the stoichiometric reaction of methane with the α-O sites bonded to Fe species of Fe-modified ZSM-5.[45] These are reactive oxygen species formed from an oxygen-atom abstraction from nitrous oxide (N_2O) by alpha-iron (α-Fe) species. Since then, much effort has been invested into the development of metal-modified zeolite systems for the upgrade of methane to methanol, and to understand the reaction mechanisms that control the process. The α-O sites in Fe-modified zeolites are introduced into the catalysts by decomposition of N_2O, and DFT studies have elucidated the reaction pathway that takes place when methane is introduced in this system. After the first abstraction of a hydrogen atom from methane by the α-O, forming Fe^{III}-O-H and CH_3 species, the CH_3 radical can further interact to the

first species, giving rise to Fe^{III}-O(H)-CH_3 which can be desorbed as methanol.[46] This process is shown in Equation 1.

$$Zeo–Fe^{IV}=O + CH_4 \longrightarrow Zeo–Fe^{III}–O–H + {}^{\cdot}CH_3 \longrightarrow Zeo–Fe^{III}–O(H)–CH_3 \longrightarrow Zeo–Fe^{IV}=O + CH_3OH$$

Equation 1

in addition to Fe-modified zeolites, where the α-O active sites are generated by the presence of extra-framework Fe species reacting with N_2O, a Fe-substituted zeotype (with the MFI framework type) has also shown to be active for the direct conversion of methane to methanol, using O_2 as an oxidant instead of N_2O.[47] However, this system required a temperature of 630 °C to achieve adequate methane conversion (30 %).

Copper-modified zeolites are another class of materials that have received interest for the direct partial oxidation of methane to methanol. These systems have been intensively studied since the first report was published by Groothaert et al. in 2005.[48] The identification of the active sites was challenging and depended on the specific environment in the zeolite framework. For instance, DFT simulations have shown that Cu-modified ZSM-5 contains $[Cu_3(\mu O)_3]^{2+}$ species at high temperature and mono(μ-oxo)dicopper species at low temperature.[49] On the other hand, the active species present in Cu-modified MOR have been proposed to be $[Cu_3(\mu O)_3]^{2+}$ placed between two Al atoms. Nevertheless, regardless of the nature of the active Cu site, the activation of methane occurs with the initial activation of the Cu-modified zeolite in an O_2 atmosphere at high temperature (> 450 °C), followed by reaction with methane at lower temperature (approximately 200 °C) and the extraction of methanol.[48] Similarly to Fe-containing systems, the methane activation pathway has been proposed to be based on the radical hydrogen atom abstraction mechanism.[49]

A viable option that was only recently introduced for the preparation of metal-modified zeolites for methane to methanol conversion is the use of Zn-containing zeolites. A fundamental difference between Zn-based systems and Fe- or Cu-based analogues is that Zn-based systems do not require the introduction of oxygen through a high-temperature activation step to form the active sites for the reaction. The first demonstration of the possibility to activate methane in a Zn-exchanged zeolite was provided by Kazansky et al. in 2004 for a Zn^{2+}/ZSM-5 system.[50] In fact, the latter has been the most studied system for this application. The reaction mechanism that takes place has been observed to involve the heterolytic cleavage of one C–H bond of methane, with formation of Zn–CH_3 species and a Brønsted acid site, illustrated in Figure 6. Evidence of this has been observed by Infrared Fourier Transform [50] and solid-state NMR [51] spectroscopic studies. It has been suggested that the first step for the activation of methane is the adsorption of CH_4 onto a Zn^{2+} extra-framework species, which acts as a Lewis acid site by

accepting electron density donated by the σ(C–H) orbital into the empty 4s orbital of Zn, leading to the complete cleavage of the C–H bond.[52]

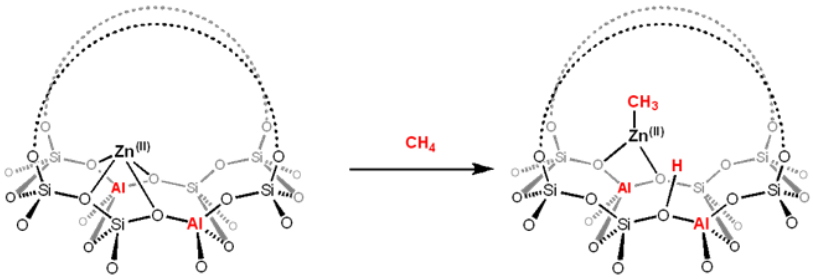

Figure 6: Reaction of CH_4 with an extra-framework Zn^{II} site, with consequent formation of a Zn-CH_3 species and a Brønsted acid site.

Despite the remarkable progress made in the field, these systems cannot be described as catalytic for the production of methanol from methane. However, once further studies elucidate the mechanisms taking place during the process and the specific requirements for the optimisation of metal-modified zeolites, the development of catalytic systems will become a concrete possibility.

1.1.4. Zeolites for the Conversion of Biomass-derived Chemicals

One of the key factors that makes biomass an excellent starting point for the production of bio-based chemicals is the possibility of converting it to a wide variety of products. The high selectivity and efficiency provided by the unique framework and chemical properties of zeolite catalysts make them optimal candidates for the chemical transformation of biomass-derived platform molecules.[20] In particular, the possibility of tuning the properties of zeolites provides important benefits for the limitation of undesired reactions that can often take place, due to the presence of many highly reactive functional groups on compounds derived from biomass. This can be achieved by tailoring the acid properties (concentration and strength) of the catalysts, controlling the shape and size selectivity and incorporating metallic heteroatoms in the zeolite framework. In fact, one extremely relevant class of zeolite catalysts for the application in biomass conversion is Lewis-acid zeolites.[21]

Major areas of application for zeolite catalysts (especially showing high acidity) are the catalytic cracking and pyrolysis of long chain hydrocarbons into gaseous and liquid organic products, water and coke.[20] Zeolite ZSM-5 shows the highest performance, especially in the production of compounds in the gasoline-range. Feedstock deriving from vegetable oils can also be valorised using zeolite catalysts. Botas et al. showed the potential of hierarchical ZSM-5 impregnated with Ni for the production of olefins, hydrogen and carbon nanotubes from rapeseed oil.[22] Porosity plays a major role in the efficiency of a zeolite catalysts; it was shown by Wang et al. that zeolites with too small pore openings (such as SAPO-34 (CHA)) showed poor

activity in the pyrolysis of corn straw fermentation residues.[23] On the other hand, larger micropores such as the ones found in BEA and FAU zeolites, could be detrimental as they allow bulkier molecules to access the active sites and participate in the reactions, resulting in quick coke deposition and deactivation of the catalyst. However, pore size is not the only factor controlling the activity and product range obtainable from zeolite catalysts. A study by Jae et al. has shown that zeolites with pore sizes comparable to ZSM-5 exhibited substantially lower aromatic selectivity in the conversion of glucose to aromatics.[24] This shows how acidity is also a fundamental property to take into account when choosing the most appropriate catalyst for biomass conversion applications.

Zeolites containing strong Brønsted acid sites can catalyse dehydration, decarbonylation, cracking, alkylation and aromatisation reactions.[20] The strength and density of these acid sites can be controlled by tuning the Si:Al ratio in zeolites; generally, low Si:Al ratios promote the increase of the aromatic yield.[25] The introduction of extra-framework cations, such as Na^+ and K^+ or metallic species (in the cationic form or as oxides), is another way of modulating the acid properties in zeolites. In particular, these modifications (i) reduce the strength of the Brønsted acid sites by replacing protons in extra-framework charge-balancing sites and (ii) introduce Lewis acidity in the system. Lewis-acid zeolites have emerged in recent years as optimal biomass-conversion catalysts for oxidation, dehydrogenation, isomerisation, aldol condensation and Diels-Alder reactions.[21], [26]

As mentioned in the previous paragraph, ethanol represents a good alternative as a biomass-derived feedstock to replace fossil fuel-based ones. The conversion of ethanol to a wide range of chemicals (such as propylene, n-butanol, 1,3-butadiene, isobutene and aromatics) takes place through acetaldehyde as a key intermediate.[27] Moreover, with an annual production of over 10^6 tons derived from non-renewable sources through the Wacker oxidation of ethylene,[28] the production of acetaldehyde from a sustainable one-step process involving bio-derived ethanol is highly desirable. The conversion of ethanol to acetaldehyde can take place through oxidative dehydrogenation (using oxygen as a co-reactant and producing water as a by-product) or non-oxidative dehydrogenation, which involves ethanol as the sole reactant, with the additional release of H_2. The latter represents a better option, as the production of hydrogen makes the process even more profitable. The use of metal-modified zeolites for this process has also been considered. Cu-exchanged ZSM-5 delivered promising results, with 93 % selectivity to acetaldehyde and 97 % ethanol conversion for 500 h.[29] This process was also carried out using Cu-exchanged Beta, prepared through introduction of Cu into the silanol nest of de-aluminated BEA. However, quick deactivation was observed for this catalyst.[30] It was suggested that the primary way of deactivation was due to the formation of Cu agglomerates, leading to Cu

sintering. Other metal species supported over zeolite frameworks and applied to the conversion of ethanol to acetaldehyde are Ag, Au and Zn.[31]–[34]

Lewis-acid zeolites represent viable options for the implementation of sustainable catalysts and processes for the one-step production of acetaldehyde from (bio)ethanol; however, more efforts are needed in order to optimise the process and avoid catalyst deactivation issues.

1.1.5. Heteroatom-substituted Zeotypes

The substitution of heteroatoms in the zeolite framework has been revealed to be successful to tailor the properties of microporous catalysts, such as their acidity, pore structure and crystal morphology. There are numerous possibilities of heteroatom substitution in a zeolite structure, with the heteroatom occupying framework sites in a tetrahedral coordination. This can be achieved using alkali-earth metals (Mg, Be, etc.), main group metals (Ga, Sn, Ge, etc.), transition metals (Ti, Fe, Zr, Cu, Mn, V, etc.) or non-metals (B, P, etc.).[35] The potential of these materials was uncovered during the first half of the 1980s, with the preparation of the first aluminophosphate (AlPOs) and silico-aluminophosphate (SAPOs) materials,[36], [37] in which PO_4 tetrahedral units are connected to $[AlO_4]^-$ and, where present, SiO_4 species. As a zeolite is defined as a crystalline aluminosilicate framework, from this point forward all materials with zeolite-like structure containing other heteroatoms in addition to or replacing Al in the framework, will be referred to as zeotypes.

In 1983 another important breakthrough was achieved, which is the synthesis of a Ti-substituted materials with the MFI framework type, named TS-1 (titanosilicate-1).[38] The interest in these materials and their peculiar properties has been increasing during the past few decades, with several studies being carried out on the design and synthesis of new materials, and the development of suitable applications in catalysis or other fields. The most interesting aspect of the novel heteroatom zeotypes is the unique acidity provided by the substituted heteroatoms; zeotypes containing elements such as Sn^{IV}, Ti^{IV} or Zr^{IV} represent well-known examples of Lewis-acid catalysts.[4], [39], [40] The isomorphous subsitution of certain heteroatoms alters the Brønsted acid character of the materials; for instance, gallosilicate zeotypes exhibited enhanced yield of aromatics compared to aluminosilicate zeolites in the CYCLAR process (dehydrocyclization of C_3-C_5 alkenes) thanks to the presence of framework Ga species and the consequent Brønsted acidity associated with them.[41], [42] Nagy et al. have observed that the acidity of the Si(OH)T protons is highly affected by the nature of the (trivalent) T heteroatoms, with T = Al showing the strongest acidity and following the trend of Al > Ga ≈ Fe >> B.[43]

The substitution of divalent transition metals in the framework is another area of interest, as it gives rise to zeotype materials with promising characteristics and enables the

enhancement of certain properties, such as the ion exchange capacity and a homogeneous dispersion of metals in the framework. When a T^{II} heteroatom is introduced in the framework in tetrahedral coordination it creates a divalent negative framework charge for every $[TO_4]^{2-}$ site. These can be directly balanced by divalent cations in extra-framework positions, introduced by ion-exchange. This would facilitate the exchange process of divalent metals in zeolites, which in aluminosilicate materials requires two $[AlO_4]^-$ centres in close proximity, a configuration which is difficult to obtain, especially in high-silica zeolites.[44]–[46] Nevertheless, the preparation of well-defined materials, with the transition metals occupying only tetrahedral framework positions is not always straightforward. The first works about heteroatom-incorporated zeotypes all reported the presence of amorphous metal oxide species located outside the framework, alongside some tetrahedral species incorporated within the zeolite.[47]–[50] Since the end of the 1980s, new methods have been developed to successfully synthesise metal-substituted zeotypes and the preparation of cobalt-,[50]–[52] nickel-,[53]–[56] magnesium-,[57]–[59] and beryllium-substituted[60]–[62] materials has been reported. A particular focus has always been put on Zn-incorporated zeotypes. The number of studies on these zeotypes is considerably greater compared to other divalent metal-substituted zeotypes. An in-depth discussion on this subject will be given in the next section.

1.1.6. Zn-substituted Zeotypes

The first report of the preparation of a zincosilicate with zeolite topology was published by McAnespie et al., who patented a method to prepare zincosilicate, stannosilicate and titanosilicate zeotype materials.[63] In the following years, attempts were made to develop synthetic methods for the preparation of zincosilicate zeotypes,[64] such as the one reported by Ball et al. for the synthesis of Zn-substituted MFI.[65] However, this showed of extra-framework Zn species and only partially substituted framework Zn sites. An important contribution to the field, marking a milestone in the area of zincosilicate synthesis, was achieved by Annen and Davis in 1991 with the preparation of the 3MR-containing framework VPI-7 (VSV).[66], [67] After this achievement, the research intensified and new structures were discovered, some of which exist only as zincosilicate phases without any aluminium-containing counterparts. Some of the most important structures discovered include VPI-8 (VET),[68], [69] VPI-9 (VNI),[70]–[72] VPI-10[67] and RUB-17 (RSN).[73] These and other major milestones are represented in Figure 7.

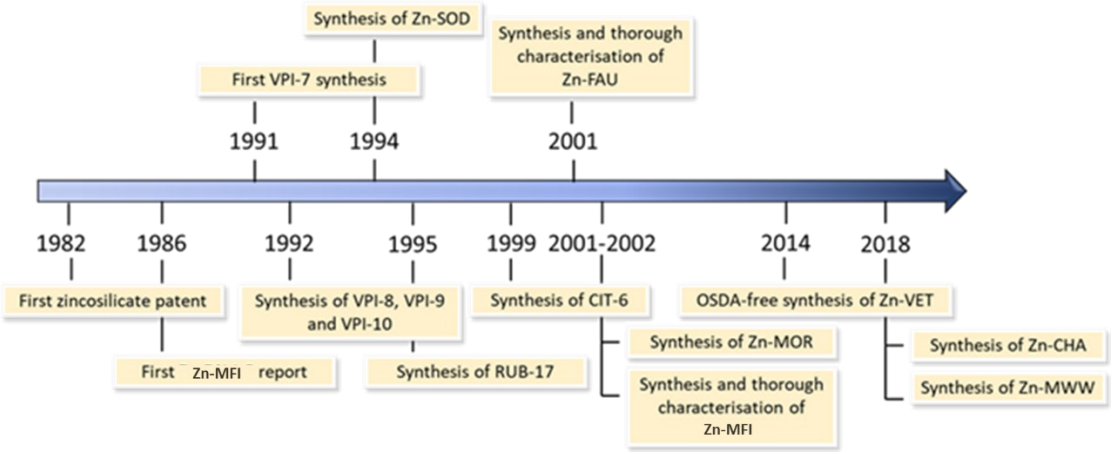

Figure 7: Important milestones reached in the field of zincosilicate zeotype synthesis.

Other molecular sieves which contain Zn^{II} framework species belong to unique zincosilicate framework classes. Some examples of these materials are Zn-AlPOs[74], [75] and zincophosphates.[76] The possibility of synthesising unique zincosilicate structures was attractive due to the specific structural properties provided by Zn heteroatoms (e.g. T–O distances and T–O–T angles). However, tailoring the properties of well-known zeolite frameworks through Zn-substitution represented a promising method to enhance certain features of these materials and exploit the structural characteristics of the zeolite frameworks. Several studies focused on the preparation of zincosilicates with zeolite topologies, such as ZSM-5 (MFI),[64], [77] sodalite (SOD),[78] analcime (ANA),[70] mordenite (MOR),[79] faujasite (FAU)[80] and CIT-6 (BEA).[81], [82] In recent years, Koike et al. showed the importance of choosing the right synthesis method, and especially the mixing procedure, for the preparation of zincosilicate chabazite (CHA),[83] whilst Yan et al. succeeded in the preparation of zincosilicate MWW (MWW).[84] In 2020, the synthesis of a 12-MR zincosilicate with structure similar to the MTW framework type was reported and named THK-2 by Sakamoto et al.[85] Table 2 shows a list of known zincosilicates with zeolite framework types, their structural features and some of the applications they are used for.

Table 2: List of known zincosilicate zeotype frameworks, their structural properties and known applications.

Name	Framework type	Unique zincosilicate framework?	Framework structure	Channel size (MRs) and dimensionality	Applications	Refs
Zn-MFI	MFI	N	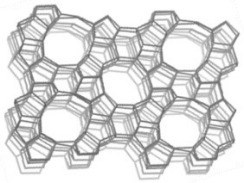	10, 6, 5, 4 3D	• Propane dehydrogenation with high selectivity towards propene • Cyclohexane conversion with high selectivity towards benzene • SCR of NO_x with NH_3 over broad range of temperatures	[86], [87]
CIT-6	BEA	N	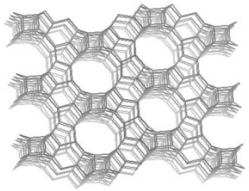	12, 6, 5, 4 3D	• More selective support for Ni^{2+} cations compared to aluminosilicate counterpart in the oligomerization of propylene • Stable support for platinum impregnation and application in propane dehydrogenation • Diels–Alder cycloaddition–dehydration reactions of ethylene with methyl 5-(methoxymethyl)furan-2- carboxylate	[88]–[90]
Zn-MOR	MOR	N	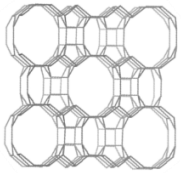	12, 8, 5, 4 2D	-	[79]
Zn-CHA	CHA	N	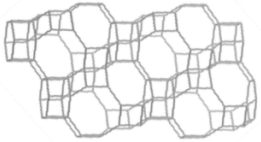	8, 6, 4 3D	• Superior divalent-cation exchange capacity compared to aluminosilicate counterpart	[83]

VPI-7	VSV	Y	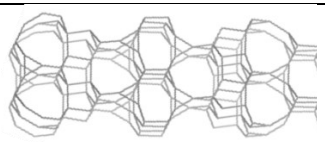	9, 8, 5, 4, **3** 3D	-	[66], [67]
VPI-8	VET	Y	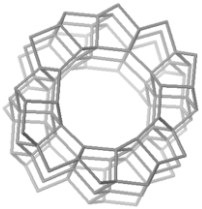	12, 8, 7, 6, 5 1D	-	[67]
VPI-9	VNI	Y	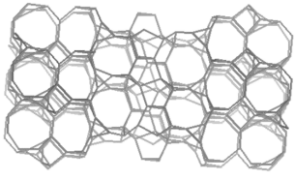	8, 5, 4, **3** 3D	• Superior divalent-cation conductivity compared to aluminosilicate zeolites	[67], [91]
RUB-17	RSN	Y	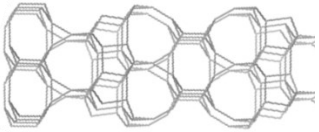	9, 8, 6, 5, 4, **3** 3D	-	[73]
Zn-SOD	SOD	N	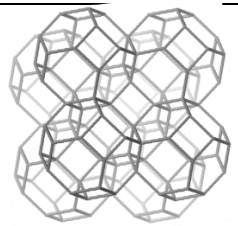	6, 4 0D	-	[78]
Zn-MWW	MWW	N	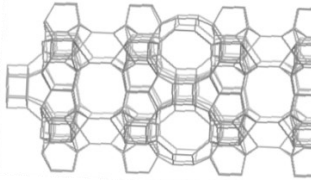	10, 6, 5, 4 2D	• Higher selectivity in oxidative dehydrogenation of 1-butene to 1,3-butadiene • Dehydrogenation of ethanol to acetaldehyde	[84]

Zn-FAU	FAU	N	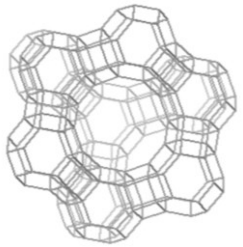	12, 6, 4 3D	○ Enhanced cation exchange capacity compared to aluminosilicate counterpart	[80]
Zn-AlPO-57	AFV	Y	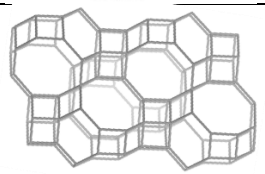	8, 6, 4 2D	-	[74]
Zn-AlPO-59	AVL	Y	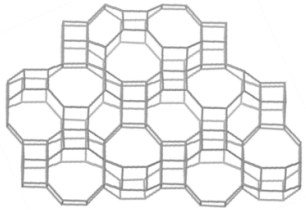	8, 6, 4 2D	-	[74]
UCSB-10GaZn	SBT	Y	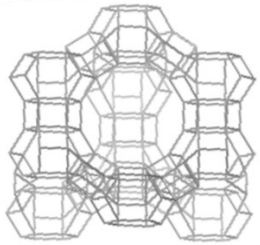	12, 8, 6, 4 3D	-	[92]
ZAPO-M1	ZON	Y	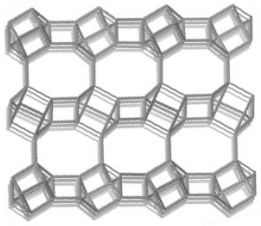	8, 6, 4 2D	-	[75]

Chiral Zincophosphate	CZP	Y	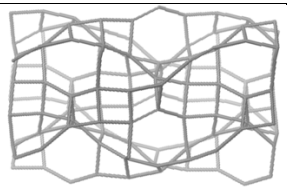	12, 8, 4 1D	-	[76]

1.1.7. Features and Applications of Zn-substituted zeotypes

Heteroatoms, and in particular Zn^{II} heteroatoms, can direct the crystallisation of a microporous framework towards unique structures that are not normally observed for aluminosilicate zeolites. For instance, the only report on the preparation of a zeolite containing 3 MR structures, ZSM-18 (MEI), involves the use of a specific quaternary ammonium cation (2,3,4,5,6,7,8,9-octahy-dro-2,2,5,5,8,8-hexamethyl-1H-benzo[1,2-c:3,4-c':5,-c'']tripyrrolium). [93], [94] On the other hand, 3 MR pore openings have been observed in the zincosilicates VPI-7 (VSV),[66] RUB-17 (RSN)[72] and VPI-9 (VNI).[70] The common feature between these frameworks is the presence of a specific spiro-5 building unit (Figure 8), which rarely occurs in tetrahedral frameworks due to the instability of the small T–O–T angles (130°).[71], [73]

In addition to structural modifications, the presence of Zn^{II} heteroatoms can potentially double the capacity of a zeotype to accommodate extra-framework cations, compared to an aluminosilicate analogue. This is due to the double negative framework charge introduced by $[ZnO_4]^{2-}$ framework tetrahedra. Koike et al. observed that the exchange of Ni^{2+} cations improved with the incorporation of framework Zn into ZSM-5 zeolites.[45] They have also shown that the uptake of monovalent cations (such as K^{+}) is favoured in aluminosilicate SSZ-13 (CHA), due to isolated monovalent negative framework charges, whilst the exchange of Ni^{2+} could only be successfully carried out in Zn-CHA.[83] However, complete exchange could not be achieved in Zn-CHA and the cause of this was attributed to the presence of "open" framework environments. These are species such as $[(SiO)_3Zn\cdots(HOSi)]^{-}$ that can be counter-balanced by a monovalent cation, as opposed to "closed" $[(SiO)_4Zn]^{2-}$ sites (Figure 9). These different framework sites have been reported by several studies and their formation is related to the synthetic and post-synthetic treatments applied to the zincosilicates.[101], [102], [115]

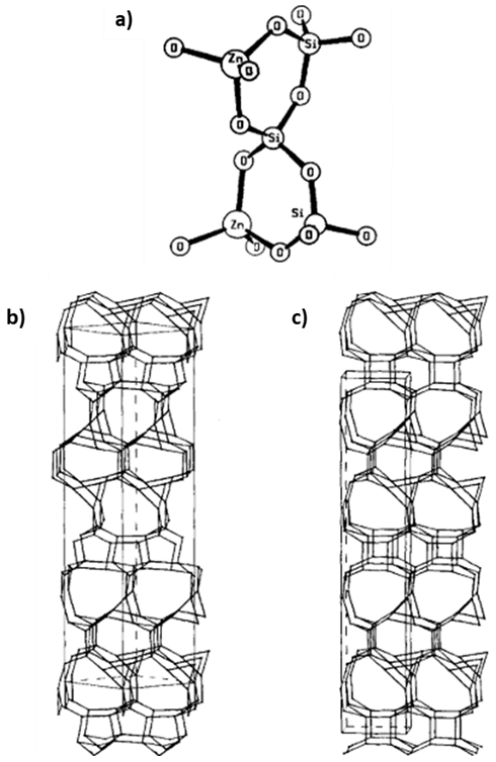

Figure 8: Spiro-5 building block contained in 3MR-based frameworks (a); representation of RUB-17 (b) and VPI-7 (c) framework structures: in the latter the building units are connected through 5MRs, while in RUB-17 this occurs through 4, 5 or 6MRs. Adapted with permission from ref [73].

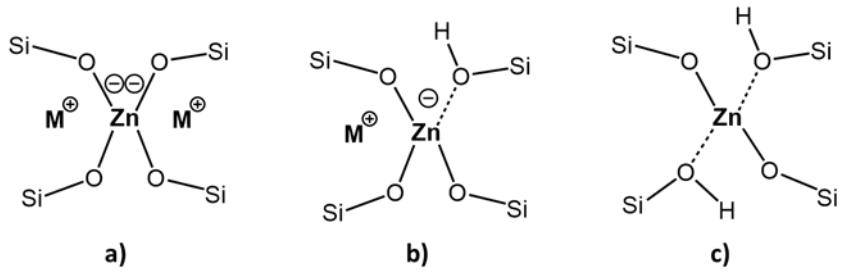

Figure 9: Representation of fully closed (a), and partially open (b) and (c) Zn^{II} sites substituted in a zeotype framework.

The acid properties of zincosilicate zeotypes are considerably different to those of aluminosilicate zeolites. Whilst the latter typically exhibit a more or less strong Brønsted acid character, with Lewis acidity present only to a certain extent and attributable to defective sites or extra-framework Al species, the substitution of Zn in framework sites was observed to shift the acid character from strong to moderate/weak. Evidence of this was collected in different studies; NH_3-TPD analysis revealed that the incorporation of Zn into the ZSM-5[95] or the MWW[84] frameworks caused a decrease in the number of strong acid sites, and a change of the materials' character to moderate acidity. Additionally, FTIR analysis coupled with pyridine adsorption over Zn-MWW showed an intense band at 1455 cm^{-1}, generally assigned to Lewis acid

sites, whilst the band assigned to Brønsted acid sites (at 1545 cm^{-1}) was almost absent.[84] This evidence, also observed in Zn-CHA,[83] Zn-MOR[79] and CIT-6 (BEA),[90] confirms that zincosilicate zeotypes are Lewis-acid materials. The strength of the Lewis acid sites in zincosilicates was found to be comparable to that of Sn-MCM-41, Sn-MFI and Zr-Beta by means of CD_3CN-FTIR.[90]

Lewis acid zeotypes are promising catalysts for reactions aimed at the production of more refined chemicals and the valorisation of feedstocks.[90] However, although some interesting examples of reactions catalysed by Zn-substituted zeotypes have been published, the full potential of these materials has not been reported yet. Orazov and Davis have reported the performance of different zincosilicates compared to other Lewis-acid or aluminosilicate zeolites for glucose isomerisation, Meerwein-Ponndorf-Verley-Oppenauer (MPVO) and Diels-Alder cycloaddition-dehydration reactions.[90] Among the results they reported, particularly noteworhy is the performance of CIT-6 in the Diels-Alder reaction of ethylene with methyl 5-(methoxymethyl)furan-2- carboxylate, where it showed a substantial increase in selectivity compared to a Zn^{2+}/Beta catalyst (50 % vs < 10 % under the same reaction conditions). Ni et al. have reported high activity, yield and lifetime with conversion as high as 100 % for the methanol to BTX reaction over a nanosized H^+/Zn,Al-ZSM-5 catalyst, compared to H^+/Al-ZSM-5 and impregnated ZnO/ZSM-5.[96] Additionally, the absence of strong Brønsted acidity in zincosilicate zeotypes makes them optimal candidates for dehydrogenation reactions, such as the dehydrogenation of ethanol to acetaldehyde. Significant evidence of the superior performance of Zn-substituted zeotypes for this application was reported by Yan et al. for a Zn-MWW catalyst, used for the oxidative dehydrogenation of 1-butene to 1,3-butadiene with CO_2 as oxidant and ethanol conversion to acetaldehyde under non-oxidative conditions. The results showed almost double selectivity and yield to 1,3-butadiene for the Zn-MWW catalyst, compared to ZnO-impregnated pure-silica MWW framework (ZnO/ITQ-1) and aluminosilicate MWW (ZnO/MCM-22). The outcome of the ethanol-to-acetaldehyde reactions were even more striking: the ethylene selectivity in the Zn-MWW catalyst was considerably lower than for ZnO/MCM-22, with 51 % acetaldehyde selectivity.[84] These results are direct effects of the replacement of the Brønsted acid character with moderate acidity provided by the Zn Lewis acid sites. Similar findings were recently reported by Qi et al. for the conversion of ethanol to acetaldehyde, achieved using Zn-substituted de-aluminated Beta catalysts.[97] In particular, they succeeded in the preparation of a bifunctional catalyst featuring isolated Zn and Y sites and observed that the dehydrogenation of ethanol to acetaldehyde took place exclusively on Zn sites, whilst the Y sites were responsible for the further conversion of acetaldehyde to 1,3-butadiene.

1.1.8. Synthesis and Characterisation of Zn-substituted Zeotypes

The most used strategy for the synthesis of zeolites is the hydrothermal treatment (temperature between 120 and 200 °C under autogenous pressure) of a synthesis gel prepared with a SiO_2 source, a metal source, alkali-metal or other metal hydroxide species and, occasionally, an organic structure directing agent (OSDA). This procedure was developed thanks to the pioneering work of Barrer et al. in the late 1940s, who tried to replicate geological hydrothermal synthesis conditions (> 200 °C and 100 bar) and prepared the first artificial zeolite (MOR).[98] Milton et al. then introduced the use of inorganic mineralising agents, fundamental to prepare zeolites at considerably lower temperature and pressure conditions (< 200 °C and autogenous pressure). This opened the way to the synthesis of zeolites with no natural counterparts.[99] In 1961 Barrer introduced the use of alkylammonium cations with the role of steering the synthesis products towards the formation of materials with specific framework structures. This was found to be extremely useful for the preparation of high-silica zeolites.[100]

The synthesis of a zeolite takes place thanks to condensation reactions occurring between O_3SiO^- and $HOSiO_3$ species:

$$O_3SiOH + OH^- \rightarrow O_3SiO^- + H_2O \qquad \text{Equation 2}$$

$$O_3SiO^- + HOSiO_3 \rightarrow O_3Si - O - SiO_3 + OH^- \qquad \text{Equation 3}$$

As shown in Equation 2 and Equation 3, the role of OH^- species as mineralising agent is extremely important, as it tailors the pH conditions of the synthesis mixture and assists the solubilisation of the silica source. The latter generally takes place at pH values of at least 10.[101] Particular care is required to identify the right amount of mineralising agent to add, as an excessive amount would promote the formation of dense phases rather than porous materials. Additionally, it is important to consider the formation of hydroxide species during the solubilisation of the precursors (Equation 3). Another noteworthy aspect is that different Si:T ratios (where T is a trivalent or divalent tetrahedral heteroatom) require different hydroxide concentrations. More specifically, high OH^- concentrations lead to high heteroatom contents and lower OH^- concentrations promote the formation of more siliceous products. This is due to the necessity to balance the negative framework charges provided by the insertion of the trivalent or divalent heteroatom in tetrahedral framework sites. Another factor that influences the insertion of the heteroatoms in the framework and, consequently, the Si:T ratio is the addition of OSDAs. Even though finding direct correlations between specific OSDAs and the formation of a particular zeolite structure is often challenging,[102], [103] it is possible to control the Si:T ratio by varying the amount or size of the OSDA employed in the synthesis.[104]

Some major challenges encountered in the design and rationalisation of the synthesis procedure and its outcome are the high number of variables that can affect the process and the metastable nature of the zeolite phases. This is due to the fact that the zeolite crystallisation is controlled by kinetic factors, as the porous phase can only form under certain conditions and naturally tends to turn into more dense phases.[105] Therefore, it is important to consider all the factors that can modify the outcome of the synthesis, especially for the synthesis of Zn-substituted zeotypes. These materials can be highly susceptible even to slight changes in the order of addition of the compounds during the synthesis or the type of inorganic cations. The latter were found to play a crucial role for the achievement of the desired zincosilicate phase. In fact, whilst some framework types, such as MFI, do not necessarily need the addition of an inorganic mineralising agent, products like VPI-8 require the use of Li^+ or Na^+, specifically (with addition of seeds for the latter). On the other hand, when the synthesis of VPI-8 was attempted using K^+, no zeolitic products were observed.[68], [69] Similarly, Zn-CHA could only be synthesised following a specific order of addition and using LiOH, whilst its replacement with NaOH or KOH led to poor results.[83]

Alongside the (limited) structure directing effect of the inorganic mineralising agent, organic structure directing agents (OSDAs) are what more profoundly affect the structural properties of the final synthesis products.[106] However, their use introduces economic and environmental issues related to a higher production cost and to the need of high temperature calcination procedures for the removal of the OSDA from the microporous products. Therefore, the development of synthesis strategies that do not include OSDAs is highly desirable. This is particularly challenging to achieve for the synthesis of zincosilicate zeotypes, due to the lower stability of Zn-substituted frameworks and to the fact that knowledge around nucleation and crystallisation mechanisms in these materials is only at an early stage.[107] Among the few reports on the preparation of OSDA-free zincosilicate zeotypes, worth noting is the contribution of Iyoki et al. for the OSDA-free synthesis of Zn-VET, achieved through the addition of VPI-8 seeds.[107] Other successful results were obtained by Koike et al. for the OSDA-free synthesis of zinco-aluminosilicate MOR and BEA zeotypes through the co-precipitation method.[108]

Given all the challenges of the design and synthesis of zincosilicate zeotypes, the characterisation of the final products is a crucial step in order to confirm the isomorphous subsitution of Zn heteroatoms in the framework. Different characterisation techniques are required in order to obtain a full picture of the features of a zincosilicate zeotype. Moreover, the use of Zn as heteroatoms introduces additional challenges, as it has been described as a "silent metal".[109] This is due to the fact that Zn^{2+} is a diamagnetic species with a filled d shell, which makes it "invisible" to certain techniques, such as UV-vis spectroscopy and Electron Para-magnetic Resonance (EPR). A technique generally extremely useful for the characterisation of

aluminosilicate zeolites is ^{27}Al solid-state NMR, used to probe the Al sites and detect the presence of extra-framework species. However, NMR spectroscopy cannot be applied to Zn, as the only NMR-active Zn isotope is ^{67}Zn, which has low natural abundance (4.04 %), low gyromagnetic ratio (γ = 1.678 x 10^7 rad T^{-1} s^{-1}) and a large quadrupole moment (Q = 0.150 x 10^{-28} m^2). These characteristics make it particularly hard to probe, in absence of isotopic enrichment or without magnetic fields higher than 18.8 T.[110] Methods used to overcome these issues rely on the use of X-ray-based spectroscopic techniques, such as X-ray Absorption Spectroscopy (XAS) carried out at synchrotron facilities.[111] The earliest report of XAS applied to the study of a zinc-modified zeotype dates back to 1993,[112] and showed the difference in the absorption edge shape between ZnO-impregnated and Zn^{2+}-exchanged ZSM-5 samples. In 1995 the first XAS analysis of a zincosilicate zeotype (Zn-ZSM-5) was published and highlighted the differences in the coordination environment of Zn species between Zn-substituted and Zn-modified materials.[113] Since then, the use of XAS to characterise framework-Zn species in zeotypes has become a consolidated and widely applied technique. Other X-ray-based techniques applied include X-Ray Photoelectron Spectroscopy (XPS)[80] and Auger spectroscopy.[114] However, there is only a limited number of studies employing these techniques, due to the higher complexity of the data analysis and limited availability of reference studies. Infrared spectroscopy can also be used to probe the vibrational modes of Si–O–T bonds, which are affected by the presence of different heteroatoms.[115] This technique was employed to probe Zn species in Zn-MOR,[79] Zn-MWW,[84] Zn-ZSM-5[116] and CIT-6.[117]

1.2. Conclusions and Areas of Future Research

Zeolites are materials with outstanding potential in several industrial applications. The presence of multidimensional channel systems, their tunable acidity and framework robustness, alongside with other physical and chemical properties, is what makes zeolites fundamental materials in applications such as ion exchange, absorption and catalysis. Recently, they are also becoming the focus of studies aimed at the implementation of sustainable alternatives to industrial processes. However, there are still aspects to be understood and improved regarding zeolites regarding their preparation and the optimisation of their properties, especially during the synthesis stage. Several studies focus on finding ways to make the zeolite synthesis itself a more sustainable process;[1] this could be achieved by introducing alternative synthesis methods, such as the microwave-assisted synthesis,[118] or reducing the use of OSDAs and solvents.

Heteroatom-substituted zeotypes represent a class of zeolite-like materials with different chemical and structural properties, which modulate fundamental features, for example

their acid properties, and design materials with specific characteristics, such as a more prominent Lewis acid character and lower Brønsted acidity. However, the profound changes due to the substitution of heteroatoms replacing Al^{III} in a microporous framework, in terms of bond angles, unit cell size and chemical properties, suggest how challenging the design and synthesis of new zeotypes can be. The simple replacement of the Al precursor for another metal precursor is not always successful, and often many attempts and changes in the synthesis method are required in order to achieve the desired products. Recently, efforts have been invested into the development of methods to control the position of heteroatoms in the framework and obtain a homogeneous heteroatom distribution. This can be achieved during the synthesis stage, by using different-sized OSDAs[119] or through alternative synthesis methods (e.g. ball milling),[116], [120], [121] or using post-synthetic treatments (e.g. metal grafting).[122]

Zinc-substituted zeotypes have been subjects of studies since 1991.[66] Since then, several framework types containing zinc heteroatoms have been prepared and their properties explored. Alongside the ability to form unique structures containing 3 MR pore openings, the presence of zinc heteroatoms allows for a more efficient exchange of divalent metal cations compared to aluminosilicate analogues.[45], [123] Additionally, the Lewis acid character provided by Zn sites makes them promising materials applicable in catalysis, as the absence of Brønsted acidity would guarantee a higher selectivity and yield for reactions such as Diels-Alder cycloaddition,[90] methanol upgrade[96] and ethanol dehydrogenation.[84], [97] This suggests that there is still more to uncover about the potential of zincosilicates as Lewis-acid catalysts. A research area that is be worth exploring is the use of zincosilicate zeotype catalysts in applications that normally employ Zn-modified zeolites. The introduction of zinc heteroatoms in framework positions, as opposed to extra-framework sites, could substantially improve the stability of the catalyst during the reaction and avoid issues related to leaching or sintering of the active metal sites. An example of this was observed by Ni et al. for the methanol-to-BTX reactions: the methanol conversion remained as high as 100% for 40 hours in H^+/Zn,Al-ZSM-5, whilst it started to decrease after only 17 hours in impregnated ZnO/ZSM-5.[96]

Despite the numerous challenges, the results obtained regarding the synthesis, property and structure characterisation and applications of zincosilicate zeotypes opened the way to a better understanding of this class of materials. Zincosilicate zeotypes have the potential to offer alternative, cost-effective solutions to various processes. Therefore, it is important that the research around these materials focuses on (i) developing more efficient synthesis strategies, (ii) elucidating the mechanisms that take place during the synthesis stages and (iii) finding suitable applications where the interesting properties of these catalysts can be beneficial.

Chapter 1 Bibliography

[1] X. Fan and Y. Jiao, *Porous Materials for Catalysis : Toward Sustainable Synthesis and Applications of Zeolites*. Elsevier Inc., **2020**.

[2] "Catalyst Market Size, Share & Trends Analysis Report," **2020**. doi: 978-1-68038-228-0.

[3] Carlo Perego and Roberto Millini, "Porous materials in catalysis: challenges for mesoporous materials," *Chem. Soc. Rev.*, 42, 9, pp. 3956–3976, **2013**, doi: 10.1039/C2CS35244C.

[4] Y. Li, L. Li, and J. Yu, "Applications of Zeolites in Sustainable Chemistry," *Chem*, 3, 6, pp. 928–949, **2017**, doi: 10.1016/J.CHEMPR.2017.10.009.

[5] G. A. Olah, "Beyond Oil and Gas : The Methanol Economy," *Angew. Chemie Int. Ed.*, 44, 18, pp. 2636–2639, **2005**, doi: 10.1002/anie.200462121.

[6] "Inventory of U.S. Greenhouse Gas Emissions and Sinks: 1990–2019," 2019. https://www.epa.gov/ghgemissions/inventory-us-greenhouse-gas-emissions-and-sinks.

[7] R. W. Howarth, "Methane emissions and climatic warming risk from hydraulic fracturing and shale gas development: implications for policy," *Energy Emiss. Control Technol.*, 3, pp. 45–54, **2015**, doi: 10.2147/EECT.S61539.

[8] K. Aasberg-Petersen, I. Dybkjær, C. V. Ovesen, N. C. Schjødt, J. Sehested, and S. G. Thomsen, "Natural gas to synthesis gas – Catalysts and catalytic processes," *J. Nat. Gas Sci. Eng.*, 3, 2, pp. 423–459, **2011**, doi: 10.1016/J.JNGSE.2011.03.004.

[9] R. Reimert F. Marschner, H.-J. Renner, W. Boll, E. Supp, M. Brejc, W. Liebner, G. Schaub, *Ullmann's Encyclopedia of Industrial Chemistry: Gas Production*. Wiley-VCH Verlag GmbH & Co. KGaA, **2011**.

[10] E. V. Kondratenko, T. Peppel, D. Seeburg, N. Kondratenko, Vita A. Kalevaru, M. Andreas, and S. Wohlrab, "Methane conversion into different hydrocarbons or oxygenates: Current status and future perspectives in catalyst development and reactor operation," *Catal. Sci. Technol.*, 7, pp. 366–381, **2016**, doi: 10.1039/C6CY01879C.

[11] "Siluria Technologies." https://www.biofuelsdigest.com/bdigest/2015/04/22/siluria-technologies-biofuels-digests-2015-5-minute-guide/ (accessed Oct. 04, 2021).

[12] B. A. Arndtsen, R. G. Bergman, T. A. Mobley, and T. H. Peterson, "Selective Intermolecular Carbon-Hydrogen Bond Activation by Synthetic Metal Complexes in Homogeneous Solution," *Acc. Chem. Res*, 28, pp. 154–162, **1995**, Accessed: Nov. 04, 2021. [Online]. Available: https://pubs.acs.org/sharingguidelines.

[13] M. Balat, H. Balat, and C. Öz, "Progress in bioethanol processing," *Prog. Energy Combust. Sci.*, 34, 5, pp. 551–573, **2008**, doi: 10.1016/J.PECS.2007.11.001.

[14] C. Manochio, B. R. Andrade, R. P. Rodriguez, and B. S. Moraes, "Ethanol from biomass: A comparative overview," *Renew. Sustain. Energy Rev.*, 80, pp. 743–755, **2017**, doi: 10.1016/J.RSER.2017.05.063.

[15] R. A. Dagle, A. D. Winkelman, K. K. Ramasamy, V. L. Dagle, and R. S. Weber, "Ethanol as a Renewable Building Block for Fuels and Chemicals," *Ind. Eng. Chem. Res.*, 59, 11, pp. 4843–4853, **2020**, doi: 10.1021/ACS.IECR.9B05729.

[16] I. Takahara, M. Saito, M. Inaba, and K. Murata, "Dehydration of Ethanol into Ethylene over Solid Acid Catalysts," *Catal. Letters*, 105, 3, pp. 249–252, **2005**, doi:

10.1007/S10562-005-8698-1.

[17] P. I. Kyriienko, O. V. Larina, S. O. Soloviev, and S. M. Orlyk, “Catalytic Conversion of Ethanol Into 1,3-Butadiene: Achievements and Prospects: A Review,” *Theor. Exp. Chem.*, 56, 4, pp. 213–242, **2020**, doi: 10.1007/s11237-020-09654-2.

[18] G. Pomalaza, P. Arango Ponton, M. Capron, and F. Dumeignil, “Ethanol-to-butadiene: The reaction and its catalysts,” *Catal. Sci. Technol.*, 10, 15, pp. 4860–4911, **2020**, doi: 10.1039/d0cy00784f.

[19] Y. Huang, “The catalytic dehydrogenation of ethanol by heterogeneous catalysts,” *Catalysis Science and Technology*, 11, 5. Royal Society of Chemistry, pp. 1652–1664, Mar. 07, 2021, doi: 10.1039/d0cy02479a.

[20] D. P. Serrano, J. A. Melero, G. Morales, J. Iglesias, and P. Pizarro, “Progress in the design of zeolite catalysts for biomass conversion into biofuels and bio-based chemicals,” *https://doi.org/10.1080/01614940.2017.1389109*, 60, 1, pp. 1–70, **2017**, doi: 10.1080/01614940.2017.1389109.

[21] H. Y. Luo, J. D. Lewis, and Y. Román-Leshkov, “Lewis Acid Zeolites for Biomass Conversion: Perspectives and Challenges on Reactivity, Synthesis, and Stability,” *Annu. Rev. Chem. Biomol. Eng.*, 7, 1, pp. 663–692, **2016**, doi: 10.1146/annurev-chembioeng-080615-034551.

[22] J. A. Botas, D. P. Serrano, A. García, and R. Ramos, “Catalytic conversion of rapeseed oil for the production of raw chemicals, fuels and carbon nanotubes over Ni-modified nanocrystalline and hierarchical ZSM-5,” *Appl. Catal. B Environ.*, 145, pp. 205–215, **2014**, doi: 10.1016/J.APCATB.2012.12.023.

[23] Z. Wang, R. Ma, and W. Song, “Influence of HSAPO-34, HZSM-5, and NaY on pyrolysis of corn straw fermentation residue via Py-GC/MS,” *J. Anal. Appl. Pyrolysis*, 122, pp. 183–190, **2016**, doi: 10.1016/J.JAAP.2016.09.025.

[24] J. Jae G. Foster, A. Hammond, K. Auerbach, R. Lobo, G. Huber, “Investigation into the shape selectivity of zeolite catalysts for biomass conversion,” *J. Catal.*, 279, 2, pp. 257–268, **2011**, doi: 10.1016/J.JCAT.2011.01.019.

[25] X. Zhao, L. Wei, S. Cheng, and J. Julson, “Review of Heterogeneous Catalysts for Catalytically Upgrading Vegetable Oils into Hydrocarbon Biofuels,” *Catal. 2017, Vol. 7, Page 83*, 7, 3, p. 83, **2017**, doi: 10.3390/CATAL7030083.

[26] Esben Taarning, C. M. Osmundsen, Xiaobo Yang, Bodil Voss, S. I. Andersen, and C. H. Christensen, “Zeolite -catalyzed biomass conversion to fuels and chemicals,” *Energy Environ. Sci.*, 4, 3, pp. 793–804, **2011**, doi: 10.1039/C004518G.

[27] Jifeng Pang, “Advances in catalytic dehydrogenation of ethanol to acetaldehyde,” *Green Chem.*, **2021**, doi: 10.1039/D1GC02799A.

[28] J. A. Keith and P. M. Henry, “The Mechanism of the Wacker Reaction: A Tale of Two Hydroxypalladations,” *Angew. Chemie Int. Ed.*, 48, 48, pp. 9038–9049, **2009**, doi: 10.1002/ANIE.200902194.

[29] J. Pang M. Zheng, C. Wang, X. Yang, H. Liu, X. Hua, J. Sun, Y. Wang, T. Zhang, “Hierarchical Echinus-like Cu-MFI Catalysts for Ethanol Dehydrogenation,” *ACS Catal.*, 10, 22, pp. 13624–13629, **2020**, doi: 10.1021/ACSCATAL.0C03860.

[30] D. Yu, W. Dai, G. Wu, N. Guan, and L. Li, “Stabilizing copper species using zeolite for ethanol catalytic dehydrogenation to acetaldehyde,” *Chinese J. Catal.*, 40, 9, pp. 1375–1384, **2019**, doi: 10.1016/S1872-2067(19)63378-4.

[31] J. Mielby, J. O. Abildstrøm, F. Wang, T. Kasama, C. Weidenthaler, and S. Kegnæs, "Oxidation of Bioethanol using Zeolite-Encapsulated Gold Nanoparticles," *Angew. Chemie*, 126, 46, pp. 12721–12724, **2014**, doi: 10.1002/ANGE.201406354.

[32] V. L. Sushkevich and I. I. Ivanova, "Mechanistic study of ethanol conversion into butadiene over silver promoted zirconia catalysts," *Appl. Catal. B Environ.*, 215, pp. 36–49, **2017**, doi: 10.1016/j.apcatb.2017.05.060.

[33] T. Yan D. Weili, W. Guangjun, L. Swen, M. Hunger, G. Naijia, L. Landong, "Mechanistic Insights into One-Step Catalytic Conversion of Ethanol to Butadiene over Bifunctional Zn-Y/Beta Zeolite," *ACS Catal.*, 8, 4, pp. 2760–2773, **2018**, doi: 10.1021/acscatal.8b00014.

[34] L. Qi, Y. Zhang, M. A. Conrad, C. K. Russell, J. Miller, and A. T. Bell, "Ethanol Conversion to Butadiene over Isolated Zinc and Yttrium Sites Grafted onto Dealuminated Beta Zeolite," *J. Am. Chem. Soc.*, 142, 34, pp. 14674–14687, **2020**, doi: 10.1021/jacs.0c06906.

[35] T. Pang Y. Xuanyu, Y. Chenyi, A. A. Elzatahry, A. Alghamdi, H. Xing, C. Xiaowei, Y. Deng, "Recent advance in synthesis and application of heteroatom zeolites," *Chinese Chem. Lett.*, 32, 1, pp. 328–338, **2021**, doi: 10.1016/J.CCLET.2020.04.018.

[36] S. T. Wilson, B. M. Lok, and E. M. Flanigen, "No Title," U.S. Pat. 4 310 440, 1982.

[37] B. M. Lok, C. A. Messina, R. L. Patton, R. T. Gajek, R. T. Cannon, and E. M. Flanigen, "No Title," US. Pat. 4 440 871, 1984.

[38] M. Taramasso, G. Perego, and B. Notari, "Preparation of porous crystalline synthetic material comprised of silicon and titanium oxides," 4410501A, 1983.

[39] M. E. Davis, "Zeolite-based catalysts for chemicals synthesis," *Microporous Mesoporous Mater.*, 21, 4–6, pp. 173–182, **1998**, doi: 10.1016/S1387-1811(98)00007-9.

[40] M. Ravi, V. L. Sushkevich, and J. A. Van Bokhoven, "Lewis Acidity Inherent to the Framework of Zeolite Mordenite," *J. Phys. Chem. C*, 123, 24, pp. 15139–15144, **2019**, doi: 10.1021/acs.jpcc.9b03620.

[41] G. L. Price, V. I. Kanazirev, and K. M. Dooley, "Characterization of [Ga]MFI via thermal analysis," *Zeolites*, 15, 8, pp. 725–731, **1995**, doi: 10.1016/0144-2449(95)00044-7.

[42] C. Otero Areán, G. Turnes Palomino, F. Geobaldo, and A. Zecchina, "Characterization of gallosilicate MFI-type zeolites by IR spectroscopy of adsorbed probe molecules," *J. Phys. Chem.*, 100, 16, pp. 6678–6690, **1996**, doi: 10.1021/jp952952a.

[43] J. B. Nagy R. Aiello, G. Giordano, A.Katovic, F. Testa, Z. Kónya, I. Kiricsi, "Isomorphous substitution in zeolites," *Molecular Sieves - Science and Technology*, 5. pp. 365–478, 2006, doi: 10.1007/3829_006.

[44] J. Dědeček, Z. Sobalík, and B. Wichterlová, "Science and Siting and Distribution of Framework Aluminium Atoms in Silicon-Rich Zeolites and impact on Catalysis," *Catal. Rev.*, 54, 2, pp. 135–223, **2012**, doi: 10.1080/01614940.2012.632662.

[45] N. Koike K. Iyoki, B. Wang, Y. Yanaba, S. P. Elangovan, K. Itabashi, W. Chaikittisilp, T. Okubo, "Increasing the ion-exchange capacity of MFI zeolites by introducing Zn to aluminosilicate frameworks," *Dalt. Trans.*, 47, 28, pp. 9546–9553, **2018**, doi: 10.1039/C8DT01391H.

[46] S. Raynes, M. A. Shah, and R. A. Taylor, "Direct conversion of methane to methanol with zeolites : towards understanding the role framework type," *Dalt. Trans.*, 48, 28, pp. 10364–10384, **2019**, doi: 10.1039/c9dt00922a.

[47] T. Sano K. Okabe, Y. Kohtoku, Y. Shimazaki, K. Saito, H. Takaya, K. Bando, “A new metal zeolite catalyst for the Fischer—Tropsch reaction,” *Zeolites*, 5, 3, pp. 194–196, **1985**, doi: 10.1016/0144-2449(85)90030-2.

[48] L. A. Rankel and E. W. Valyocsik, “No Title,” US Pat. 4 388 285, 1983.

[49] G. Dodwell, “PhD thesis,” Worcester Polytechnic Institute, **1984**.

[50] J. A. Rossin, C. Saldarriaga, and M. E. Davis, “Synthesis of cobalt containing ZSM-5,” *Zeolites*, 7, 4, pp. 295–300, **1987**.

[51] S. Jong and S. Cheng, “Reduction behavior and catalytic properties of cobalt containing ZSM-5 zeolites,” *Appl. Catal. A Gen.*, 126, pp. 51–66, **1995**.

[52] T. Inui, J.-B. Kim, and T. Takeguchi, “Synthesis and catalytic performance of cobalt-incorporated MFI-type silicates,” *Zeolites*, 17, 4, pp. 354–360, **1996**.

[53] K. Urabe, M. Koga, and Y. Itumi, “Synthetic Ni-substituted Saponite as a Catalyst for Selective Dimerization of Ethene,” *J. Chem. Soc., Chem. Commun.*, 12, pp. 807–808, **1989**.

[54] C. I. Round, C. D. Williams, K. Latham, and C. V. A. Duke, “Ni-ZSM-5 and Cu-ZSM-5 synthesized directly from aqueous fluoride gels,” *Chem. Mater.*, 13, 2, pp. 468–472, **2001**, doi: 10.1021/cm000591s.

[55] K. B. Sidhpuria and Æ. P. A. Parikh, “Simplified synthesis of isomorphously nickel substituted ZSM-5,” *J Porous Mater*, 15, pp. 481–489, **2008**, doi: 10.1007/s10934-007-9108-4.

[56] S. Naser and M. Yousefpour, “Isomorphous Substitution of Iron and Nickel into Analcime Zeolite,” *J. Inorg. Gen. Chem.*, 637, 6, pp. 759–765, **2011**, doi: 10.1002/zaac.201100059.

[57] R. Fernandez, M. Giotto, H. Pastore, and D. Cardoso, “Synthesis of characterization of MAPO-11 molecular sieves,” *Microporous Mesoporous Mater.*, 53, 1–3, pp. 135–144, **2002**, doi: 10.1016/S1387-1811(02)00333-5.

[58] Y. Wei, L. Zhang, and Z. Tian, “Isomorphous substitution induced ionothermal synthesis of magnesium aluminophosphate zeolites in fluoride-free media,” *RSC Adv.*, 6, 66, pp. 61915–61919, **2016**, doi: 10.1039/c6ra12678b.

[59] T. Wang, “Solvent-Free Synthesis of Mg-Incorporated Nanocrystalline SAPO-34 Zeolites via Natural Clay for Chloromethane-to-Olefin Conversion,” *Cite This ACS Sustain. Chem. Eng*, 8, pp. 4185–4193, **2020**, doi: 10.1021/acssuschemeng.9b07129.

[60] V. N. Romannikov, L. S. Chumachenko, V. M. Mastikhin, and K. G. Ione, “Synthesis and study of catalytic properties of beryllium silicates having zeolite-type structure,” *J. Catal.*, 94, 2, pp. 508–513, **1985**, doi: 10.1016/0021-9517(85)90215-5.

[61] T. E. Gier and G. D. Stucky, “Low-temperature synthesis of hydrated zinco(beryllo)-phosphate and arsenate molecular sieves,” *Nature*, 349, 6309, pp. 508–510, **1991**, doi: 10.1038/349508a0.

[62] S. Han, K. D. Schmitt, D. S. Shihabi, and C. O. Chang, “Isomorphous Substitution of Be*+ into ZSM-5 Zeolite with Ammonium Tetraf luoroberyllate,” *J. Chem. Soc., Chem. Commun.*, **1993**.

[63] P. McAnespie, A. Dyer, and J. M. Bharati, “Method of synthesizing zincosilicate or stannosilicate or titanosilicate material,” US4329328A, 1982.

[64] A. Katovic, E. Szymkowiak, G. Giordano, S. Kowalak, A. Fonseca, and J. B. Nagy,

"Preparation of zinc containing zeolite catalysts," in *Stud. Surf. Sci. Catal.*, 135, Elsevier, **2001**, p. 337.

[65] W. J. Ball, S. A. I. Barri, S. Cartlidge, B. M. Maunders, and D. W. Walker, "Zinc and aluminium substitutions in MFI-structures; Synthesis, characterisation and catalysis," in *Studies in Surface Science and Catalysis*, **1986**, 28, C, pp. 951–956, doi: 10.1016/S0167-2991(09)60969-1.

[66] M. J. Annen, M. E. Davis, J. B. Higgins, and J. L. Schlenker, "VPI-7: the first zincosilicate molecular sieve containing three-membered T-atom rings," *J. Chem. Soc. Chem. Commun.*, 17, pp. 1175–1176, **1991**.

[67] M. J. Annen, "Synthesis and characterization of novel molecular sieves containing three-membered rings," Virginia Tech, **1992**.

[68] M. Yoshikawa, S. I. Zones, and M. E. Davis, "Synthesis of VPI-8. I. The effects of reaction components," *Microporous Mater.*, 11, 3–4, pp. 127–136, **1997**, doi: 10.1016/S0927-6513(97)00031-X.

[69] M. Yoshikawa, S. I. Zones, and M. E. Davis, "Synthesis of VPI-8. II. Mechanism of crystallization," *Microporous Mater.*, 11, 3–4, pp. 137–148, **1997**, doi: 10.1016/S0927-6513(97)00032-1.

[70] M. J. Annen and M. E. Davis, "Raman and 29Si MAS NMR spectroscopy of framework materials containing three-membered rings," *Microporous Mater.*, 1, 1, pp. 57–65, **1993**, doi: 10.1016/0927-6513(93)80008-I.

[71] M. A. Camblor and M. E. Davis, "MAS NMR Spectroscopy of Tectozincosilicates," **1994**. Accessed: Jul. 21, 2020. [Online]. Available: https://pubs.acs.org/sharingguidelines.

[72] L. B. McCusker, R. W. Grosse-Kunstleve, C. Baerlocher, M. Yoshikawa, and M. E. Davis, "Synthesis optimization and structure analysis of the zincosilicate molecular sieve VPI-9," *Microporous Mater.*, 6, 5–6, pp. 295–309, **1996**, doi: 10.1016/0927-6513(96)00015-6.

[73] C. Röhrig and H. Gies, "A New Zincosilicate Zeolite with Nine-Ring Channels," *Angew. Chemie Int. Ed. English*, 34, 1, pp. 63–65, **1995**, doi: 10.1002/anie.199500631.

[74] R. W. Broach N. Greenlay, P. Jakubczak, L. M. Knight, S. R. Miller, J. P.S. Mowat, J. Stanczyk, G. J. Lewis, "New ABC-6 net molecular sieves ZnAPO-57 and ZnAPO-59: Framework charge density-induced transition from two- to three-dimensional porosity," *Microporous Mesoporous Mater.*, 189, pp. 49–63, **2014**, doi: 10.1016/j.micromeso.2013.09.022.

[75] B. Marler, J. Patarin, and L. Sierra, "Crystal structure of a novel porous MeAPO phase: ZAPO-M1, {N(CH3)4}8[Zn8Al24P32O128]," *Microporous Mater.*, 5, 3, pp. 151–159, **1995**, doi: 10.1016/0927-6513(95)00056-F.

[76] N. Rajić, N. Z. Logar, and V. Kaučič, "A novel open framework zincophosphate: Synthesis and characterization," *Zeolites*, 15, 8, pp. 672–678, **1995**, doi: 10.1016/0144-2449(95)00083-I.

[77] S. Kowalak, E. Szymkowiak, M. Gierczyńska, and G. Giordano, "Preparation and properties of MFI zincosilicate," in *Studies in Surface Science and Catalysis*, 142, R. Aiello, G. Giordano, and F. Testa, Eds. Elsevier, **2002**, pp. 351–358.

[78] M. A. Camblor, R. F. Lobo, H. Roller, and M. E. Davis, "Synthesis and Characterization of Zincosilicates with the SOD Topology," *Chem. Mater.*, 6, 11, pp. 2193–2199, **1994**, doi: 10.1021/cm00047a046.

[79] M. Dong, J. Wang, and Y. Sun, “Synthesis of zincosilicate mordenite using citric acid as complexing agent,” *Microporous Mesoporous Mater.*, 43, 2, pp. 237–243, **2001**, doi: 10.1016/S1387-1811(01)00211-6.

[80] R. A. Hunsicker, K. Klier, T. S. Gaffney, and J. G. Kirner, “Framework zinc-substituted zeolites: Synthesis, and core-level and valence-band XPS,” *Chem. Mater.*, 14, 11, pp. 4807–4811, **2002**, doi: 10.1021/cm0206690.

[81] T. Takewaki, L. W. Beck, and M. E. Davis, “Synthesis of CIT-6, a zincosilicate with the *BEA topology,” *Top. Catal.*, 9, 1–2, pp. 35–42, **1999**, doi: 10.1023/A:1019150203436.

[82] T. Takewaki, L. W. Beck, and M. E. Davis, “Zincosilicate CIT-6: A precursor to a family of *BEA-type molecular sieves,” *J. Phys. Chem. B*, 103, 14, pp. 2674–2679, **1999**, doi: 10.1021/jp9845726.

[83] N. Koike, K. Iyoki, S. H. Keoh, W. Chaikittisilp, and T. Okubo, “Synthesis of New Microporous Zincosilicates with CHA Zeolite Topology as Efficient Platforms for Ion-Exchange of Divalent Cations,” *Chem. - A Eur. J.*, 24, 4, pp. 808–812, **2018**, doi: 10.1002/chem.201705277.

[84] W. Yan X. Shibo, D. Yonghua, M. K. Schreyer, T. S. Xing, L. Yan, A. Borgna, “Heteroatomic Zn-MWW Zeolite Developed for Catalytic Dehydrogenation Reactions: A Combined Experimental and DFT Study,” *ChemCatChem*, 10, 14, pp. 3078–3085, **2018**, doi: 10.1002/cctc.201800199.

[85] Y. Sakamoto, H. Zhao, H. Gies, K. Yamamoto, U. Kolb, and T. Ikeda, “A new microporous 12-ring zincosilicate THK-2 with many terminal silanols characterized by automated electron diffraction tomography,” *Dalt. Trans.*, 49, 37, pp. 12960–12969, **2020**, doi: 10.1039/d0dt02290j.

[86] S. Kowalak E. Janiszewska, M. Gierczyliska, V. l. Dolata, N. Evmiridis, T. Katranas, A. Vlessidis, V. Tsiatouras, F. Roessner, E. Schneider, “Catalytic activity of zincosilicate MFI for the dehydrogenation of hydrocarbons,” *Stud. Surf. Sci. Catal.*, 154 C, pp. 2200–2207, **2004**, doi: 10.1016/s0167-2991(04)80477-4.

[87] E. Yuan, K. Zhang, G. Lu, Z. Mo, and Z. Tang, “Synthesis and application of metal-containing ZSM-5 for the selective catalytic reduction of NOx with NH3,” *J. Ind. Eng. Chem.*, 42, pp. 142–148, **2016**, doi: 10.1016/J.JIEC.2016.07.030.

[88] M. A. Deimund, J. Labinger, and M. E. Davis, “Nickel-exchanged zincosilicate catalysts for the oligomerization of propylene,” *ACS Catal.*, 4, 11, pp. 4189–4195, **2014**, doi: 10.1021/cs501313z.

[89] P. Andy and M. E. Davis, “Dehydrogenation of propane over platinum containing CIT-6,” *Ind. Eng. Chem. Res.*, 43, 12, pp. 2922–2928, **2004**, doi: 10.1021/ie030357m.

[90] M. Orazov and M. Davis, “Catalysis by framework zinc in silica-based molecular sieves,” *Chem. Sci.*, 7, pp. 2264–2274, **2016**, doi: 10.1039/C5SC03889H.

[91] J. C. McKeen and M. E. Davis, “Conductivity of mono- and divalent cations in the microporous zincosilicate VPI-9,” *J. Phys. Chem. C*, 113, 22, pp. 9870–9877, **2009**, doi: 10.1021/jp902235z.

[92] X. Bu, P. Feng, and G. D. Stucky, “Large-cage zeolite structures with multidimensional 12-ring channels,” *Science (80-.).*, 278, 5346, pp. 2080–2085, **1997**, doi: 10.1126/science.278.5346.2080.

[93] J. Ciric, “Synthetic zeolite ZSM-18,” 1976.

[94] S. L. Lawton and W. J. Rohrbaugh, “The Framework Topology of ZSM-18, a Novel Zeolite

Containing Rings of Three (Si,Al)-O Species," *Science (80-.).*, 247, 4948, pp. 1319–1322, **1990**, doi: 10.1126/SCIENCE.247.4948.1319.

[95] E. H. Yuan , K. Zhang, G. Lu, Z. Mo, and Z. Tang, "Structural and Textural Characteristics of Zn-Containing ZSM-5 Zeolites and Application for the Selective Catalytic Reduction of NOx with NH3 at High Temperatures," *Catal. Surv. from Asia*, 20, 1, pp. 41–52, **2016**, doi: 10.1007/s10563-015-9205-3.

[96] Y. Ni, S. Aiming, W. Xiaoling, H. Guoliang, H. Jianglin, L. Tao, L. Guangxing, "The preparation of nano-sized H[Zn, Al]ZSM-5 zeolite and its application in the aromatization of methanol," *Microporous Mesoporous Mater.*, 143, 2–3, pp. 435–442, **2011**, doi: 10.1016/j.micromeso.2011.03.029.

[97] L. Qi, Y. Zhang, M. A. Conrad, C. K. Russell, J. Miller, and A. T. Bell, "Ethanol Conversion to Butadiene over Isolated Zinc and Yttrium Sites Grafted onto Dealuminated Beta Zeolite," *J. Am. Chem. Soc.*, 142, 34, pp. 14674–14687, **2020**, doi: 10.1021/jacs.0c06906.

[98] R. M. Barrer, "Syntheses and Reactions of Mordenite.," *J. Chem. Soc.*, pp. 2158–2163, **1948**, doi: /10.1039/JR9480002158.

[99] R. M. Milton, "U.S. Patent 2882243," U.S. Patent 2882243, 1959.

[100] R. M. Barrer and P. J. Denny, "Hydrothermal Chemistry of the Silicates. Part IX. Nitrogenous Alurninosilicates.," *J. Chem. Soc.*, 201, pp. 971–982, **1961**, Accessed: Aug. 14, 2020. [Online].

[101] J. Cejka, R. E. Morris, and P. Nachtigall, *Zeolites in Catalysis: Properties and Applications*. RSC, **2017**.

[102] S. L. Lawton and W. J. Rohrbaugh, "The Framework Topology of ZSM-18, a Novel Zeolite Containing Rings of Three (Si,Al)-O Species," *Science (80-.).*, 247, 4948, pp. 1319–1322, **1990**.

[103] J. P. Arhancet and M. E. Davis, "Systematic Synthesis of Zeolites That Contain Cubic and Hexagonal Stackings of Faujasite Sheets," *ChEMisrayof Mater. Vol.*, 3, 4, Accessed: Oct. 25, 2021. [Online]. Available: https://pubs.acs.org/sharingguidelines.

[104] R. Millini and G. Bellussi, "Chapter 1 Zeolite Science and Perspectives," pp. 1–36, **2017**, doi: 10.1039/9781788010610-00001.

[105] A. Navrotsky, O. Trofymluk, and A. A. Levchenko, "Thermochemistry of Microporous and Mesoporous Materials," *Chem. Rev.*, 109, 9, pp. 3885–3902, **2009**, doi: 10.1021/CR800495T.

[106] M. Moliner, "Basic principles of zeolite synthesis," in *Zeolites and Ordered Porous Solids: Fundamentals and Applications*, C. Martínez and J. Pérez-Pariente, Eds. Editorial Universitat Politècnica de València, **2011**, pp. 37–56.

[107] K. Iyoki K. Itabashi, W. Chaikittisilp, S. P. Elangovan, T. Wakihara, S. Kohara, T. Okubo, "Broadening the applicable scope of seed-directed, organic structure-directing agent-free synthesis of zeolite to zincosilicate components: A case of VET-type zincosilicate zeolites," *Chem. Mater.*, 26, 5, pp. 1957–1966, **2014**, doi: 10.1021/cm500229f.

[108] N. Koike W. Chaikittisilp, K. Iyoki, Y. Yanaba, T. Yoshikawa, S. P. Elangovan, K. Itabashi, T. Okubo, "Organic-free synthesis of zincoaluminosilicate zeolites from homogeneous gels prepared by a co-precipitation method," *Dalt. Trans.*, 46, 33, pp. 10837–10846, **2017**, doi: 10.1039/c7dt02001e.

[109] O. McCubbin Stepanic, J. Ward, J. E. Penner-Hahn, A. Deb, U. Bergmann, and S. Debeer, "Probing a Silent Metal: A Combined X-ray Absorption and Emission Spectroscopic Study

of Biologically Relevant Zinc Complexes," *Inorg. Chem.*, **2020**, doi: 10.1021/acs.inorgchem.0c01931.

[110] K. H. Mroué and W. P. Power, "High-field solid-state 67Zn NMR spectroscopy of several zinc-amino acid complexes," *J. Phys. Chem. A*, 114, 1, pp. 324–335, **2010**, doi: 10.1021/jp908325n.

[111] M. Juneau, R. Liu, Y. Peng, A. Malge, Z. Ma, and M. D. Porosoff, "Characterization of Metal-zeolite Composite Catalysts: Determining the Environment of the Active Phase," *ChemCatChem*, pp. 1826–1852, **2019**, doi: 10.1002/cctc.201902039.

[112] C. Hennig, F. Thiel, K. H. Hallmeiér, R. Szargan, A. Hagen, and F. Roessner, "Characterization of Zn centers in ZSM-5 zeolites with X-ray absorption spectroscopy," *Spectrochim. Acta Part A Mol. Spectrosc.*, 49, 10, pp. 1495–1497, **1993**, doi: 10.1016/0584-8539(93)80054-E.

[113] A. Hagen, K. Hallmeier, C. Hennig, R. Szargan, T. Inui, and F. Roessner, "State of Zn in MFI type zeolites characterized by XANES and EXAFS," in *Studies in Surface Science and Catalysis*, H. K. Beyer, J. B. Nagy, H. G. Karge, and I. Kiricsi, Eds. Elsevier, **1995**, pp. 195–202.

[114] X. Collard, P. Louette, S. Fiorilli, and C. Aprile, "High surface area zincosilicates as efficient catalysts for the synthesis of ethyl lactate: an in-depth structural investigation," *Phys. Chem. Chem. Phys.*, 17, 40, pp. 26756–26765, **2015**, doi: 10.1039/C5CP03577E.

[115] D. Scarano A. Zecchina, S. Bordiga, F. Geobaldo, G. Spoto, "Fourier-transform Infrared and Raman Spectra of Pure and Al-, B-, Ti-and Fe-substituted Silicalites: Stretching-mode Region," **1993**.

[116] P. Hu K. Iyoki, H.i Yamada, Y. Yanaba, K. Oharac, N. Katadad, T. Wakihara, "Synthesis and characterization of MFI-type zincosilicate zeolites with high zinc content using mechanochemically treated Si–Zn oxide composite," *Microporous Mesoporous Mater.*, 288, p. 109594, **2019**, doi: 10.1016/J.MICROMESO.2019.109594.

[117] S. R. Tomlinson, T. McGown, J. R. Schlup, and J. L. Anthony, "Infrared Spectroscopic Characterization of CIT-6 and a Family of *BEA Zeolites," *Int. J. Spectrosc.*, 2013, pp. 1–7, **2013**, doi: 10.1155/2013/961404.

[118] Z. Sun, Y. Yan, G. Li, Y. Zhang, and Y. Tang, "Microwave Influence on Different M − O Bonds During MFI-Type Heteroatom (M) Zeolite Preparation," *Ind. Eng. Chem. Res.*, 56, 39, pp. 11167–11174, **2017**, doi: 10.1021/acs.iecr.7b03072.

[119] Mizuho Yabushita, Ryota Osuga, and Atsushi Muramatsu, "Control of location and distribution of heteroatoms substituted isomorphously in framework of zeolites and zeotype materials," *CrystEngComm*, 23, 36, pp. 6226–6233, **2021**, doi: 10.1039/D1CE00912E.

[120] K. Yamamoto, S. E. Borjas García, and A. Muramatsu, "Zeolite synthesis using mechanochemical reaction," *Microporous Mesoporous Mater.*, 101, 1-2 SPEC. ISS., pp. 90–96, **2007**, doi: 10.1016/j.micromeso.2006.09.034.

[121] S. E. Borjas Garcia, K. Yamamoto, and A. Muramatsu, "Synthesis of Ti-Beta via mechanochemical route," in *Journal of Materials Science*, **2008**, 43, 7, pp. 2367–2371, doi: 10.1007/s10853-007-2104-x.

[122] D. T. Bregante, J. Zhi Tan, Andre Sutrisno, and D. W. Flaherty, "Heteroatom substituted zeolite FAU with ultralow Al contents for liquid-phase oxidation catalysis," *Catal. Sci. Technol.*, 10, 3, pp. 635–647, **2020**, doi: 10.1039/C9CY01886G.

[123] M. A. Deimund, J. Labinger, and M. E. Davis, “Nickel-exchanged zincosilicate catalysts for the oligomerization of propylene,” *ACS Catal.*, 4, 11, pp. 4189–4195, **2014**, doi: 10.1021/cs501313z.

1

2. Chapter 2: Project Aims

2.1. Project Aims

Several aspects of the synthesis, characterisation and applications of zincosilicate zeotypes still remain to be explored. In particular, it is yet to be fully understood how the various synthesis parameters influence the outcome of the process. As reported by Yoshikawa et al. and Koike et al., a fundamental role during the synthesis of zincosilicate zeotypes is played by the inorganic cations,[1]–[3] which can profoundly change the nature of the reaction products. Another aspect to consider, which directly affects the properties of the zeotype, is the presence of structural defects in the form of Si–OH sites. The presence of these defective sites has been reported in previous studies,[2]–[4] and they have been observed to affect the ability of the zincosilicates to reach higher levels of divalent cation exchange. In addition to this, the acidity associated with Si–OH protons could compromise the performance of the materials in applications that require the absence of Brønsted acidity. The mechanisms and conditions of formation of these defective sites is mostly unknown; however, Dib et al. reported the evidence of correlations between defective sites in zeolites and the interactions of the structure with OSDA molecules.[5], [6]

The full characterisation of zincosilicate zeotypes is fundamental to understand their properties and potential applications. The most important information needed for the characterisation of a zincosilicate zeotype is the coordination environment of the Zn^{II} heteroatoms in the framework. In particular, it is fundamental to confirm that they occupy tetrahedral framework sites, ideally in a fully closed environment.

The substitution of Zn^{II} heteroatoms in a zeotype framework produces a divalent negative framework charge associated to each Zn^{II} site (if in a fully closed environment). This provides these materials with the ability to accommodate and stabilise divalent extra-framework cations more easily and efficiently than aluminosilicate zeolites, by eliminating the need of having two metal sites in close proximity.[3], [7]–[9] Moreover, various reports highlighted the potential of framework Zn^{II} sites in catalysis, thanks to their Lewis acid character.[9]–[11] Yan et al. demonstrated that the framework-Zn sites in Zn-MWW were able to catalyse the dehydrogenation of ethanol to acetaldehyde with high selectivity (51 %) compared to a Zn-modified aluminosilicate analogue.[10] Qi et al. also showed that Zn^{II} sites post-synthetically substituted in de-aluminated BEA were able to produce acetaldehyde from ethanol with as high as 65 % selectivity.[11] However, there are still several other applications to be explored using zincosilicate zeotypes as catalysts.

This work was aimed at the study of zincosilicate zeotypes, in particular Zn-ZSM-5. The first part of the project was dedicated to finding a suitable synthesis method that would deliver highly crystalline products. The synthesis method was then optimised in order to obtain good

ion-exchange capacity in the Zn-ZSM-5 samples and improve other aspects, such as the particle size distribution. Additionally, the healing of framework defective sites and the identification of open and closed framework environments around the Zn^{II} sites were carefully analysed.

The materials obtained were thoroughly characterised by means of several techniques. XAS was employed in to confirm the presence of tetrahedrally coordinated Zn^{II} sites, and detect changes in their chemical environment caused by coordination with water in samples exposed to atmospheric moisture. Solid-state NMR spectroscopy was used to reveal the nature of the ^{29}Si atoms and the presence of defects in the form of Si–OH sites. Other characterisation techniques helped corroborate these observations, such as diffuse-reflectance FT-IR spectroscopy (DRIFTS) and TGA analysis.

The completely characterised Zn-ZSM-5 samples were finally used in chemical reactions. The direct methane-to-methanol conversion was attempted using Zn-ZSM-5 samples upon zinc vapour deposition, using the methods developed in the group by Shah et al.[12] Additionally, Zn-ZSM-5 samples were employed for the dehydrogenation of ethanol to acetaldehyde using a flow reactor and procedures adapted from the work of Raynes et al.[13] Other Lewis-acid catalysed reactions were also explored, in order to expand the collection of applications that could benefit by the isomorphous substitution of Zn^{II} heteroatoms in the microporous framework of a zeolite-like material.

Chapter 2 Bibliography

[1] M. Yoshikawa, S. I. Zones, and M. E. Davis, "Synthesis of VPI-8. I. The effects of reaction components," *Microporous Mater.*, 11, 3–4, pp. 127–136, **1997**, doi: 10.1016/S0927-6513(97)00031-X.

[2] M. Yoshikawa, S. I. Zones, and M. E. Davis, "Synthesis of VPI-8. II. Mechanism of crystallization," *Microporous Mater.*, 11, 3–4, pp. 137–148, **1997**, doi: 10.1016/S0927-6513(97)00032-1.

[3] N. Koike, K. Iyoki, S. H. Keoh, W. Chaikittisilp, and T. Okubo, "Synthesis of New Microporous Zincosilicates with CHA Zeolite Topology as Efficient Platforms for Ion-Exchange of Divalent Cations," *Chem. - A Eur. J.*, 24, 4, pp. 808–812, **2018**, doi: 10.1002/chem.201705277.

[4] M. J. Annen and M. E. Davis, "Raman and 29Si MAS NMR spectroscopy of framework materials containing three-membered rings," *Microporous Mater.*, 1, 1, pp. 57–65, **1993**, doi: 10.1016/0927-6513(93)80008-I.

[5] E. Dib, J. Grand, S. Mintova, and C. Fernandez, "Structure-Directing Agent Governs the Location of Silanol Defects in Zeolites," *Chem. Mater.*, 27, 22, pp. 7577–7579, **2015**, doi: 10.1021/acs.chemmater.5b03668.

[6] E. Dib, J. Grand, A. Gedeon, S. Mintova, and C. Fernandez, "Control the position of framework defects in zeolites by changing the symmetry of organic structure directing agents," *Microporous Mesoporous Mater.*, p. 110899, **2021**, doi: 10.1016/j.micromeso.2021.110899.

[7] N. Koike, K. Iyoki, B. Wang, Y. Yanaba, S. P. Elangovan, K. Itabashi, W. Chaikittisilp, T. Okubo "Increasing the ion-exchange capacity of MFI zeolites by introducing Zn to aluminosilicate frameworks," *Dalt. Trans.*, 47, 28, pp. 9546–9553, **2018**, doi: 10.1039/C8DT01391H.

[8] B. Wang, N. Koike, K. Iyoki, Y. Wang, and T. Okubo, "Insights into the ion-exchange properties of Zn(ii)-incorporated MOR zeolites for the capture of multivalent cations," *Phys. Chem. Chem. Phys.*, 21, 7, pp. 4015–4021, **2019**, doi: 10.1039/c8cp06975a.

[9] M. Orazov and M. Davis, "Catalysis by framework zinc in silica-based molecular sieves," *Chem. Sci.*, 7, pp. 2264–2274, **2016**, doi: 10.1039/C5SC03889H.

[10] W. Yan, X. Shibo, D. Yonghua, M. K. Schreyer, T. S. Xing, L. Yan, A. Borgna "Heteroatomic Zn-MWW Zeolite Developed for Catalytic Dehydrogenation Reactions: A Combined Experimental and DFT Study," *ChemCatChem*, 10, 14, pp. 3078–3085, **2018**, doi: 10.1002/cctc.201800199.

[11] L. Qi, Y. Zhang, M. A. Conrad, C. K. Russell, J. Miller, and A. T. Bell, "Ethanol Conversion to Butadiene over Isolated Zinc and Yttrium Sites Grafted onto Dealuminated Beta Zeolite," *Cite This J. Am. Chem. Soc*, 142, pp. 14674–14687, **2020**, doi: 10.1021/jacs.0c06906.

[12] M. A. Shah, S. Raynes, D. C. Apperley, and R. A. Taylor, "Framework Effects on Activation and Functionalisation of Methane in Zinc-Exchanged Zeolites," *ChemPhysChem*, 21, pp. 673–679, **2020**, doi: 10.1002/cphc.201900973.

[13] S. J. Raynes and R. A. Taylor, "Zinc oxide-modified mordenite as an effective catalyst for the dehydrogenation of (bio)ethanol to acetaldehyde," *Sustain. Energy Fuels*, 5, 7, pp. 2136–2148, **2021**, doi: 10.1039/d1se00091h.

3. Chapter 3: Experimental Details and Characterisation Techniques

3.1. Experimental Methods

3.1.1. Experimental Details for Chapter 4

3.1.1.1. Hydrothermal Synthesis and Calcination

The hydrothermal syntheses were carried out in stainless steel autoclaves fitted with Teflon liners on a 25 ml scale. The zeolite materials were prepared starting from known procedures, conveniently modified. The synthesis gels were prepared using water as a solvent, a source of silica, a metal salt, an inorganic mineralising agent (if required) and an organic structure directing agent (if required). After an aging time depending on the desired product, carried out under magnetic stirring, the synthesis gels were transferred into the autoclaves and placed in a Carbolite AX 30 oven in static conditions, at temperatures ranging between 160 and 180 °C for the required amount of time. After the hydrothermal treatment, the products were separated from their mother liquor, washed with de-ionised water and centrifuged to eliminate the washing water for a number of times necessary to lower the pH of the latter to approximately 8; the products were then dried overnight in an oven at 100 °C. When an organic structure directing agent was used in the synthesis, the materials needed to undergo a high-temperature calcination procedure in order to remove it. This was carried out in a crucible placed in a muffle furnace (Carbolite CWF 11/13, Carbolite HTC 16/3 or Carbolite RHF 14/3) and heated to 150 °C at 5 °C/min for 1 h and subsequently to 550 °C at 5 °C/min for 6 h.

Detailed descriptions of the synthesis procedures are reported in Chapter 4.

All chemicals used in this Chapter are listed in Table 3.

Table 3: Chemicals used in Chapter 4, their providers and purities.

Name	Source	Purity/concentration
Zinc acetate dihydrate	ACROS Organics	98% extra pure
Lithium hydroxide monohydrate	Alfa Aesar	98%
LUDOX AS-30	Sigma Aldrich	30% SiO_2 in water
Pyrrolidine	Sigma Aldrich	99%
Zinc nitrate hexahydrate	ACROS Organics	98% extra pure
Ammonium nitrate	Sigma Aldrich	≥98%
Magnesium nitrate hexahydrate	Alfa Aesar	98%
Tetraethyl orthosilicate	Fisher Scientific UK	98%
Nickel nitrate hexahydrate	Alfa Aesar	98%
Potassium hydroxide	Fisher Scientific UK	86%
Tetrapropyl ammonium hydroxide	ACROS Organics	25% in water
Zinc chloride anhydrous	Fisher Scientific UK	≥97 %
Tetraethyl ammonium hydroxide	Alfa Aesar	20% in water
Magnesium chloride hexahydrate	Alfa Aesar	≥98%
Titanium isopropoxide	Sigma Aldrich	97%
Cobalt nitrate hexahydrate	Fisher Scientific UK	98%
Potassium nitrate	ACROS Organics	99%
Cobalt chloride hexahydrate	Sigma Aldrich	≥97%
Nickel chloride hexahydrate	Sigma Aldrich	99.9%

3.1.1.2. Microwave-assisted Synthesis

The microwave-assisted synthesis was carried out in an Anton Parr Multiwave GO microwave equipped with Teflon vessels and was employed to synthesise zincosilicate ZSM-5 samples in a considerably shorter amount of time compared to the hydrothermal procedure. The synthesis gel was prepared following the same procedure used for hydrothermally synthesised Zn-ZSM-5 samples and transferred to the microwave vessel. The vessel was heated to 170 °C from room temperature in 10 minutes and subsequently maintained at 170 °C for 1 h or 2.5 h. The solid products were recovered, separated from the mother liquor and washed as described above.

3.1.2. Experimental Details for Chapter 6

3.1.2.1. ZnO Impregnation

The impregnation of ZnO into the zeolite samples was carried out using 0.5 g of zeotype powder and 1.4 ml of $Zn(NO_3)_2$ solution. The amount of $Zn(NO_3)_2$ to use was calculated according to the desired loading of Zn in specific samples. The mixture of zeolite and Zn solution was manually stirred and then dried at room temperature, prior to being fully dried under vacuum at 50 °C for 2 hours. Subsequently, the powder obtained was ground in a mortar for 20 minutes and finally calcined at 550 °C for 6 hours.

3.1.2.2. Zn^0 Chemical Vapour Deposition

The vapourisation of zinc metal was carried out in a custom-made quartz u-tube equipped with a close fitting borosilicate glass insert according to the procedure reported by Shah et al.[1] The u-tube containing the previously dehydrated zeolite (approximately 100 mg) was loaded with a known amount of Zn^0 powder (Goodfellow, 99.9%, max particle size 150 µm) in an Ar-filled glovebox (Ar purchased from BOC, 99.998% purity); the Zn^0 powder and the zeolite were held between two glass wool plugs. Once sealed and removed from the glovebox, the u-tube was attached to a Schlenk line and placed under reduced pressure (< 10^{-2} mbar). The u-tube was then sealed and inserted in a Carbolite tube furnace, making sure that the zeolite and Zn^0 powder were placed in the isothermal zone of the furnace. The latter was then heated to 500 °C with a 5 °C/min ramp rate and held for 1 h under static vacuum. Subsequently, the u-tube was opened to the Schlenk line and held at 500 °C for 2 h under dynamic vacuum conditions, in order to remove excess unreacted zinc vapour, which condensed on the inside of the borosilicate glass insert. This setup would allow to remove the insert and recover the zeolite powder avoiding contamination with excess Zn^0. The Zn^0 vapour deposition setup is shown in Figure 10**.**

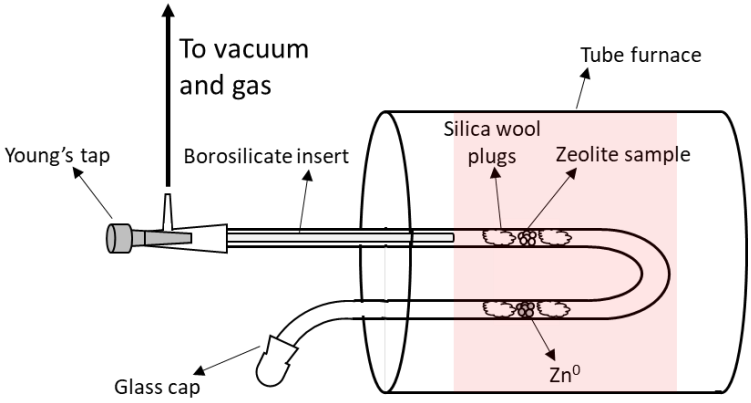

Figure 10: Experimental setup for the Zn^0 vapour deposition procedure carried out on zeolite powders. The area highlighted in red represents the isothermal zone of the tube furnace.

3.1.2.3. Methane Activation Reaction

Methane activation reactions were carried out directly after the Zn^0 vapour deposition procedure by exposing the u-tube to 1 atm of methane (purchased from BOC, 99.995% purity) at 250 °C. After the exposure to methane, the tube was sealed and held at 250 °C for 15 minutes. After cooling, the sealed tube was taken into the Ar glovebox, where an NMR rotor was packed with the sample and the NMR experiment carried out straight after the reaction. When labelled $^{13}CH_4$ (Sigma Aldrich, 99% ^{13}C) was used, the Schlenk line was backfilled with N_2 (BOC, oxygen free) prior to the exposure of the u-tube to the gas at 250 °C for three briefs intervals of 5 seconds, after which the system was maintained at 250 °C for 15 minutes.

3.1.3. Experimental Details for Chapter 7

3.1.3.1. Epoxidation Reaction of 1-hexene with H_2O_2

The reaction conditions were adapted from Li et al.[2] The epoxidation of 1-hexene (ACROS organics, 97 %) was carried out in a 100 ml round bottom flask equipped with an air condenser and immersed in an oil bath. 32 mmol of 1-hexene were reacted with 29 mmol of H_2O_2 (Fisher Scientific UK, 30 vol % in water, Extra Pure) using methanol (Fisher Scientific UK, 99.8 %) as a solvent (30 ml). 400 mg of catalyst were then added and the reaction was stirred at 60 °C for 5 hours. After this time, the reaction was cooled down to room temperature and the solids were separated from the liquid phase by centrifugation. Subsequently, the aqueous and organic phases were separated using a separation funnel and the organic layer was dispersed in diethyl ether (Fisher Scientific UK, ≥99%). The latter was then analysed by GC-MS (Shimadzu GC-2010 Plus).

3.1.3.2. Prins Condensation Reaction of β-pinene with Paraformaldehyde

The reaction conditions were adapted from Marakatti et al.[3] The condensation reaction was carried out in a 100 ml round bottom flask equipped with a water condenser and immersed in an oil bath. 10 mmol of β-pinene (Merck Life Science UK, 98 %) and 20 mmol of paraformaldehyde (Alfa Aesar, 97 %) were added to 10 ml of acetonitrile (Fisher Scientific UK, HPLC grade), with 400 mg of catalyst, and the reaction was heated up to 90 °C and stirred at this temperature for 6 hours. 1 ml aliquots were withdrawn every hour and analysed by GC-MS (Shimadzu GC-2010 Plus).

3.1.3.3. Ethanol Conversion Reactions

The reaction conditions were adapted from Raynes et al.[4] The ethanol conversion reactions were performed using a HEL FlowCAT flow reactor, feeding ethanol (absolute, Fisher Scientific UK, 99.8 %) via an Eldex Optos 1 HPLC pump. The catalysts were prepared for the

reaction by pressing them at 10 tons for 1 minute using an Apollo Scientific XRF die equipped with 32 mm KBX-320 pellets and using a Specac hydraulic press. Subsequently, the catalysts were sieved between 40 to 60 mesh (420–250 mm) and the desired amount of catalyst transferred to a stainless-steel reactor with a 4 mm internal diameter. The reactor was packed with a 1.4 g SiC (technical grade, Fisher Scientific UK, approx. 80 grit) pre-bed, the catalyst diluted with approximately 1.4 g SiC and a 1.5 g SiC post-bed. The catalysts were pre-treated in-situ at 150 °C for 1 hour and then at 400 °C for 30 minutes under flowing N_2. Following the pre-treatment, the reactor was adjusted at the desired temperature (350 °C or 400 °C) with a ramping rate of 10 °C/min. The system was then further purged with flowing N_2 for 30 minutes before starting the ethanol flow (0.015 or 0.025 ml/min). The products were analysed on-line by GC-MS-BID (Shimadzu GC-2010 Plus) equipped with BPX90 (SGE Analytical) or RTX-VMS (Thames Restek) columns for mass spectrometry (MS) detection and a ShinCarbon ST (Thames Restek) column for barrier ionisation discharge (BID) detection.

3.2. Characterisation Techniques

3.2.1. Powder X-ray Diffraction

Powder X-ray diffraction (p-XRD) is a technique used for the characterisation of crystalline materials. It is a highly accessible, straightforward, non-destructive technique and it is widely applied to the structural investigation of zeolites and zeolite-like materials. Powder-XRD is especially useful to identify the phases present in the bulk of a sample; The p-XRD pattern of a zeolite framework provides, therefore, a fingerprint of that specific framework type.[5]–[8] For these reasons, p-XRD was regularly used to assess the crystallinity and phase purity of synthesised zincosilicates and other heteroatom-substituted zeolite-like materials. The typical X-ray wavelength λ is around 1 Å, which is comparable with the distance d between two crystallographic planes (Figure 11). Bragg's formulation of the diffraction phenomenon (Equation 4) describes the necessary geometric conditions required in order to observe constructive interference between scattered X-rays. In a p-XRD pattern, the positions of the peaks (or reflections) are related to the unit cell size, whilst their intensity is an indication of the type and positions of the atoms in the unit cell. The peak width and background depend on the quality of the sample and the presence of amorphous species.[5]

Powder-XRD measurements were carried out on a Bruker D8 Advance instrument using a Cu X-ray tube. The powders were ground in a mortar and spread over a silicon wafer; if enough material was available, the powder was compacted on the wafer and flattened until a smooth surface was achieved. Alternatively, the wafer was coated with a thin layer of Vaseline and the powder spread over it. The wafer was then placed on a glass slide and transferred into the

instrument on a support that allows the sample to rotate. The patterns were acquired over a range of 2ϑ = 5 ° - 55 ° with a 0.02 ° spacing.

$$n\lambda = 2d\ sin\vartheta \qquad \text{Equation 4}$$

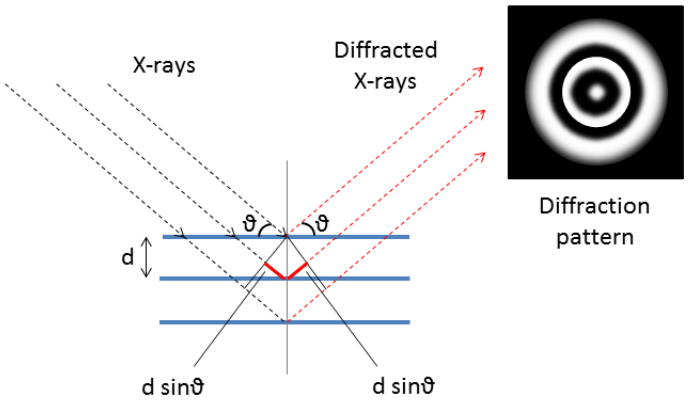

Figure 11: Representation of X-ray diffraction by a crystalline solid. The diffraction pattern shown is typical of powder samples.

3.2.2. X-ray Fluorescence

Energy Dispersive X-ray Fluorescence (ED-XRF) was used to quantify the amount of elements of interest present in the sample. X-rays generated from a source interact with the electrons of the inner shells of atoms within a sample and eject it from the atom. This causes electrons from higher energy levels to fill the gap left by the first electron, releasing the energy correspondent to the gap between the two energy states (Figure 12). The further the electrons are from the nucleus, the higher their energy gap, and therefore their fluorescence energy, will be.ED-XRF measurements on the samples were performed using a benchtop Malvern Panalytical Epsilon 1 ED-XRF analyser, equipped with a 50 kV Ag anode X-ray tube and calibrated using zeolite standards. The samples (approximately 0.2–1 g) were provided as powders and were gently compacted by hand with a flat glass surface to reduce intraparticle voids within a sample cup containing a 4 mm polypropylene film. The final XRF spectrum was acquired utilising 3 different filters (Ag, Cu and Al) and a single unfiltered spectral acquisition. The uncertainty on the values obtained from XRF analyses was found considering the standard error over 10 measurements on a standard sample of commercial zeolite BEA (Si:Al = 12.5). The values obtained are reported in section 9.9 of the Appendix. The uncertainty on the measurements was evaluated as the 6.4% of the values.

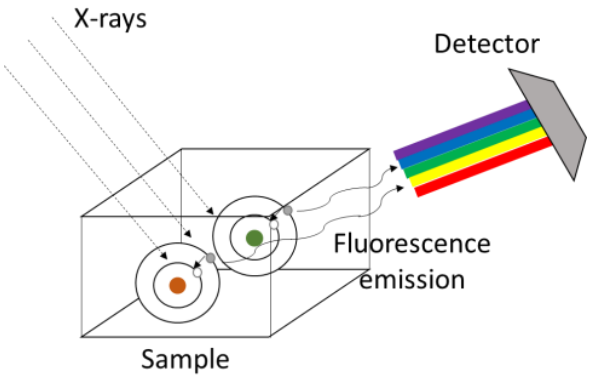

Figure 12: Representation of the X-ray Fluorescence phenomenon that allowed to study the elemental composition of the samples.

3.2.3. Elemental Microanalysis (CHN)

CHN analysis were carried out using the dynamic flash combustion method. The sample is placed in a tin container and purged with a helium flow; subsequently, the sample holder is dropped into a combustion reactor maintained at 900°C, where oxygen is added to the helium stream. Under these conditions, the sample can be successfully oxidised. After the oxidation step, the material is passed over a copper layer in order to remove the excess oxygen and reduce the nitrogen oxides to elemental nitrogen. The gases are then analysed by a chromatographic column equipped with a Thermal Conductivity Detector, which is able to separate molecular nitrogen, carbon dioxide and water and provide the C, H and N levels in the sample. This analysis technique is particularly useful in zeolite science because it detects the presence of organic and nitrogen containing species (such as ammonium and organoammonium cations) in the zeolite, therefore it can provide useful information about the calcination state of the sample or residual carbonaceous deposits in spent catalysts.

3.2.4. Solid State NMR

Nuclear Magnetic Resonance is a spectroscopic method used to study the structure and chemical environment of compounds by means of transitions between nuclear energy levels split by the application of magnetic fields. The magnetic properties of a nucleus result from its spin angular momentum, J, which generates a magnetic momentum, μ. The spin angular momentum depends on the spin quantum number I, which can take zero, integer or half-integer values: I = n/2 (n = 1, 2, 3, 4, …) (Equation 5 and Equation 6).

$$\vec{J} = \hbar \vec{I}$$ Equation 5

$$\vec{\mu} = \gamma \vec{J} = \gamma \hbar \vec{I} \qquad \text{Equation 6}$$

The symbol γ represents the gyromagnetic ratio (rad $s^{-1}T^{-1}$), which is an intrinsic characteristic of the nucleus. When an external magnetic field B_0 is applied to the nucleus, μ can align with B_0 (Zeeman interaction, Figure 13), with a projection on the B_0 axis. The orientation of the I_z projection is indicated with m and can assume values between $-\ell$ and $+\ell$, therefore m can assume $(2\ell+1)$ values. After the interaction between μ and B_0 the degeneracy of the $(2\ell+1)$ states is resolved, and the states with different values of m have different energies; the transitions between these energy states are used for NMR analysis.

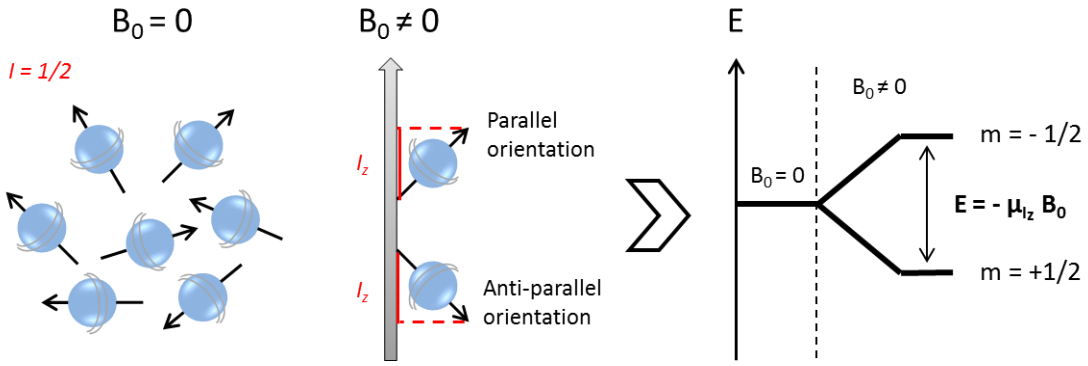

Figure 13: Representation of the Zeeman effect due to the interaction between the magnetic field B_0 and the nuclei with I = ½ (e.g. ^{1}H nucleus).

The population *N* in each spin state is determined by the Boltzmann distribution (Equation 7).

$$\frac{N_{m_{I=-\frac{1}{2}}}}{N_{m_{I=\frac{1}{2}}}} = e^{\left(-\frac{\Delta E}{k_B T}\right)} \qquad \text{Equation 7}$$

Where *T* is the temperature and k_B is the Boltzmann constant. The magnetic momentum precesses with a frequency called the Larmor frequency, which is proportional to the energy gap ΔE between the two states: the greater the external magnetic field B_0, the wider the separation between the two energy levels. The NMR signal is obtained from the relaxation of the nuclei after a second magnetic field B_1 with frequency equal to the Larmor frequency is applied to the sample and interacts with the nuclei, changing the orientation of the spin precession from parallel to anti-parallel. This results in resonance phenomena, depending on the chemical surroundings of the nuclei. The relaxation of the spins from the excited to the ground state depends on the energy gap ΔE, which is directly influenced by the chemical environment. For instance, the shielding of the nucleus by surrounding electrons (chemical shift anisotropy) and space interaction between nuclear spins (dipolar coupling) play a major role affecting the spin energy. To obtain an NMR

spectrum, the spin relaxation time is recorded and a free induction decay (FID) obtained. A Fourier transform is finally carried out to obtain a frequency-domain spectrum where each peak is associated to a transition between different energy states.

Nuclear interactions such as dipolar coupling and shielding are anisotropic; in solution, molecules move chaotically, therefore it is possible to identify an average molecular orientation and an isotropic chemical shift corresponding to the average of the anisotropic interactions. On the other hand, this does not occur in a solid sample (e.g. a powder), as the nuclear interactions will depend on the different orientations of individual particles. As a consequence of this, the spectra resulting from NMR analyses on solid samples exhibit substantially broad lines.[9] In addition to dipolar coupling and shielding interactions, for nuclei with I > ½ another effect plays a critical role, which is the quadrupolar interaction. This is due to the interaction of the quadrupolar nucleus with the electric field gradient of the surrounding electron cloud. A quadrupolar nucleus, i.e. a nucleus with I > ½ has lower charge distribution symmetry than a nucleus with I = ½, and its interaction with the electric field gradient causes a further broadening of the signal. A commonly used signal enhancement technique which overcomes the broadening problems caused by these interactions is the magic angle spinning (MAS) technique. The average perturbation caused by internal interactions can be expressed as a Legendre polynomial, P(θ) (Equation 8). The condition that cancels P is $\cos^2(\theta) = ⅓$. Therefore, if the sample rapidly spins about an axis inclined at the magic angle $\theta_m = 54.74°$ to the external magnetic field, the $\cos^2(\theta) = ⅓$ condition is satisfied and the effect of the anisotropic interactions is removed or reduced.[10]

$$P(\theta) = 1/2\ [3\ (\cos)^2\ (\theta) - 1] \qquad \text{Equation 8}$$

When the spin rate is greater than the magnitude of the anisotropic nuclear interactions a single line will be observed in the NMR spectrum, corresponding to the isotropic chemical shift. If the sample spinning is not fast enough, the central isotropic signal will be accompanied by spinning sidebands, separated from the main signal by an amount equal to the sample spin rate. Table 4 reports the nuclei probed in this work and some relevant NMR characteristics.

Table 4: Characteristics of relevant nuclei.

Nucleus	Natural Abundance (%)	Nuclear Spin	Gyromagnetic Ratio (10^6 rad/s T)	Relative Sensitivity to ^{1}H	Reference
^{1}H	99.98	1/2	267.5	1.0000	[11]
^{13}C	1.11	1/2	67.3	0.0002	[11]
^{29}Si	4.70	1/2	-53.1	0.0004	[11]
^{67}Zn	4.04	5/2	16.8	0.0025	[11]

3.2.4.1. Experimental Details: ^{13}C NMR

Studies carried out through ^{13}C NMR analyses were used to identify the formation of $[Zn\text{-}CH_3]^+$ species in zeolite and zeotype samples after exposure to methane[12] and for the investigation of structural properties in samples containing organic SDA molecules. The natural abundance of the NMR active ^{13}C isotope is 1.1 % (I = ½) and its nucleus can be detected using direct-excitation NMR techniques. However, the acquisition time can be drastically reduced by the implementation of the cross-polarisation (CP) signal enhancement technique. CP analyses are based on the transfer of polarisation from the more abundant ^{1}H nuclei to the ^{13}C nuclei. The transfer of polarisation is achieved through the so-called Hartmann-Hans matching, when both spin types are locked after the initial 90° excitation pulse and, therefore, the energy splitting ΔE of both nuclei is matched (Figure 14). Solid-state MAS ^{13}C NMR measurements were run on a Varian VNMRS at 100.57 MHz or a Bruker Avance III HD spectrometer at 100.62 MHz at a spin-rate of 10 KHz and recycle delay of 1 s. For CP experiments, a contact time of 2 ms and 10,000 or 60,000 scans for carbon labeled or unlabeled methane, respectively, were used. The recycle delay was increased to 10 s with 720 scans for direct-excitation measurements. An external sample of tetramethylsilane (TMS) was used for spectral referencing, which was carried out by setting the high-frequency signal from adamantane to 38.5 ppm.

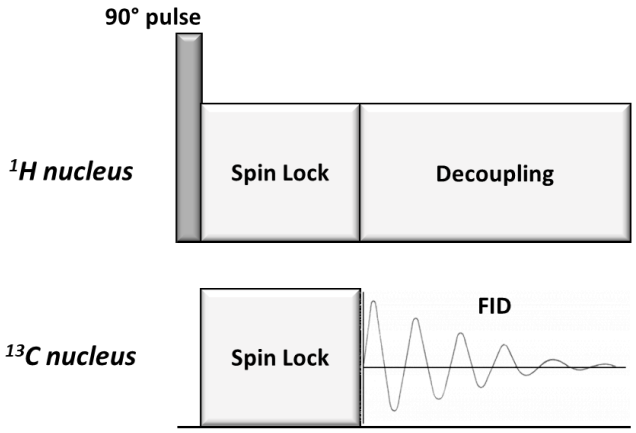

Figure 14: Representation of the CP pulse sequence for a ^{1}H-^{13}C CP MAS NMR experiment.

3.2.4.2. Experimental Details: ^{29}Si NMR

The chemical shifts of Si environments in zeolite samples are dependent on the species surrounding the Si atoms in the framework; the tetrahedral Si sites are identified with Q_n, with n indicating the number of Si-O-T bonds in the first shell around the probed Si atom (n = 0,1,2,3,4), represented in Table 5. The electron cloud surrounding other atoms bonded to the probed Si atom has the effect of shielding the Si from the applied magnetic field. The value of the chemical shift will be higher if the Si atom is highly shielded, therefore the chemical shifts related to each

Si environment can be classified as: $\delta_{Q0}>\delta_{Q1}>\delta_{Q2}>\delta_{Q3}>\delta_{Q4}$. In the presence of heteroatoms, the chemical environment of Si atoms in Q_n sites is different from an environment where only Si, O and H atoms are present. As a consequence, the different shielding effect provided by the heteroatoms will cause changes in the chemical shift values. The classification of the chemical shifts of the different sites is similar to the one established for the Q_n environments: $\delta_{Q4(4T)}>\delta_{Q4(3T)}>\delta_{Q4(2T)}>\delta_{Q4(1T)}>\delta_{Q4(0T)}$ (with T indicating a tetrahedral heteroatom). Therefore, in principle, ^{29}Si MAS NMR enables to differentiate between the Q_4 sites. However, a considerable challenge in the interpretation of a ^{29}Si MAS NMR spectrum is related to the peak assignment, because some of the environments have overlapping chemical shift range (e.g. Q_3, Q_4(0T), Q_4(1T) and Q_4(2T) generally have chemical shifts between -100 ppm and -120 ppm).[14]

Table 5: Different chemical environments of tetrahedral Si coordinated to O atoms and to Si or other heteroatoms, typically observed in zeolite frameworks, and their denomination.[14]

Name	Chemical Shift (ppm)	Site	Name	Chemical Shift (ppm)	Site
Q_0	-80 ↔ -60	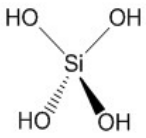	**Q_4(0T)**	-120 ↔ -100	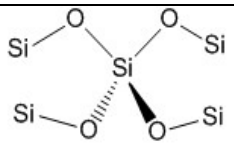
Q_1	-90 ↔ -70	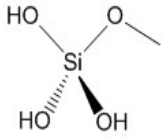	**Q_4(1T)**	-120 ↔ -90	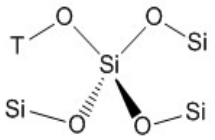
Q_2	-100 ↔ -80	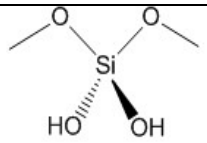	**Q_4(2T)**	-110 ↔ -80	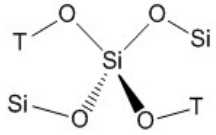
Q_3	-110 ↔ -90	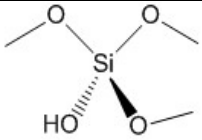	**Q_4(3T)**	-100 ↔ -70	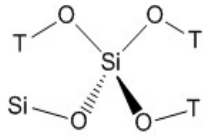
Q_4	-120 ↔ -100	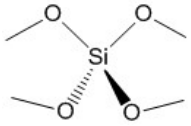	**Q_4(4T)**	-90 ↔ -60	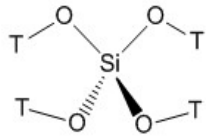

^{29}Si NMR analyses were carried out in both direct-excitation and CP modes. Even though the latter cannot be considered as quantitative, because the signal of ^{29}Si species detected with CP MAS NMR is enhanced by the proximity of hydrogen atoms, ^{1}H-^{29}Si CP MAS NMR spectra of zeolites are able to provide important information on the presence of structural defects in the framework in the form of Si-O^-···HO-Si species.[15]–[18]

SS ^{29}Si NMR spectra were recorded on a Varian VNMRS spectrometer at 79.44 MHz and spinning rate of 6 KHz using a 6 mm probe, with recycle delay of 30 s over 400 scans for the direct excitation and 1 s over 3600 scans for the cross-polarisation mode (5 ms contact time). An external sample of tetramethylsilane (TMS) was used for spectral referencing, which was carried out by setting the high-frequency signal to -9.9 ppm.

3.2.4.3. Experimental Details: ^{1}H NMR

A Bruker Avance III HD spectrometer was used for ^{1}H NMR analyses, carried out at 400.17 MHz using a pulse-acquire experiment with DEPTH background suppression.[19] Proton spectra were acquired at a spin rate of 40 kHz and 10 s recycle delay. Cross-Polarisation (CP) experiments involving a transfer of magnetisation from protons to other nuclei were carried out using the CP pulse sequence and, when needed, TOSS spinning sideband suppression.[20]

3.2.4.4. Experimental Details: ^{67}Zn NMR

The direct observation of the Zn nucleus through NMR is challenging, due to the undesirable characteristics of the only NMR-active ^{67}Zn isotope, such as the low gyromagnetic ratio, causing the Larmor frequency to be very small even using high-field spectrometers (56.3 MHz at 21.1 T). This, alongside the fact that the ^{67}Zn isotope has a quadrupolar nucleus with a non-negligible quadrupole moment (0.15×10^{-28} m^2) translates into extremely low NMR sensitivity and very broad signals.[21] For these reasons, the number of reports about ^{67}Zn SSNMR analyses applied to Zn-containing zeolites or zeotypes is very limited. The NMR signal can however be improved by (i) isotopic enrichment, (ii) high Zn loadings and (iii) high-magnetic field spectrometers. The studies that have reported the use of this techniques benefited from the application of signal enhancement techniques such as the quadrupolar Carr-Purcell Meiboom-Gill (QCPMG) pulse sequence, paired with cross-polarisation or hyperbolic secant pulses.[22]–[27] The only report of ^{67}Zn SSNMR studies carried out on a Zn-contenting zeolite concerns the extra-framework zinc cations in aluminosilicate zeolites. This was achieved by Qi et al. using ^{67}Zn HS-QCPMG and ^{1}H-{^{67}Zn} S-RESPDOR ssNMR experiments and a 18.8 T spectrometer.[25] They were able to identify the chemical shift values associated with Zn^{2+} (224 ppm) and ZnO species (238 ppm).

The ^{67}Zn NMR analysis of Zn-ZSM-5 samples prepared in this work was attempted at The UK High-Field Solid-State NMR Facility using a 18.8 T spectrometer and the experiments were kindly carried out by Dr. Dinu Iuga.

3.2.4.5. 2D Heteronuclear Correlation (HETCOR) Analysis

Two-dimensional Nuclear Magnetic Resonance Spectroscopy (2D NMR) can be used to solve the structure of molecules or compounds that are too difficult to solve using 1D experiments due to signal overlap. The data obtained from 2D NMR analyses are plotted in a space defined by two frequency axes. Hetero-Nuclear Correlation (HETCOR) experiments with the lghetfq sequence are used to correlate two different nuclei by means of single bond spin-spin

coupling, and provide information on which groups of the nuclei are interacting with each other.[28]–[31]

All 2D HETCOR spectra were acquired in a 4 mm or a 1.8 mm magic-angle spinning probe on a Bruker Avance III HD spectrometer at 100.62 MHz and spinning rate of 10 KHz or 40 KHz, using the method of van Rossum et al.[32] The ^{1}H-^{13}C HETCOR experiments were carried out with a 1 ms contact time and a recycle delay of 2 s over 48 repetitions with 64 increments. A Frequency-Switched Lee-Goldberg decoupling step was introduced in order to improve the resolution. The ^{1}H-^{29}Si HETCOR spectra were acquired under the same conditions (1 ms contact time and a recycle delay of 2 s) but with 512 repetitions per increment (Figure 15).

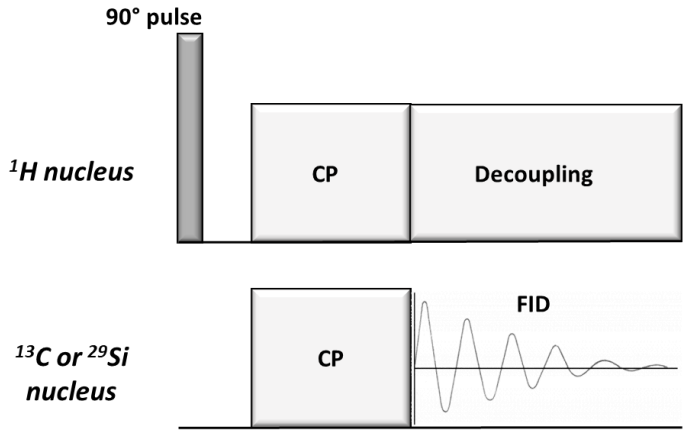

Figure 15: Representation of the HETCOR pulse sequence to observe correlation signals between two nuclei.

3.2.4.6. 2D Double-Quantum/Single-Quantum (DQ/SQ) Analysis

Double-Quantum/Single-Quantum (DQ/SQ) NMR experiments were carried out in order to detect correlation phenomena between protons belonging to the same chemical environment (auto-correlation) or to different groups. The DQ/SQ spectra were recorded on a Bruker Avance III HD spectrometer at 100 MHz and spinning rate of 40 KHz, with 96 increments each of 64 repetitions and a recycle delay of 2 s. A back-to-back (baba2rot) pulse sequence element was included for proton spin recoupling. This method was adapted from Feike *et al.*[33] (Figure 16).

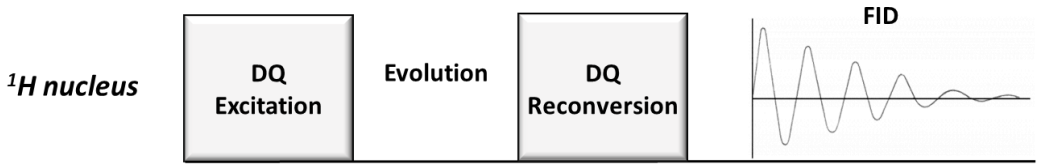

Figure 16: Representation of the baba2rot pulse sequence used for DQ/SQ experiments. The excitation and reconversion steps are based on the duration τ: 4 τ are included in the excitation step and 1 τ in the reconversion step.

3.2.4.7. Electron Microscopy Analysis

Electron microscopy analyses are employed to study the morphology and determine the crystal size and potential presence of metal clusters or impurities in zeolites. For the purpose of this work, Scanning Electron Microscopy (SEM) was mainly used to detect changes in the crystal morphology of the heteroatom-substituted zeotypes related to variations of the synthesis conditions. In order to produce an SEM image, the surface of a sample is scanned with a focused electron beam with kinetic energy ranging between 5 and 15 keV. When the electron beam interacts with the sample, it gives rise to a variety of phenomena such as secondary electrons (SE) formation, back-scattered electrons (BSE) or characteristic X-ray emission. Secondary electrons (SE) arise from the ionisation of valence electrons of the material due to inelastic collisions with the electron beam (Figure 17(a)). A scintillator detects and converts the SE into photons, resulting in a topographical map of the surface of the sample. Back-scattered electrons (BSE) are instead produced when the trajectory of the electron beam is deflected (Figure 17(b)) and the electron re-emerge from the surface with lower kinetic energy. BSE are useful to obtain further insights on the elemental composition of the samples, as they are particularly sensitive to heavy elements. SEM analyses were performed on powder samples after being dispersed in isopropanol. One drop of the dispersion was placed on a silicon wafer and let dry in air, then transferred on the microscope stub and coated with approximately 20 nm of a gold-palladium layer using a sputter coater and subsequently analysed. The images were acquired using a FEI Helios Nanolab microscope operated at 5 kV on samples which had been coated with a 20 nm gold layer using a Cressington sputter coater 108 Auto. The particle size distribution of the materials was measured using the software ImageJ[34] by selecting 60 individual crystals and measuring their surface area on the same crystal face, as represented in Figure 18.

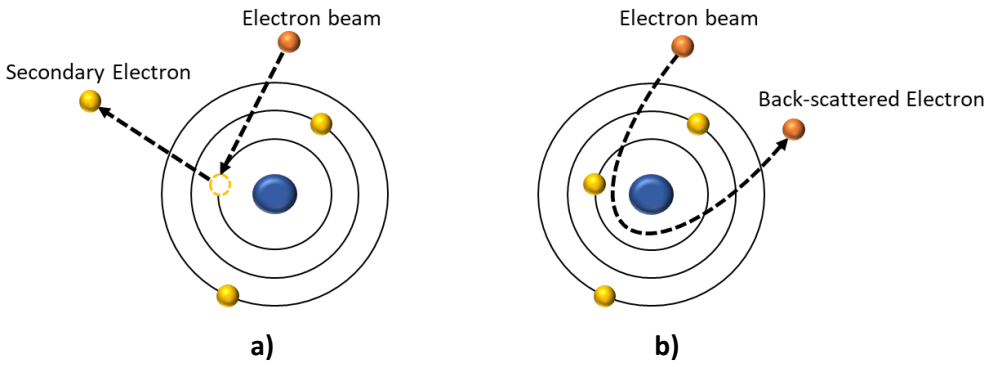

Figure 17: Secondary electron emission due to inelastic scattering (a) – back-scattered electron emission due to elastic scattering (b).

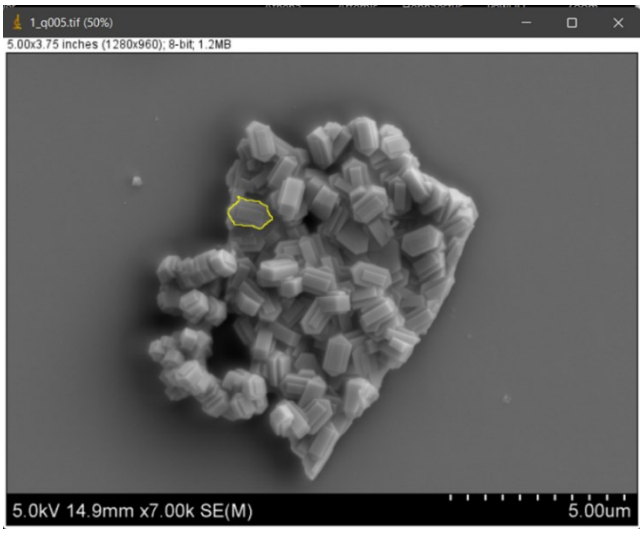

Figure 18: Example of the measuring procedure using ImageJ of the surface area of a single crystallite for a Zn-ZSM-5 sample.

3.2.5. X-ray Absorption Spectroscopy

X-ray Absorption Spectroscopy (XAS) is a characterisation technique which probes the local chemical environment of a target atom. This is achieved through the interaction of an X-ray beam with the sample. X-ray photons are absorbed by atoms and their energy is transferred to their core-level electrons, which are ejected and become so-called photoelectrons. After the photoelectron emission, the atom is left in an excited state through the creation of a core-hole. The atom will de-excite back to its ground state with the emission of X-ray fluorescence or through the Auger effect (Figure 19).[35]–[41] For this work, XAS measurements were carried out for two regimes: the X-ray Absorption Near-Edge Spectroscopy (XANES) and the Extended X-ray Absorption Fine Structure (EXAFS). XANES spectra account for photoelectrons with energies within 50 eV of the absorption edge energy, whilst EXAFS spectra show high-energy photoelectrons (50 eV to 1000 eV). The EXAFS region represents the oscillatory components generated due to the auto-interference of the photoelectrons within a scattering path, which modifies the absorption coefficient value μ(E) of the atom. The oscillations in the EXAFS spectra are produced by constructive and destructive interference.

The information provided by XANES and EXAFS spectrum analyses are related but different: the first one is useful to determine the oxidation state and local site symmetry of the probed atom, whilst the latter provides insights on the type and number of neighbors and bond distances. Therefore, XAS analyses were crucial for the present work and were employed in order to determine whether the framework Zn^{II} sites in zincosilicate ZSM-5 samples had octahedral or tetrahedral coordination and confirm the presence of Zn-O-Si environments.

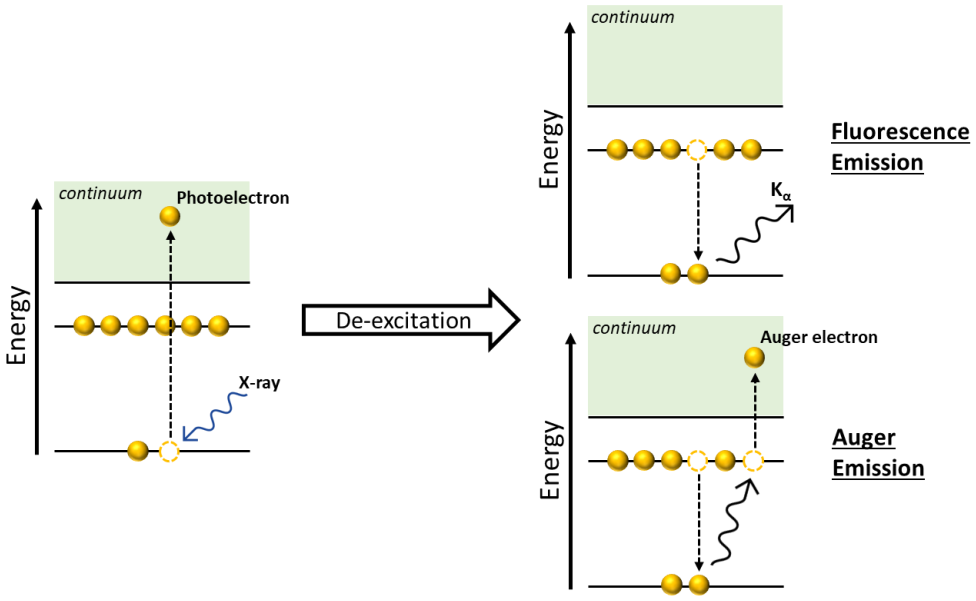

Figure 19: Representation of the excitation phenomenon and de-excitation pathways for the absorption of an X-ray and the formation of a photoelectron from a core-level of the probed atom.

For a XAS experiment carried out in transmission mode, the value of the intensity I_t of the detected radiation corresponds to the incident radiation intensity I_0 reduced by a factor dependent on the absorption coefficient μ and the thickness of the sample, t (Figure 20, Equation 9). This is in accordance with Lambert-Beer law for absorption phenomena in solid samples.

$$\frac{I_t}{I_0} = e^{-\mu t} \qquad \text{Equation 9}$$

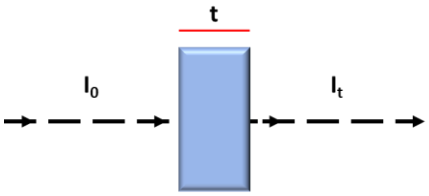

Figure 20: Representation of the transmission phenomenon in a solid sample of thickness *t*.

Considering the EXAFS region, changes of the value of the absorption coefficient $\mu(E)$ due to the presence of neighbouring atoms are contained in the term $\chi(E)$ (Equation 10), indicated as the normalised oscillatory part of the absorption coefficient.

$$\mu(E) = \mu_0 [1 + \chi(E)] \qquad \text{Equation 10}$$

The EXAFS equation (Equation 11) allows to model the term $\chi(E)$, which is usually referred to as a function of the frequency, through the wavenumber k:

$$k = \sqrt{\frac{2\,m\,(E - E_0)}{\hbar^2}}$$ Equation 11

$$\chi(k) \approx S_0^2 \sum_i N_i \frac{f_i(k)}{k\,R_i^2}\, e^{-2R/\lambda(k)} e^{-2k^2\sigma_i^2} sin\,[2kR + \delta_i(k)]$$ Equation 12

Where:

S_0^2 is the amplitude reduction term and is due to the relaxation of all the other electrons to the core hole created in the probed atom;

N is the number of neighbouring atoms;

f is the scattering amplitude;

R is the distance between the probed atom and a neighbouring atom;

σ^2 is related to the mean-square disorder of the neighbouring atom distance;

δ is the phase shift.

XAS experiments were carried out at B18 beamline of the Diamond Light Source synchrotron facility. The samples were prepared by mixing approximately 25 mg of zeolite sample with 15 mg of cellulose binder. The measurements were carried out using an electron beam with a 3 KeV energy and average stored current of 300 mA as the source of X-ray radiation. The X-ray energy was monitored with a channel cut Si(111) monochromator. The spectra were recorded in transmission mode (where possible) with steps of 0.3 eV. The data were analysed using the Demeter software package.[42]

3.2.6. UV-Vis Spectroscopy

UV-vis spectroscopy measurements were carried out in the diffuse reflectance setup, which is generally employed for powder samples. The radiation reflected by the surface of the sample gets collected and analysed as a function of the wavelength λ of the radiation. It is important to point out that radiation hitting the surface of a powder sample is scattered and reflected at angles independent on the angle of the incident radiation (Figure 21); additionally, the sample can also absorb the incident radiation. Diffuse reflectance spectra are normally analysed using the Kubelka-Munk theory (Equation 13), which converts the diffuse reflectance spectrum to an "absorbance" spectrum, similar to one that would be obtained in transmission mode. In the Kubelka-Munk equation, *R* is the absolute reflectance of the sample, *k* is the molar

absorption coefficient and *s* is the scattering coefficient (Equation 14 and Equation 14). The latter is regarded as a constant in the Kubelka-Munk model, although in reality it exhibits a weak dependence on the radiation wavelength. Its value depends mostly on the refractive index of the sample, particle size and packing density.

$$f(R) = \frac{(1-R^2)}{2R} = \frac{k}{s} \qquad \text{Equation 13}$$

$$R = 1 + \frac{k}{s} - \sqrt{\frac{k}{s}\left(2 + \frac{k}{s}\right)} \qquad \text{Equation 14}$$

$$\frac{k}{s} = \frac{(1-R)^2}{2R} \qquad \text{Equation 15}$$

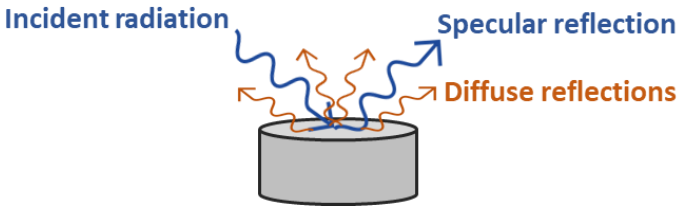

Figure 21: Representation of the reflection phenomena that can arise from the interaction of radiation with a solid surface: specular reflection or diffused reflections.

3.2.7. Diffuse Reflectance Fourier Transform Infra-Red Spectroscopy

Similarly to UV-vis spectroscopy, FT-IR spectroscopy applied to powder samples also needs the diffuse reflectance experimental setup. The Diffuse Reflectance Fourier Transform Infra-red Spectroscopy (DRIFTS) accessory operates by directing the IR radiation into a sample holder where a mixture of the sample and an IR-transparent material (usually KBr) is contained. The IR radiation reflected and diffused by the surface is captured by an output mirror and directed to the detector. The signal is then generated from the altered IR radiation. In order to obtain well-resolved IR spectra, it is necessary to collect a KBr background which is then subtracted from the spectrum obtained from the sample.[43] The DRIFTS measurements were carried out using a Bruker Invenio-R controlled by Bruker OPUS software. The machine has a constant flow of N_2 to ensure no moisture build-up in the detectors or sample chamber. In order to dehydrate the zeolite framework, reduced pressure and raised temperatures are required. Therefore, a Harrick Praying Mantis cell was equipped with a heating element controlled by a Harrick ATK. In order to provide cooling to the cell to extend the lifetime of the seals, a Haake F3 circulates room temperature oil as a coolant. Vacuum was provided by a Pfeiffer Duo 3 rotary pump for initial +pump down, before pumping down with a Pfeiffer HiCube 80 eco turbopump.

Pressure measurement for the sample cell was taken from the closest pressure gauge to the cell, which is a Pfeiffer PKR360C. The sample was loaded and placed under vacuum overnight, with a constant flow of N_2 established to purge the Praying Mantis cell of atmospheric moisture from the beam path. The sample cell was heated from room temperature to 500 °C at 5 °C/min ramp rate, before holding at 500 °C for 2 hours. The cell was then cooled at 5 °C/min to 200 °C and held for 20 minutes, before cooling at 5°C/min to 100 °C and held for 20 minutes.

Chapter 3 Bibliography

[1] M. A. Shah, S. Raynes, D. C. Apperley, and R. A. Taylor, "Framework Effects on Activation and Functionalisation of Methane in Zinc-Exchanged Zeolites," *ChemPhysChem*, 21, pp. 673–679, **2020**, doi: 10.1002/cphc.201900973.

[2] H. Li, B. Xu, B. Deng, X. Yan, and Y. Zheng, "Epoxidation of 1-hexene with hydrogen peroxide over nitrogen-incorporated TS-1 zeolite," *Catal. Commun.*, 46, pp. 224–227, **2014**, doi: 10.1016/j.catcom.2013.12.023.

[3] V. S. Marakatti, A. B. Halgeri, and G. V. Shanbhag, "Metal ion-exchanged zeolites as solid acid catalysts for the green synthesis of nopol from Prins reaction," *Catal. Sci. Technol.*, 4, 11, pp. 4065–4074, **2014**, doi: 10.1039/c4cy00596a.

[4] S. J. Raynes and R. A. Taylor, "Zinc oxide-modified mordenite as an effective catalyst for the dehydrogenation of (bio)ethanol to acetaldehyde," *Sustain. Energy Fuels*, 5, 7, pp. 2136–2148, **2021**, doi: 10.1039/d1se00091h.

[5] S. Smeets and X. Zou, "Zeolite Structures," in *Zeolites in Catalysis: Properties and Applications*, Royal Society of Chemistry, **2017**, pp. 37–72.

[6] C. Röhrig and H. Gies, "A New Zincosilicate Zeolite with Nine-Ring Channels," *Angew. Chemie Int. Ed. English*, 34, 1, pp. 63–65, **1995**, doi: 10.1002/anie.199500631.

[7] M. A. Camblor, R. F. Lobo, H. Roller, and M. E. Davis, "Synthesis and Characterization of Zincosilicates with the SOD Topology," *Chem. Mater.*, 6, 11, pp. 2193–2199, **1994**, doi: 10.1021/cm00047a046.

[8] L. B. McCusker, R. W. Grosse-Kunstleve, C. Baerlocher, M. Yoshikawa, and M. E. Davis, "Synthesis optimization and structure analysis of the zincosilicate molecular sieve VPI-9," *Microporous Mater.*, 6, 5–6, pp. 295–309, **1996**, doi: 10.1016/0927-6513(96)00015-6.

[9] M. Hunger, "Solid-State NMR Spectroscopy," in *Zeolite Characterization and Catalysis*, A. W. Chester and E. G. Derouane, Eds. Springer Science+Business Media, **2009**, pp. 65–105.

[10] M. J. Duer, "The Basics of Solid-State NMR," *Solid-State NMR Spectrosc. Princ. Appl.*, pp. 1–72, **2007**, doi: 10.1002/9780470999394.CH1.

[11] R. K. Harris, E. D. Becker, S. M. C. De Menezes, R. Goodfellow, and P. Granger, "NMR Nomenclature: Nuclear Spin Properties and Conventions for Chemical Shifts: IUPAC Recommendations 2001," *Solid State Nucl. Magn. Reson.*, 22, 4, pp. 458–483, **2002**, doi: 10.1006/SNMR.2002.0063.

[12] A. G. Stepanov, "Basics of Solid-State NMR for Application in Zeolite Science: Material and Reaction Characterization," *Zeolites Zeolite-like Mater.*, pp. 137–188, **2016**, doi: 10.1016/B978-0-444-63506-8.00004-5.

[13] A. S. Borisov, P. Hazendonk, and P. G. Hayes, "Solid-state nuclear magnetic resonance spectroscopy: A review of modern techniques and applications for inorganic polymers," *J. Inorg. Organomet. Polym. Mater.*, 20, 2, pp. 183–212, **2010**, doi: 10.1007/S10904-010-9358-5.

[14] G. Paul, C. Bisio, I. Braschi, M. Cossi, G. Gatti, E. Gianotti, L. Marchese "Combined solid-state NMR, FT-IR and computational studies on layered and porous materials," *Chemical Society Reviews*, 47, 15. Royal Society of Chemistry, pp. 5684–5739, Aug. 07, 2018, doi: 10.1039/c7cs00358g.

[15] I. Grosskreuz, H. Gies, and B. Marler, “Alteration and curing of framework defects by heating different as-made silica zeolites of the MFI framework type,” *Microporous Mesoporous Mater.*, 291, p. 109683, **2020**, doi: 10.1016/j.micromeso.2019.109683.

[16] G. Brunklaus, H. Koller, and S. I. Zones, “Defect Models of As-Made High-Silica Zeolites: Clusters of Hydrogen-Bonds and Their Interaction with the Organic Structure-Directing Agents Determined from 1 H Double and Triple Quantum NMR Spectroscopy,” *Angew. Chemie Int. Ed.*, 55, 46, pp. 14459–14463, **2016**, doi: 10.1002/anie.201607428.

[17] E. Dib, J. Grand, S. Mintova, and C. Fernandez, “Structure-Directing Agent Governs the Location of Silanol Defects in Zeolites,” *Chem. Mater.*, 27, 22, pp. 7577–7579, **2015**, doi: 10.1021/acs.chemmater.5b03668.

[18] E. Dib, J. Grand, A. Gedeon, S. Mintova, and C. Fernandez, “Control the position of framework defects in zeolites by changing the symmetry of organic structure directing agents,” *Microporous Mesoporous Mater.*, p. 110899, **2021**, doi: 10.1016/j.micromeso.2021.110899.

[19] S. Odedra and S. Wimperis, “Improved background suppression in 1H MAS NMR using composite pulses,” *J. Magn. Reson.*, 221, pp. 41–50, **2012**, doi: 10.1016/J.JMR.2012.05.010.

[20] N. C. Nielsen, H. Bildsoe, and H. J. Jakobsen, “TOSS in high-speed MAS NMR,” *J. Magn. Reson.*, 80, 1, pp. 149–154, **1988**, doi: 10.1016/0022-2364(88)90068-6.

[21] Y. Huang and A. Sutrisno, “Recent Advances in Solid-State 67Zn NMR Studies: From Nanoparticles to Biological Systems,” *Annu. Reports NMR Spectrosc.*, 81, pp. 1–46, **2014**, doi: 10.1016/B978-0-12-800185-1.00001-2.

[22] K. H. Mroué and W. P. Power, “High-field solid-state 67Zn NMR spectroscopy of several zinc-amino acid complexes,” *J. Phys. Chem. A*, 114, 1, pp. 324–335, **2010**, doi: 10.1021/jp908325n.

[23] F. H. Larsen, H. J. Jakobsen, P. D. Ellis, and N. C. Nielsen, “Sensitivity-enhanced quadrupolar-echo NMR of half-integer quadrupolar nuclei. Magnitudes and relative orientation of chemical shielding and quadrupolar coupling tensors,” *J. Phys. Chem. A*, 101, 46, pp. 8597–8606, **1997**, doi: 10.1021/jp971547b.

[24] P. He, B. E. G. Lucier, V. V. Terskikh, Q. Shi, J. Dong, Y. Chu, A. Zheng, A. Sutrisno, Y. Huang “Spies within metal-organic frameworks: Investigating metal centers using solid-state NMR,” *J. Phys. Chem. C*, 118, 41, pp. 23728–23744, **2014**, doi: 10.1021/jp5063868.

[25] G. Qi, W. Qiang, X. Jun, J. TrØbosc, O. Lafon, W. Chao, J. P. Amoureux, F. Deng “Synergic Effect of Active Sites in Zinc-Modified ZSM-5 Zeolites as Revealed by High-Field Solid-State NMR Spectroscopy,” *Angew.Chem.Int. Ed.*, 55, pp. 15826–15830, **2016**, doi: 10.1002/anie.201608322.

[26] J. Xu, Q. Wang, and F. Deng, “Metal Active Sites and Their Catalytic Functions in Zeolites: Insights from Solid-State NMR Spectroscopy,” *Acc. Chem. Res.*, 52, 8, pp. 2179–2189, **2019**, doi: 10.1021/acs.accounts.9b00125.

[27] S. Li, O. Lafon, W. Wang, Q. Wang, X. Wang, Y. Li, J. Xu, F. Deng “Recent Advances of Solid-State NMR Spectroscopy for Microporous Materials,” *Adv. Mater.*, 32, 44, p. 2002879, **2020**, doi: 10.1002/adma.202002879.

[28] A. D. Bax, “Broadband Homonuclear Decoupling in Heteronuclear Shift Correlation NMR Spectroscopy,” *J. Magn. Reson.*, 53, pp. 517–520, **1983**.

[29] A. Bax and G. A. Morris, “An improved method for heteronuclear chemical shift

correlation by two-dimensional NMR," *J. Magn. Reson.*, 42, 3, pp. 501–505, **1981**, doi: 10.1016/0022-2364(81)90272-9.

[30] V. Rutar, "Suppression of homonuclear J couplings in 1H-13C chemical-shift correlation maps," *J. Magn. Reson.*, 58, 2, pp. 306–310, **1984**, doi: 10.1016/0022-2364(84)90219-1.

[31] J. A. Wilde and P. H. Bolton, "Suppression of homonuclear couplings in heteronuclear two-dimensional spectroscopy," *J. Magn. Reson.*, 59, 2, pp. 343–346, **1984**, doi: 10.1016/0022-2364(84)90180-X.

[32] B.-J. van Rossum, H. Förster, H. J. M. de Groot, B.-J. van Rossum, H. Förster, and H. J. M. de Groot, "High-Field and High-Speed CP-MAS ¹³C NMR Heteronuclear Dipolar-Correlation Spectroscopy of Solids with Frequency-Switched Lee-Goldburg Homonuclear Decoupling," *JMagR*, 124, 2, pp. 516–519, **1997**, doi: 10.1006/JMRE.1996.1089.

[33] M. Feike, D. E. Demco, R. Graf, J. Gottwald, S. Hafner, and H. W. Spiess, "Broadband Multiple-Quantum NMR Spectroscopy," *J. Magn. Reson. Ser. A*, 122, 2, pp. 214–221, **1996**, doi: 10.1006/JMRA.1996.0197.

[34] C. A. Schneider, W. S. Rasband, and K. W. Eliceiri, "NIH Image to ImageJ: 25 years of image analysis," *Nat. Methods 2012 97*, 9, 7, pp. 671–675, **2012**, doi: 10.1038/nmeth.2089.

[35] J. A. van Bokhoven and C. Lamberti, "XAS Techniques to Determine Catalytically Active Sites in Zeolites: The Case of Cu-Zeolites," *XAFS Tech. Catal. Nanomater. Surfaces*, pp. 299–316, **2017**, doi: 10.1007/978-3-319-43866-5_20.

[36] D. E. Doronkin, M. Casapu, T. Günter, O. Müller, R. Frahm, and J.-D. Grunwaldt, "Operando Spatially- and Time-Resolved XAS Study on Zeolite Catalysts for Selective Catalytic Reduction of NOx by NH3," *J. Phys. Chem. C*, 118, 19, pp. 10204–10212, **2014**, doi: 10.1021/JP5028433.

[37] G. Turnes Palomino, S. Bordiga, A. Zecchina, G. L. Marra, C. Lamberti, "XRD, XAS, and IR Characterization of Copper-Exchanged Y Zeolite," *J. Phys. Chem. B*, 104, 36, pp. 8641–8651, **2000**, doi: 10.1021/JP000584R.

[38] S. M. T. Almutairi, B. Mezari, P. C. M. M. Magusin, E. A. Pidko, and E. J. M. Hensen, "Structure and Reactivity of Zn-Modified ZSM-5 Zeolites: The Importance of Clustered Cationic Zn Complexes," *ACS Catal.*, 2, 1, pp. 71–83, **2011**, doi: 10.1021/CS200441E.

[39] A. Oda, T. Ohkubo, T. Yumura, H. Kobayashi, and Y. Kuroda, "Synthesis of an unexpected [Zn2]2+ species utilizing an MFI-type zeolite as a nano-reaction pot and its manipulation with light and heat," *Dalt. Trans.*, 44, 21, pp. 10038–10047, **2015**, doi: 10.1039/c5dt01088h.

[40] C. Hennig, F. Thiel, K. H. Hallmeiér, R. Szargan, A. Hagen, and F. Roessner, "Characterization of Zn centers in ZSM-5 zeolites with X-ray absorption spectroscopy," *Spectrochim. Acta Part A Mol. Spectrosc.*, 49, 10, pp. 1495–1497, **1993**, doi: 10.1016/0584-8539(93)80054-E.

[41] Y. Joly and S. Grenier, "Theory of X-Ray Absorption Near Edge Structure," *X-Ray Absorpt. X-Ray Emiss. Spectrosc. Theory Appl.*, 1–2, pp. 73–97, **2015**, doi: 10.1002/9781118844243.CH4.

[42] B. Ravel, M. Newville, and IUCr, "ATHENA, ARTEMIS, HEPHAESTUS: data analysis for X-ray absorption spectroscopy using IFEFFIT," *urn:issn:0909-0495*, 12, 4, pp. 537–541, **2005**, doi: 10.1107/S0909049505012719.

[43] Jonathan P. Blitz, “Diffuse Reflectance Spectroscopy,” in *Modern Techniques in Applied Molecular Spectroscopy*, F. M. Mirabella, Ed. John Wiley & Sons Ltd, **1998**, pp. 185–219.

4. Chapter 4: Synthesis of Heteroatom-substituted Zeotypes

4.1. Introduction to Zeotype Synthesis

It was at the beginning of the 1980s that the isomoprhous substitution of Zn heteroatoms in zeolite frameworks started to draw the attention of the scientific community, with the first zincosilicate zeotype patent published in 1982.[1] The early reports were mostly focused on the synthesis of the MFI framework type; however, an important milestone was reached in 1991 by Annen and Davies with the preparation of the first Zn-containing 3-MR zeotype framework, VPI-7 (VSV).[2] After this breakthrough, Annen and Davies worked on the synthesis of more zincosilicate zeotytes, namely VPI-8 (VET), VPI-9 (VNI) and VPI-10.[3]–[5] Since then, the synthesis of several other zincosilicate zeotypes has been reported, both as Zn-substituted versions of already known aluminosilicate zeolites and as unique zincosilicate or zincophosphate frameworks.[6]–[16]

After the discovery of the VPI-8 zincosilicate framework, it was observed that certain synthesis conditions would steer the synthesis products towards the formation of the VPI-8 phase instead of the desired products. Some studies have focused on the identification of the parameters that would affect the outcome of a zincosilicate synthesis. Particularly worth noting is the work of Yoshikawa *et al.*, who have observed that the formation of the VPI-8 phase was favoured by the use of Li^+ cations but was hindered by Na^+ cations. On the other hand, the use of the latter in presence of low Zn levels lead to the formation of the MFI phase.[17], [18] Koike *et al.* have highlighted the importance of the order of addition of the reagents and of the mixing procedure of the synthesis gel, which could completely change the outcome of the preparation and result in the production of impure or totally amorphous phases. [15], [19]

With zincosilicate zeotypes having only recently started to gain importance as a novel class of catalysts, there are not many studies focused on alternative synthesis methods for these materials. This is also due to the intrinsic difficulty of the preparation of zincosilicate zeotypes, even with conventional hydrothermal methods. This often limits the outcome of the synthesis to highly siliceous materials, in order to avoid issues related to the formation of excess extra-framework Zn species.[20]

Finding alternatives to typical batch-like synthesis setups, which would ideally shorten the synthesis time and be more energy-efficient, is one key aspect to explore in order to make new catalysts suitable candidates to make the leap between academia and industry. For aluminosilicate zeolites, techniques such as microwave-assisted synthesis,[21]–[24] continuous flow synthesis[25] or mechanical ball-milling[20], [26]–[28] have been proven to be promising alternatives, as they have enabled a significant decrease in the crystallisation time of the products, without compromising their quality. The mechanical ball-milling method has recently been successfully employed for the preparation of a Zn-substituted ZSM-5 zeotype,[20] and

previously for Ti-, Sn- and Mn-substituted ZSM-5 zeotypes.[26], [27], [29] For the Zn-ZSM-5 sample prepared this way, a lower tendency of precipitation of Zn species and a high exchange capacity to divalent cations has been reported. Nevertheless, despite these advantages, some drawbacks mostly related to contamination and production of highly-defective materials could be due to the use of ball-milling. Introduced for the first time by Mobil in 1986,[23] microwave radiation-assisted synthesis has been mainly employed for the preparation of aluminosilicates and aluminophosphates. To date, the only report about the synthesis of heteroatom-substituted zeotypes using microwave radiation has been published by Sun *et al.*[21] They have shown that the incorporation of several metals (Mn^{II}, Ga^{III}, Ti^{IV}, Sn^{IV}, Cr^{III} and Zr^{IV}) into a zeotype framework could be achieved in a short amount of time with the aid of microwave radiation. The characteristic that regulated this process was found to be the electronegativity difference between the M–O bonds: the larger it was, the more the bond was inclined to be polarised by microwave radiation. Despite all the evidences of the benefits in terms of energy and time saving, to the best of our knowledge, the microwave-assisted synthesis of a zincosilicate zeotype has not been reported yet.

4.2. Results and Discussion

4.2.1. Hydrothermal Synthesis of Zn-MFI

The first attempt to prepare zincosilicates with the MFI framework topology (Zn-MFI) was carried out adapting the synthesis procedure described by Göğebakan et al.[30] SiO_2 (LUDOX AS-30 solution, 7.42 g) was added to a solution of LiOH (0.29 g) in H_2O (7 g) and stirred for two hours at room temperature. Subsequently, $Zn(OAc)_2$ (0.82 g or 0.45 g) was solubilised in water (7 g) and pyrrolidine (2.56 g) was added dropwise to the solution, under intense stirring. The obtained zinc-containing solution was then carefully poured into the first solution containing the silica source, forming a cloudy synthesis gel with composition SiO_2:$Zn(OAc)_2$:Py:LiOH:H_2O=1:*x*:0.97:0.19:30 with *x* = 0.1 or 0.06 (Table 6). The synthesis gel was stirred for further five minutes and then transferred into a Teflon-lined stainless-steel autoclave, as shown in Figure 22(a). The hydrothermal treatment was carried out in a pre-heated oven for 7 days at 180 °C. After the synthesis, the products were removed from the autoclave and washed until the washing water reached a pH of 8 and subsequently dried in an oven at 100 °C overnight. Calcination to remove pyrrolidine (when needed) was carried out in a muffle furnace at 150 °C for 1 hour and 550 °C for 5 hours with temperature ramps of 5 °C/min.

In order to improve the purity and crystallinity of the Zn-ZSM-5 samples, a second attempt was made and the samples prepared using a procedure based on one of the synthesis

methods reported by Mal et al. and Kolyagin et al.[31], [32] for the preparation of Sn-substituted MFI zeotypes. Initially, tetrapropyl-ammonium hydroxide (TPAOH, 25 vol % in water, 9.7 g) was added to tetraethyl orthosilicate (TEOS, 5.66 g) and stirred for 30 minutes the addition of the Zn precursor. When potassium hydroxide was used as the inorganic mineralising agent, a known amount of KOH (between 0.082 g and 0.185 g) was dissolved in 1.8 g of water and added to the mixture of TPAOH and Si source. The Zn precursors used for this preparation were $ZnCl_2$, $Zn(NO_3)_2$ or $Zn(OAc)_2$. After the addition of the metal salt (0.054 g for $ZnCl_2$, 0.081 g for $Zn(NO_3)_2$, 0.059 g for $Zn(OAc)_2$) dissolved in 3.7 g of water, the synthesis mixture was vigorously stirred for another hour before 3.3 g of water were added to it, followed by stirring for 15 minutes. After this step, the synthesis gel with composition $TEOS:Zn(NO_3)_2:TPAOH:KOH:H_2O=1:0.01:0.44:x:45$ (with $0.18 < x < 0.4$) was transferred to a Teflon-lined stainless steel autoclave and placed in an oven at 180 °C for 3 days (Figure 22 (b)). After this time, the autoclave was removed from the oven and quenched in ice before being opened. The synthesis products were separated from their mother liquor and washed, centrifuged and decanted using de-ionised water until the washing water reached a pH of 8. Subsequently, the products were dried in a drying oven at 100 °C overnight. The resulting materials at this point were zincosilicates containing TPA^+ cations. In order to remove the organic cations, the materials underwent a calcination step, carried out in a muffled furnace at 150 °C for 1 hour and at 550 °C for 5 hours (5 °C/min ramp), as represented in Figure 23.

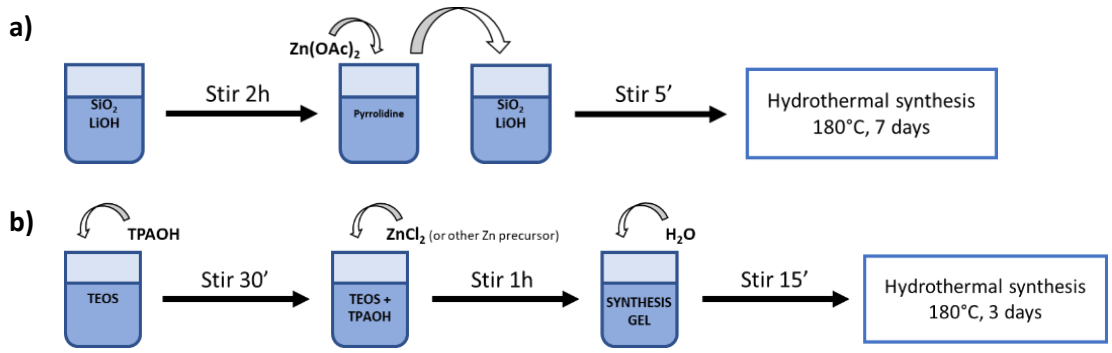

Figure 22: Schematic of the steps involved in the synthesis of zincosilicate zeotypes with ZSM-5 framework type using the "pyrrolidine method" (a) and the "TEOS-method" (b).

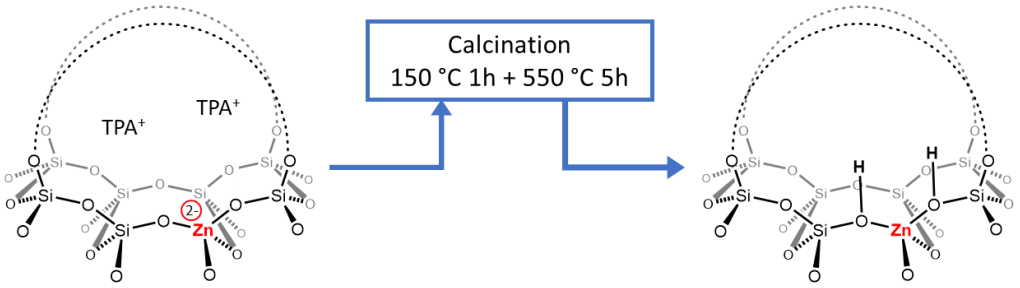

Figure 23: Representation of the calcination procedure and conditions applied in order to remove the organic cations and obtain the protic form of the materials.

In order to confirm the purity and phases present in the samples, powder-XRD analyses (p-XRD) were carried out on the synthesised zincosilicate samples in their protic form and compared to a commercial aluminosilicate ZSM-5 sample. The products obtained using the pyrrolidine method were initially two separate solid layers, i.e., a yellow product below a white product. Powder-XRD analyses revealed that the yellow phase was a rather amorphous product, while the white phase had typical features of the MFI framework type, with the presence of an amorphous component (Figure 24(a)). Furthermore, the two solid layers had different elemental compositions, as shown by XRF analyses. In particular, the yellow phase was rich in Zn and low in Si content (Table 7, entries 1 and 2). Therefore, a second batch containing a lower Zn content was prepared and analysed by p-XRD and XRF. The synthesis gel compositions used in the first and second attempt are reported in Table 6. A study on the influence of the hydrothermal treatment time was also carried out on Zn-MFI samples prepared with 4, 5, 6 or 7 days of hydrothermal synthesis times and analysed by pXRD. As the Zn content was decreased, no yellow phase was observed in the synthesis products (Figure 24(a)). The p-XRD patterns reported in Figure 24(b) show that synthesis times shorter than 7 days deliver materials with low crystallinity, as the main peaks between 20 ° and 30 ° are not fully developed. However, the sample synthesised with a 7-day hydrothermal treatment showed the highest crystallinity, with the presence of a certain degree of amorphous background.

Table 6: Synthesis gel molar ratios and type of products obtained from two attempts at the "pyrrolidine-based" synthesis of Zn-MFI.

Sample	Synthesis gel	Products
Py_Zn-MFI	$1SiO_2$:$0.1Zn(OAc)_2$:0.97Py:0.19LiOH:$30H_2O$	Zn-MFI amorphous zinc-rich product
Py_Zn-MFI Less Zn	$1SiO_2$:$0.06Zn(OAc)_2$:0.97Py:0.19LiOH:$30H_2O$	Zn-MFI

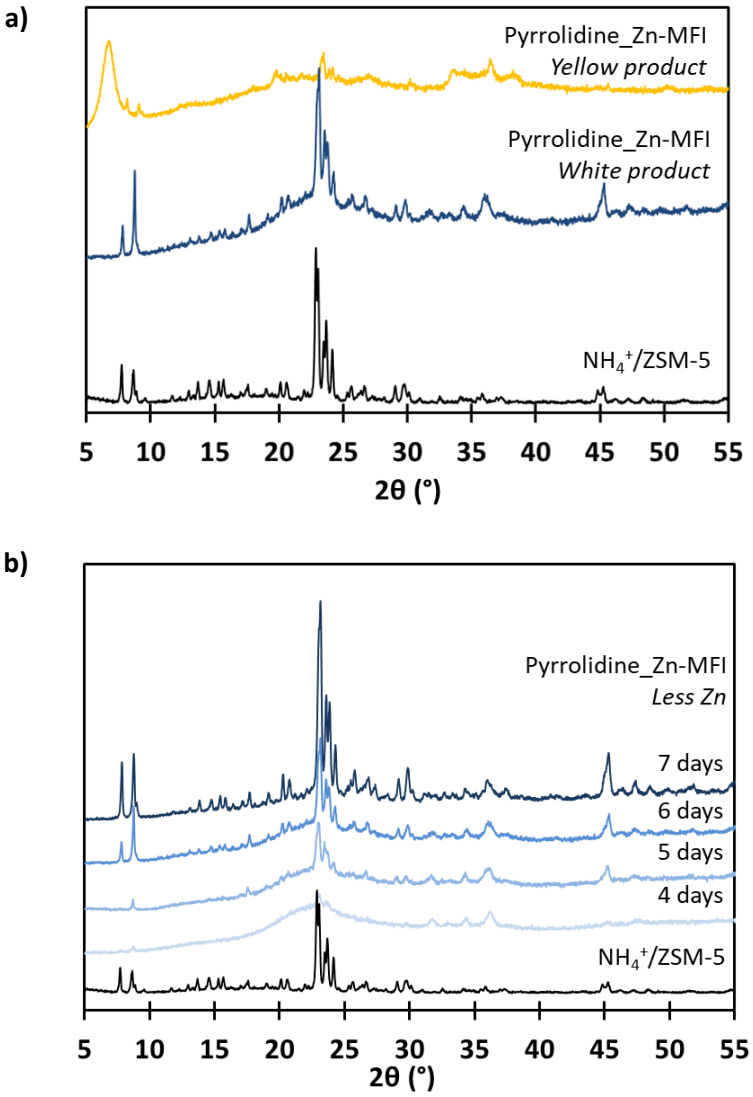

Figure 24: PXRD patterns of the white and yellow phases of the products obtained from the first attempt at the pyrrolidine-based synthesis of Zn-MFI (a) and of synthesis products obtained from the second attempt, containing less Zn, and prepared with different synthesis times (4, 5, 6 or 7 days) (b).

Table 7: Elemental analysis results (obtained by XRF) of the products of the first and second attempts at the pyrrolidine-based synthesis of Zn-MFI. The uncertainty on the measurements is the 6% of the values (only reported for Si:Zn ratios).

Entry	Sample	Si:Zn Solid	Si (wt. %)	Zn (wt. %)
1	***Py_Zn-MFI Yellow Product***	1.5 ± 0.1	18.9	30.0
2	***Py_Zn-MFI White Product***	25 ± 1.5	47.1	6.5
3	***Py_Zn-MFI Less Zn***	20 ± 1.2	38.4	4.4

The Zn-MFI samples obtained from the TEOS-based synthesis were also analysed by means of p-XRD and XRF. The resulting p-XRD patterns are reported in Figure 25(a) and (b). Figure

25(a) shows that the samples are highly crystalline and the signature peaks of the ZSM-5 phase are observed in the patterns obtained from Zn-MFI samples prepared using various amounts of the Zn precursor ($ZnCl_2$). Specifically, the materials were targeted to contain Si:Zn ratios of 150, 100, 50 and 25. This confirmed that higher amounts of Zn do not compromise the purity of the samples prepared using this synthesis method, as no amorphous phases or ZnO impurities were detected by p-XRD. The p-XRD patterns obtained from Zn-MFI samples synthesised using different Zn precursors ($ZnCl_2$ (C), $Zn(NO_3)_2$ (N) and $Zn(OAc)_2$ (A)) are shown in Figure 25(b) and do not show visible differences, suggesting that the three samples have the same crystallinity and phase purity.

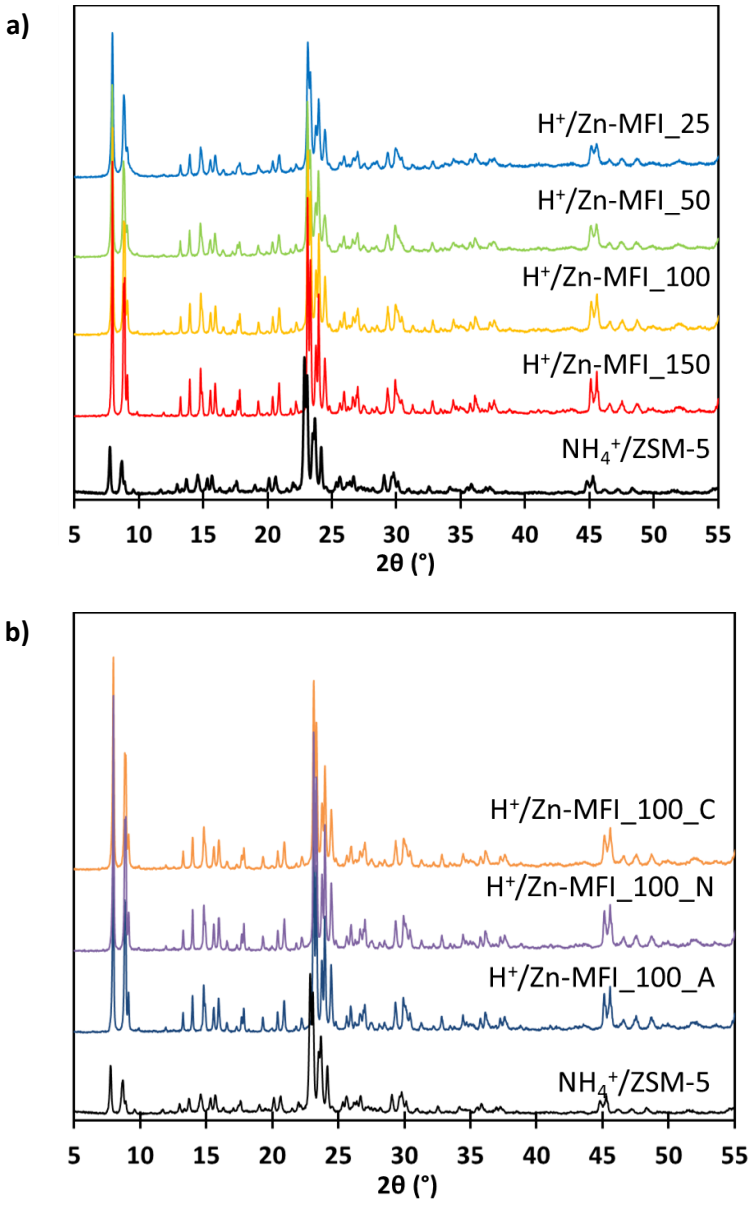

Figure 25: Powder-XRD patterns of Zn-MFI samples prepared with various Zn contents (a) and using different Zn precursors (b), compared to an aluminosilicate ZSM-5 sample.

Zn-MFI samples with different Si:Zn ratios were also compared to a synthesised Silicalite-1 sample (Figure 26(a)), *i.e.* an MFI framework that contains only Si atoms. The latter was prepared following the same procedure used for the preparation of other Zn-MFI samples, omitting the addition of the Zn source. Figure 26(b) shows the p-XRD pattern between 22.5° and 25.5°. Changes in the highlighted peak centred at a 2θ value of 23.1° and between 24° and 24.5° suggest the presence of different crystallographic environments due to the substitution of Zn heteroatoms, as opposed to the absence of heteroatoms in Silicalite-1. More specifically, a shift to greater 2θ values is observed between Silicalite-1 and the Zn-MFI samples with Si:Zn ratios of 100, 50 and 25, in this order. However, this observations are very sensitive towards misalignment of the sample holder or the instrument;[33] therefore, definitive conclusions on the sole basis of p-XRD peak shifting cannot be made to confirm heteroatom substitution.

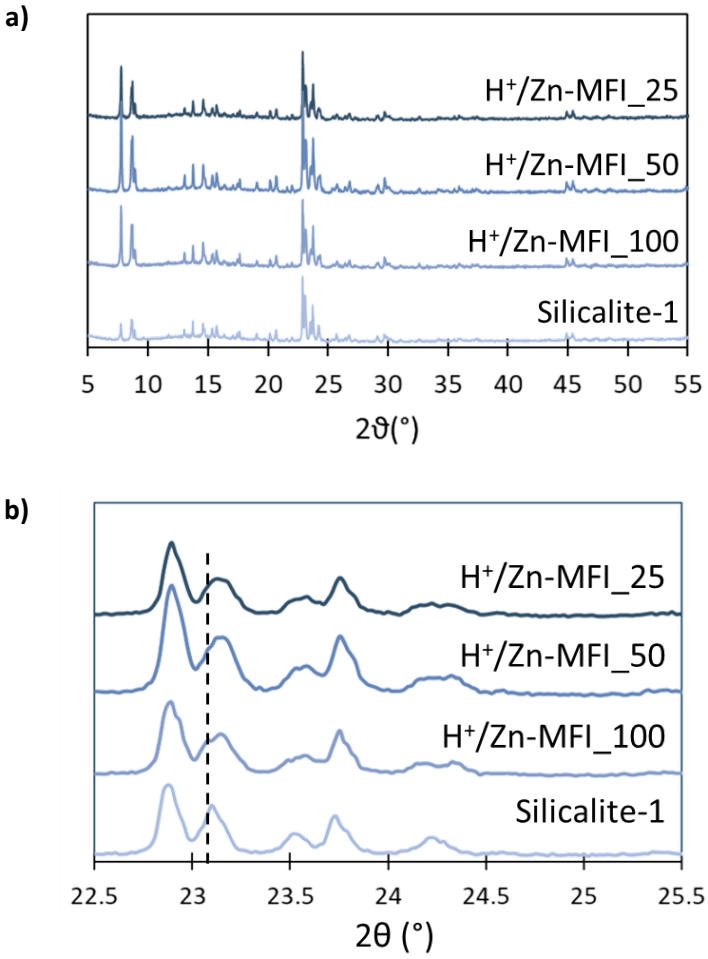

Figure 26: Comparison between the p-XRD patterns of Zn-MFI samples and a Silicalite-1 sample (a). Enlargement of the area included between 2ϑ values of 22.5° and 25.5° and comparison of the specific peak shapes of the samples (b).

The synthesised zincosilicate samples were analysed by means of X-ray Fluorescence (XRF) in order to obtain their elemental composition. The results are reported in Table 8. A discrepancy between expected Si:Zn ratio values and Si:Zn ratio values determined by XRF can

be noticed. In particular, the latter are lower than the expected ones. This could be due to the presence of unreacted silica that is removed during the washing phase after the synthesis. Whilst the nature of the Zn precursor did not have an influence on the crystallinity of the samples, XRF results show that the Si:Zn ratio is highly affected by the type of precursor used. The measured Si:Zn ratio of the sample prepared using $Zn(OAc)_2$ is the closest to the expected value of 100. The experimental values progressively divert from the expected one for samples prepared using $Zn(NO_3)_2$ and $ZnCl_2$, respectively. This may be due to the properties of the counter-anion, especially the basicity. This is suggested by the trend observed between the basicity of the counter-anions and the amount of Zn incorporated in the materials. The acetate counter-anion (the strongest base, $pKa_{CH3COOH}$=4.76) corresponds to the Si:Zn ratio closest to 100, whilst the weakest base, the chloride counter-anion (pKa_{HCl}=-5.9), delivers the sample with the lowest Si:Zn ratio. The nitrate counter-anion, which has intermediate basicity (pKa_{HNO3}=-1.3), corresponds to a Si:Zn ratio between the ones measured for $ZnCl_2$ and $Zn(OAc)_2$.

Table 8: Elemental analysis results (XRF) of Zn-MFI samples prepared with various Zn contents (Si:Zn ratios of 25, 50, 100 or 150) and different Zn precursors (Zn acetate, Zn chloride or Zn nitrate) and compared to a Silicalite-1 sample. The uncertainty on the measurements is the 6% of the values (only reported for Si:Zn ratios).

Entry	Sample	Si:Zn Synth. gel	Si:Zn Solid	Si (wt. %)	Zn (wt. %)
1	***H^+/Zn-MFI_25***	*25*	17.1 ± 1.0	38.5	5.2
2	***H^+/Zn-MFI_50***	*50*	32.4 ± 1.9	37.2	2.7
3	***H^+/Zn-MFI_100***	*100*	65.4 ± 3.9	46.3	1.7
4	***H^+/Zn-MFI_150***	*150*	129.6 ± 7.8	46.7	0.8
5	***H^+/Zn-MFI_100_Acetate***	*100*	94.7 ± 5.7	41.2	1.0
6	***H^+/Zn-MFI_100_Chloride***	*100*	65.4 ± 3.9	46.3	1.7
7	***H^+/Zn-MFI_100_Nitrate***	*100*	82.5 ± 5.0	40.8	1.2
8	***Silicalite-1***	∞	∞	46.4	0

4.2.1.1. Preparation of other M^{II}- and M^{IV}-substituted MFI Zeotypes

The preparation method used for the synthesis of Zn-MFI samples could be adapted for other heteroatom-substituted samples with the MFI topology by simply replacing the Zn precursor with another M^{II} metal precursor. The metal screening was carried out using metal salts containing the NO_3^- and the Cl^- anions. The metals employed in the preparation of

M^{II}-substituted ZMS-5 samples were Ni^{II}, Co^{II} and Mg^{II}. A material containing Ti^{IV}, which therefore produced a neutral framework, was also synthesised using the same synthesis procedure.

Powder-XRD analysis carried out on the heteroatom-substituted MFI samples prepared using this method revealed that the samples are highly crystalline and show the characteristic peaks of the MFI phase, as well as the absence of crystalline impurities. Figure 27(a) shows the p-XRD patterns of Co- and Ni-MFI samples prepared with Si:M^{II} ratios of 100 and 50, compared to a Silicalite-1 sample. A detailed portion of the pattern is shown in Figure 27(b), with focus on the region between 22.5° and 25.5°. A difference in position and shape of the peaks is observed, especially between Silicalite-1 and heteroatom-containing samples. Figure 27(c) and Figure 27(d) show, respectively, the full p-XRD pattern and detailed portion of the patterns for Mg-MFI samples prepared with Si:Mg ratios of 100, 50 and 25 and compared to a Silicalite-1 sample. The results confirm that the samples are pure and highly crystalline and changes in peak shape/position due to changes in the unit cell suggest the presence of Mg heteroatoms in framework positions.

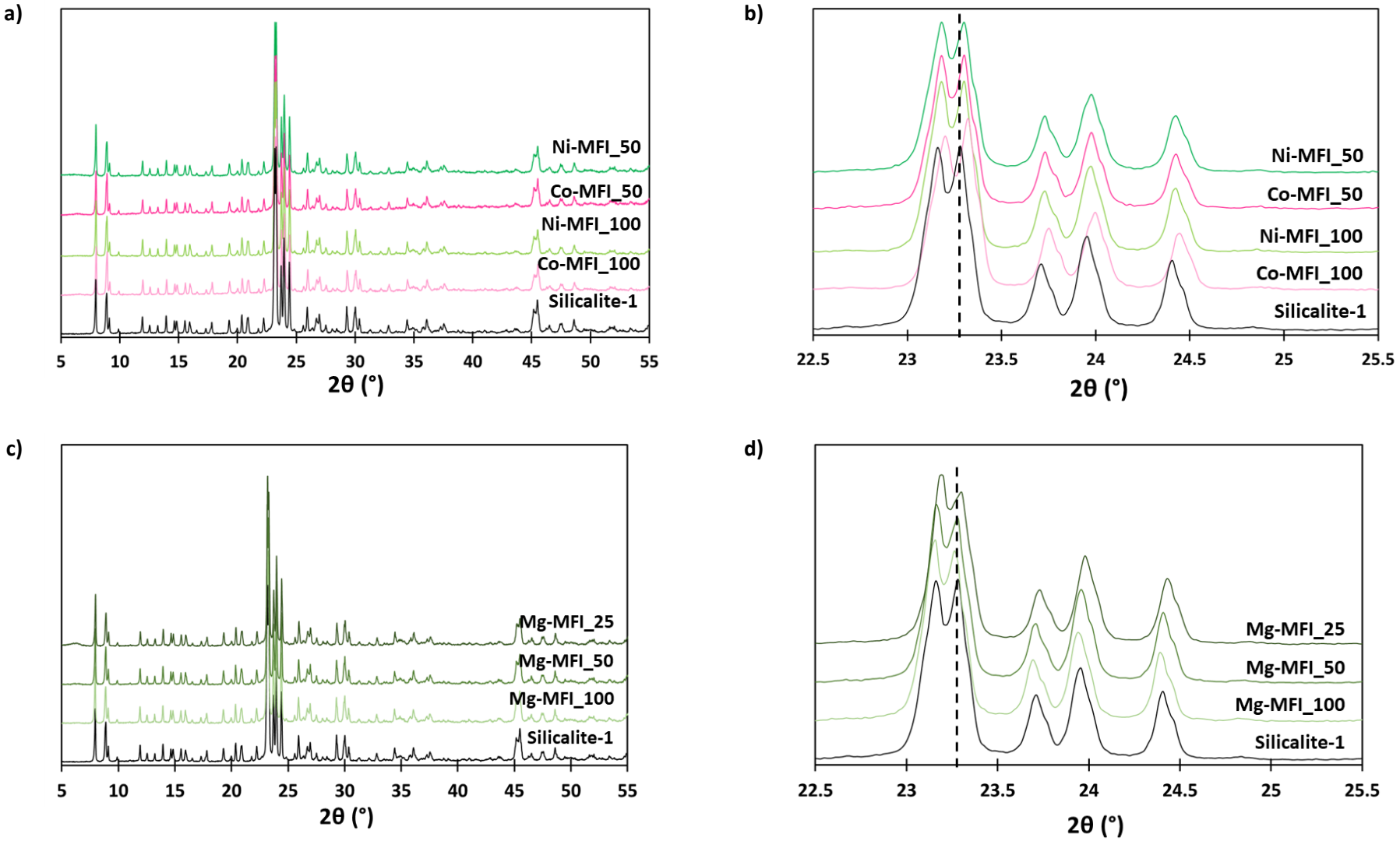

Figure 27: Powder-XRD patterns of heteroatom-substituted MFI samples with Co and Ni (a) and (b) and Mg (e) and (d).

The neutral TS-1 titanosilicate material was prepared using the same method employed for the synthesis of the other heteroatom-substituted MFI zeotypes, but with titanium isopropoxide ($Ti(iPrO)_4$) as Ti source. The hydrothermal synthesis was carried out for 3 days at 180 °C, the material obtained was washed until the pH of the washing water reached a value of 8 and subsequently dried at 100 °C overnight.

The TS-1 sample obtained was analysed by p-XRD and the results show a highly crystalline sample and the absence of impurities in the form of TiO_2 phases (Figure 28(a)). Visible changes in the peak shape and position (Figure 28(b)) could be evidence of isomorphous substitution of Ti heteroatoms in the framework.

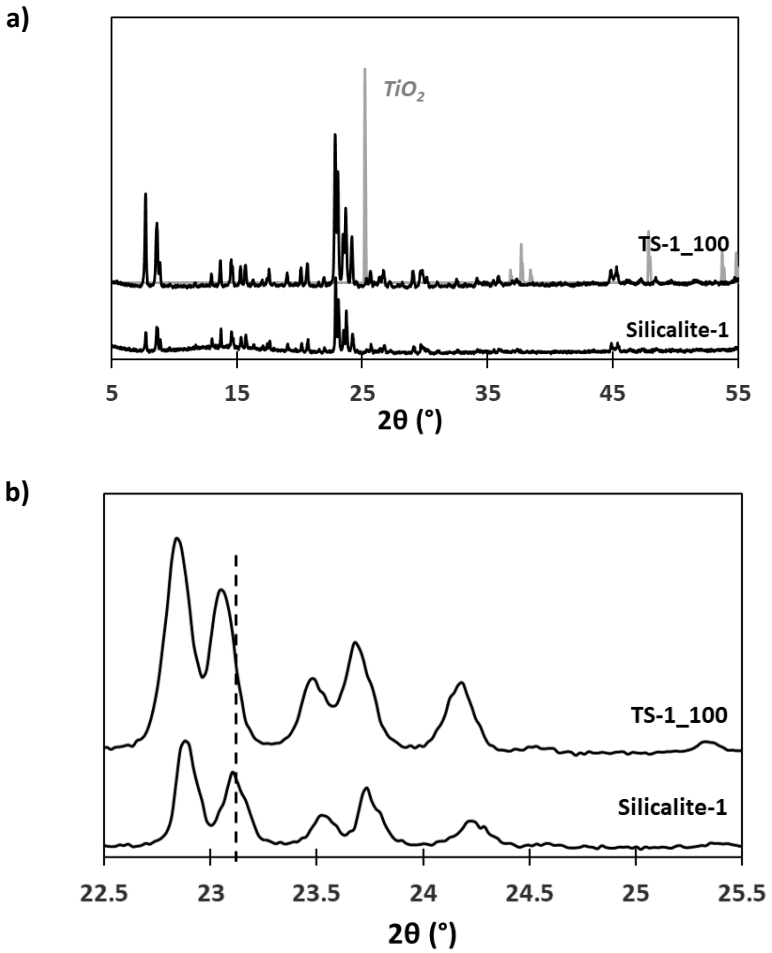

Figure 28: Powder-XRD patterns of TS-1 titanosilicate compared to a Silicalite-1 sample and anatase impurities (a) and the same p-XRD patterns with a focus on features between 22.5 and 25.5 ° (b).

The elemental composition of the synthesised heteroatom-substituted zeotypes was obtained through XRF analysis. The results reported in Table 9 indicate that a good agreement between the expected and the real Si:M ratios of the samples can be observed, with the exception of Ni-MFI_50 and Mg-MFI_50 samples. In the first, the lower Si:Ni ratio could be due to the double effect of the presence of unreacted silica and the incorporation of an excessive

amount of Ni, whilst in the case of Mg-MFI_50 it appears that a number of Mg heteroatoms did not successfully occupy framework positions, causing a higher Si:Mg ratio.

Table 9: Elemental composition obtained by XRF analyses on Co-, Ni-, Mg- and Ti-substituted MFI zeotypes. The uncertainty on the measurements is the 6% of the values (only reported for Si:M ratios).

Entry	Sample	Si:M Synth. gel	Si:M Solid	Si (wt. %)	M (wt. %)
1	***Co-MFI_100***	*100*	80.9 ± 4.9	44.8	1.2
2	***Co-MFI_50***	*50*	40.3 ± 2.4	45.8	2.9
3	***Ni-MFI_100***	*100*	98.2 ± 5.9	48.3	1.0
4	***Ni-MFI_50***	*50*	27.5 ± 1.7	39.3	2.8
5	***Mg-MFI_100***	*100*	107.2 ± 6.4	38.4	0.3
6	***Mg-MFI_50***	*50*	64.2 ± 3.9	37.1	0.5
7	***Mg-MFI_25***	*25*	22.6 ± 1.4	38.1	1.5
8	***TS-1***	*100*	88.2 ± 5.3	43.9	0.9

Part of this work was also dedicated to the preparation of zincosilicates with different framework types other than MFI. The synthesis method employed for the preparation of Zn-ZSM-22 (TON) and results of p-XRD, SEM and ssNMR analysis are reported in Section 9.1 of the Appendix. This material, however, showed the presence of a crystalline impurity in the p-XRD pattern, therefore it has not been further employed in catalysis or other applications. In Appendix 9.2 SEM images of heteroatom-substituted MFI materials prepared with Ni^{II}, Co^{II} and Ti^{IV}, are reported.

4.2.2. Role of KOH Mineralising Agent

In order to further characterise zincosilicate samples, solid-state NMR (ssNMR) was used and revealed that the samples contained framework defects in the form of Si-OH or Si-O^-···HO sites (see Section 5.2.1). The number of defect sites decreased to some extent after the samples underwent the calcination procedure, however residual defect sites were still detected by ssNMR. The use of an inorganic mineralising agent was, therefore, considered in order to reduce the formation of defects in the structure.

Potassium hydroxide was selected as mineralising agent and added with TEOS and TPAOH to the synthesis gel in order to ensure its complete dissolution. The amount of TPAOH added to the synthesis gel was modified, so that the total number of OH^- ions in the synthesis gel would not change. This choice was made with the aim of keeping the pH of the gel constant for all the samples. Zincosilicate zeotypes with varying KOH content were prepared and analysed in order to find the most suitable TPAOH:KOH ratio to reduce the level of silanol defects in the framework, improve the solubilisation of the Si source and, consequently, the incorporation of zinc heteroatoms in a fully closed environment.[34] All the zincosilicate samples discussed in the next sections were prepared using $Zn(NO_3)_2$ as Zn precursor. Using the TEOS-based synthesis, a range of materials were prepared where the TPAOH:KOH ratio varied between 3 and 8. The p-XRD patters of these materials are reported in Figure 29 and they all show high crystallinity.

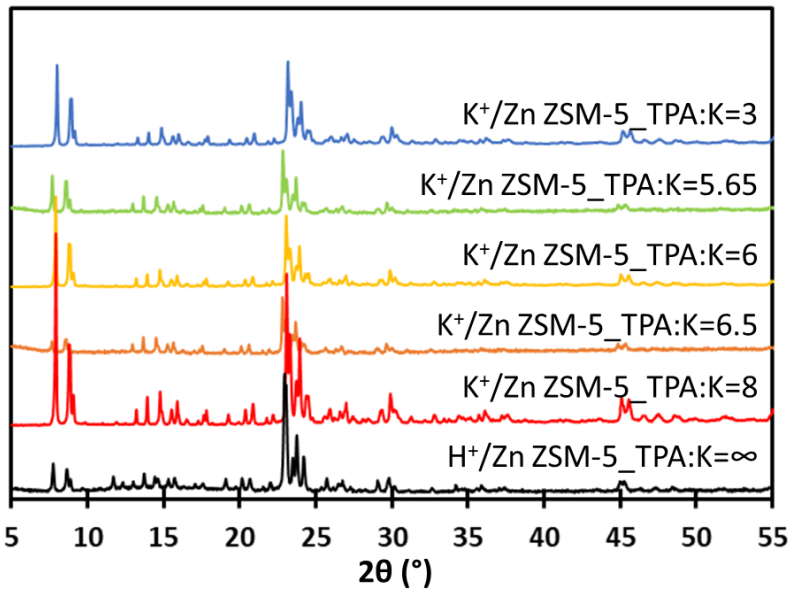

Figure 29: Powder-XRD patterns of Zn-MFI samples prepared with various amounts of KOH in the synthesis gel compared to a sample prepared without KOH.

Elemental analysis results of the calcined Zn-ZMFI samples are listed in Table 10 and show how the amount of KOH incorporated in the samples affects the elemental composition of

the materials. Specifically, compared to the other samples, the material prepared with the highest amount of KOH (K^+/Zn-MFI_TPA:K=3) shows the Si:Zn ratio closest to the expected value of 100 (96.39), as well as the highest potassium content (2.96 wt%), corresponding to a K:Zn ratio of 4.1. This indicates an over-incorporation of potassium in the material, as the expected K:Zn ratio for a fully charge-balanced sample, containing only closed tetrahedral Zn sites, would be equal to 2. The over-incorporation can be explained considering the formation of Si-O^--K^+ species in K-containing materials, as opposed to the formation of silanol Si-O-H sites in H-containing materials. As the KOH content decreases, the Si:Zn ratio assumes lower values, with K^+/Zn-MFI_TPA:K=8 (the sample prepared with the lowest potassium content) showing a Si:Zn ratio of 86.31. This sample also shows a K:Zn ratio < 2, which suggests the presence of some open Zn sites. It is worth noting that the Zn content in the samples is not affected by the addition of KOH in the synthesis and remains constant between 1.18 and 1.24 wt%. On the other hand, the presence of KOH appears to have an influence on the Si content, with KOH-containing samples showing higher incorporation of Si and, consequently, Si:Zn ratios closer to the expected value of 100.

Table 10: Elemental composition obtained by XRF analyses on K-containing Zn-MFI samples. The uncertainty on the measurements is the 6% of the values (only reported for Si:Zn and K:Zn ratios).

Entry	Sample	Si:Zn Synth. gel	Si:Zn Solid	K:Zn Solid	Si (wt. %)	Zn (wt. %)	K (wt. %)
1	***K^+/Zn-MFI_TPA:K=3***	*100*	96.4 ± 5.8	4.1 ± 0.3	48.3	1.2	3.0
2	***K^+/Zn-MFI_TPA:K=5.65***	*100*	90.3 ± 5.4	2.9 ± 0.2	47.5	1.2	2.2
3	***K^+/Zn-MFI_TPA:K=6***	*100*	87.7 ± 5.3	2.4 ± 0.1	46.9	1.3	1.8
4	***K^+/Zn-MFI_TPA:K=6.5***	*100*	88.0 ± 5.3	2.3 ± 0.1	44.7	1.2	1.6
5	***K^+/Zn-MFI_TPA:K=8***	*100*	86.3 ± 5.2	1.5 ± 0.1	44.1	1.2	1.1
6	***H^+/Zn-MFI_TPA:K=∞***	*100*	68.4 ± 4.1	0	36.4	1.2	0

4.2.3. Ion Exchange

In order to evaluate the ability of the zincosilicates synthesised using the TEOS-based method to accommodate divalent metal cations in charge-balancing positions, ion-exchange (IE) experiments were carried out using Ni^{2+} cations. Initially, the samples were exchanged to their

NH_4^+ form using a 0.3 M solution of NH_4NO_3. 50 mg of sample were immersed in 50 ml of NH_4NO_3 solution in a centrifuge tube and placed on a tube roller for 1 h, then centrifuged and decanted, before 50 ml of fresh solution were poured in the tube and the procedure repeated 10 times. Finally, the samples were washed with de-ionised water and dried at 100 °C overnight. In order to achieve the ion-exchange of the Ni^{2+} cations in the NH_4^+ exchanged samples, they were stirred in a 0.032 M $Ni(NO_3)_2$ solution placed in a round bottom flask equipped with an air condenser at 80 °C for 5 days.[35] The ratio between the amount of sample and solution was maintained at 1:1 (mg_{sample}:$ml_{solution}$). At the end of the procedure, the samples were separated from the solution by centrifugation, washed with 500 ml of de-ionised water in order to remove residual excess Ni and dried at 100 °C overnight. XRF analyses were carried out on the samples in order to evaluate the extent of the ion-exchange achieved. Elemental analysis results thus obtained are reported in Table 11 and Figure 30.

Elemental analyses revealed changes in the Si:Zn and the K:Zn ratios of calcined, NH_4^+ exchanged and Ni^{2+} exchanged samples, as well as the effectiveness of the Ni^{2+} exchange procedures. Interestingly, the results appeared to be dependent on the KOH content in the starting materials (Figure 30(a)). More specifically, samples with a K:Zn ratio > 2 in the starting material ("calcined" samples in Table 11**)** retained some residual potassium after being exchanged to their ammonium form; however, all the potassium was removed by the Ni^{2+} exchange procedure. Similarly, the Ni:Zn ratios of these samples was > 1, indicating the presence of a certain extent of over-exchange, whilst the starting material showing a K:Zn ratio < 2 (1.54) could only be partially exchanged to a Ni:Zn ratio of 0.64 (entry 4 in Table 11). These observations indicate that the presence of K^+ cations in the starting materials, deriving from the addition of KOH in the synthesis gel, facilitate the exchange of Ni^{2+} and suggest a decrease of framework -OH defects bearing a single negative charge. This behaviour has been previously reported by Corma et al. for the preparation of a Pt-containing zeolite (MFI) catalyst. They observed by means of IR spectroscopy that the number of –OH groups decreased significantly after the introduction of K^+ cations, together with TPAOH. It was proposed that this was due the formation of $–O^-K^+$ species.[36] In the case of our zincosilicate materials, the observations suggest that in the presence of K^+, the Zn heteroatoms in framework positions occupy a fully closed framework environment, bearing a formal divalent negative charge on every metal site, thanks to the absence of Si-O-H defect sites. The latter would cause the presence of monovalent negative or neutral Zn sites in the framework, unable to fully charge-balance Ni^{2+} cations. This "defect healing" effect is not observed to its full extent, however, if the amount of KOH in the starting material is too low and, in particular, results in under-exchanged materials. However, the results showed the presence of a higher-than-expected amount of K^+ in some of the materials (K:Zn > 2). This evidence, alongside with the proposed effect of limiting the formation of -OH defects,

suggests that these defects may be replaced with $-O^-K^+$ species instead, similarly to what was reported by Corma et al.[36] Otherwise, the higher amount of K^+ detected could be explained with the presence of potassium species occluded in the micropores of the materials. Another observation worth noting after NH_4- and Ni-exchange experiments is the increase in the Si:Zn ratios of the samples compared to those of the starting materials (Figure 30(b)). These changes are minor or completely absent in the NH_4^+ exchanged samples; however, the elevated temperature conditions of the Ni^{2+} exchange procedure cause a certain extent of "de-zincification" with the consequence of the increase of the Si:Zn ratios. In order to avoid this phenomenon, milder ion-exchange conditions were attempted using (i) a lower temperature, *i.e.* 40 °C or (ii) room temperature, lower $Ni(NO_3)_2$ concentration (0.005 M) and higher volume (1 L). However, attempt (i) delivered a poor Ni^{2+} exchange (Ni:Zn = 0.11), with the loss of some framework Zn, whilst no sign of ion-exchange was observed for attempt (ii).

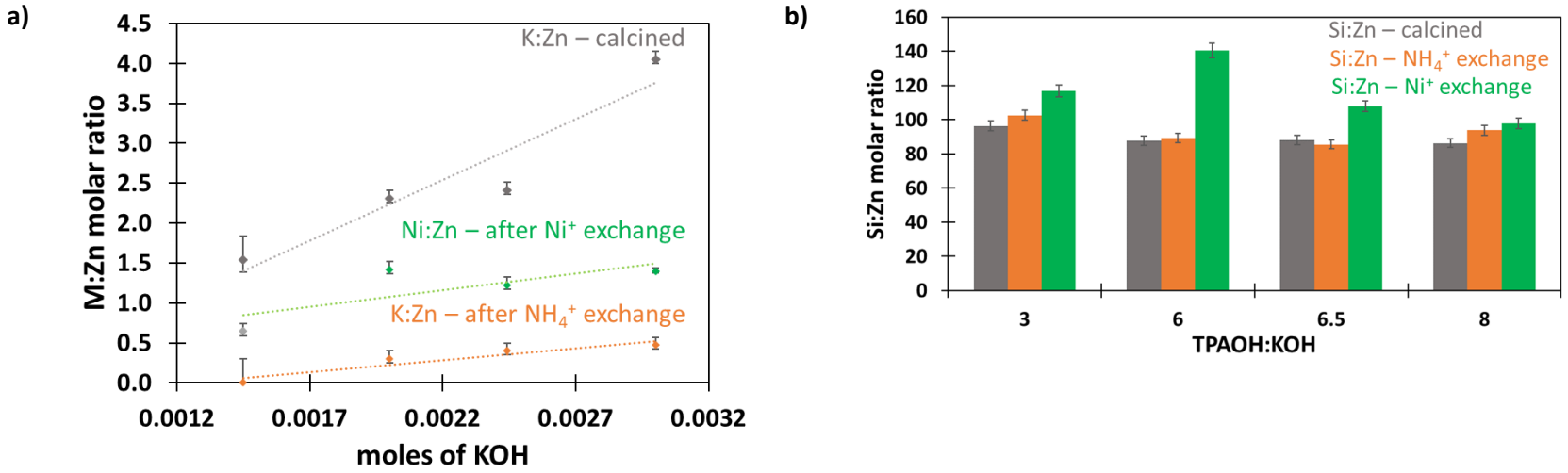

Figure 30: Plot of the M:Zn ratio (M = K or Ni) in the samples as a function of the moles of KOH used to prepare them (a) and variations in the Si:Zn ratio after the various ion-exchange experiments (b).

Table 11: Ni^+-exchange results obtained from NH_4^+-exchanged samples, starting from their K^+ form. The uncertainty on the measurements is the 6% of the values.

Entry	Sample	KOH (mol)	Si:Zn Solid			K:Zn Solid			Ni:Zn Solid
			calcined	NH_4^+ exchanged	Ni^+ exchanged	calcined	NH_4^+ exchanged	Ni^+ exchanged	
1	***K^+/Zn-MFI_TPA:K=3***	***0.003***	96.4 ± 5.8	102.7 ± 6.2	117.0 ± 7.0	4.1 ± 0.3	0.5 ± 0.03	0	1.4 ± 0.1
2	***K^+/Zn-MFI_TPA:K=6***	***0.0019***	87.7 ± 5.3	89.2 ± 5.4	140.6 ± 8.4	2.4 ± 0.1	0.4 ± 0.02	0	1.2 ± 0.1
3	***K^+/Zn-MFI_TPA:K=6.5***	***0.002***	88.0 ± 5.3	85.5 ± 5.1	107.9 ± 6.5	2.3 ± 0.1	0.3 ± 0.02	0	1.4 ± 0.1
4	***K^+/Zn-MFI_TPA:K=8***	***0.0015***	86.3 ± 5.2	93.8 ± 5.6	97.8 ± 5.9	1.5 ± 0.1	0	0	0.6 ± 0.04

4.2.4. Microwave-assisted Synthesis of Zn-MFI

The microwave-assisted synthesis of Zn-substituted MFI zeotypes was carried out using an Anton Parr Multiwave Go microwave oven. The synthesis gels were prepared using the same TEOS-based procedure reported for the synthesis of the Zn-MFI sample shown in Table 8 (entry 3), using $ZnCl_2$, without the addition of KOH and aiming at a SI:Zn ratio of 100, and transferred into the Multiwave Go teflon vessels. Highly pure and crystalline Zn-MFI products could be achieved with a 1-hour synthesis at 170 °C. After the synthesis, the samples were extracted from the vessels and washed and centrifuged using DI water until the washing water had a pH = 8. After this step, the products were dried in a drying oven at 100 °C overnight and then calcined at 550 °C for 5 hours to remove the organic structure directing agent.

The products obtained from the microwave-assisted synthesis procedure were analysed by p-XRD and their crystallinity appeared to be comparable to the one observed for a sample synthesised using the same synthesis gel and the hydrothermal synthesis method (Figure 31). From the p-XRD patterns it appears that the crystallinity of the samples was unaffected by the use of microwave radiation. The latter, on the other hand, helped reduce the synthesis time drastically, from 3 days of hydrothermal synthesis to 1 hour of microwave-assisted synthesis. This result is in line with what was observed by Sun *et al.* who reported the microwave-assisted preparation of various metal-substituted MFI zeotypes, which was achieved in under 1 hour for ZSM-5 samples prepared with Mn or Ti heteroatoms.[21] However, whilst in their case the samples underwent a pre-treatment carried out at 80 °C for 90 minutes, the Zn-MFI samples reported here were synthesised in only 1 hour of microwave heating at 170 °C. Elemental analysis carried out on the products (Table 12) revealed that the Si:Zn molar ratio of the sample synthesised in 1 hour is comparable to the ratio measured for a sample with the same composition, synthesised using the hydrothermal method (62.82 for the first and 65.38 for the latter). On the other hand, if the microwave synthesis was carried out for 2 hours and 30 minutes, the Si:Zn ratio decreased to 52.27, indicating a loss of silica incorporation in the sample corresponding to a too long microwave synthesis.

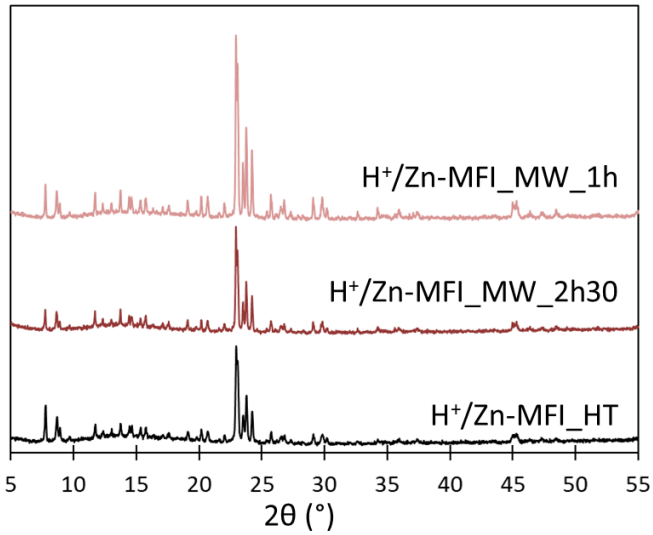

Figure 31: Powder-XRD patterns of Zn-MFI samples synthesised using the microwave-assisted method and compared to a sample prepared with conventional hydrothermal synthesis.

Table 12: Elemental composition obtained by XRF analyses on Zn-MFI samples prepared using the microwave-assisted synthesis method. The uncertainty on the measurements is the 6% of the values (only reported for Si:Zn ratios).

Sample	Si:Zn Synth. gel	Si:Zn Solid	Si (wt. %)	Zn (wt. %)
H⁺/Zn-MFI_HT	*100*	65.4 ± 3.9	46.3	1.7
H⁺/Zn-MFI_MW_1h	*100*	62.8 ± 3.8	45.2	1.7
H⁺/Zn-MFI_MW_2h30	*100*	52.3 ± 3.1	41.1	1.8

In order to assess the presence of closed/open Zn framework sites, the sample synthesised using microwave radiation (H^+/Zn-MFI_MW_1h) was ion-exchanged with Ni^{2+} cations adopting the procedure reported in the previous paragraph. The results obtained showed a partial exchange corresponding to a Ni:Zn ratio of 0.46 and a Si:Zn ratio of 67 in the final material. This suggests that not all the framework Zn sites present in the material occupy fully closed framework environments.

4.2.5. Thermo-gravimetric Analysis

The Thermo-Gravimetric Analysis (TGA) technique was used in order to quantify the number of TPA^+ molecules present in the materials and gain insights on the exact composition of the frameworks before calcination.[1] The samples were heated from room temperature to 700 °C with 5 °C/min ramps under a N_2 atmosphere, in order to prevent the oxidation of the materials.

[1] TGA experiments were kindly carried out by Mr. William Carswell at Durham University.

The weight of the materials was monitored throughout the analysis and a TGA curve obtained showing the sample weight as a function of the temperature. The total weight loss was calculated using the second derivative of the TGA curve (d2TG) in order to localise the beginning point of the pyrolysis, which is the process of decomposition of the SDA. The decomposition ends when a constant weight of the sample could be measured at high temperature. The results obtained are summarised in Table 13. A trend can be observed between TPA:Zn molar ratios and samples prepared with increasing amounts of KOH. In fact, the TPA:Zn ratio increases with the increasing of the KOH content for samples with TPA:K between 6 and 3. The sample with TPA:K=8 shows the highest TPA:K calculated ratio (5.40). In this sample the K:Zn molar ratio was < 2, therefore the incorporation of a greater number of SDA cations could be due to the need of more charge-balancing species in the sample.

Table 13: Weight loss of the samples following a heat treatment through TGA analyses and calculation of the TPA:Zn ratio.

Entry	Sample name	Sample weight (g)	Weight loss (%)	TPA:Zn
1	***Zn-MFI_TPA:K=∞***	0.013	10	3.2
2	***Zn-MFI_TPA:K=8***	0.012	12	5.5
3	***Zn-MFI_TPA:K=6***	0.033	11	3.8
4	***Zn-MFI_TPA:K=5.65***	0.006	11	4.0
5	***Zn-MFI_TPA:K=3***	0.007	11	4.5

The results obtained from TGA analyses were also used to calculate an empirical formula for the as synthesised zincosilicate MFI samples, using formula:

$$TPA_aK_bZn_nSi_{(96-n)}O_{192} \cdot 16\ H_2O$$

The values of a, b and n were estimated using the moles of SDA calculated from the weight loss values obtained from TGA and the moles of K, Si and Zn calculated from elemental analysis results (XRF). The values of the indexes a, b and n were calculated knowing the molar ratios between TPA^+, K, Zn and Si and the general unit cell formula, using the following equations:

$$\frac{mol_{Si}}{mol_{Zn}} = \frac{96-n}{n} \rightarrow n = \frac{96}{\left({}^{mol_{Si}}/_{mol_{Zn}} + 1\right)} \qquad \text{Equation 16}$$

$$\frac{mol_K}{mol_{Zn}} = \frac{b}{n} \rightarrow b = \frac{mol_K}{mol_{Zn}}\, n \qquad \text{Equation 17}$$

$$\frac{mol_{TPA}}{mol_{Zn}} = \frac{a}{n} \rightarrow a = \frac{mol_{TPA}}{mol_{Zn}}\, n$$ Equation 18

The values obtained for the indexes are reported in Table 14. Overall, the average calculated values of the indexes are 4.40 for a, 2.59 for b and 1.11 for n. A trend can be identified for decreasing values of a with the increasing of the potassium content in the samples, with the exception of the sample Zn-MFI_TPA:K=6, which shows a value lower than expected. The same is observed for the value of n in the same sample, with 0.99 being lower than the average among the samples. Nevertheless, these observations helped shed some light on the real elemental composition of the zincosilicate structure and the role of the species in it. More specifically, a competitive behaviour can be identified between TPA^+ and K^+ species for most of the samples. It appears that the charge balancing role is preferably played by K^+ cations to fully counter-balance the negative charges associated with Zn heteroatoms (when possible). This may be due to the large size difference between the TPA^+ and K^+ cations and the difficulty to accommodate two TPA^+ molecules in close proximity within the framework channels. Additionally, it is suggested that the SDA molecules interact with the framework, leading to the formation of defects which are healed after calcination and removal of the SDA, especially in potassium-containing samples. Ultimately, the amount of Zn incorporated in the samples appears to be independent from the SDA or KOH contents, as the value of n is close to 1 in all samples.

Table 14: Calculated values of indexes a, b and n from the general unit cell formula of Zn-MFI $TPA_aK_bZn_nSi_{(96-n)}O_{192} \cdot 16\ H_2O$.

Entry	Sample name	a	b	n
1	***Zn-MFI_TPA:K=∞***	4.8	-	1.2
2	***Zn-MFI_TPA:K=8***	5.4	1.3	1.1
3	***Zn-MFI_TPA:K=6***	3.4	2.3	1.0
4	***Zn-MFI_TPA:K=5.65***	4.4	3.0	1.2
5	***Zn-MFI_TPA:K=3***	3.9	3.7	1.1

4.3. Chapter 4 Conclusions

Two different synthesis procedures were used for the preparation of Zn-MFI samples. The samples made using the first one, adapted from the preparation of ferrierite (FER) zeolite by Göğebakan et al.,[30] were not fully crystalline, even after a long synthesis time (7 days). Therefore, a different synthesis method was attempted, which was similar to the one reported by Mal *et al.* (procedure B) for the synthesis of Sn-MFI zeotypes.[31] In the original preparation $SnCl_2$ was used as metal precursor, therefore $ZnCl_2$ was the first choice for the preparation of Zn-MFI using this method. However, the p-XRD patterns of samples prepared using different Zn precursors all show highly crystalline and pure products. From the p-XRD patterns it can also be concluded that the Zn-MFI samples prepared with low Si:Zn ratio (25 or 50) do not exhibit the presence of visible impurities (such as ZnO). This shows that the synthesis method applied ensures a good degree of solubilisation of the Zn source and consequent incorporation in the framework, even at high Zn concentration. Based on these observations, the samples with high Si:Zn ratios (100 or 150) are also assumed to be impurity-free based on their p-XRD patterns; however, the presence of impurity-related peaks in the patterns is unlikely for these samples given the low Zn content. A difference between the patterns can be noticed for peaks centred at 23.1°. The peak observed at this value corresponding to a Silicalite-1 sample (prepared using the same procedure but without the addition of Zn) appears as a single, sharp peak, whilst in samples prepared with increasing Zn content a change in the peak features can be observed. Specifically, the peak becomes rounded and it emerges as made up of two distinct peaks. A similar behaviour can also be noticed for the peaks centred at 23.5°. This could be explained considering that an increasing amount of Zn incorporated in the samples is causing alterations in the unit cell size of the crystals, due to the different size of the Zn atoms compared to Al atoms.

The results obtained from elemental analysis characterisation of the washed and dried synthesis products provide some insights on the real amount of Zn contained in the samples. A discrepancy was noticed between the Si:Zn molar ratio of the synthesis gel and the Si:Zn ratio measured in the products. This is probably due to a lower amount of silicon incorporated in the products. Elemental analysis carried out on samples prepared using different Zn precursors revealed that the Si:Zn ratio dependent on the Zn source. The XRF results show that the synthesis method based on $ZnCl_2$ as the Zn source would deliver the lowest Si:Zn ratio in the products. When $Zn(OAc)_2$ was used, the expected and experimental Si:Zn ratios were the closest, whilst product prepared using $Zn(NO_3)_2$ had an intermediate Si:Zn ratio. These differences could be explained considering to the properties of the counter-anions in the Zn precursors, causing variations in the incorporation levels of Si and/or Zn. Therefore, whilst the crystallinity of the samples was not affected by it, the use of different Zn precursors has an impact on the Si:Zn

molar ratio of the products. The exact compositions of the zincosilicate materials were evaluated by the combination of TGA experiments and elemental analysis in order to obtain a unit cell formula. The results suggested that a competitive behaviour is established between TPA^+ and K^+ cations as charge-balancing species.

The same synthesis method employed for the preparation of zincosilicate samples was adapted to the synthesis of other heteroatom-substituted zeotypes, *i.e.* Ni-, Co- and Mg-MFI, as well as a sample of TS-1. The synthesis procedure revealed itself to be easily adaptable to the preparation of these materials, which showed high crystallinity and elemental analysis results in line with expectations.

The addition of KOH as inorganic mineralising agent in the synthesis was considered to limit the formation of defect sites and ensure the presence of Zn sites in closed framework environments. The ion exchange of divalent cations (Ni^{2+}) was used as a probe of the absence of low charge-bearing Zn sites. Elemental analysis results of the ion-exchanged samples show that the Ni-exchange of starting materials with K:Zn ratios > 2 was > 100%, whilst when the K:Zn ratio in the starting material was < 2 only a partial exchange could be achieved. In conclusion, a correlation could be observed between the potassium content and the ion-exchange capacity of the samples. In addition to this, the Ni-exchanged samples exhibited Si:Zn ratios higher than the one measured in the starting materials, indicating a loss of framework Zn sites due to the elevated temperature conditions used for the procedure.

The materials prepared using $ZnCl_2$ without the addition of KOH were used in further characterisation (such as X-Ray absorption analyses) and methane activation experiments. The materials prepared using $Zn(NO_3)_2$ and varying amounts of KOH were employed in NMR studies, aimed at a better understanding of the defects in the materials, and for ethanol conversion reactions, due to the presence of a lower degree of silanol sites.

Chapter 4 Bibliography

[1] P. McAnespie, A. Dyer, and J. M. Bharati, “Method of synthesizing zincosilicate or stannosilicate or titanosilicate material,” US4329328A, 1982.

[2] M. J. Annen, M. E. Davis, J. B. Higgins, and J. L. Schlenker, “VPI-7: the first zincosilicate molecular sieve containing three-membered T-atom rings,” *J. Chem. Soc. Chem. Commun.*, 17, pp. 1175–1176, **1991**.

[3] M. J. Annen, “Synthesis and characterization of novel molecular sieves containing three-membered rings,” Virginia Tech, **1992**.

[4] M. J. Annen and M. E. Davis, “Raman and 29Si MAS NMR spectroscopy of framework materials containing three-membered rings,” *Microporous Mater.*, 1, 1, pp. 57–65, **1993**, doi: 10.1016/0927-6513(93)80008-I.

[5] A. J. M. de Man, S. Ueda, M. J. Annen, M. E. Davis, and R. A. van Santen, “The stability and vibrational spectra of three-ring containing zeolitic silica polymorphs,” *Zeolites*, 12, 7, pp. 789–800, **1992**, doi: 10.1016/0144-2449(92)90051-P.

[6] M. A. Camblor, R. F. Lobo, H. Roller, and M. E. Davis, “Synthesis and Characterization of Zincosilicates with the SOD Topology,” *Chem. Mater.*, 6, 11, pp. 2193–2199, **1994**, doi: 10.1021/cm00047a046.

[7] N. Rajić, N. Z. Logar, and V. Kaučič, “A novel open framework zincophosphate: Synthesis and characterization,” *Zeolites*, 15, 8, pp. 672–678, **1995**, doi: 10.1016/0144-2449(95)00083-I.

[8] Y. Sakamoto, H. Zhao, H. Gies, K. Yamamoto, U. Kolb, and T. Ikeda, “A new microporous 12-ring zincosilicate THK-2 with many terminal silanols characterized by automated electron diffraction tomography,” *Dalt. Trans.*, 49, 37, pp. 12960–12969, **2020**, doi: 10.1039/d0dt02290j.

[9] T. Takewaki, L. W. Beck, and M. E. Davis, “Zincosilicate CIT-6: A precursor to a family of *BEA-type molecular sieves,” *J. Phys. Chem. B*, 103, 14, pp. 2674–2679, **1999**, doi: 10.1021/jp9845726.

[10] M. Dong, J. Wang, and Y. Sun, “Synthesis of zincosilicate mordenite using citric acid as complexing agent,” *Microporous Mesoporous Mater.*, 43, 2, pp. 237–243, **2001**, doi: 10.1016/S1387-1811(01)00211-6.

[11] L. Wang, S. Sang, S. Meng, Y. Zhang, Y. Qi, and Z. Liu, “Direct synthesis of Zn-ZSM-5 with novel morphology,” *Mater. Lett.*, 61, pp. 1675–1678, **2007**, doi: 10.1016/j.matlet.2006.07.097.

[12] A. Palčić, F. Z. Abellán, A. Vicente, C. Fernandez, V. Georgieva, J. Bronić, V. Valtchev “Formation mechanism of three-membered ring containing microporous zincosilicate RUB-17,” *CrystEngComm*, 17, 37, pp. 7063–7069, **2015**, doi: 10.1039/c5ce01394a.

[13] M. E. Davis and M. J. Dusselier, “Processes for preparing zincoaluminosilicates with AEI, CHA, AND GME topologies and compositions derived therefrom.,” US20160243531A1, 2016.

[14] N. Koike, W. Chaikittisilp, K. Iyoki, Y. Yanaba, T. Yoshikawa, S. P. Elangovan, K. Itabashi, T. Okubo, “Organic-free synthesis of zincoaluminosilicate zeolites from homogeneous gels prepared by a co-precipitation method,” *Dalt. Trans.*, 46, 33, pp. 10837–10846, **2017**, doi: 10.1039/c7dt02001e.

[15] N. Koike, K. Iyoki, S. H. Keoh, W. Chaikittisilp, and T. Okubo, “Synthesis of New Microporous Zincosilicates with CHA Zeolite Topology as Efficient Platforms for Ion-Exchange of Divalent Cations,” *Chem. - A Eur. J.*, 24, 4, pp. 808–812, **2018**, doi: 10.1002/chem.201705277.

[16] W. Yan, X. Shibo, D. Yonghua, M. K. Schreyer, T. S. Xing, L. Yan, A. Borgna “Heteroatomic Zn-MWW Zeolite Developed for Catalytic Dehydrogenation Reactions: A Combined Experimental and DFT Study,” *ChemCatChem*, 10, 14, pp. 3078–3085, **2018**, doi: 10.1002/cctc.201800199.

[17] M. Yoshikawa, S. I. Zones, and M. E. Davis, “Synthesis of VPI-8. I. The effects of reaction components,” *Microporous Mater.*, 11, 3–4, pp. 127–136, **1997**, doi: 10.1016/S0927-6513(97)00031-X.

[18] M. Yoshikawa, S. I. Zones, and M. E. Davis, “Synthesis of VPI-8. II. Mechanism of crystallization,” *Microporous Mater.*, 11, 3–4, pp. 137–148, **1997**, doi: 10.1016/S0927-6513(97)00032-1.

[19] Koike Natsume, “Synthesis of Zinc-Containing Zeolites with a Focus on Mixing Methods of Raw Materials,” **2018**.

[20] P. Hu, K. Iyoki, H.i Yamada, Y. Yanaba, K. Oharac, N. Katadad, T. Wakihara “Synthesis and characterization of MFI-type zincosilicate zeolites with high zinc content using mechanochemically treated Si–Zn oxide composite,” *Microporous Mesoporous Mater.*, 288, June, p. 109594, **2019**, doi: 10.1016/j.micromeso.2019.109594.

[21] Z. Sun, Y. Yan, G. Li, Y. Zhang, and Y. Tang, “Microwave Influence on Different M − O Bonds During MFI-Type Heteroatom (M) Zeolite Preparation,” *Ind. Eng. Chem. Res.*, 56, 39, pp. 11167–11174, **2017**, doi: 10.1021/acs.iecr.7b03072.

[22] G. A. Tompsett, W. C. Conner, and K. S. Yngvesson, “Microwave synthesis of nanoporous materials,” *ChemPhysChem*, 7, 2. Wiley-VCH Verlag, pp. 296–319, Feb. 13, 2006, doi: 10.1002/cphc.200500449.

[23] P. Chu, W. Deptford, F. G. Dwyer, and J. C. Vartuli, “Crystallization Method Employing Microwave Radiation,” EP0358827B1, Dec. 04, 1986.

[24] J. Liu and J. Yu, “Toward Greener and Designed Synthesis of Zeolite Materials,” in *Zeolites and Zeolite-like Materials*, B. F. Sels and L. M. Kustov, Eds. Elsevier Inc., **2016**, pp. 1–32.

[25] Z. Liu, J. Zhu, T. Wakihara, T. Okubo “Ultrafast and continuous flow synthesis of silicoaluminophosphates,” *Chem. Mater.*, 28, 13, pp. 4840–4847, **2016**, doi: 10.1021/acs.chemmater.6b02141.

[26] K. Yamamoto, S. E. Borjas García, and A. Muramatsu, “Zeolite synthesis using mechanochemical reaction,” *Microporous Mesoporous Mater.*, 101, 1-2 SPEC. ISS., pp. 90–96, **2007**, doi: 10.1016/j.micromeso.2006.09.034.

[27] S. E. Borjas Garcia, K. Yamamoto, and A. Muramatsu, “Synthesis of Ti-Beta via mechanochemical route,” in *Journal of Materials Science*, **2008**, 43, 7, pp. 2367–2371, doi: 10.1007/s10853-007-2104-x.

[28] A. Deneyer, Q. Ke, J. Devos, and M. Dusselier, “Zeolite Synthesis in Non-Conventional Conditions : Reagents , Reactors and Modi Operandi,” *Chem. Mater.*, **2020**, doi: 10.1021/acs.chemmater.9b04741.

[29] T. Iida, A. Takagaki, S. Kohara, T. Okubo, and T. Wakihara, “Sn-Beta Zeolite Catalysts with High Sn Contents Prepared from Sn-Si Mixed Oxide Composites,” *ChemNanoMat*, 1, 3,

pp. 155–158, **2015**, doi: 10.1002/cnma.201500038.

[30] Z. Göğebakan and H. Yu, “Crystallization Field and Rate Study for the Synthesis of Ferrierite,” *Ind. Eng. Chem. Res.*, 46, 7, pp. 2006–2012, **2007**, doi: 10.1021/IE061013.

[31] N. K. Mal, V. Ramaswamy, P. R. Rajamohanan, and A. V Ramaswamy, “Sn-MFI molecular sieves : synthesis methods , 29Si liquid and solid MAS-NMR , 119Sn static and MAS NMR studies,” *Microporous Mater.*, 12, pp. 331–340, **1997**.

[32] Y. G. Kolyagin, A. V. Yakimov, S. Tolborg, P. N. R. Vennestrøm, and I. I. Ivanova, “Application of 119Sn CPMG MAS NMR for Fast Characterization of Sn Sites in Zeolites with Natural 119Sn Isotope Abundance,” *J. Phys. Chem. Lett.*, 7, 7, pp. 1249–1253, **2016**, doi: 10.1021/ACS.JPCLETT.6B00249.

[33] C. Weidenthaler, “Pitfalls in the characterization of nanoporous and nanosized materials,” *Nanoscale*, 3, 3, pp. 792–810, **2011**, doi: 10.1039/C0NR00561D.

[34] L. Van Tendeloo, E. Gobechiya, E. Breynaert, J. A. Martens, and C. E. A. Kirschhock, “Alkaline cations directing the transformation of FAU zeolites into five different framework types,” *Chem. Commun.*, 49, 100, pp. 11737–11739, **2013**, doi: 10.1039/C3CC47292B.

[35] M. C. Dalconi, G. Cruciani, A. Alberti, P. Ciambelli, and M. T. Rapacciuolo, “Ni 2+ ion sites in hydrated and dehydrated forms of Ni-exchanged zeolite ferrierite,” *Microporous Mesoporous Mater.*, 39, pp. 423–430, **2000**.

[36] L. Liu, M. L.-Haro, C. W. Lopes, C. Li, P. Concepcion, L. Simonelli, J. J. Calvino, A. Corma “Regioselective generation and reactivity control of subnanometric platinum clusters in zeolites for high-temperature catalysis,” *Nat. Mater. 2019 188*, 18, 8, pp. 866–873, **2019**, doi: 10.1038/S41563-019-0412-6.

1

5. Chapter 5: Characterisation of Zn-MFI Zeotypes

5.1. Brief Introduction to Characterisation Techniques

In order to fully characterise the zincosilicates, a wide range of techniques were employed. The aims of the analysis techniques were to (i) identify the framework type, (ii) quantify the amounts of elements present in the material, (iii) exclude the presence of extra-framework oxide or hydroxide species, (iv) identify the crystallite morphology and size distribution and (v) probe the local environment around the Zn heteroatoms. In order to achieve this, X-ray based techniques (XRD, XRF, XAS), SS NMR, diffuse reflectance UV-vis spectroscopy (DR UV-vis), diffuse reflectance IR Fourier transform spectroscopy (DRIFTS), electron microscopy (SEM) and thermal analysis (TGA) were applied. The local environment around Zn heteroatoms was the most challenging piece of evidence to obtain, due to the "silent" nature of Zn atoms towards certain techniques.[1] The identification of framework or extra-framework Al species in aluminosilicate zeolites is easily carried out using well-known techniques such as SS NMR,[2] this cannot be achieved for Zn-substituted zeotypes without isotopic enrichment of the samples and/or extremely high magnetic fields (see Section 3.2.4.4 for further details).[3] Nevertheless, certain characterisation techniques are able to detect the chemical environment around the Zn heteroatoms inserted in the microporous framework, such as IR spectroscopy[4] or X-ray Absorption spectroscopy.[5]–[7] The next paragraphs in this chapter will focus on the results obtained from the characterisation techniques applied to Zn-ZSM-5 samples prepared using the TEOS-based synthesis (with and without KOH) and compared to the ones prepared with the pyrrolidine synthesis (where applicable). The results obtained from XRD, XRF and TGA analyses have already been reported in Chapter 4.

5.2. Results and Discussion

5.2.1. Solid State NMR

Solid-State NMR spectroscopy was employed to probe ^{1}H and ^{29}Si nuclei in the zincosilicate zeotypes, in order to gain insights on the chemical environment of the species present in the materials. This could be particularly useful to identify the types of framework sites present in the samples, *i.e.* closed or open/partially open sites, and to evaluate the effect of post-synthetic treatments on the structures. More specifically, the materials in the as-made form are expected to show the presence of defect sites around Si atoms and the presence of TPA^{+} cations, possibly interacting with each other. The calcination procedure usually plays a "healing" effect of the defect sites, by eliminating the SDA molecules occluded in the framework cavities and allowing for the condensation of silanols.[8], [9] Additionally, the effects of the post-synthesis treatments on the structural integrity of the materials were analysed in dehydrated and re-hydrated materials after calcination (Figure 32). In the absence of extra-framework

inorganic cations, the presence of atmospheric moisture was thought to cause structural damage to the framework, producing partially open sites (Figure 32(a)). Partially open Zn sites were proposed by Orazov and Davis for CIT-6 materials studied with CD_3CN FTIR[10] and post-synthetically treated under acidic conditions, whilst CIT-6 (and other zincosilicate) materials bearing monovalent cations (Li^+ or Na^+) showed mainly closed Zn sites. Based on this evidence, it was expected that the Zn-MFI materials studied in our work, which contained K^+ cations, would show a greater amount of closed Zn sites after calcination, even if exposed to atmospheric moisture (Figure 32(b)).

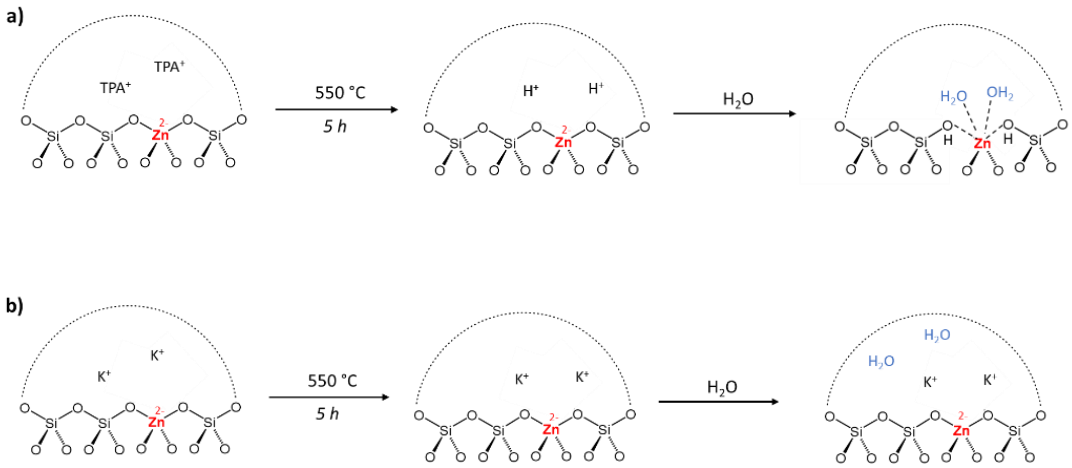

Figure 32: Structures of the Zn-MFI materials in the "as-made" and calcined forms for materials prepared with the TEOS-based synthesis with (a) and without (b) the addition of KOH.

A series of ^1H and ^{13}C NMR, coupled with 2D double-quantum/single-quantum (DQ/SQ) and heteronuclear-correlation (HETCOR) analyses were also carried out on as-synthesised Zn-MFI samples (TPA^+-K^+/Zn-MFI) in order to study (i) the potential influence of the organic SDA on the formation of defective sites and, specifically, how acidic silanol sites in the framework would interact with carbon and hydrogen species in the SDA and (ii) the role of inorganic cations in extra-framework positions as defect-healing species. Similar studies have been previously reported for aluminosilicate zeolites,[11]–[13] however there are no reports of the same analysis carried out on Zn-ZSM-5 materials and, additionally, on the role of potassium cations and their effect on the formation of framework defects. All the experiments discussed in the following sections were carried out on a Bruker Avance III HD spectrometer using a 4 mm MAS NMR probe according to the experimental details in Section 3.2.4. The materials employed for these experiments were all synthesised using the TEOS-based method and $Zn(NO_3)_2$ as Zn precursor. This choice was made because the TEOS-based synthesis produced the purest and most crystalline samples. $Zn(NO_3)_2$ was chosen as the Zn source because it is less hygroscopic than

$ZnCl_2$ and results easier to handle during the preparation. The evaluation of the uncertainty on the area of the peaks obtained through deconvolution of the NMR signal was not performed, as the NMR experiments on the single samples were not repeated.

5.2.1.1. Study of the Defect Sites through ^{29}Si and ^{1}H MAS NMR Experiments

In order to obtain more information about the presence of silanol defects in the latter, ^{29}Si MAS NMR experiments were carried out on a set of samples prepared using various amounts of KOH as inorganic mineralising agent, resulting in materials with ratios of TPAO:K equal to 3, 5.65, 6.5 and ∞ (Table 15).

Table 15: Elemental composition of the zincosilicate zeotype materials obtained through XRF analysis, expressed as wt% of the elements and molar ratios between the elements. The uncertainty on the measurements is the 6.4% of the values (only reported for Si:Zn and K:Zn ratios).

Entry	Sample	Si:Zn Synth. gel	Si:Zn Solid	K:Zn Solid	Si (wt. %)	Zn (wt. %)	K (wt. %)
1	***K^+/Zn-MFI_TPA:K=3***	*100*	96.4 ± 5.8	4.1 ± 0.3	48.3	1.2	2.9
2	***K^+/Zn-MFI_TPA:K=5.65***	*100*	90.3 ± 5.4	2.9 ± 0.2	47.5	1.2	2.2
3	***K^+/Zn-MFI_TPA:K=6.5***	*100*	88.0 ± 5.3	2.3 ± 0.1	44.7	1.2	1.6
4	***H^+/Zn-MFI_TPA:K=∞***	*100*	68.4 ± 4.1	0	36.4	1.2	0

The samples were analysed in their as-made, calcined, dehydrated and re-hydrated forms, in order to detect how the presence of organic SDA and water molecules affected the amount of framework defects. The materials marked as "as-made" are the as-synthesised samples, *i.e.* washed and dried overnight at 100 °C. The "calcined" form of the samples results from thermal treatment carried out at 550°C for 6 hours to decompose TPA^+ species, and anaylised at room temperature. The "dehydrated" samples underwent an additional thermal treatment at 550 °C performed under reduced pressure (< 10^{-2} mbar); the NMR rotor containing the sample was packed in an Ar-filled glovebox and analysed at room temperature. Finally, the "re-hydrated" materials are the "dehydrated" samples exposed to atmospheric moisture at room temperature for a certain time (7 or 8 days) after being analysed. The ^{29}Si NMR spectra were recorded at room temperature and deconvoluted in order to extract the signals corresponding to Q_4 and Q_3 silicon sites. Figure 33 shows a representation of the Q_4 and Q_3 silicon sites and their corresponding chemical shifts in the ^{29}Si NMR spectrum.

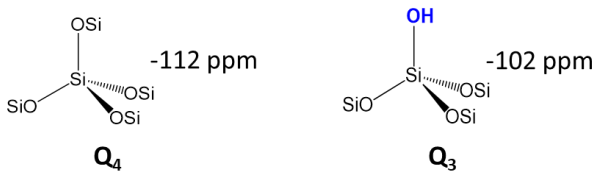

Figure 33: Representation of Q_4 and Q_3 tetrahedral silicon sites and their chemical shifts typically observed in ssMAS NMR analysis.

Figure 34 shows the ^{29}Si MAS NMR spectra acquired in the direct excitation mode for the as-made, calcined, dehydrated and re-hydrated Zn-MFI samples. The spectra show presence of the two silicon environments corresponding to: Q_4 sites (*i.e.* a Si atom bonded to four -OSi species) generally detected at -112 ppm, and Q_3 sites (*i.e.* a Si atom bonded to three -OSi species and one hydroxyl group) which appear at -102 ppm.[14] The possibility of detecting Q_4(1Zn) sites between -95 and -105 ppm[15]–[17] is not likely due to the low concentration of Zn in the materials, causing the signal corresponding to this environment to be covered by the more intense Q_4(0T) signal.

The spectral features observed in Figure 34 are in line with evidence reported in the literature. [14], [15] More specifically, the presence of defects at -104 ppm was reported by Andy and Davis for their CIT-6 (BEA) materials after being treated with acetic acid. The authors attributed the formation of these defects to the removal of Zn heteroatoms from the framework due to the acidic conditions of the treatment,[15] A different study carried out on CIT-6 also showed a decrease of the intensity of signals between -95 and -105 ppm after calcination at 550 °C.[16] The results show that after calcination the intensity of the signal corresponding to Q_3 sites decreases with respect to Q_4 sites. This indicated that the defect sites are healed during calcination. Additionally, this confirms the assignment of the -102 ppm signal to Q_3(0T) sites and not to Q_3(1Zn) sites, because it is not likely that the latter would disappear after calcination. However, this is not observed in the Zn-MFI sample prepared without KOH (H^+/Zn-MFI_TPA:K=∞, Figure 34(d)), as the presence of residual signal at -102 ppm could still be detected in the calcined sample. This suggests that the presence of inorganic K^+ cations modifies the type of defects present in the materials by bonding with framework oxygen species. This generates Si-O^--K^+ species, preventing the formation of silanol defects, allowing for a full healing (i.e. absence of Q_3 sites) during the calcination step. From the spectra recorded it can be noticed that the intensity of the peaks corresponding to the Q_4 and Q_3 silicon sites does not exhibit any detectable variation between the dehydrated and re-hydrated samples, indicating that the number of Q_3 sites present in the calcined materials is not affected by further treatments performed on the sample. However, an exception to this was observed for the sample containing a TPA:K ratio of 6.5 (Figure 34(c)), which showed a slightly more intense Q_3 peak than the one observed in the calcined form in both the dehydrated and the re-hydrated forms.

Further ^{29}Si MAS NMR results are reported in Section 9.3.1 of the Appendix and show Direct Excitation and ^{1}H-^{29}Si CP spectra of Zn-MFI materials prepared using the TEOS-based synthesis and $ZnCl_2$ as Zn source, with Si:Zn ratios of 25, 50 and 100. The spectra show the presence of signals at the chemical shifts attributed to Q_4 and Q_3 sites (-120 ppm and -102 ppm). In addition to this, the Zn-MFI calcined materials with Si:Zn = 25 or 50 also exhibit the presence of another signal centred at -99 ppm. Based on the data reported by Takewaki et al. for CIT-6,[16] it is reasonable to assume that the signal at -99 ppm in the Zn-MFI materials can be assigned to Q_3(1Zn) sites. The decreasing of the intensity of this signal in the materials prepared with a lower Zn content corroborates this hypothesis. These results were not observed in the materials prepared with $Zn(NO_3)_2$ most likely due to a too low concentration of Zn in these materials.

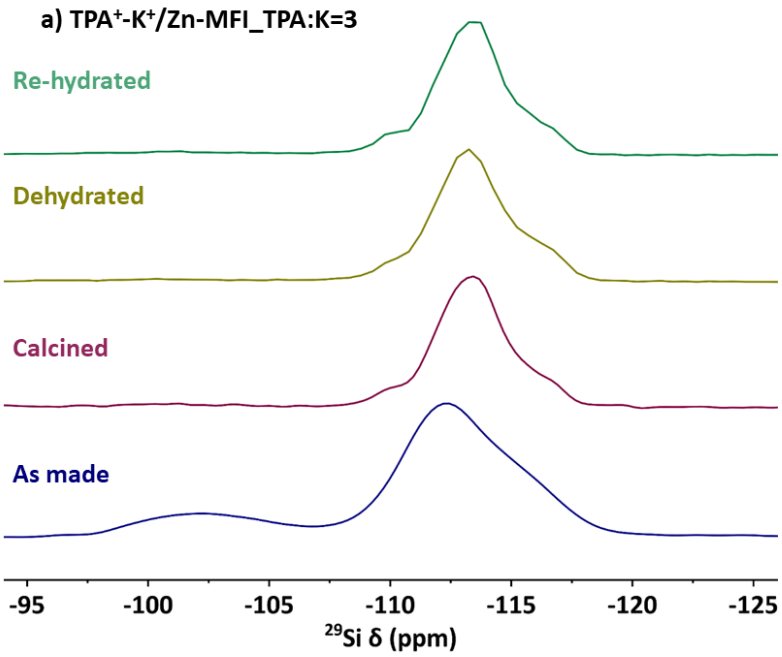

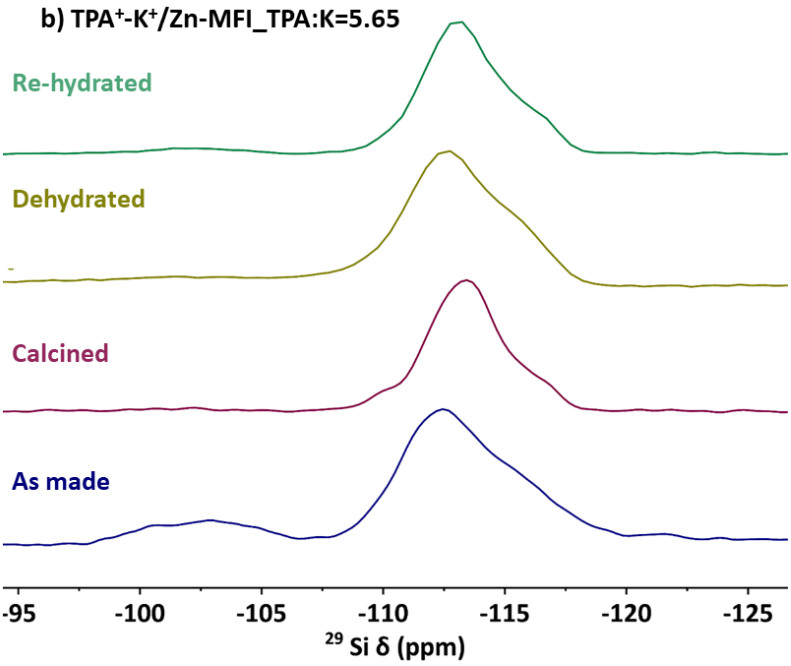
b) TPA+-K+/Zn-MFI_TPA:K=5.65
Re-hydrated
Dehydrated
Calcined
As made
-95
-100
-105
-110
-115
-120
-125
29 Si δ (ppm)

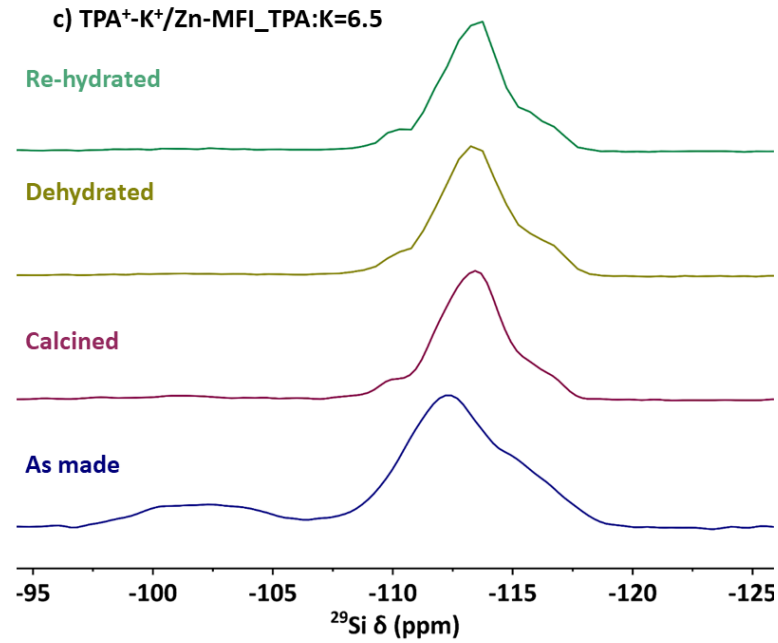
c) TPA+-K+/Zn-MFI_TPA:K=6.5
Re-hydrated
Dehydrated
Calcined
As made
-95
-100
-105
-110
-115
-120
-125
29Si δ (ppm)

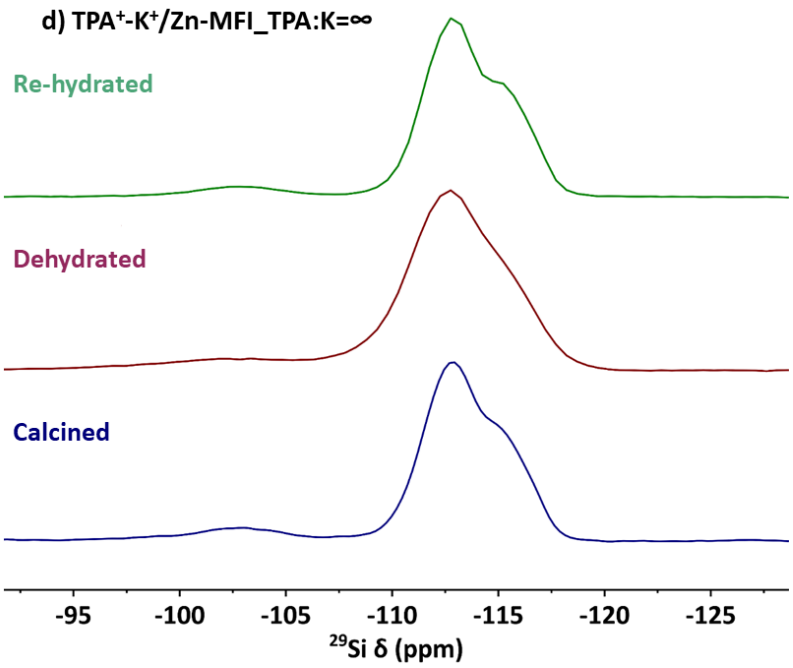

Figure 34: ^{29}Si MAS NMR spectra acquired in the direct excitation mode showing signals corresponding to Q_4 and Q_3 silicon environments in TPA^+-K^+/Zn-MFI samples prepared with TPA:K ratios of 3 (a), 5.65 (b), 6.5 (c) and no KOH (d).

Figure 35 shows the results from the deconvolution and integration of the signals corresponding to Q_4 and Q_3 silicon sites plotted as functions of the TPA:K ratios of calcined Zn-MFI samples. The numeric values are reported in Table 30 in Section 9.3.1 of the Appendix. The results indicate that the percentage of Q_4 environments reaches a maximum value in the sample containing a TPA:K ratio of 6.5 (closest to 100%), whilst the samples prepared with the highest amount of KOH (TPA:K = 3) and no KOH exhibit similar percentages of Q_4 sites. This suggests that a "sweet spot" for the TPA:K ratio of 6.5, corresponding to the almost total absence of silanol defects in the calcined samples. Figure 36 shows the variation of the Q_4 and Q_3 percentages as a function of the post-synthetic treatments, compared to the as-made form. As expected, a decrease of the Q_3 percentage and an increase of the Q_4 percentage is observed for calcined, dehydrated and re-hydrated materials and the Zn-MFI material prepared without the addition of KOH shows the lowest and the highest Q_4 and Q_3 values, respectively.

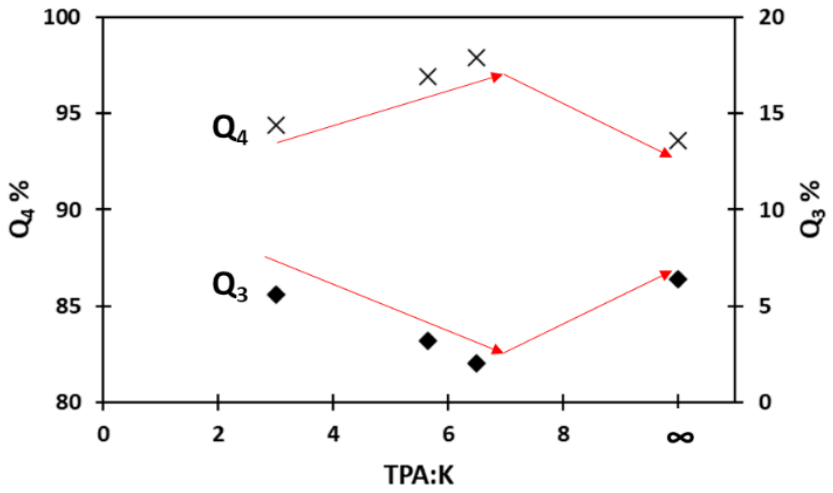

Figure 35: Plot of the Q_4 and Q_3 Si environments, reported as their % contribution to the total area of the signal and obtained through deconvolution, as a function of the TPA:K ratio in calcined materials.

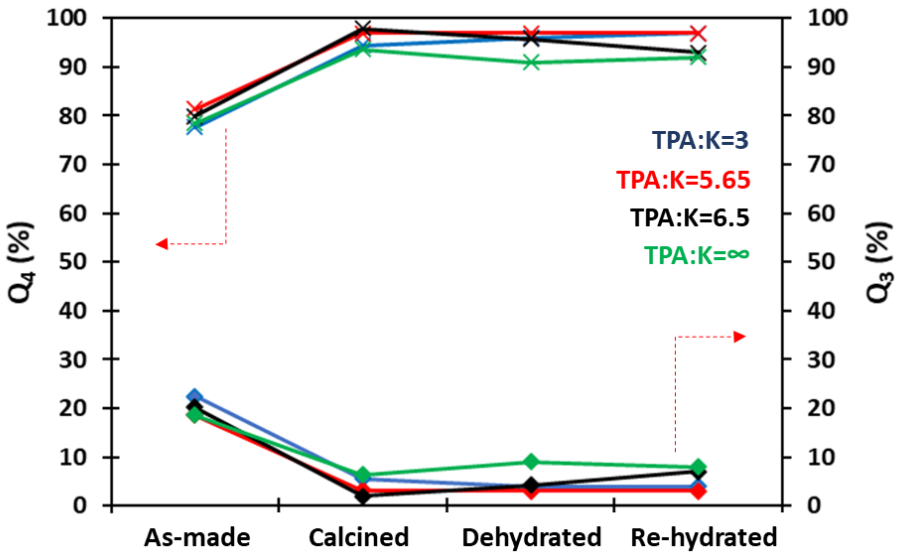

Figure 36: Plot of the Q_4 and Q_3 percentages in zincosilicate materials prepared with different TPA:K ratios as a function of the post-synthetic treatments.

The Zn-MFI materials were also studied by means of ^{1}H MAS NMR, with the aim of identifying the proton species belonging to the occluded TPA^+ molecules and those belonging to silanol defects in the frameworks. Figure 37(a) shows the ^{1}H MAS NMR spectra of Zn-MFI materials in the "as-made" form, namely TPA^+-K^+/Zn-MFI_TPA:K=3, TPA^+-K^+/Zn-MFI_TPA:K=5.65 and TPA^+-K^+/Zn-MFI_TPA:K=6.5. The spectra show three signals centred at chemical shifts of 10.5, 12.5 and 16 ppm, assigned to hydrogen-bonding defects. According to Grosskreuz et al., the chemical shift values observed at high frequency for these protic species indicate the presence of a negative charge associated with a defective site.[8] Moreover, the different

chemical shift values are indicative of different O-H···O distances and, therefore, different hydrogen bond strengths. Specifically, a shift to higher frequencies is associated with a stronger hydrogen bond [8], [18] The broad signal detected centred at 1.3 ppm contains signals arising from protons belonging to TPA^+ cations and to isolated Si-OH sites, whilst peaks at 5 and 5.5 ppm are due to the presence of physisorbed water molecules.[8], [11] After calcination, all peaks associated to TPA^+ and defect sites are suppressed and the only signals remaining in the spectra are the ones arising from physisorbed water at 5 ppm and isolated silanol sites (Figure 37(b)). Figure 38(a) and (b) represent the comparison of ^1H spectra of two potassium-containing Zn-MFI samples before and after exposure to D_2O for 7 days. The results show that acidic protons belonging to hydrogen bonded SiOH···$^-$OSi defects are easily exchangeable to deuterium, as signals appearing at 10.5, 12.5 and 16 ppm disappear after D_2O exchange. The intensity of the broad peak centred at 1.3 ppm, however, is not affected by the exposure to the D_2O atmosphere. The behaviour of the signals assigned to physisorbed water, shifting between 5 and 5.5 ppm, indicates a slight change of environment of the latter.

a)

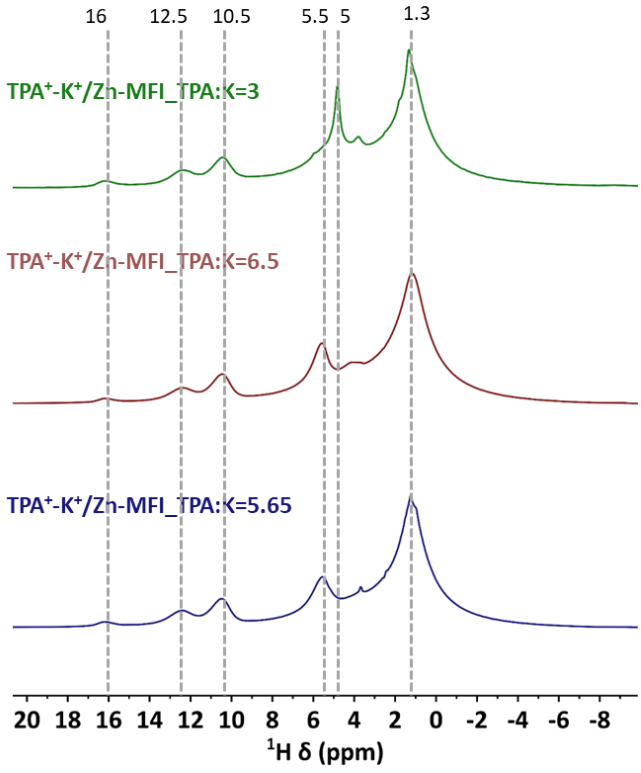

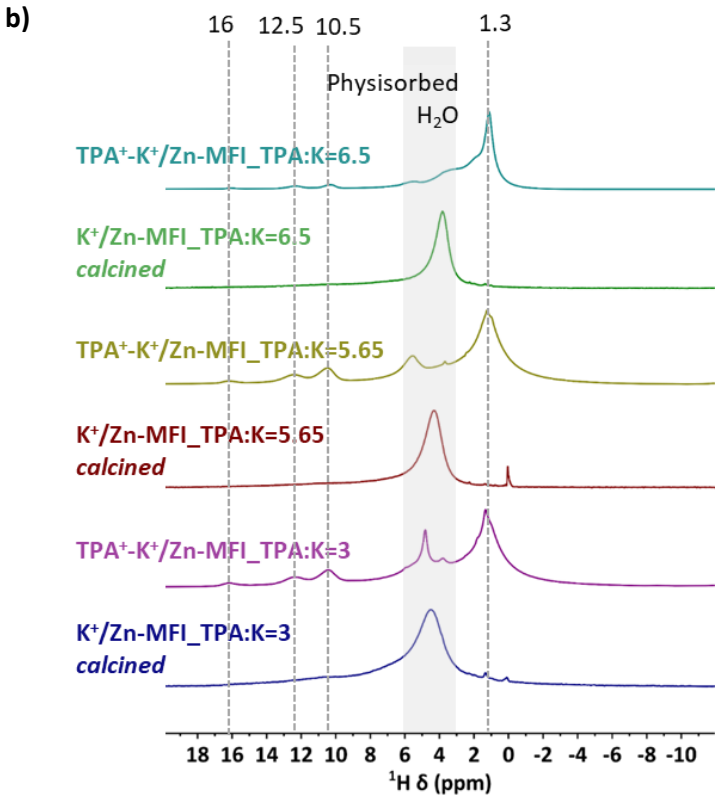

Figure 37: Spectra acquired through ^{1}H MAS NMR analysis of TPA^{+}-K^{+}/Zn-MFI samples (with TPA:K = 3, 5.65, 6.5) in the as-made form (a) and comparison between as-made and calcined forms of the same materials (b).

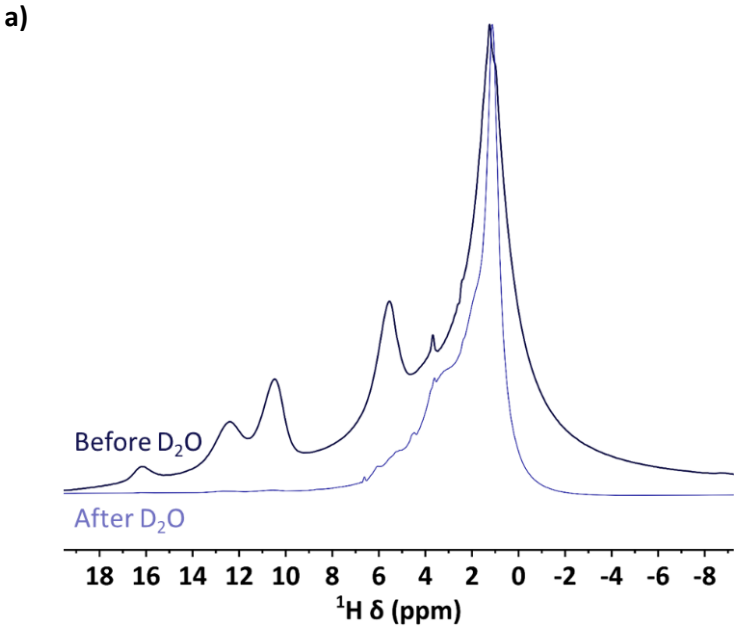

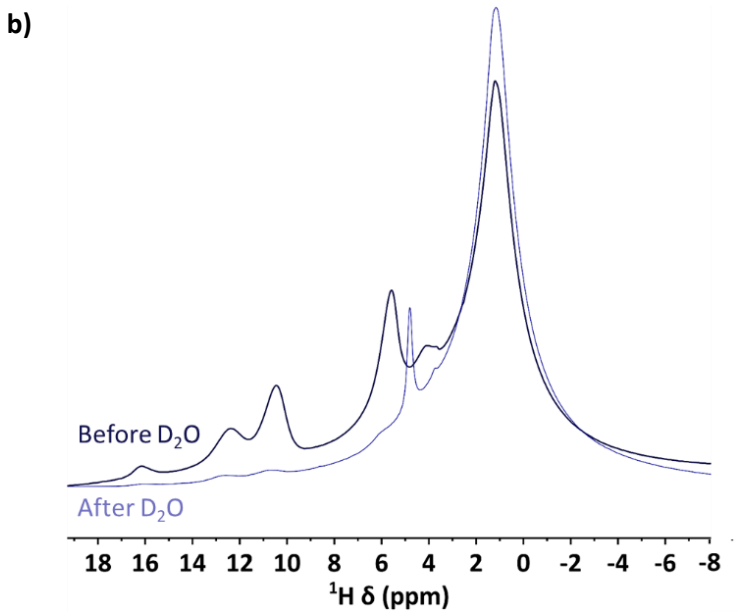

Figure 38: Comparison of ^{1}H signals before and after D_2O exchange for TPA^+-K^+/Zn-MFI samples prepared with TPA:K ratios of 5.65 (a) and 6.5 (b).

5.2.1.2. Study of the Role of the SDA Molecules through ^{1}H-^{29}Si HETCOR NMR

With the aim of understanding the interactions of the organic SDA cations (TPA^+) with framework species, potentially giving rise to defective sites, heteronuclear correlation (HETCOR) NMR experiments were carried out. These experiments also helped understand the role of K^+ cations in extra-framework positions in the charge-balancing of framework negative charges due to the presence of Zn heteroatoms. Figure 39 shows the defect sites that are expected to be observed in the materials. In Figure 39(a) hydrogen-bonded silanol sites are represented, which are usually observed at ^{1}H chemical shifts between 10 and 16 ppm.[18], [19] This type of defect site has been observed to be in close proximity with organic SDA molecules in zeolites,[12], [13] due to the fact that, in order to achieve local charge balancing, an anionic species is required to be in close proximity to TPA^+ cations. Additionally, the presence of a high number of TPA^+ cations is thought to induce the formation of siloxy Si–O^- sites,[20] which can interact with other silanol defects (Figure 39(b)). The presence of extra-framework inorganic cations could be a useful way to overcome issues related to defect sites in the zeotype frameworks. It has been reported that K^+ cations can form isolated potassium siloxide (KOSi) groups,[21] preventing the formation of silanol defect sites (Figure 39(c)). This may also limit the interactions between the OSDA molecules and the zeotype framework.

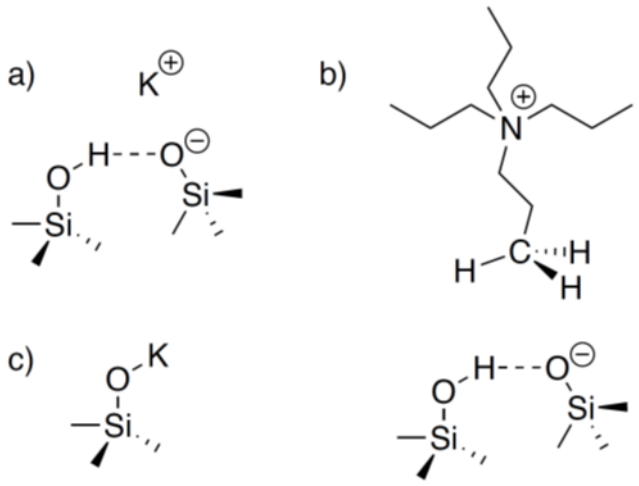

Figure 39: Representation of a hydrogen-bonded defect site (a), the same defect site in close proximity and interacting with the terminal group of a TPA^+ molecule (b) and an isolated K^+ cation bonded to framework oxygen species (c).

Initially, the ^1H-^{13}C spectrum of a TPA^+-K^+/Zn-MFI_TPA:K=6.5 material, containing TPA^+ cations, was acquired and is reported in Figure 40. The ^{13}C spectrum is very similar to prior studies on TPA^+ cations encapsulated in high silica zeolites.[22]–[24] The signal at higher chemical shift (65 ppm) was assigned to the $-CH_2$ carbon closest to the nitrogen, as it would be more heavily de-shielded. The peak at 16 ppm belongs to the central $-CH_2$ carbon group and the terminal $-CH_3$ groups were assigned to a peak split in two between 10 and 13 ppm. The presence of a split peak is due to the fact that the TPA^+ molecules are occluded in the framework and the chains can assume different orientations in the channels of the microporous framework. In particular, changes in the Van der Waals interactions between the organic molecules and framework species in straight or sinusoidal channels cause the splitting of the methyl signal in the ^{13}C spectrum.[22]–[24] From the spectrum it can also be noticed that correlation is present between the ^{13}C signals and ^1H signals between 1 and 4 ppm. Peaks associated with TPA^+ protons are normally observed at chemical shift values of 0.9 ($-CH_3$), 1.8 ($-CH_2-$) and 3.2 ppm ($N-CH_2$),[12] therefore, the correlation signals found in Figure 40 arise from interactions between proton and carbon atoms in occluded TPA^+ molecules.

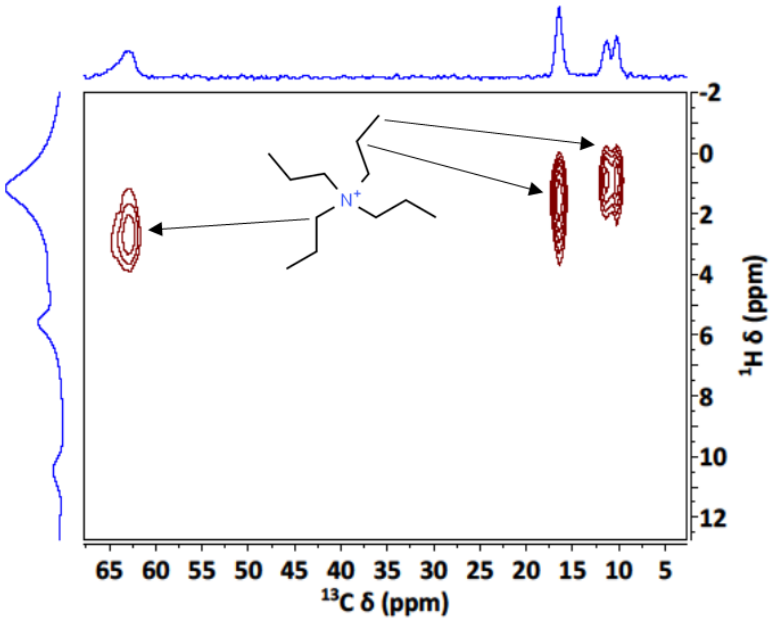

Figure 40: Spectrum representing the ^{1}H-^{13}C HETCOR NMR analysis of TPA^{+} cations occluded in a TPA^{+}-K^{+}/Zn-MFI_TPA:K=6.5 material.

Additional ^{1}H-^{29}Si HETCOR NMR experiments were carried out on the TPA^{+}/Zn-MFI materials prepared with the TEOS-based synthesis and using $Zn(NO_3)_2$, with and without KOH. Figure 41 shows the results obtained for a TPA^{+}/Zn-MFI_TPA:K=∞ sample, prepared without the addition of KOH. The ^{1}H-^{29}Si correlation signals were compared to the signals detected for TPA^{+} cations in order to confirm possible interactions between SDA protons and framework Si species.

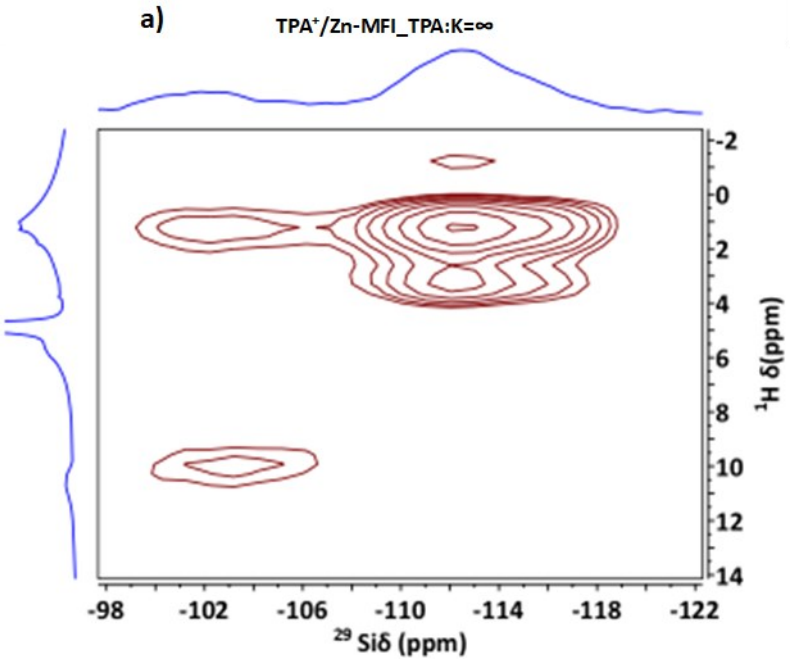

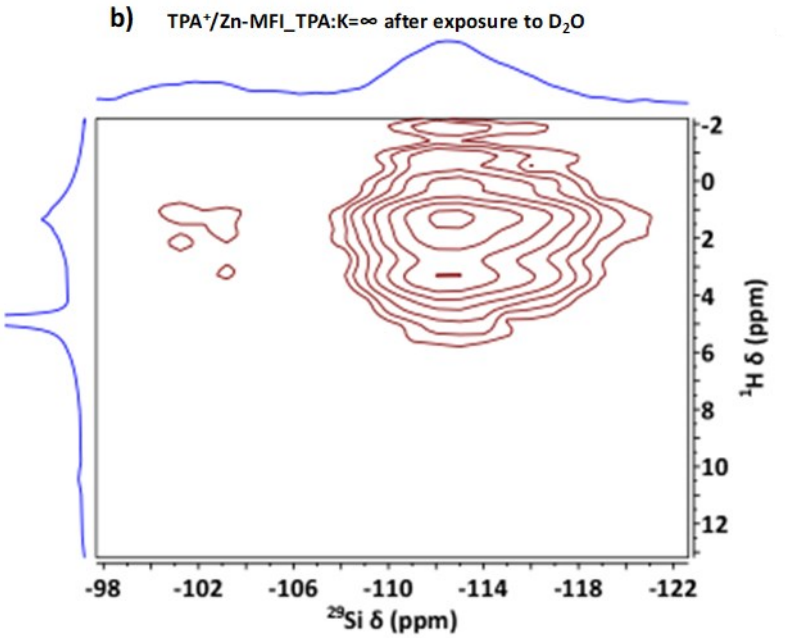

Figure 41: ^{1}H-^{29}Si HETCOR NMR spectra of TPA^{+}/Zn-MFI_TPA:K=∞ sample before (a) and after (b) D_2O exposure and consequent exchange of acidic protons to deuterium. The red lines highlight the position of the ^{1}H NMR signals of the occluded SDA protons (0.9, 1.8 and 3.2 ppm).The corresponding correlation between Q_4 (-112 ppm) and Q_3 (-102 ppm) Si sites and terminal CH_3 groups of the SDA after D_2O exchange is indicated. The intense peak at 5 ppm (^{1}H) corresponds to adsorbed H_2O.

The ^{29}Si-^{1}H HETCOR spectra exhibit correlations between the signals arising from Q_4 and Q_3 silicon environments and protons from framework species and TPA^{+} molecules. The presence of signal correlation between the low-frequency proton signals (between 1 and 3 ppm) and the silicon signals at -112 ppm arises from interactions of Q_4 silicon environments with protons. The correlation of the -102 ppm silicon signal with the 1 ppm signal of the proton can be attributed to $Si(OSi)_3OH$ environments in close contact with terminal CH_3 groups of the SDA. [12], [25], [26] The -102 ppm silicon signal correlates with the 10 ppm proton signal as well, indicating the presence of interactions between Si-OH defective sites. Similar signals have been observed in high-silica zeolites with 1D and/or 2D experiments[8], [19], [25] and assigned to hydrogen-bonded $SiOH\cdots^{-}OSi$ species. In order to obtain better resolution for the correlation signals of the Q_4 silicon sites and the low-frequency protons from the SDA cations, the sample was placed in a D_2O-saturated environment and the spectrum recorded again after approximately 100 days[2]. This choice was made with the aim of exchanging acidic protons from defective sites to deuterium and eliminate the signal arising from them. Figure 41(b) shows that the signal assigned

[2] The exposure to D_2O started before the Chemistry Department at Durham University had to close down, following the rules indicated by the British Government to address the COVID-19 pandemic. A period of 100 days is estimated for the exposure to D_2O between the closing and reopening dates of the Chemistry Department.

to SiOH···$^{-}$OSi species disappears after D_2O exposure, suggesting that considerably acidic Si-OH protons were successfully exchanged to deuterium and, therefore, appear invisible to ^{1}H NMR. The low-frequency proton signals still detectable after exposure to D_2O confirm that these signals are assignable to SDA-protons, as they are non-acidic and therefore are not easily exchanged. Another aspect worth noting is the good agreement between the proton signals obtained from TPA^{+} cations and the correlation signals between proton and silicon observed for the Zn-MFI material, especially after D_2O exchange. This indicates that the framework is also interacting with protons from the SDA.

The ^{29}Si-^{1}H HETCOR spectrum was also acquired for a TPA^{+}-K^{+}/Zn-MFI_TPA:K=6.5 sample before and after exposure to D_2O,[3] and is shown in Figure 42. The signals detected correspond to Q_4 and Q_3 silicon sites (-112 ppm and -102 ppm, respectively, on the ^{29}Si axis) correlating with protons mainly at 1.8 and at 3.7 ppm. Intense correlation signals can also be observed between Q_3 sites and proton species belonging to hydrogen-bonding defective sites at 10.5 and 12.5 ppm on the ^{1}H axis. This represents further evidence of the fact that Q_3 Si sites produce silanol groups that interact with each other through hydrogen bonding interactions. Dib et al. showed that the interaction between defective sites in Silicalite-1 and TPA^{+} cations takes place on the methyl groups and, therefore, the Si-OH defects are preferentially placed near the methyl groups of the TPA^{+} cation at the mid distance between the channels intersections, with a distance between silanol and methyl protons of approximately 3.3 Å.[12]

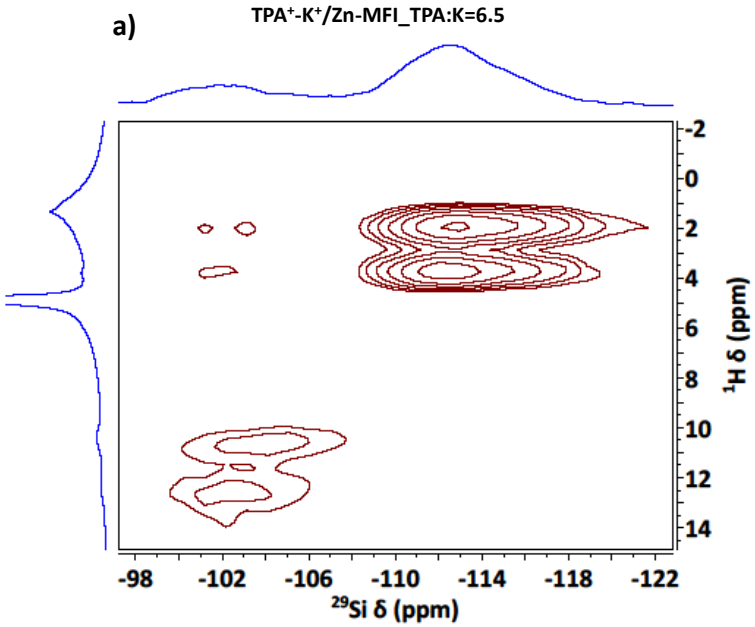

[3] In this case the exposure to D_2O was carried out for 7 days.

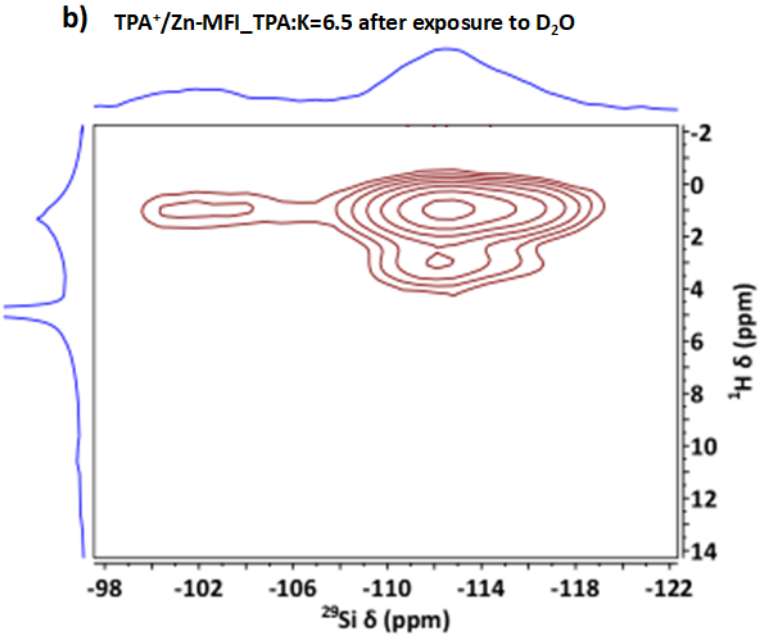

Figure 42: ^{1}H-^{29}Si HETCOR spectra of a TPA^{+}-K^{+}/Zn-MFI sample (TPA:K=6.5) before (a) and after (b) D_2O exposure and consequent exchange of acidic protons to deuterium. The ^{1}H chemical shifts of the SDA protons (0.9, 1.8 and 3.2 ppm) are highlighted in red and the corresponding correlation between Q_4 (-112 ppm) and Q_3 (-102 ppm) Si sites and terminal CH_3 groups of the SDA after D_2O exchange is indicated. The intense peak at 5 ppm (^{1}H) corresponds to adsorbed H_2O.

Figure 43 shows the ^{1}H-^{29}Si HETCOR NMR spectra for TPA^{+}/Zn-MFI_TPA:K=∞, TPA^{+}-K^{+}/Zn-MFI_TPA:K=6.5 and TPA^{+}-K^{+}/Zn-MFI_TPA:K=3. From the results obtained it appears that a correlation exists between the amount of K^{+} cations present in the samples and the presence of defective sites. More specifically, in TPA^{+}/Zn-MFI_TPA:K=∞ Q_3 sites only appear to correlate with protons at 10.5 ppm, whilst in TPA^{+}-K^{+}/Zn-MFI_TPA:K=6.5 the correlation signals between Q_3 Si sites and defect protons can be seen at 10 and 12 ppm and appears broader and weaker. The correlation signals between Q_3 and proton species are absent in K^{+}/Zn-MFI_TPA:K=3. These results match well with the observation reported by Corma et al. for K^{+}-containing MFI zeolites modified with Pt. In particular, the zeolites were prepared using a mixture of TEOS and TPA^{+} with the addition of controlled amounts of KOH and the authors reported the evidence of a decreasing of the number of –OH groups in the materials containing K^{+} cations possibly due to the formation of $–O^{-}K^{+}$ groups.[21]

In order to assess the effect of the extra-framework K^{+} cations, the results obtained from ^{29}Si-^{1}H HETCOR experiments carried out on TPA^{+}/Zn-MFI, TPA^{+}-K^{+}/Zn-MFI_TPA:K=6.5 and TPA^{+}-K^{+}/Zn-MFI_TPA:K=3 were compared. The spectra are shown in Figure 43. From the results obtained it appears that a correlation exists between the amount of K^{+} cations present in the samples and the presence of defective sites. More specifically, the correlation signals between

Q_3 Si sites and defect protons at 10 and 12 ppm appear broader in the TPA^+-K^+/Zn-MFI_TPA:K=6.5 sample and they disappear in the K^+/Zn-MFI_TPA:K=3 material.

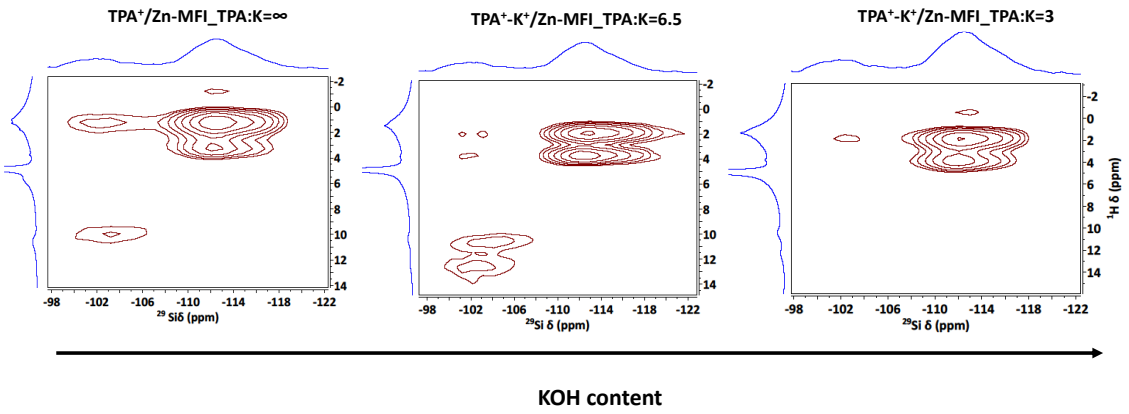

Figure 43: ^{1}H-^{29}Si HETCOR spectra of TPA^+/Zn-MFI (left), TPA^+-K^+/Zn-MFI_TPA:K=6.5 (centre) and TPA^+-K^+/Zn-MFI_TPA:K=3 (right) samples showing the evolution of the correlation signals as a function of the increasing of the amount of K^+ cations in the samples.

A ^{1}H-^{2}D HETCOR spectrum for a sample of TPA^+-K^+/Zn-MFI_TPA:K=6.5 after a 7-day exposure to D_2O was acquired and is shown in Figure 44(a). Three signals at 3.7, 10 and 15.6 ppm and a shoulder at 12 ppm could be detected, despite the low signal-to-noise ratio of the ^{2}D spectrum. The 3.7 ppm signal falls in the chemical shift range of the TPA^+ cations, however it is unlikely that protons from the SDA were exchanged to deuterium; this signal is therefore assigned to residual acidic Si-OH framework species.[27] The higher-frequency signals from the hydrogen-bonded SiOH···$^-$OSi species can be clearly observed in the CP spectrum, indicating (i) a complete exchange of these protons to deuterium atoms and/or (ii) the presence of a high number of proton species in close proximity, which would enhance the polarisation effect. Moreover, the spectrum confirms the presence of correlations between deuterium species exchanged in defect sites and TPA^+ protons. These correlation signals appear as very intense peaks between 10 and 16 ppm on the deuterium axis and 1 and 4 ppm on the proton axis, which indicates that the SDA protons are effectively interacting with deuterons from defective sites in the framework.

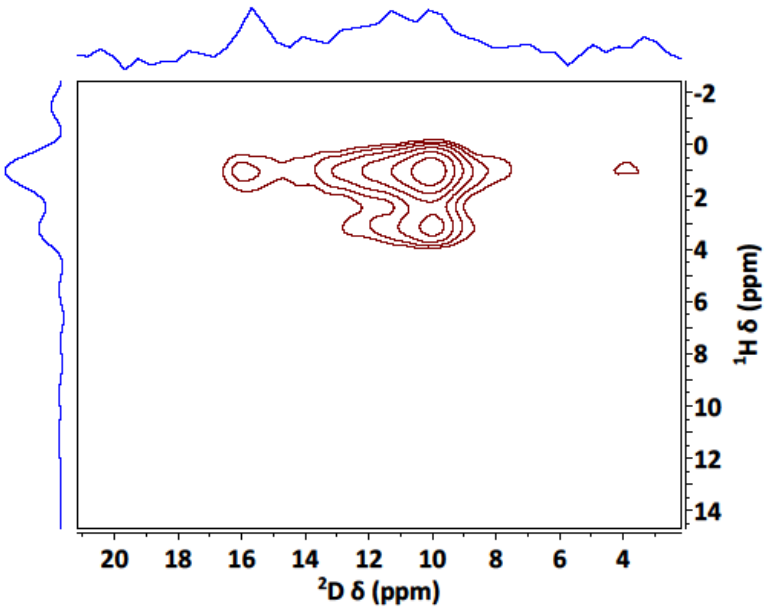

Figure 44: Spectrum acquired through ^{1}H-^{2}D HETCOR analysis of a TPA$^+$-K$^+$/Zn-MFI sample after D_2O exchange.

5.2.1.3. Double-Quantum/Single-Quantum ^{1}H NMR

A Double-Quantum/Single-Quantum experiment was carried out on a TPA$^+$-K$^+$/Zn-MFI_TPA:K=3 sample in order to have a more in-depth understanding on how protons in the sample interact with each other. The experiment was carried out using the method of Feike et al.[28] Figure 45 shows the SQ/DQ spectrum. The presence of a signal in the ^{1}H DQ MAS spectrum indicates that two protons are in close proximity (<5 Å), as the DQ coherences observed are strongly dependent on the internuclear distance.[29], [30] Proton species with the same chemical shift, equivalent protons (e.g.in a CH_3 group) or isolated protons in close proximity produce auto-correlation signals and appear on the diagonal, whilst protons correlating with other protons in different environments generate signals outside the diagonal axis. The chemical shift of the signals on the DQ axis correspond to the sum of the ^{1}H chemical shifts of the interacting species. In Figure 45 a broad signal is observed between 0 and 8 ppm (SQ axis), lying on the diagonal and with substantial intensity off the diagonal. This corresponds to TPA$^+$ protons auto-correlating among NCH_2, -CH_2 and CH_3 species. Additionally, the broad correlation between 6 and 8 ppm (SQ) could be ascribed to strongly hydrogen-bonded, not fully isolated protons.[27], [31] The two higher-frequency signals on the diagonal are generated by the sum of two 10.5 and two 12.5 ppm signals, arising from protons involved in SiOH···$^-$OSi hydrogen bonds in close proximity.[8],[10] The peaks detected outside the diagonal at 11.4 ppm (10.5 + 0.9 ppm), 13.4 ppm (12.5 + 0.9 ppm), 13.7 ppm (10.5 + 3.2 ppm) and 17.4 ppm (16 + 1.4 ppm show that defect sites are located in close proximity to the structure directing agent, in particular with the terminal

methyl group of the TPA^+ cations (with proton chemical shifts of 0.9 ppm). This finding is corroborated by the results reported in the previous sections and by analogous conclusions reported by Brunklaus et al. for high-silica ZSM-5[25] and by Dib et al. for Silicalite-1.[13]

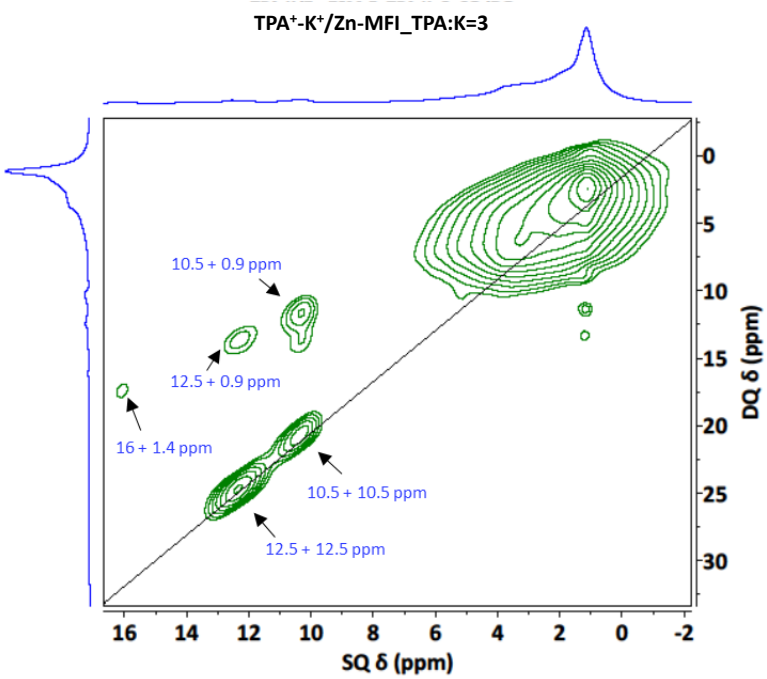

Figure 45: DQ/SQ proton spectrum of a TPA^+-K^+/Zn MFI sample, showing auto-correlation and correlation between protons from TPA^+ and defective sites.

5.2.1.4. High-field ^{67}Zn NMR analysis

As mentioned in Chapter 3, there are only two reported ^{67}Zn NMR studies of zinc-exchanged zeolites, where zinc is in extra-framework positions.[3], [32] This is despite a number of ^{67}Zn NMR studies of MOFs giving valuable structural information about the Zn centres.[33] High-field ^{67}Zn NMR analyses were carried out in order to directly probe the Zn heteroatoms and attempt to identify their chemical environment in the zincosilicate materials. Ten days spectrometer time was allocated at the UK High-Field Solid-State NMR Facility (Warwick), with plans to analyse TPA^+-K^+/Zn-MFI_TPA:K=6.5, K^+/Zn-MFI_TPA:K=6.5 and H^+/Zn-MFI_TPA:K=∞ materials. Prior to the experiments, some preliminary analyses were carried out on a K^+/Zn-MFI zeotype in order to make sure that the signal could be detected, and the spectra obtained are reported in Figure 46(a). Spectra were acquired on a 1 GHz (23.5 T) spectrometer using a Hahn echo experiment with a RF fieldstrength of 25 kHz and a recycle delay of 0.1 s. In order to acquire the full spectrum 'frequency-sweeping' methods (e.g., variable offset cumulative spectroscopy (VOCS)) were required, with 7 offsets acquired (5 hours for each). Dynamic frequency selection (DFS) methods were also used to enhance the signal. The presence of signal in the ^{67}Zn NMR spectrum was a promising sign for a potential characterisation of the materials using this technique. A sample of

Zn-CHA prepared in the group by Ryan Kerrigan with a higher Zn content (7 wt%) was also analysed in order to make sure that the experiments could provide useful information on the Zn chemical environment. The spectrum is reported in Figure 46(b).

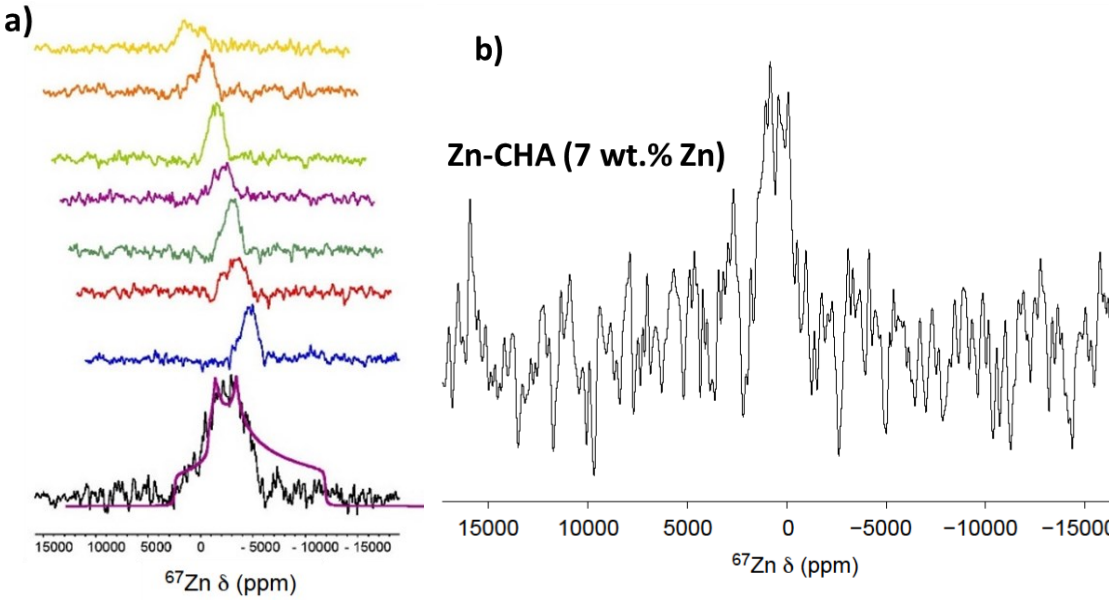

Figure 46: Static ^{67}Zn (23.5 T) NMR spectrum of K^+/Zn-MFI-5(Si/Zn=85) (a) and of a Zn-CHA material containing a greater amount of Zn (b) acquired using a Hahn echo, DFS and VOCS. The purple line represents the simulated spectrum.

Further analyses suggested that the spectra reported in Figure 46 were not generated by the materials but by parts of the experimental setup (e.g. the spectrometer coil). Therefore, more experiments were needed in order to confirm the authenticity of the ^{67}Zn signals. Unfortunately, this could not be achieved with the current setup and the allocated 10 days of spectrometer time, even with the introduction of more offsets (12-14) and additional signal enhancement techniques such as Quadrupolar Carr–Purcell Meiboom–Gill (QCPMG). The main reason for this may be the low Zn content in the samples and the absence of isotopic enrichment. The fact that signal can be observed in a zincosilicate sample is encouraging; however, more work is needed to optimise the experiment and the conditions.

5.2.2. X-ray Absorption Spectroscopy

X-Ray Absorption (XAS) experiments were carried out at the Diamond Light Source facility. The aim of the experiment was to obtain in-depth information on the coordination environment of the Zn heteroatoms in the zincosilicate materials, including oxidation state, coordination number, geometry and neighbouring atoms. Loss of framework zinc is known to be facile under certain conditions, for example if the zincosilicate material is in contact with an acidic

solution even at mild temperature (60 °C).[16] Therefore, during the course of the work, we were concerned that the acidic form of the framework could be affected by hydrolysis of the Zn sites, leading to the removal of Zn from framework positions. As such, the XAS experiments aimed to probe changes in the local structure of the zinc centres upon exposure to atmospheric moisture. A pathway for the hydrolysis of framework zinc to extra-framework zinc species via a partially hydrolysed framework zinc centre is given in Scheme 2.

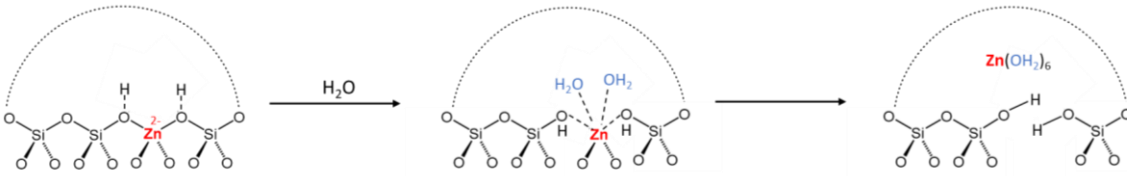

Scheme 2: Representation of the possible interactions with water of a Zn heteroatom in the framework and its hydrolysis to an octahedral extra-framework Zn species.

XAS experiments were carried out on Zn-MFI samples to detect any changes in the chemical environment around Zn centres in presence or absence of water. Two H^+/Zn-MFI samples (prepared using the TEOS-based synthesis with $ZnCl_2$, without the addition of KOH and aiming to a Si:Zn ratio of 100) were analysed. After calcination to remove the SDA, one was heated at 550 °C under reduced pressure (< 10^{-2} mbar) for 5 hours and sealed in an Ar-filled glovebox to ensure the absence of moisture, the other sample was used without any further treatments besides calcination, and contained water molecules. The materials are indicated as H^+/Zn-MFI_dehydrated and H^+/Zn-MFI_hydrated, respectively. In Table 16 the elemental analysis of the H^+/Zn-ZSM-5_hydrated material is reported. The details for the dehydrated sample could not be reported as the material needed to be maintained in an inert environment. However, the dehydration step is not expected to cause damage to the framework and/or leaching of framework Zn.

Table 16: Elemental composition(XRF) of the H^+/Zn-MFI_hydrated material. The uncertainty on the measurements is the 6.4% of the values (only reported for Si:Zn ratio).

Sample Name	Si content (wt%)	Zn content (wt%)	Si:Zn ratio
H^+/Zn-MFI_hydrated	*46.3*	*1.7*	65.4 ± 3.9

Figure 47 shows the XANES (X-ray Absorption Near Edge Structure) spectra of the materials. The spectra collected show the normalised absorption coefficient as a function of the X-Ray energy. The energy of the edge measured for dehydrated H^+/Zn-MFI is 9662.4 eV and for hydrated H^+/Zn-MFI is 9662.5. These values are different to the one reported by Hagen et al. for a Zn-substituted MFI material (9660.8 eV),[5] however, this can be due to a different point

selected for the start of the edge. In this thesis, the point has been selected as first maximum in the derivative spectrum. The shift of the value towards higher energy observed for the hydrated material is in agreement with previously reported results.[5],[34] As expected, no pre-edge features are observed. The latter are usually detected for first-row elements and arise from transitions from 1s to 3d energy levels.[35] Zn has a fully occupied 3d level, therefore pre-edge features are not detected in the XANES spectrum. By comparing the spectral features of the H^+/Zn-MFI samples to those reported in the literature,[5], [7] it can be suggested that extra-framework $[Zn(H_2O)_6]2^+$ species (octahedral coordination) can be excluded as major species. Recently reported results, pinpoint the edge position for fully hydrated, octahedrally coordinated Zn^{2+} species at 9663.8 eV, a considerably higher value than those measured for Zn-MFI materials and almost overlapping the second feature of the most intense absorption band in Zn-MFI samples.[36] The comparison between experimental results obtained for our zincosilicate materials and results reported in the literature for a Zn^{2+}-exchanged zeolite[36] are reported in Figure 47. The hydrated and dehydrated H^+/Zn-MFI materials (on the left) show a "double-peak" feature which appears to be different from the spectral feature of Zn foil. Additionally, these features appear similar to those observed in a Zn^{2+}-exchanged zeolite (on the right), with edge position at 9662.6 eV, which was pre-treated at 420 °C in air (i.e., the sample does not contain water). On the other hand, the spectrum obtained from the fully hydrated Zn^{2+}-exchanged zeolite, shown in the same figure, exhibits a remarkably different shape, very similar to Zn^{2+} octahedrally coordinated with water molecules.[36] The spectrum collected for ZnO as a reference material shows different absorption features, which are not observed in the spectra collected for our zincosilicate materials. From the comparison of the latter with the results from the literature in Figure 47 it emerged that the absorption bands of our zincosilicate materials are similar to those reported for a dehydrated Zn^{2+}-exchanged zeolite. However, this only due to the fact that, in the absence of water, the chemical environment and the nearest neighbours of the Zn species are similar for the two samples (i.e. Si and O atoms), with a lower coordination number to O neighbours.[36] The Zn species present in the zincosilicate materials cannot be extra-framework Zn^{2+} species, as the materials do not contain other metal sites which would require charge-balacing species. Additionally, other characterisation analyses and ion exchange experiments corroborate the hypothesis that the Zn species present in the samples are tetrahedrally coordinated in framework positions.

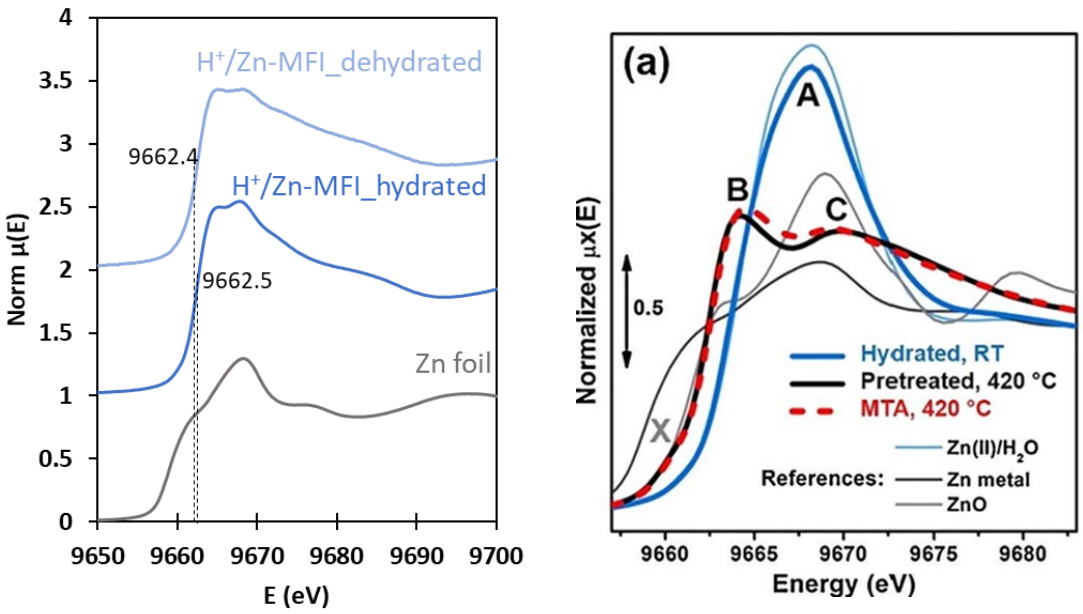

Figure 47: Plot of the normalised absorption coefficient as a function of the photoelectron energy in the XANES region for hydrated and dehydrated H^+/Zn-MFI samples, compared to a Zn foil standard (left); XANES spectra of Zn^{2+}-exchanged ZSM-5 zeolites exposed to different pre-treatments collected by Pinilla-Herrero et al. (right). Adapted with permission from ref [36]. Feature A indicates the absorption band corresponding to Zn^{2*} in octahedral coordination; features B and C indicate the post-edge peaks at 9664 and 9669 eV observed in a pre-treated sample at 420 °C and in a sample analysed under methanol-to-aromatic (MTA) conditions, both in the absence of water.

To further confirm this hypothesis, the XANES spectra were compared to the ones reported in other XAS studies of Zn compounds.[37], [38] Chouillet et al. analysed a series of Zn-impregnated SiO_2 samples dried at different temperatures and reported the presence of a single, intense band typical of Zn in octahedral coordination in the materials dried at low temperature. On the other hand, samples dried at > 120 °C showed a less intense band slightly shifted to lower energy values. This indicates (i) a decrease in the number of first neighbours of Zn and (ii) a shorter first coordination shell distance.[37] In the case of our materials, the broad, lower-energy signal is clearly split in two bands, a feature observed in several zincosilicate materials, which is unique to this class of compounds.[38] Therefore, based on this evidence it may be concluded that hydrated and dehydrated H^+/Zn-MFI materials analysed in this work exhibit typical XANES features of tetrahedrally-coordinated Zn, and an evolution of the signal towards a higher energy single peak, generally observed for aqueous octahedral Zn^{2+} was not detected in the hydrated sample. However, the spectra of the zincosilicate materials in Figure 47 show a minor difference between the second peak of the most intense absorption band of the hydrated and dehydrated materials. In particular, the hydrated material exhibits a slightly more

pronounced second peak compared to the dehydrated material. This may be due to the formation of partially hydrolysed Zn sites in the presence of water molecules, as explained above.

The Fourier transform of the oscillatory component of the absorption coefficient is reported in the EXAFS (Extended X-ray Absorption Fine Structure) spectra (Figure 48), plotted as the magnitude of the absorption coefficient as functions of the uncorrected radial distance *R*. The bands observed in the R space correspond to absorption and scattering phenomena relative to specific chemical environments around the probed atom. The H^+/Zn-MFI_hydrated and H^+/Zn-MFI_dehydrated materials do not show major visible differences. The data fitting was carried out[39] in order to identify the coordination environment of the Zn heteroatoms in each sample.

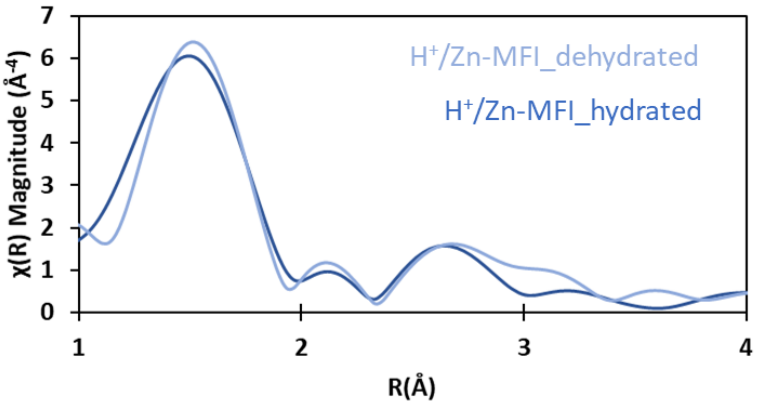

Figure 48: EXAFS spectra representing the Fourier transform of the oscillatory component of the absorption coefficient as a function of the uncorrected radial distance for hydrated and dehydrated H^+/Zn-MFI samples.

Initially, the data were fitted using ZnO and willemite[40] (Zn_2SiO_4, structure shown in Figure 49) as reference materials for tetrahedral Zn–O and Zn–Si scattering paths, respectively. In Figure 50 the EXAFS data and fit of the hydrated and dehydrated samples are shown, plotted as functions of the phase-shifted radial distance. The values of the radial distance reported in the figure match the data reported in Table 17, however in the next section the discussion will be carried out referring to Figure 51 and Figure 52. Figure 51(a) shows the results obtained from the H^+/Zn-MFI_dehydrated material. It can be immediately noticed that, despite showing good agreement with the experimental data, the fit performed using willemite and ZnO does not fully represent the absorption spectrum of the zincosilicate zeotype. The disagreement between the data and the scattering paths from the chosen crystalline structures can be better visualised in Figure 51(a), bottom spectrum. Similar observation can be drawn from Figure 51(b), which represents the EXAFS data and fitting for H^+/Zn-MFI_hydrated. In the latter, the agreement between the experimental data and the fit appears to be improved; however, a certain degree of mismatch can still be noticed between the data and the single scattering paths (Figure 51(b),

bottom). This can be explained considering that in ZnO and Willemite the coordination environment around Zn heteroatoms is *similar* but not the same as the one of a zincosilicate zeotype. In ZnO the Zn is bonded to four oxygen atoms in a tetrahedral coordination with bond length of 1.89 Å. The presence of Si in the framework of a zincosilicate zeotype would cause changes to the bond length between Zn and O atoms, therefore ZnO is not the best choice to represent the first coordination shell of Zn atoms in a zincosilicate zeotype. Despite containing Zn, O and Si atoms in a tetrahedral coordination environment, willemite is also not the best material to be used for the fitting of the EXAFS data of a zincosilicate zeotype. The main difference between the mineral and the microporous zincosilicate is the crystal structure and, more specifically, the position of the Zn sites in the material. In a zeotype, Zn atoms occupy specific tetrahedral (T) sites, due to the presence of channels and cavities which produce specific constraint on the position of the T sites. This also induces variations in the bond lengths between framework heteroatoms.

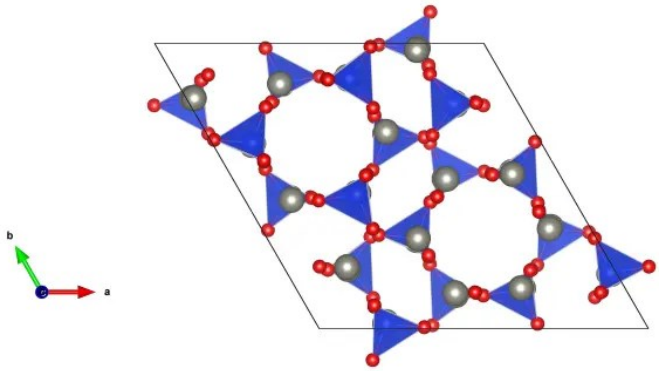

Figure 49: Crystal structure of willemite. Grey atoms represent Zn, blue tetrahedra and red atoms represent SiO_4 units.[41]

In order to produce a better fit for our experimental data, a (calcined) H^+/ZSM-5 zeolite[42] was used as a reference material instead of Willemite and ZnO (.cif file downloaded from the IZA Database of Zeolite Structures). A Zn atom was positioned in a T site, replacing Al, with a 109.5° bond angle between Zn and two oxygen atoms and water was added for the hydrated material using the crystallographic data of a hexaqua zinc compound.[43][4] The best fit for our experimental data was achieved considering the lengths of various scattering paths for the photoelectron in the reference material, between the probed atom (Zn) and the neighbouring atoms. The scattering paths considered for the fit are represented in Scheme 3.

[4] This analysis was carried out in collaboration with Dr. Simon K. Beaumont at Durham University.

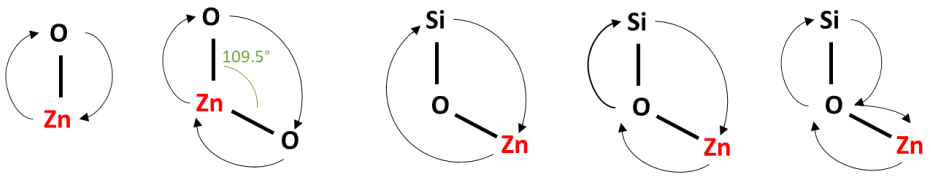

Scheme 3: Possible scattering paths between the first and second coordination shells of Zn heteroatoms in a zeotype framework.

The results of the fitting are reported in Figure 52 and the fitting parameters in Table 17. From the comparison between Figure 51(a) and Figure 52(a) it can be noticed that the data fit of H^+/Zn-MFI_dehydrated carried out using the scattering path from H^+/ZSM-5 matches the experimental data more accurately. A major contribution is given by the Zn–O scattering path from the zeolite material, which better represents the chemical environment of the zincosilicate sample, and by the inclusion of other multiple scattering paths. The latter is very important in order to provide a more accurate representation of the possible scattering phenomena which the photoelectrons incur and, as a consequence, a more complete description of the chemical environment around the probed atom. In Figure 52(b) the EXAFS data of the H^+/Zn-MFI material in the hydrated form are reported. In addition to the H^+/ZSM-5 scattering paths, this material was fitted using additional Zn–O paths from a hexaqua zinc complex, in order to demonstrate the presence of water molecules coordinating with the Zn atoms. The latter were found to provide a non-negligible contribution to the broadening of the absorption band relative to the first coordination shell, indicating the presence of a certain number of water molecules coordinating with the Zn atoms. The number of water molecules was estimated to be 1.75 ± 0.34 (Table 17), which is in line with the hypothesis of water coordinating with framework Zn species in the material, rather than causing a complete extraction of the Zn atoms, generating aqueous extra-framework Zn species (Scheme 2). The values of the bond length of the first and second coordination shells of the Zn atoms were evaluated. The H^+/Zn-MFI_dehydrated material exhibits a Zn–O distance of 1.975 Å, which is in agreement with results reported in the literature for Zn-MWW (1.98 ± 0.01 Å)[7] and Zn-BEA (1.97 ± 0.01 Å).[44] The distance of the second coordination shell (Zn–Si) of both materials is also in agreement with the value of 3.22 ± 0.02 Å reported for a Zn-MWW material by Yan et al.[7] The value of the distance between O and Si atoms can be evaluated thanks to the contribution of multiple scattering paths on the energy of the photoelectron, as reported in Scheme 3. The Zn–O bond distance of the H^+/Zn-MFI_hydrated sample is slightly longer than the one evaluated for the dehydrated form of the material (1.993 Å). This can be explained considering the coordination with water taking place on the Zn atoms, forming an octahedral complex. The increase in coordination number could be increasing the steric congestion around the metal causing the bond lengths to increase, and/or the dative bond of water to zinc would be longer than the covalent Zn-O bond, making the average Zn-O distance

longer. However, the uncertainties on the Zn-O bond length values are 0.009 Å and 0.021 Å for the dehydrated and the hydrated sample, respectively. This introduces a certain degree of overlap between the two values. Nevertheless, it is reasonable to consider a longer Zn-O distance in the hydrated sample, given the evidence provided by XANES measurements and bearing in mind the presence of a certain degree of coordination with water molecules.

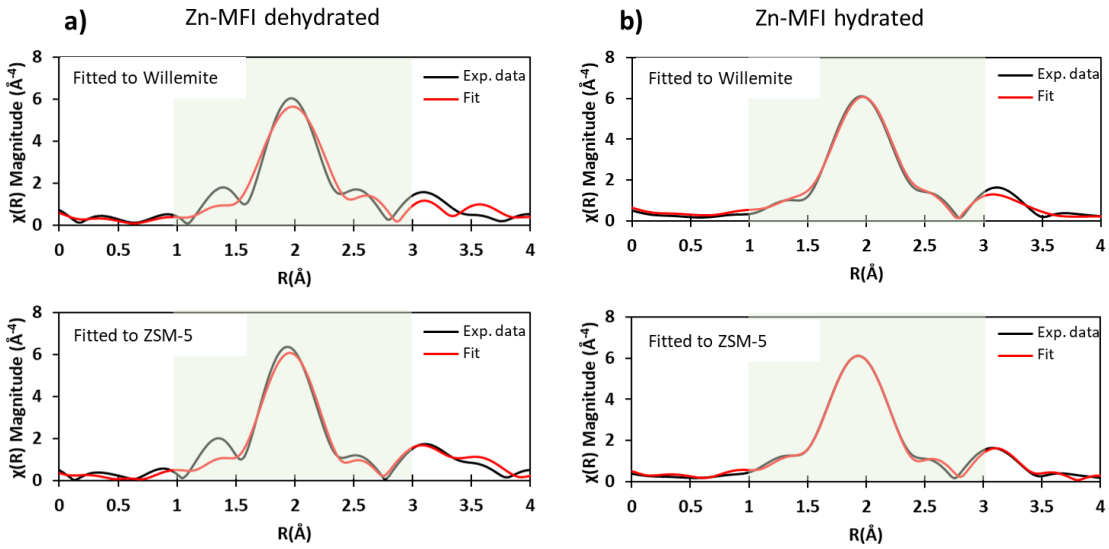

Figure 50: Phase-shifted EXAFS spectra of dehydrated (a) and hydrated (b) Zn-MFI materials, showing experimental data and fit carried out using crystallographic data from Willemite or ZSM-5 structures. The portion highlighted in green represents the spectral region considered for the data fitting.

Table 17: EXAFS fitting parameters for H^+/Zn-MFI (hydrated and dehydrated) materials, using H^+/ZSM-5 as standard material for the fit.

Sample	*R Zn-O (Å)*	*R O-Si (Å)*	*R Zn-Si (Å)*	*σ^2 O ($Å^{-2}$)*	*σ^2 Si ($Å^{-2}$)*	*CN H_2O*
H^+/Zn-MFI dehydrated	**1.975** ± 0.009	**1.653** ± 0.030	**3.211** ± 0.021	**0.0066** ± 0.0007	**0.0083** ± 0.0018	ND
H^+/Zn-MFI hydrated	**1.993** ± 0.021	**1.623** ± 0.040	**3.221** ± 0.015	**0.0092** ± 0.0035	**0.0104** ± 0.0018	**1.75** ± 0.34

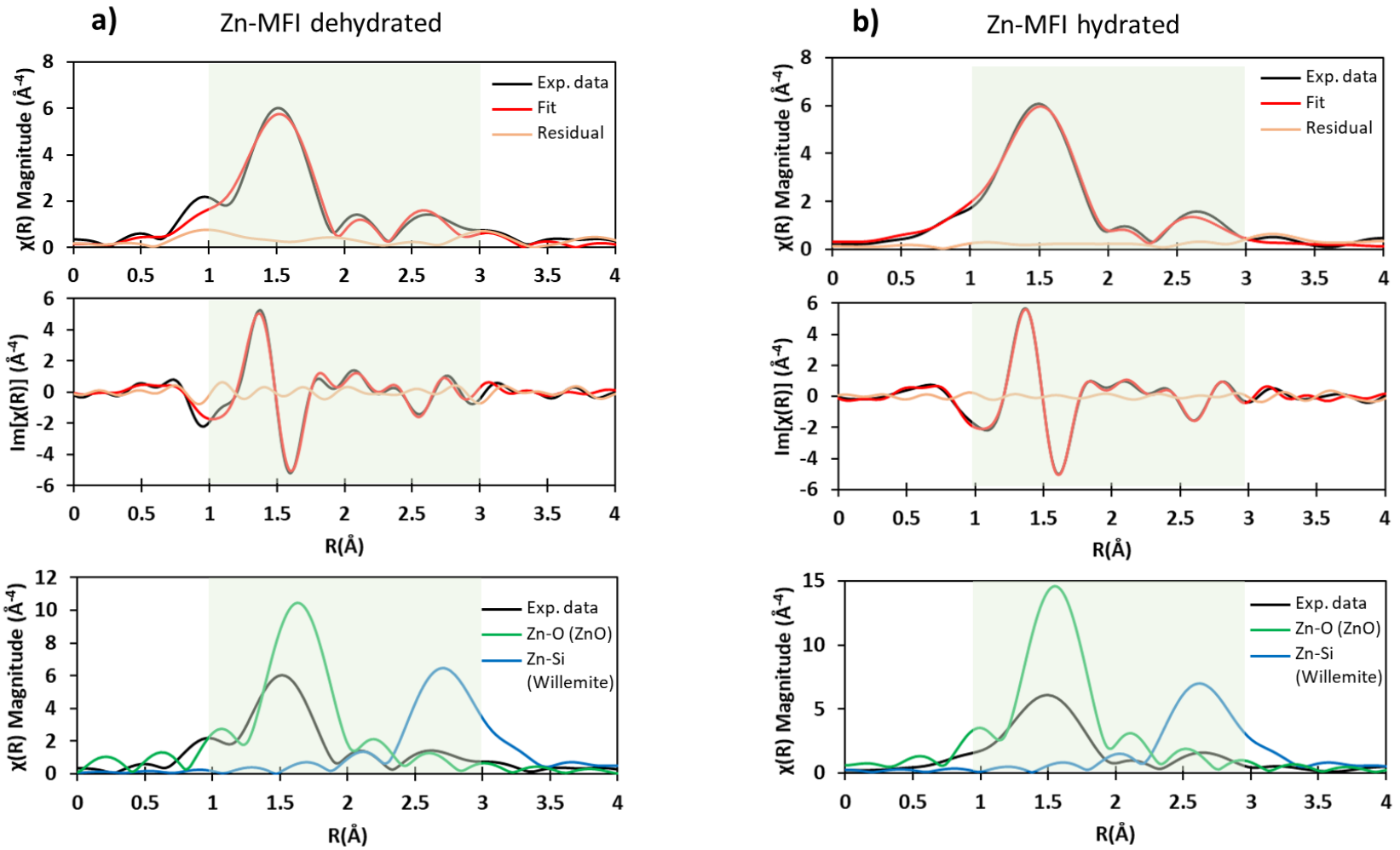

Figure 51: EXAFS spectra (fitted using Willemite and ZnO) of dehydrated (a) and hydrated (b) H^+/Zn-MFI materials. The spectra show the magnitude of the Fourier transform of the absorption coefficient (top), its imaginary part (centre) and the superimposition of the experimental data and the scattering paths used for the fitting (bottom). The portion highlighted in green represents the spectral region considered for the data fitting.

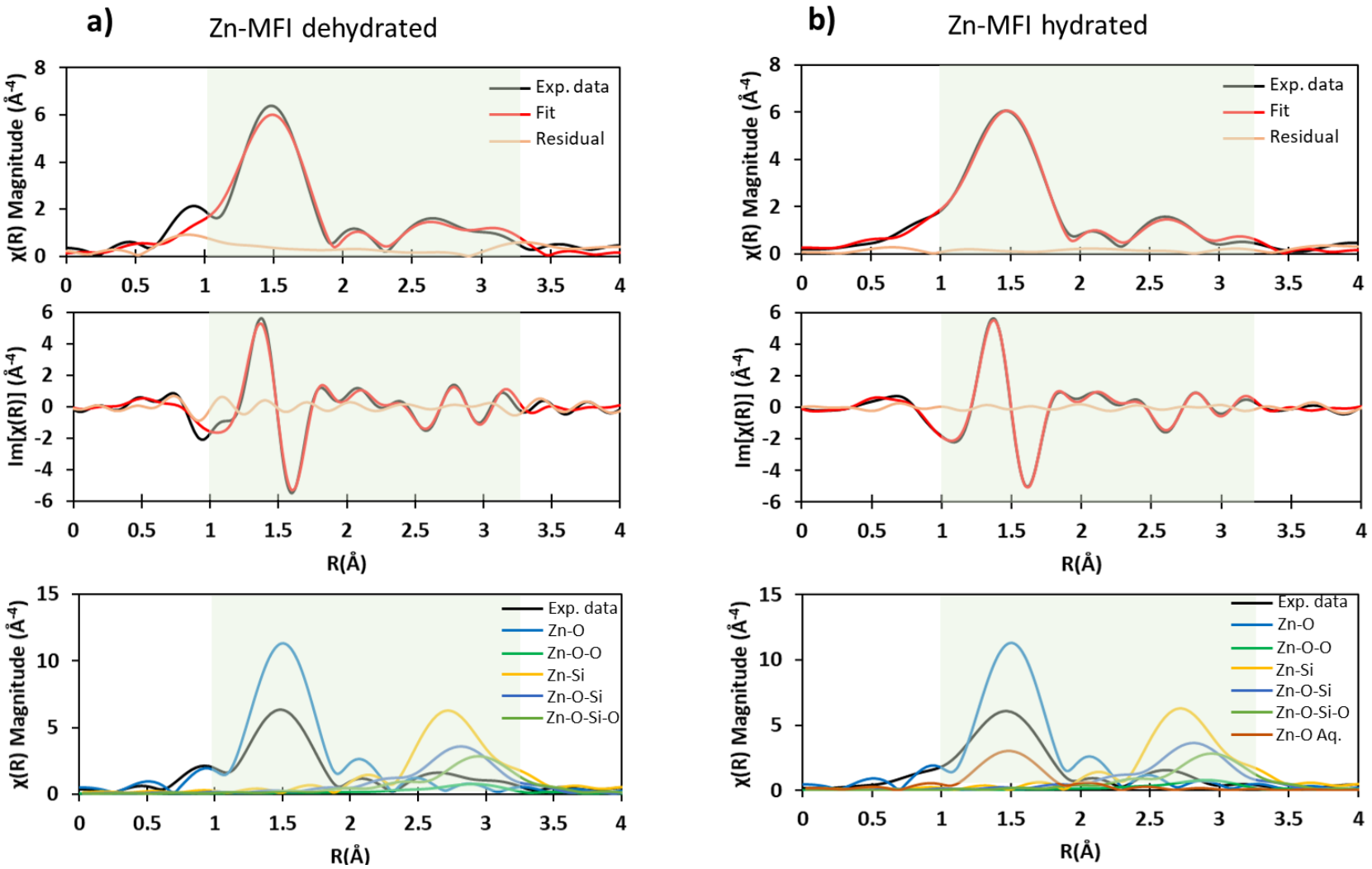

Figure 52: EXAFS spectra (fitted using H^+/ZSM-5) of dehydrated (a) and hydrated (b) H^+/Zn-ZSM-5 materials. The spectra show the magnitude of the Fourier transform of the absorption coefficient (top), its imaginary part (centre) and the superimposition of the experimental data and the scattering paths used for the fitting (bottom). The portion highlighted in green represents the spectral region considered for the data fitting.

5.2.3. Diffuse Reflectance Infrared Fourier Transform Spectroscopy

Infrared Spectroscopy analyses were carried out on the zincosilicate samples in the diffuse reflectance mode (DRIFTS). After being dehydrated overnight at 500 °C under reduced pressure, the spectra were acquired at three different temperatures of 100, 200 and 500 °C in between 4000 cm^{-1} and 600 cm^{-1}. This technique is extremely useful to detect changes in the structure of the framework due to the presence of different heteroatoms, as reported by several studies. [4], [6], [7], [45], [46] Figure 53 shows the spectra collected from (i) Zn-MFI samples prepared with the TEOS-based synthesis with $Zn(NO_3)_2$ and the additon of KOH and (ii) a Silicalite-1 sample, as summarised in Table 18. The TPA^+-K^+/Zn-MFI and Silicalite-1 materials were calcined at 550 °C for 6 hours to remove the SDA and obtain K^+/Zn-MFI_TPA:K=3, K^+/Zn-MFI_TPA:K=6.5 and Silicalite-1.

Table 18: Elemental composition of the samples analysed by DRIFTS, obtained from XRF analyses. The uncertainty on the measurements is the 6% of the values (only reported for Si:Zn and K:Zn ratios).

Entry	Sample name	Si (wt %)	Zn (wt %)	K (wt %)	Si:Zn	K:Zn
1	***Silicalite-1***	46.4	ND	ND	ND	ND
2	***K^+/Zn-MFI_TPA:K=6.5***	44.7	1.2	1.6	88.0 ± 5.3	2.3 ± 0.1
3	***K^+/Zn-MFI_TPA:K=3***	55.5	1.2	3.0	96.4 ± 5.8	4.1 ± 0.3
4	***H^+-K^+/Zn-MFI_TPA:K=6***	51.1	1.3	0.2	94.7 ± 5.7	0.3 ± 0.02
5	***K^+/Zn-MFI_TPA:K=6***	53.5	1.7	2.4	73.6 ± 4.4	2.4 ± 0.1

Figure 53(a), (b) and (c) show the DRIFTS spectra between 1400 and 600 cm^{-1} collected at 100, 200 and 500 °C. Generally, bands at wavenumbers between 650 and 850 cm^{-1} are associated with Si–O–T symmetric vibrational modes (with T = Si or other heteroatom). [6], [7], [45], [47] In the spectra reported these bands appear to be very similar between zincosilicate materials and Silicalite-1, therefore it is reasonable to assume that they correspond to symmetrical Si–O–Si stretching vibrations. [46], [48] A noticeable difference between the spectra can be observed at 900 cm^{-1}, where a weak band is detected in Silicalite-1 but not in the zincosilicate materials. The asymmetrical Si – O – T stretching vibrations can be associated with signals in the range between 1000 and 1250 cm^{-1}. Differences in the signal position of these stretching vibrations usually enable differences between Si–O–Si and Si–O–T bonds to be distinguished.[49] In particular, the substitution of heteroatoms in the framework causes the bands to shift to lower wavenumbers.[4], [46], [50] This is due to changes in the Si–O–T bond

length in the materials. This effect is observed for the two K^+/Zn-MFI samples compared to Silicalite-1 and, therefore, confirms the presence of heteroatoms (zinc) other than Si in the frameworks. Similar results were reported by Hu et al. for their Zn-MFI material synthesised using mechanochemical treatments.[46] They observed a broadening towards lower frequencies of the Si–O–T asymmetrical stretching vibration in Zn-MFI compared to Silicalite-1, which was ascribed to the substitution of Zn in the framework.[46] Signals appearing in the spectral region between 3000 and 4000 cm^{-1} are ascribed to OH stretching modes. The higher the frequency of the stretching mode, the stronger is the O–H bond, corresponding to lower Brønsted acidity.[49] Signals between 3675 and 4000 cm^{-1} arise from (perturbed or) isolated silanol sites.[49], [51] The K^+/Zn-MFI materials analysed in this study (Figure 54) show a total absence of signals in this region, except for a very weak signal at 3750 cm^{-1} that is generally assigned to isolated external silanol sites.[49] On the other hand, Silicalite-1 exhibits the presence of a broad band between 3250 and 3750 cm^{-1}, which is generated by silanol groups interacting with each other through hydrogen bonding.[51]

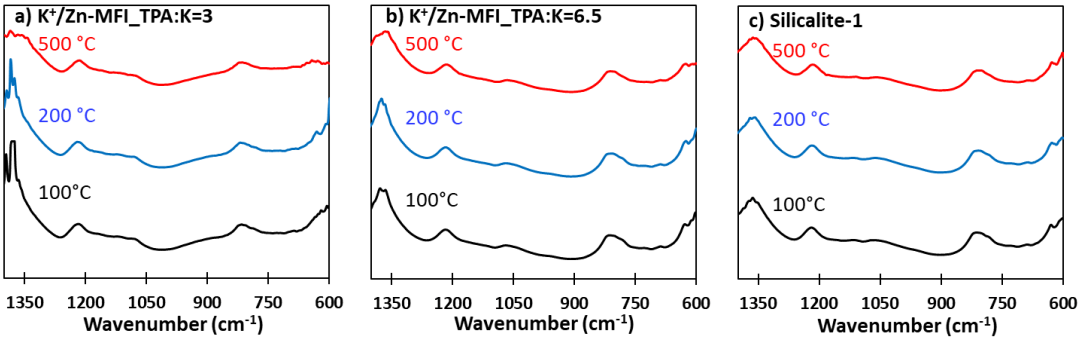

Figure 53: DRIFTS spectra obtained for K^+/Zn-MFI_TPA:K=3 (a), K^+/Zn-MFI_TPA:K=6.5 (b) and Silicalite-1 (c) at 100 °C, 200°C and 500°C for wavenumbers between 600 and 1400 cm^{-1}.

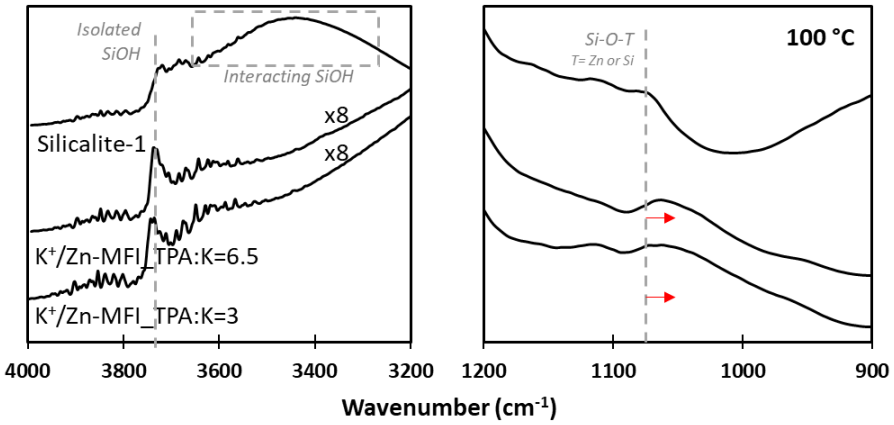

Figure 54: DRIFTS spectra obtained for Silicalite-1, K^+/Zn-MFI_TPA:K=6.5 and K^+/Zn-MFI_TPA:K=3 at 100 °C for wavenumbers between 600-1400 cm^{-1} and 3000-4000 cm^{-1}.

In Figure 55 a direct comparison between two Zn-MFI materials is reported. K^+/Zn-MFI_TPA:K=6 was analysed after calcination to remove the OSDA without any further treatment, whilst H^+-K^+/Zn-MFI_TPA:K=6 was the product of calcination and ion-exchange with NH_4NO_3 and further thermal treatment at 550 °C for 6 hours in order to obtain the protic form of the parent material, with some residual potassium species. The broad band assigned to hydrogen bonded defects at approximately 3500 cm^{-1}, not detected in K^+/Zn-MFI_TPA:K=6, is observed in H^+-K^+/Zn-MFI_TPA:K=6. This may be due to the fact that K^+ extra-framework species is interacting with siloxy defect sites in the framework, therefore there is no formation of silanol defects which would interact with each other through hydrogen bonds. As a consequence, the Zn-MFI materials containing K^+ cations in extra-framework positions only show very weak silanol signals for isolated Si–OH sites (3750 cm^{-1}).

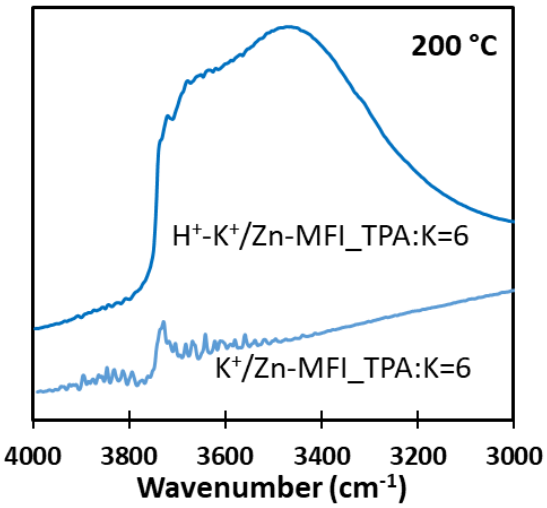

Figure 55: DRIFTS spectra between 3000 and 4000 cm-1 acquired for K^+/Zn-MFI_TPA:K=6 and H^+-K^+/Zn-MFI_TPA:K=6 materials at 200 °C.

The evidence collected through DRIFTS analysis match the results obtained from ssNMR HETCOR experiments which showed a lower intensity of correlation signal between Q_3 silicon sites and protons from defective sites in K^+-containing samples. ^1H MAS and ^1H-^{29}Si HETCOR solid-state NMR experiments were also able to detect silanol nest defects in the zincosilicate materials that can interact through hydrogen bonds. These species, however, appear to be present only after calcination and ion exchange with NH_4^+, with consequent elimination of most of the K^+ species. DRIFTS analyses were also able to confirm the presence of framework Zn sites, by comparing the Si–O–T stretching vibrations in the zincosilicate materials and in Silicalite-1.

5.2.4. Diffuse Reflectance UV-vis Spectroscopy

In order to rule out the presence of ZnO in the prepared zincosilicate materials, diffuse reflectance UV-vis (DR UV-vis) spectroscopy experiments were performed. In Figure 56(a) the spectrum obtained from a Zn-MFI sample synthesised using pyrrolidine as a template is reported, whilst Figure 56(b) shows two H^+/Zn-MFI samples prepared using the TEOS-based synthesis with $ZnCl_2$, aiming at Si:Zn ratios of 100 and 50 in the synthesis gel (Zn-MFI_100 and Zn ZSM-5_50). All samples were analysed after being thermally treated at 550 °C to remove organic SDA molecules. A ZnO standard was also analysed and is reported in both plots for comparison. The pyrrolidine_Zn-MFI_100 sample shows a main absorption band at wavelength below 230 nm, alongside a minor band at ≈ 250 nm, identifying the presence of ZnO clusters and a plateau for wavelengths higher than 300 nm.[53] The latter two features are in common with the spectrum of the ZnO standard. On the other and, the H^+/Zn-MFI_100 and H^+/Zn-MFI_50 prepared using the TEOS-based synthesis show a single main absorption band centred at ≈ 220 nm. Absorption bands below 230 nm are generally assigned to charge transfer transitions between framework Zn and lattice oxygen species;[54][46], [55] therefore, this suggests the successful incorporation of Zn heteroatoms in framework positions. Moreover, the samples analysed which were prepared using the TEOS-based method do not exhibit any spectral feature that can be ascribed to the presence of ZnO impurities, as opposed to the pyrrolidine_Zn-MFI samples, which shows features overlapping those of the ZnO standard.

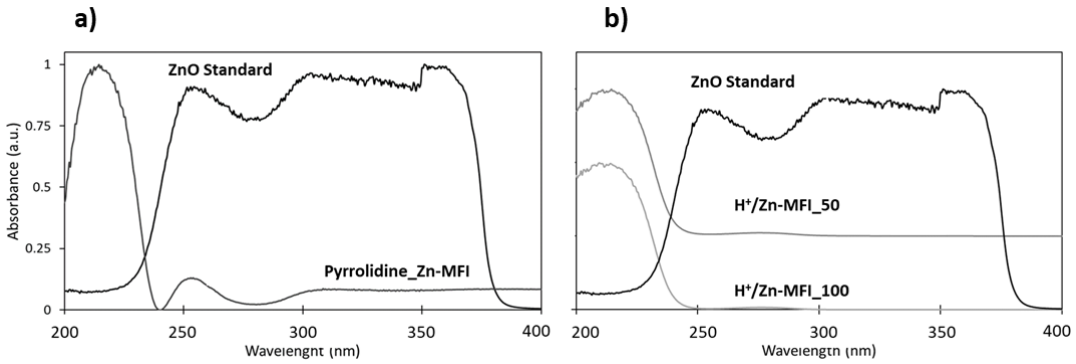

Figure 56: Plot of the absorbance as a function of the wavelength of the radiation for Zn-MFI samples prepared with the pyrrolidine synthesis (a) and the TEOS-based synthesis with different Zn contents (b) and compared to a ZnO standard. The spectra are plotted after normalisation.

5.2.5. Scanning Electron Microscopy

Scanning electron microscopy (SEM) was also employed to check the morphology of the samples. The morphology of zeolite crystals is strongly dependent on the synthesis conditions and it is hard to predict. Materials belonging to the MFI family usually show a characteristic coffin-like elongated hexagonal shape when prepared with TPA^+ ion-containing structure directing agents; however, it was also reported that the size of the crystals decreases with increasing levels of alkalinity in the synthesis gel.[56]–[59] The SEM analyses were carried out on the Zn-MFI materials prepared with the pyrrolidine-based synthesis and the TEOS-based synthesis (with and without KOH) The H^+/Zn-MFI samples prepared using the pyrrolidine synthesis method exhibited a peculiar "peanut-like" shape and the crystallites appeared to be rather large, with a length of approximately 20 µm (Figure 57).

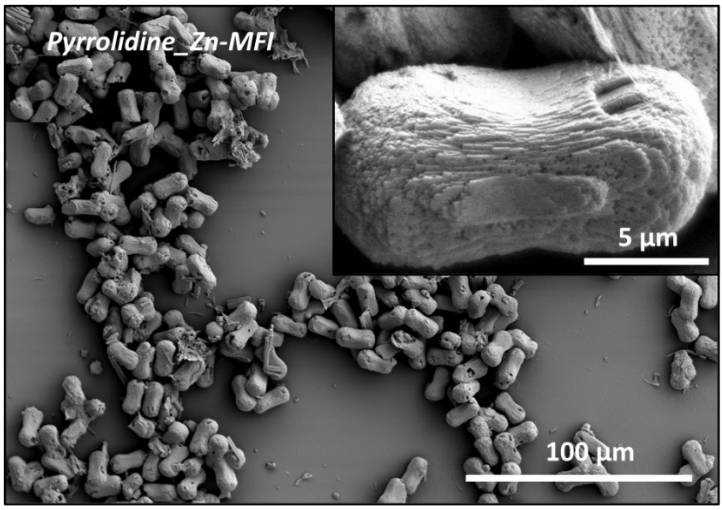

Figure 57: SEM image acquired with a beam voltage of 5 kV and a 3.5k and a 25k magnification for a pyrrolidine_Zn-MFI_100 sample.

The images reported in Figure 58 show the crystal morphology of Zn-MFI_100 materials prepared using the TEOS-based synthesis method, without the addition of KOH, with different Zn precursors other than $Zn(NO_3)_2$ ($Zn(OAc)_2$ and $ZnCl_2$). They show small hexagonal-shaped crystallites and elongated crystallites. Compared to the pyrrolidine_Zn-MFI_100 material, they show (i) a completely different morphology (ii) smaller particles and (iii) an irregular distribution of crystal sizes (Figure 58): most of them show the same size (≈ 500 nm) and a hexagonal button-like shape, however bigger structures are also present, which are elongated over one dimension. This might be due to the lack of an inorganic mineralising agent in the synthesis to assist and direct the crystallisation of the products. The presence of particles with elongated shape may cause diffusion-related issues, therefore catalysts with such crystal morphology are preferably avoided.[60]

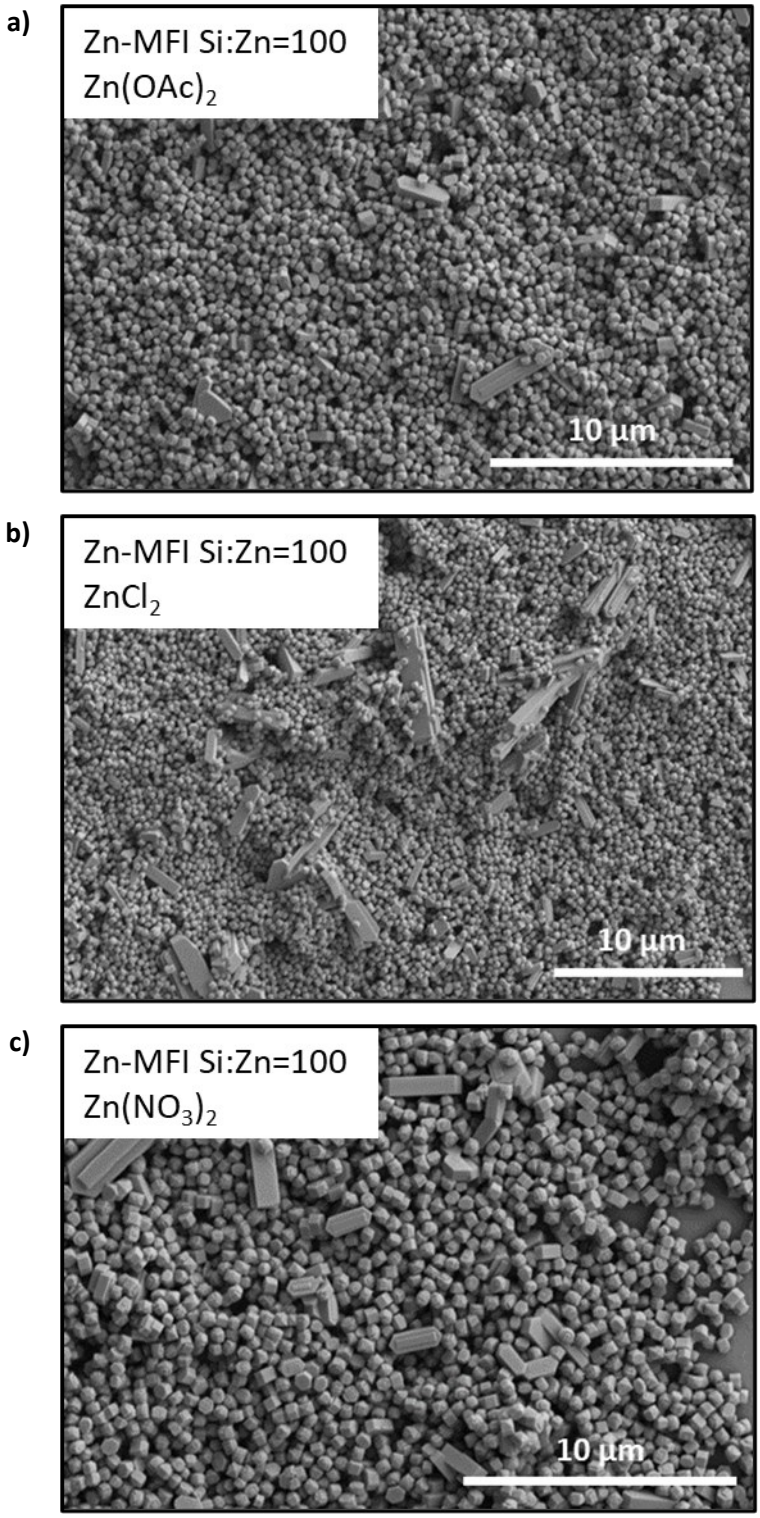

Figure 58: SEM images acquired at 5 kV of Zn-MFI samples prepared with Si:Zn ratios of 100 using $Zn(OAc)_2$ (a), $ZnCl_2$ (b) and $Zn(NO_3)_2$ (c), showing the presence of small, hexagonal-shaped crystals alongside bigger, elongated particles.

SEM analysis was employed to study the morphology of the Zn-MFI materials (prepared using the TEOS-synthesis and $ZnCl_2$ as Zn precursor) with Si:Zn ratios of 25, 50 and 100 and compare them to Silicalite-1, synthesised using the TEOS-synthesis without the addition of any heteroatom. From the images acquired, reported in Figure 59, it can be observed that the morphology of the materials is somehow related to the levels of Zn present in the synthesis gel. The shape of the crystals in Silicalite-1 (Figure 59(a)) appears to be regular, with very well-defined crystal faces and borders, and with high levels of particles with elongated shape. The regular shape of the crystals can also be observed in the Zn-MFI sample with Si:Zn = 100 (Figure 59(b)); however, lower Si:Zn ratios produce crystals with rougher surface. This is particularly noticeable in Figure 59(d), for the Zn-MFI sample with Si:Zn = 25.

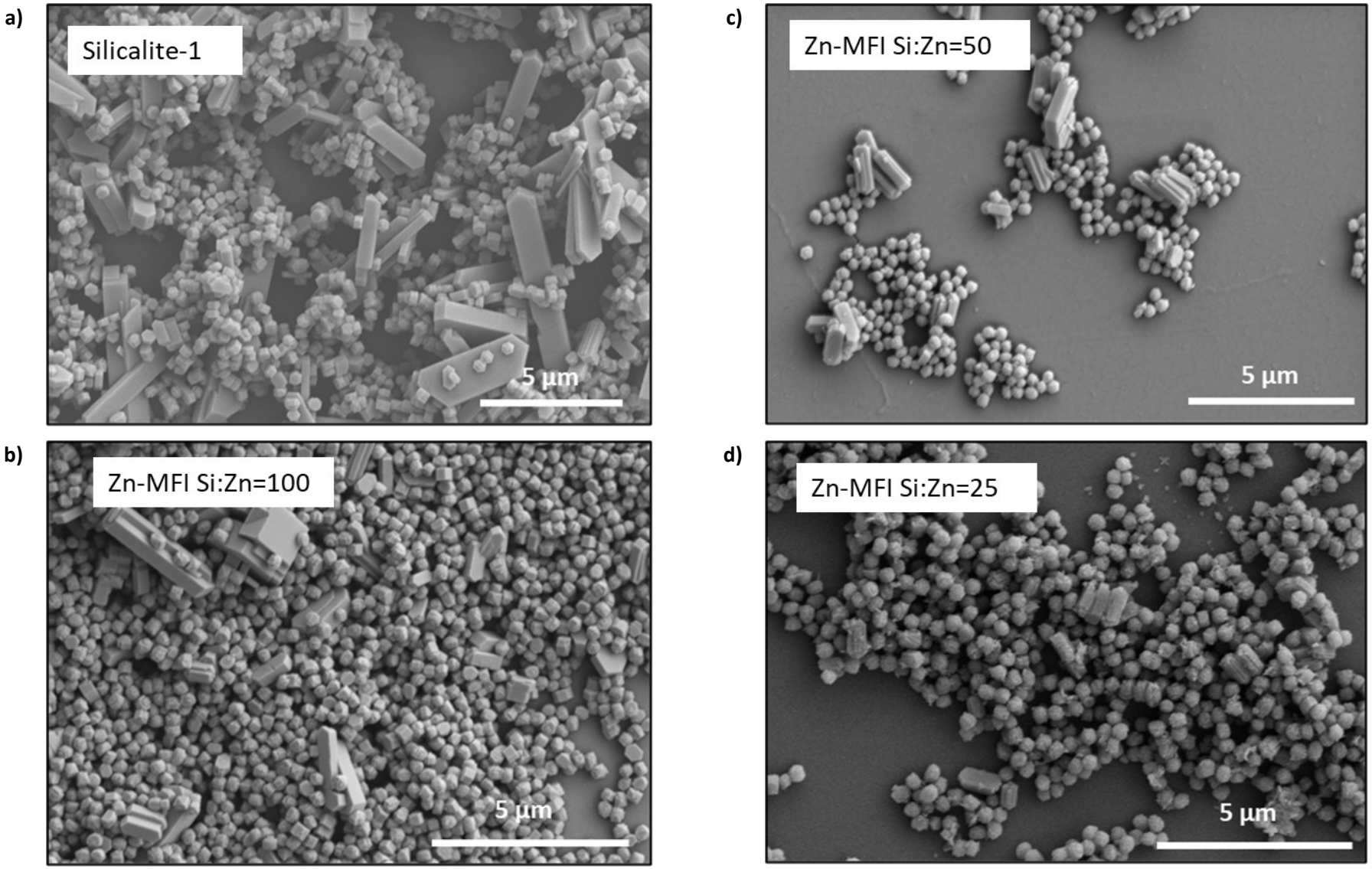

Figure 59: SEM images acquired at 5 kV of Silicalite-1 (a) and Zn-MFI samples prepared with Si:Zn ratios of 100 (b), 50 (c) and 25 (d) using $ZnCl_2$, showing the presence of small, hexagonal-shaped crystals alongside bigger, elongated particles.

Changes to the zincosilicates' morphology caused by the use of microwave-assisted synthesis method were also detected through SEM analysis. The images obtained are reported in Figure 60 for two Zn-MFI materials with Si:Zn = 100 (Figure 60(a)) or Si:Zn = 25 (Figure 60(b)). Noteworthy features of these samples are (i) the size of the crystallites, considerably bigger than the ones observed for samples prepared using the hydrothermal synthesis method, (ii) the morphology and (iii) the size distribution. The latter is totally homogeneous, with no presence of bigger or elongated particles among smaller particles. This may be due to the considerably shorted synthesis time compared to the hydrothermal synthesis, which prevents the excessive growth of the crystals over one dimension. Additionally, the sample with Si:Zn = 25 shows a rougher crystal surface, analogously to the sample prepared with the hydrothermal method.

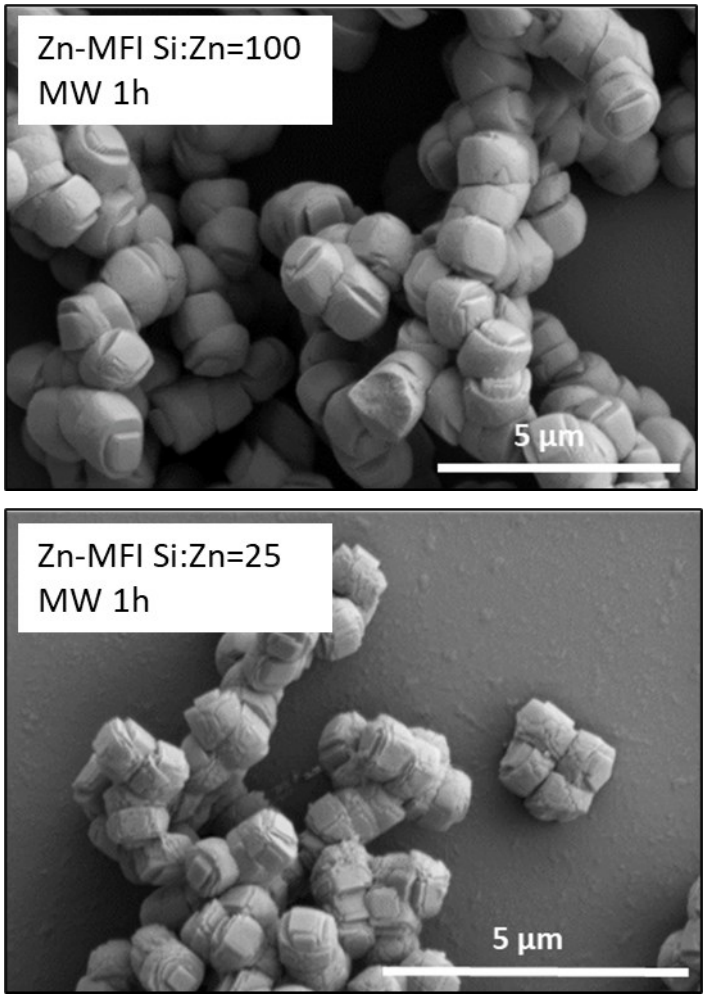

Figure 60: SEM images acquired at 5 kV of Zn-MFI samples prepared using the microwave-assisted synthesis method for 1 h at 170 °C with Si:Zn ratios of 100 (a) and 25 (b), showing small, cubic-like shaped particles with a homogeneous size distribution. The surface of the particles with a Si:Zn ratio of 25 appears to be rougher than the ones from the sample containing less zinc.

The K^+/Zn-MFI_TPA:K=*n* materials prepared with the addition of KOH in the synthesis gel were analysed by SEM and the results compared to those obtained for the H^+/Zn-MFI_TPA:K=∞

material synthesised without KOH. Figure 61 shows the difference in morphology and crystal size distribution of the samples: in the H^+/Zn-MFI_TPA:K=∞ (Figure 61(a)) the particle size distribution is broad, with the elongated particles giving a non-negligible contribution to it, despite being significantly less numerous than the small hexagonal particles. In Figure 61(b), (c), (d) and (e) the crystal size distribution in the Zn-MFI samples prepared with the addition of KOH (with TPAOH:KOH ratios of 6.5, 6, 5.65 and 3, respectively) is shown. It is evident how the presence of the mineralising agent under the same synthesis conditions drastically changed the particle area distribution. More specifically, the particles appear to be larger (≈ 1 μm) and their size distribution much narrower with most of the particle area measurements falling between values separated by less than 0.2 μm^2. The elongated and the small hexagonal-shaped particles were not observed in these samples. The possibility of controlling the properties of the synthesis products by the co-operative effect of the SDA and the inorganic cations has been reported for various zeolite framework types.[62], [63] In particular, it was observed that the combination of cetyltrimethylammonium (CTA^+) and K^+ steered the MFI synthesis products towards smaller particles than those obtained using TPA^+ and Na^+.[63] However, the hexagonal shape of the particles was only observed when TPA^+ cations were used.

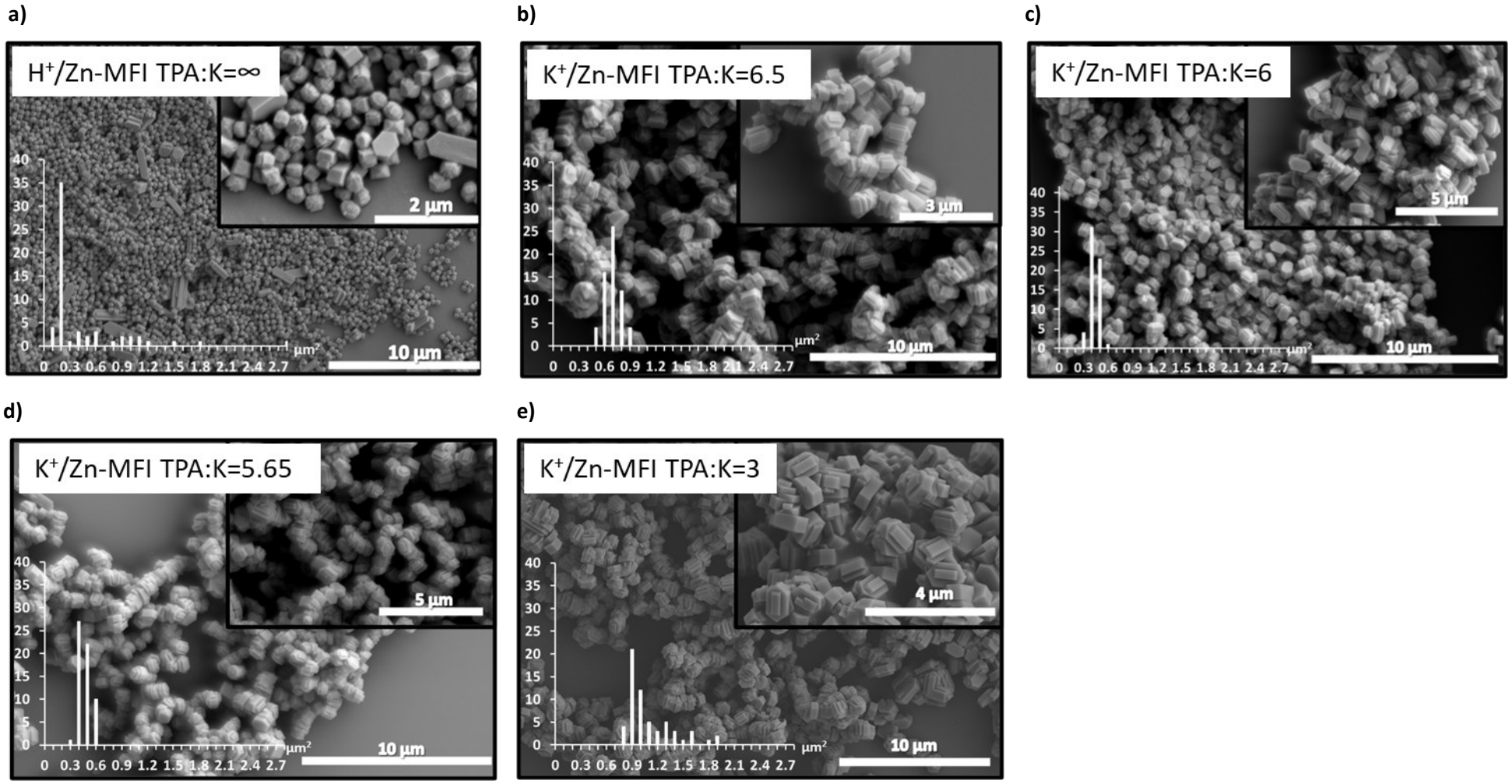

Figure 61: SEM images acquired with a beam voltage of 5 kV and magnifications between 4k and 25k for Zn-MFI samples prepared using $Zn(NO_3)_2$ without KOH (a) and TPA:K ratios of 6.5 (b), 6 (c), 5.65 (d) and 3 (e). Plots of the particle area distributions are represented on the images.

Electron microscopy was also employed to carry out elemental microanalysis by means of Energy Dispersive X-ray Spectroscopy (EDS) and the elemental maps acquired are shown in Figure 62. In order to obtain a smooth and homogeneous surface, the samples were initially pressed into pellets and then transferred onto the microscope stub, before being coated with approximately 30 nm of carbon using a sputter coater and transferred into the microscope. A surface of approximately 75 µm x 50 µm was selected on each sample and the EDS analysis carried out on this site. The same analysis was also carried out on another portion of the surface of the sample to ensure reproducibility (See Appendix). The results were collected and reported as: an image of the analysed surface area, the layered image containing the contributions from all the elements and the distributions of the single elements. Figure 62(a), (b), (c) and (d) represent, respectively, H^+/Zn-MFI_TPA:K=∞ (material prepared without KOH) and the K^+/Zn-MFI_TPA:K=*n* materials, with n = 6, 5.65 and 3. The Zn distribution appears overall homogeneous in all samples; however, some Zn-rich areas can be observed for samples with TPA:K=6 and TPA:K = 5.65 (Figure 62(b) and Figure 62(c)). These areas correspond to a higher concentration of K as well, suggesting that the potassium is "associated" with the position of the Zn heteroatoms in the framework, creating more or less concentrated Zn environments. Interestingly, this behaviour was not observed in the sample prepared with the highest potassium content, in which the Zn and K elemental distributions appear to be highly homogeneous and the Zn distribution in this sample is very similar to the one observed for the sample prepared without KOH (Figure 62(a)). The contribution to the overall charge density and location provided by SDA and inorganic cations has been previously reported to have the effect of influencing the position of heteroatoms in zeolite frameworks.[62] These effects, however, are very specific to the framework type and the OSDA/inorganic cation combination. For example, the combination of trimethyladamantylammonium ($TMAda^+$) and K^+ in aluminosilicate CHA resulted in the formation of isolated Al sites in the 8-MR windows.[62] In our case, more studies are required in order to identify the framework positions occupied by Zn heteroatoms. DFT calculations could be employed for this purpose and they would also provide a tool to confirm the structure directing role of K^+ and TPA^+ cations.

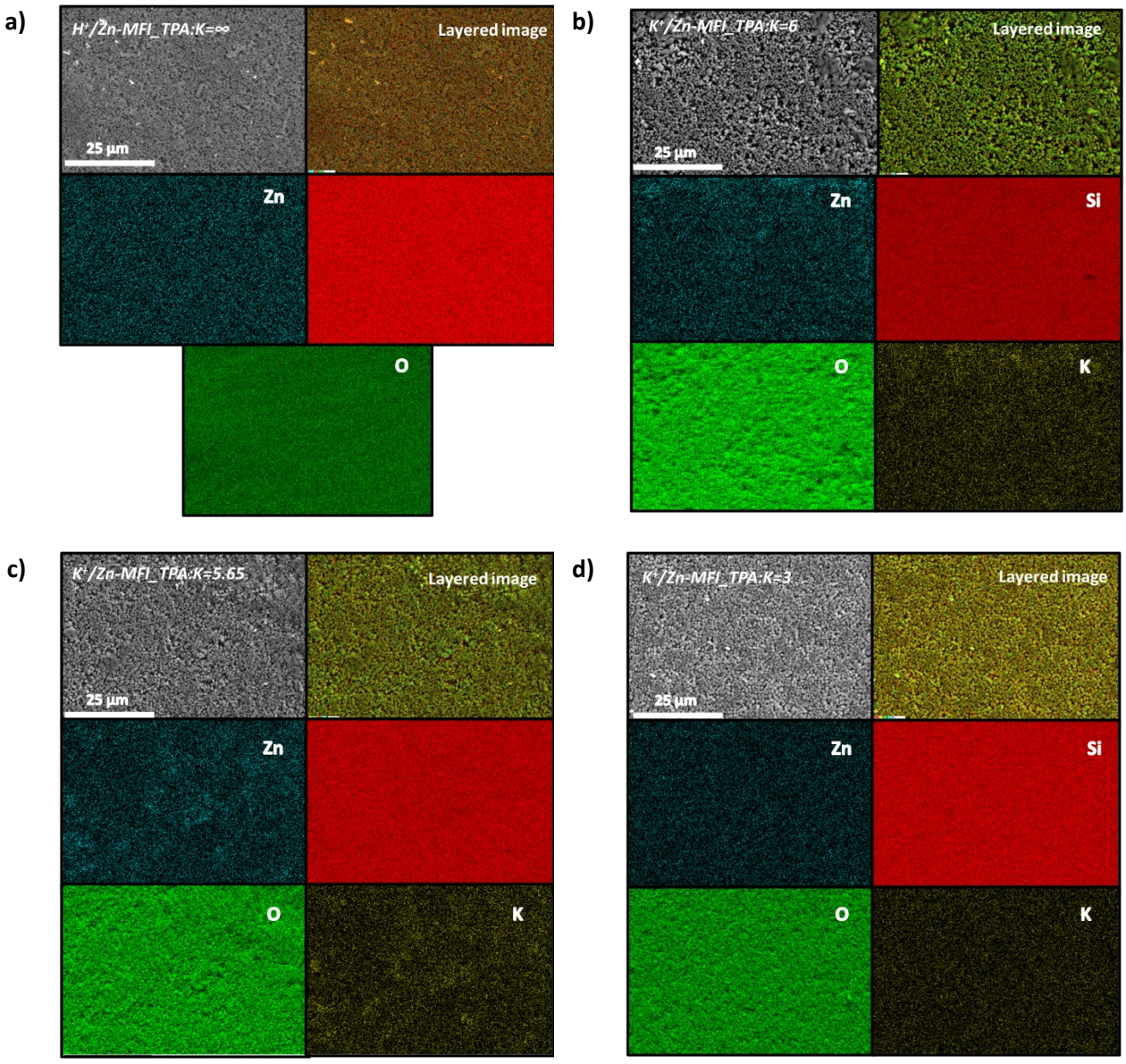

Figure 62: Elemental distribution of Zn, Si, O and K (where present) in the samples. Images acquired using SEM and EDS analysis through the software AZtec.

5.3. Chapter 5 Conclusions

Several characterisation techniques were applied to study the synthesised zincosilicate MFI samples and the combination of the information acquired enables an in-depth picture of the zincosilicate frameworks to be drawn. NMR analyses determined that different defect sites were present in the samples, but a more advanced characterisation (^{1}H-^{29}Si HETCOR NMR) shed light on the origin of these defects and the way they interact with the organic cations used to synthesise the materials. The evidence collected showed that the SiOH···$^{-}$OSi hydrogen bonds are in close spatial proximity to terminal methyl groups of the TPA^{+} organic structure directing agent cations, similarly to what has been previously observed for aluminosilicate and all-silica zeolites.[8], [11]–[13], [25], [26] The role played by inorganic extra-framework cations was also investigated using NMR experiments.

Direct-excitation ^{29}Si MAS NMR analyses revealed that the number of Si-OH defect sites present in the samples after calcination was drastically reduced by the addition of KOH in the synthesis. Interestingly, extra-framework K^+ cations were found to play an important role, as the intensity of the interactions between defect sites and framework silicon sites was observed to decrease with the increasing of K^+ content in the materials. This is possibly due to the formation of $–O^-K^+$ species as opposed to –OH species.[21]

The influence of K^+ cations on the properties of the Zn-MFI samples was also observed by electron microscopy, used to evaluate how the particle size and morphology distributions were considerably improved by the addition of KOH as mineralising agent. Moreover, EDS analyses revealed that K-rich areas corresponded to Zn-rich areas on the same sample. The evidence points towards a conclusion of K^+ cations playing a major charge-balancing and structure-directing role in the materials.

Another crucial point to determine was the chemical environment of Zn heteroatoms in the materials, in order to confirm their isomorphous substitution and therefore the formation of a microporous zincosilicate zeotype. The techniques applied were X-ray absorption spectroscopy and diffuse reflectance UV-vis and FT-IR spectroscopies. XAS was employed to probe the chemical environment around Zn heteroatoms and detect whether the Zn centres were undergoing a partial hydrolysis in the presence of water. The results obtained showed minor differences between XANES spectra of dehydrated and hydrated Zn-MFI samples, suggesting that the coordination of water at the Zn heteroatoms did not result in loss of Zn from the framework and forming $[Zn(H_2O)_6]^{2+}$. However, EXAFS analysis revealed that in the hydrated material the inclusion of 1.75 water molecules would produce a better fit to the experimental data and cause a slight increase in the bond length of the first Zn–O coordination shell. XAS studies confirmed that Zn was present in the zeotype framework in tetrahedral positions and suggested the coordination with water molecules was taking place in the hydrated material (Scheme 4).

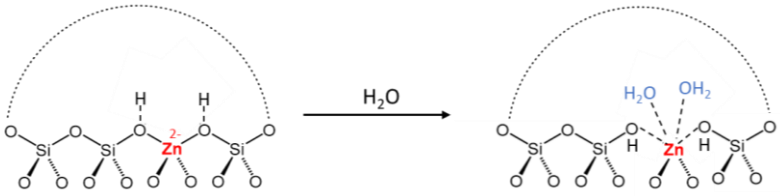

Scheme 4: Extract from Scheme 2 showing the coordination with water of framework Zn sites in a dehydrated Zn-MFI material after exposure to atmospheric moisture.

Additionally, UV-vis experiments ruled out the presence of ZnO cluster impurities in the samples and showed evidence of charge transfer transitions between framework Zn and lattice oxygen species, in agreement with literature results.[54][53], [55] DRIFTS studies showed that the bands associated with asymmetrical Si–O–T stretching vibrations exhibit different features between Silicalite-1 and zincosilicate MFI materials, in particular a shift towards lower wavenumbers for the

latter, generally associated to the substitution of heteroatoms in framework positions.[4], [46], [51] Additionally, the results from DRIFTS analysis were able to corroborate the evidence of the presence of hydrogen-bonding silanol defects, detected though ssNMR experiments.

Chapter 5 Bibliography

[1] O. McCubbin Stepanic, J. Ward, J. E. Penner-Hahn, A. Deb, U. Bergmann, and S. Debeer, "Probing a Silent Metal: A Combined X-ray Absorption and Emission Spectroscopic Study of Biologically Relevant Zinc Complexes," *Inorg. Chem.*, **2020**, doi: 10.1021/acs.inorgchem.0c01931.

[2] A. G. Stepanov, "Basics of Solid-State NMR for Application in Zeolite Science: Material and Reaction Characterization," *Zeolites Zeolite-like Mater.*, pp. 137–188, **2016**, doi: 10.1016/B978-0-444-63506-8.00004-5.

[3] A. Sutrisno, L. Liu, J. Xu, and Y. Huang, "Natural abundance solid-state 67Zn NMR characterization of microporous zinc phosphites and zinc phosphates at ultrahigh magnetic field," *Phys. Chem. Chem. Phys.*, 13, 37, pp. 16606–16617, **2011**, doi: 10.1039/c1cp20947g.

[4] S. R. Tomlinson, T. Mcgown, J. R. Schlup, and J. L. Anthony, "Infrared Spectroscopic Characterization of CIT-6 and a Family of ∗ BEA Zeolites," *Int. J. Spectrosc.*, 2013, **2013**.

[5] A. Hagen, K. Hallmeier, C. Hennig, R. Szargan, T. Inui, and F. Roessner, "State of Zn in MFI type zeolites characterized by XANES and EXAFS," in *Studies in Surface Science and Catalysis*, H. K. Beyer, J. B. Nagy, H. G. Karge, and I. Kiricsi, Eds. Elsevier, **1995**, pp. 195–202.

[6] M. Dong, J. Wang, and Y. Sun, "Synthesis of zincosilicate mordenite using citric acid as complexing agent," *Microporous Mesoporous Mater.*, 43, 2, pp. 237–243, **2001**, doi: 10.1016/S1387-1811(01)00211-6.

[7] W. Yan, X. Shibo, D. Yonghua, M. K. Schreyer, T. S. Xing, L. Yan, A. Borgna "Heteroatomic Zn-MWW Zeolite Developed for Catalytic Dehydrogenation Reactions: A Combined Experimental and DFT Study," *ChemCatChem*, 10, 14, pp. 3078–3085, **2018**, doi: 10.1002/cctc.201800199.

[8] I. Grosskreuz, H. Gies, and B. Marler, "Alteration and curing of framework defects by heating different as-made silica zeolites of the MFI framework type," *Microporous Mesoporous Mater.*, 291, p. 109683, **2020**, doi: 10.1016/j.micromeso.2019.109683.

[9] I. C. Medeiros-Costa, E. Dib, N. Nesterenko, J. P. Dath, J. P. Gilson, and S. Mintova, "Silanol defect engineering and healing in zeolites: opportunities to fine-tune their properties and performances," *Chem. Soc. Rev.*, 50, 19, pp. 11156–11179, **2021**, doi: 10.1039/D1CS00395J.

[10] M. Orazov and M. Davis, "Catalysis by framework zinc in silica-based molecular sieves," *Chem. Sci.*, 7, pp. 2264–2274, **2016**, doi: 10.1039/C5SC03889H.

[11] H. Koller, R. F. Lobo, S. L. Burkett, and M. E. Davis, "SiO ** * *HOSi Hydrogen Bonds in As-Synthesized High-Silica Zeolites," **1995**. Accessed: Nov. 05, 2020. [Online]. Available: https://pubs.acs.org/sharingguidelines.

[12] E. Dib, J. Grand, S. Mintova, and C. Fernandez, "Structure-Directing Agent Governs the Location of Silanol Defects in Zeolites," *Chem. Mater.*, 27, 22, pp. 7577–7579, **2015**, doi: 10.1021/acs.chemmater.5b03668.

[13] E. Dib, J. Grand, A. Gedeon, S. Mintova, and C. Fernandez, "Control the position of framework defects in zeolites by changing the symmetry of organic structure directing agents," *Microporous Mesoporous Mater.*, p. 110899, **2021**, doi: 10.1016/j.micromeso.2021.110899.

[14] G. Paul, C. Bisio, I. Braschi, M. Cossi, G. Gatti, E. Gianotti, L. Marchese "Combined solid-state NMR, FT-IR and computational studies on layered and porous materials," *Chemical Society Reviews*, 47, 15. Royal Society of Chemistry, pp. 5684–5739, Aug. 07, 2018, doi: 10.1039/c7cs00358g.

[15] P. Andy and M. E. Davis, “Dehydrogenation of propane over platinum containing CIT-6,” *Ind. Eng. Chem. Res.*, 43, 12, pp. 2922–2928, **2004**, doi: 10.1021/ie030357m.

[16] T. Takewaki, L. W. Beck, and M. E. Davis, “Zincosilicate CIT-6: A precursor to a family of *BEA-type molecular sieves,” *J. Phys. Chem. B*, 103, 14, pp. 2674–2679, **1999**, doi: 10.1021/jp9845726.

[17] M. A. Camblor and M. E. Davis, “MAS NMR Spectroscopy of Tectozincosilicates,” **1994**. Accessed: Jul. 21, 2020. [Online]. Available: https://pubs.acs.org/sharingguidelines.

[18] H. Eckert, J. P. Yesinowski, L. A. Silver, and E. M. Stolper, “Water In Silicate Glasses: Quantitation and Structural Studies by 1H Solid Echo and MAS-NMR Methodsf,” *J. Phys. Chem*, 92, p. 2055, **1988**.

[19] H. Koller, R. F. Lobo, S. L. Burkett, and M. E. Davis, “SiO ** * *HOSi Hydrogen Bonds in As-Synthesized High-Silica Zeolites,” **1995**.

[20] A. P. Palči´c, S. Moldovan, H. El Siblani, A. Vicente, and V. Valtchev, “Defect Sites in Zeolites: Origin and Healing,” *Adv. Sci.*, p. 2104414, **2021**, doi: 10.1002/ADVS.202104414.

[21] L. Liu, M. Lopez-Haro, C. W. Lopes, C. Li, P. Concepcion, L. Simonelli, J. J. Calvino, A. Corma “Regioselective generation and reactivity control of subnanometric platinum clusters in zeolites for high-temperature catalysis,” *Nat. Mater. 2019 188*, 18, 8, pp. 866–873, **2019**, doi: 10.1038/S41563-019-0412-6.

[22] J. B. Nagy, Z. Gabelica, and E. G. Derouane, “Position and configuration of the guest organic molecules within the framework of the ZSM-5 and ZSM-11 zeolites,” *Zeolites*, 3, 1, pp. 43–49, **1983**, doi: 10.1016/0144-2449(83)90084-2.

[23] Z. Gabelica, J. B. Nagy, P. Bodart, N. Dewaele, and A. Nastro, “Structure and stability of tetrapropyl-ammonium (TPA) ions in various alkali—aluminosilicate hydrogel precursors to crystalline (M)ZSM—5 zeolites,” *Zeolites*, 7, 1, pp. 67–72, **1987**, doi: 10.1016/0144-2449(87)90123-0.

[24] S. L. Burkett and M. E. Davis, “Mechanisms of Structure Direction in the Synthesis of Pure-Silica Zeolites. 1. Synthesis of TPA/Si-ZSM-5,” *Chem. Mater*, 7, pp. 920–928, **1995**.

[25] G. Brunklaus, H. Koller, and S. I. Zones, “Defect Models of As-Made High-Silica Zeolites: Clusters of Hydrogen-Bonds and Their Interaction with the Organic Structure-Directing Agents Determined from 1 H Double and Triple Quantum NMR Spectroscopy,” *Angew. Chemie Int. Ed.*, 55, 46, pp. 14459–14463, **2016**, doi: 10.1002/anie.201607428.

[26] X. Liu and Q. Luo, “Solid State NMR Spectroscopy Studies of the Nature of Structure Direction of OSDAs in Pure-Silica Zeolites ZSM-5 and Beta,” *J. Phys. Chem. C*, 121, 24, pp. 13211–13217, **2017**, doi: 10.1021/acs.jpcc.7b03350.

[27] Eddy Dib, I. Medeiros Costa, G. N. Vayssilov, H. A. Aleksandrov, and Svetlana Mintova, “Complex H-bonded silanol network in zeolites revealed by IR and NMR spectroscopy combined with DFT calculations,” *J. Mater. Chem. A*, **2021**, doi: 10.1039/D1TA06908J.

[28] M. Feike, D. E. Demco, R. Graf, J. Gottwald, S. Hafner, and H. W. Spiess, “Broadband Multiple-Quantum NMR Spectroscopy,” *J. Magn. Reson. Ser. A*, 122, 2, pp. 214–221, **1996**, doi: 10.1006/JMRA.1996.0197.

[29] S. Li, O. Lafon, W. Wang, Q. Wang, X. Wang, Y. Li, J. Xu, F. Deng “Recent Advances of Solid-State NMR Spectroscopy for Microporous Materials,” *Adv. Mater.*, p. 2002879, **2020**, doi: 10.1002/adma.202002879.

[30] S. P. Brown and H. W. Spiess, “Advanced Solid-State NMR Methods for the Elucidation of Structure and Dynamics of Molecular, Macromolecular, and Supramolecular Systems,” *Chem.*

Rev., 101, 12, pp. 4125–4155, **2001**, doi: 10.1021/CR990132E.

[31] C. Schroeder, V. Siozios, M. Hunger, M. R. Hansen, and H. Koller, "Disentangling Brønsted Acid Sites and Hydrogen-Bonded Silanol Groups in High-Silica Zeolite H-ZSM-5," *J. Phys. Chem. C*, 124, pp. 23380–23386, **2020**, doi: 10.1021/acs.jpcc.0c06113.

[32] G. Qi, W. Qiang, X. Jun, J. TrØbosc, O. Lafon, W. Chao, J. P. Amoureux, F. Deng "Synergic Effect of Active Sites in Zinc-Modified ZSM-5 Zeolites as Revealed by High-Field Solid-State NMR Spectroscopy," *Angew. Chemie Int. Ed.*, 55, 51, pp. 15826–15830, **2016**, doi: 10.1002/anie.201608322.

[33] B. E. G. Lucier, S. Chen, and Y. Huang, "Characterization of Metal−Organic Frameworks: Unlocking the Potential of Solid-State NMR," **2017**, doi: 10.1021/acs.accounts.7b00357.

[34] S. A. Thomas, B. Mishra, and S. C. B. Myneni, "High Energy Resolution-X-ray Absorption Near Edge Structure Spectroscopy Reveals Zn Ligation in Whole Cell Bacteria," *J. Phys. Chem. Lett.*, 10, pp. 2585–2592, **2019**, doi: 10.1021/acs.jpclett.9b01186.

[35] M. L. Baker, M. W. Mara, J. J. Yan, K. O. Hodgson, B. Hedman, and E. I. Solomon, "K- and L-edge X-ray absorption spectroscopy (XAS) and resonant inelastic X-ray scattering (RIXS) determination of differential orbital covalency (DOC) of transition metal sites," *Coord. Chem. Rev.*, 345, pp. 182–208, **2017**, doi: 10.1016/J.CCR.2017.02.004.

[36] I. Pinilla-Herrero, E. Borfecchia, J. Holzinger, U. V. Mentzel, F. Joensen, K. A. Lomachenko, S. Bordiga, C. Lamberti, G. Berlier, U. Olsbye, S. Svelle, J. Skibsted, P. Beato "High Zn/Al ratios enhance dehydrogenation vs hydrogen transfer reactions of Zn-ZSM-5 catalytic systems in methanol conversion to aromatics," *J. Catal.*, 362, pp. 146–163, **2018**, doi: 10.1016/j.jcat.2018.03.032.

[37] C. Chouillet, F. Villain, M. Kermarec, H. Ne Lauron-Pernot, and C. Louis, "Relevance of the Drying Step in the Preparation by Impregnation of Zn/SiO 2 Supported Catalysts," **2003**, doi: 10.1021/jp022481.

[38] E. Castorina, E. D. Ingall, P. L. Morton, D. A. Tavakoli, and B. Lai, "Zinc *K* -edge XANES spectroscopy of mineral and organic standards," *J. Synchrotron Radiat.*, 26, 4, pp. 1302–1309, **2019**, doi: 10.1107/S160057751900540X.

[39] B. Ravel, M. Newville, and IUCr, "ATHENA, ARTEMIS, HEPHAESTUS: data analysis for X-ray absorption spectroscopy using IFEFFIT," *urn:issn:0909-0495*, 12, 4, pp. 537–541, **2005**, doi: 10.1107/S0909049505012719.

[40] N. A. Simonov, P. A. Sandomirskii, Yu. K. Egorov-Tismenko, "Crystal structure of willemite, Zn_2SiO_4.," *Dokl. Akad. Nauk SSSR*, 237, 3, pp. 581–584, **1977**, Accessed: Jan. 09, **2022**.

[41] "Glowing green – Willemite | Crystallography365." https://crystallography365.wordpress.com/2014/10/30/glowing-green-willemite/ (accessed Jan. 09, 2022).

[42] H. van Koningsveld, J. C. Jansen, and H. van Bekkum, "The monoclinic framework structure of zeolite H-ZSM-5. Comparison with the orthorhombic framework of as-synthesized ZSM-5," *Zeolites*, 10, 4, pp. 235–242, **1990**, doi: 10.1016/0144-2449(94)90134-1.

[43] E. N. Maslen, K. J. Watson, S. C. Ridout, and F. H. Moore, "Electron density in diammonium hexaaquazinc(II) sulfate – an X-ray and neutron study," *Acta Crystallographica Section C Crystal Structure Communications*, Sep. 15, **1988.**

[44] L. Qi, Y. Zhang, M. A. Conrad, C. K. Russell, J. Miller, and A. T. Bell, "Ethanol Conversion to Butadiene over Isolated Zinc and Yttrium Sites Grafted onto Dealuminated Beta Zeolite," *Cite This J. Am. Chem. Soc*, 142, pp. 14674–14687, **2020**, doi: 10.1021/jacs.0c06906.

[45] D. Scarano, A. Zecchina, S. Bordiga, F. Geobaldo, G. Spoto "Fourier-transform Infrared and Raman Spectra of Pure and Al-, B-, Ti-and Fe-substituted Silicalites: Stretching-mode Region," **1993**.

[46] P. Hu, K. Iyoki, H.i Yamada, Y. Yanaba, K. Oharac, N. Katadad, T. Wakihara "Synthesis and characterization of MFI-type zincosilicate zeolites with high zinc content using mechanochemically treated Si–Zn oxide composite," *Microporous Mesoporous Mater.*, 288, June, p. 109594, **2019**, doi:10.1016/j.micromeso.2019.109594.

[47] E.M. Flanigen, H. Khatami, H.A. Szimanski, "Infrared Structural Studies of Zeolite Frameworks," **1974**, pp. 201–229.

[48] Y. Meng, H. C. Genuino, C.-H. Kuo, H. Huang, S.-Y. Chen, L. Zhang, A. Rossi, S. L. Suib "One-step hydrothermal synthesis of manganese-containing MFI-type zeolite, Mn-ZSM-5, characterization, and catalytic oxidation of hydrocarbons," *J. Am. Chem. Soc.*, 135, 23, pp. 8594–8605, **2013**, doi: 10.1021/JA4013936/SUPPL_FILE/JA4013936_SI_001.PDF.

[49] S. Bordiga, C. Lamberti, F. Bonino, A. Travert, and F. Thibault-Starzyk, "Probing zeolites by vibrational spectroscopies," *Chem. Soc. Rev.*, 44, 20, pp. 7262–7341, **2015**, doi: 10.1039/C5CS00396B.

[50] G. Vitale, H. Molero, E. Hernandez, S. Aquino, V. Birss, and P. Pereira-Almao, "One-pot preparation and characterization of bifunctional Ni-containing ZSM-5 catalysts," *Appl. Catal. A Gen.*, 452, pp. 75–87, **2013**, doi: 10.1016/J.APCATA.2012.11.026.

[51] L. Lin, X. Zhang, N. He, J. Liu, Q. Xin, and H. Guo, "Operando Dual Beam FTIR Study of Hydroxyl Groups and Zn Species over Defective HZSM-5 Zeolite Supported Zinc Catalysts," *Catal. 2019, Vol. 9, Page 100*, 9, 1, p. 100, **2019**, doi: 10.3390/CATAL9010100.

[52] J. Chen, Z. Feng, P. Ying, and C. Li, "ZnO Clusters Encapsulated inside Micropores of Zeolites Studied by UV Raman and Laser-Induced Luminescence Spectroscopies," *J. Phys. Chem. B*, 108, 34, pp. 12669–12676, **2004**, doi: 10.1021/JP048746X.

[53] L. Wang, S. Sang, S. Meng, Y. Zhang, Y. Qi, and Z. Liu, "Direct synthesis of Zn-ZSM-5 with novel morphology," *Mater. Lett.*, 61, pp. 1675–1678, **2007**, doi: 10.1016/j.matlet.2006.07.097.

[54] N. Koike, K. Iyoki, B. Wang, Y. Yanaba, S. P. Elangovan, K. Itabashi, W. Chaikittisilp, T. Okubo "Increasing the ion-exchange capacity of MFI zeolites by introducing Zn to aluminosilicate frameworks," *Dalt. Trans.*, 47, 28, pp. 9546–9553, **2018**, doi: 10.1039/C8DT01391H.

[55] D. T. Hayhurst, R. Aiello, J. B.Nagy, F. Crea, G. Giordano, A. Nastro, J. C. Lee "Effect of NaOH , TPAOH , and TPABr Concentration on the Growth Rate and Morphology of Silicalite-1 H and TPABr on the," in *Perspectives in Molecular Sieve Science*, W. H. Flank and T. E. Whyte, Eds. American Chemical Society, **1988**, pp. 277–291.

[56] M. Ghamami and L. B. Sand, "Synthesis and crystal growth of zeolite," *Zeolites*, 3, 2, pp. 155–162, **1983**.

[57] F. Yaripour, Z. Shariatinia, S. Sahebdelfar, and A. Irandoukht, "Conventional hydrothermal synthesis of nanostructured H-ZSM-5 catalysts using various templates for light ole fi ns production from methanol," *J. Nat. Gas Sci. Eng.*, 22, pp. 260–269, **2015**, doi: 10.1016/j.jngse.2014.12.001.

[58] G. Bonilla, I. Díaz, M. Tsapatsis, H. K. Jeong, Y. Lee, and D. G. Vlachos, "Zeolite (MFI) crystal morphology control using organic structure-directing agents," *Chem. Mater.*, 16, 26, pp. 5697–5705, **2004**, doi: 10.1021/CM048854W/SUPPL_FILE/CM048854WSI20040920_054933.PDF.

[59] F. Di Renzo, "Zeolites as tailor-made catalysts: Control of the crystal size," *Catal. Today*, 41, 1–3, pp. 37–40, **1998**, doi: 10.1016/S0920-5861(98)00036-4.

[60] J. R. Di Iorio *et al.*, “Cooperative and Competitive Occlusion of Organic and Inorganic Structure-Directing Agents within Chabazite Zeolites Influences Their Aluminum Arrangement,” *J. Am. Chem. Soc.*, 142, 10, pp. 4807–4819, **2020**, doi: 10.1021/JACS.9B13817/SUPPL_FILE/JA9B13817_SI_002.ZIP.

[61] A. Chawla, R. Li, R. Jain, R. J. Clark, J. G. Sutjianto, J. C. Palmer, J. D. Rimer “Cooperative effects of inorganic and organic structure-directing agents in ZSM-5 crystallization,” *Mol. Syst. Des. Eng.*, 3, 1, pp. 159–170, **2018**, doi: 10.1039/c7me00097a.

6. Chapter 6: Methane Activation over Zn-substituted Zeotypes

6.1. Introduction to Methane Activation

The direct conversion of methane to methanol under mild conditions is still considered as one of the Holy Grail reactions in C1 chemistry. Methane is one of the most abundant and inexpensive resources on the planet, but also one of the most polluting.[1] Therefore, both academia and industry have been investing resources and efforts into finding viable methods for the production of methanol from methane *via* one single step, by-passing the 2-step syngas-based process.[2]–[6] The direct conversion of methane to methanol has been explored using homogeneous and heterogeneous systems, with metal-exchanged zeolites showing promising results.[6] Fe- and Cu-exchanged zeolites resulted to be very promising materials, also leading to the aqueous extraction of methanol,[7], [8] however, none of these systems has been commercialised yet.[9] The reason for this is found in some practical key factors, reported by de Klerk, such as improving the selectivity to methanol and simultaneously reducing the selectivity to CO_2, reducing the use of pure oxygen and decreasing the reaction pressure.[10], [11] Nevertheless, the scientific community is still active in this field, with new promising findings that in the future could potentially be adapted to the industrial scale.

An element that has drawn the attention of the scientific community for its potential in the application of the direct conversion of methane to more valuable chemicals is zinc. The first demonstration of the ability of Zn^{2+} cations to break the C-H bond in CH_4 was provided by Kazansky et al. through IR spectroscopy analysis [12] Subsequently, Ivanova and Stepanov provided spectroscopic characterisations (NMR, FT-IR) of the Zn-containing zeolites interacting with CH_4, in order to understand the reaction mechanism and localise the active sites.[12], [13] The latter has been identified as a Zn^{2+} framework-bound cation (Figure 63(a)), which interacts with methane forming a $[Zn^{II}\text{-}CH_3]$ species following the cleavage of one C-H bond.[12], [14]–[17] It was observed that the method used to introduce the Zn^{2+} cations in the zeolite has a profound impact on the level of exchange and, therefore, the efficiency of the methane activation reaction.[12], [15]–[18] The most used introduction methods for metal cations are Incipient Wetness Impregnation (IWI), Ion Exchange (IE) and Chemical Vapour Deposition (CVD). Whilst the first two methods often fail to deliver high exchange levels, especially in high-silica zeolites, due to difficulties associated to the stabilisation of the 2+ charges on Zn^{2+} cations by remote $[AlO_4^-]$ pairs, the CVD method is particularly effective in achieving complete exchange of Brønsted acid sites with Zn^{2+} cations. [12], [19], [20] Equation 19 shows the ZnVD reaction, where the introduction of Zn^0 in the presence of Brønsted acid sites in the zeolite framework results in the formation of extra-framework Zn^{2+} cations (replacing the Brønsted acid sites) and consequent formation of hydrogen gas.

$$Zn^0_{(s)} + 2H^+_{(s)} = Zn^{2+}_{(s)} + H_{2(g)} \qquad \text{Equation 19}$$

Alternatively, the substitution of Zn heteroatoms in framework positions, associated with [ZnO_4^{2-}] sites, would provide better stabilisation for Zn^{2+} extra-framework cations, allowing for higher exchange levels and Zn-loading.[21]–[24] The introduction of Zn^{2+} cations stabilised by framework-Zn species should provide an efficient platform for CH_4 activation (Figure 63(b)). Whilst several studies have focused on the activation and functionalisation of CH_4 using Zn-modified zeolites, to the best of our knowledge, there are no reports about the same reaction carried out on zincosilicates. To this end, we have carried out CH_4 activation experiments using Zn-MFI samples and Zn CVD, in order to obtain Zn^{2+}/Zn-MFI samples.

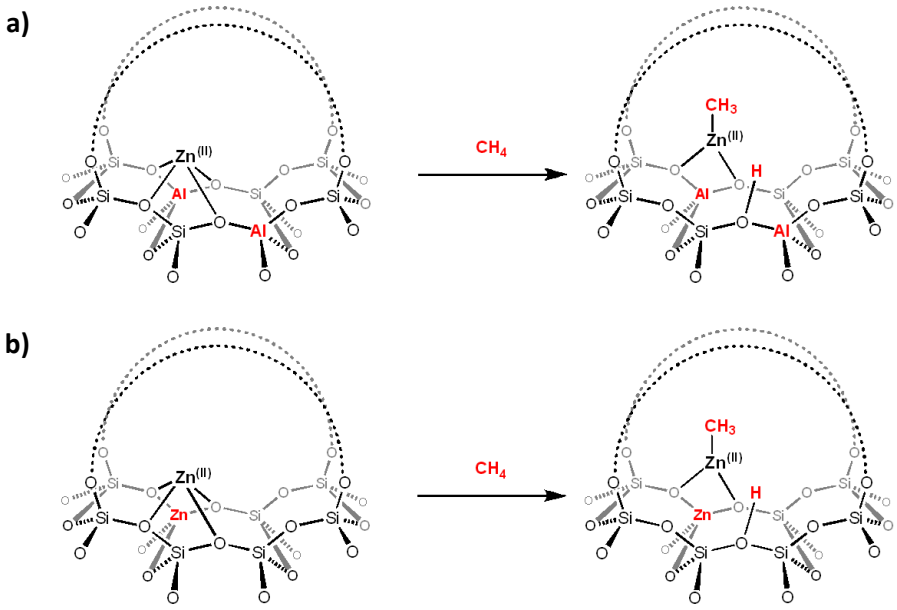

Figure 63: Representation of the reaction between a Zn^{2+} extra-framework cation and a CH_4 molecule, producing a Brønsted acid site in an aluminosilicate zeolite (a) and in a zincosilicate zeotype (b).

6.2. Results and Discussion

Zincosilicate MFI samples with different Si:Zn ratios were prepared using the TEOS-based synthesis using $ZnCl_2$ without the addition of KOH and thoroughly characterised in order to make sure that Zn heteroatoms had been successfully substituted in framework positions. The H^+/Zn-MFI samples prepared in this way were then thermally treated, modified with Zn^{2+} *via* CVD of Zn^0 and finally used for the activation of CH_4 at 250 °C in stoichiometric conditions. The outcome of the reaction was monitored through solid state ^{13}C and ^{1}H MAS NMR, in order to detect evidence of the formation of the [Zn^{II}-CH_3] species, which shows a peak at -19 ppm in the ^{13}C NMR spectrum, typical of the methyl group in organozinc compounds.[14], [26]

6.2.1. Details and preparation of ZnVD/Zn-MFI samples

In order to evaluate the effect on CH_4 activation of (i) framework Zn loading in the samples and (ii) aging (i.e. exposure of the sample to atmospheric moisture for a long period of time) different H^+/Zn-MFI samples were selected, with various Si:Zn ratios (Si:Zn = 100, 50 or 25 in the synthesis gel) and analysed immediately after the synthesis ("*fresh*" Zn-MFI) or after the exposure to atmospheric moisture for at least two weeks at room temperature ("*aged*" Zn-MFI). The samples used and their properties before the reactions are listed in Table 19. The samples were also analysed by means of p-XRD and SEM before and after being used for CH_4 activation reactions in order to check if the reaction conditions would cause loss of crystallinity. The p-XRD patterns and SEM images acquired for the parent materials are reported in Figure 64 and Figure 65. Elemental analysis results show that the Si:Zn ratios of the samples are lower than the Si:Zn ratios of the synthesis gels, however the amount of Zn incorporated in the samples is in line with what was expected and the Si content appears consistent in the three zincosilicate samples. From the p-XRD analysis it can be concluded that all the samples used are highly crystalline and show the typical MFI framework pattern. Finally, SEM images show the shape and size of the crystallites; as expected, the samples exhibit the presence of small hexagonal-shaped particles (approximately 500 nm) and elongated particles (approximately 1 – 6 µm). Further ^{1}H-^{29}Si CP NMR analyses were carried out on Silicalite-1 materials in the as-made and calcined forms and after Zn vapour deposition in order to assess how the treatments affected the framework Si sites and the presence of defects. The results are reported in Section 9.3.2 of the Appendix.

Table 19: Elemental analysis results obtained by XRF for Zn-MFI and Silicalite-1 samples. The uncertainty on the measurements is the 6% of the values (only reported for Si:Zn ratios).

Entry	Sample	Si (wt%)	Zn (wt%)	Si:Zn
1	***H^+/Zn-MFI_25***	38.5	5.2	17.1 ± 1.0
2	***H^+/Zn-MFI_50***	37.2	2.7	32.4 ± 1.9
3	***H^+/Zn-MFI_100***	39.8	1.4	65.0 ± 3.9
4	***Silicalite-1***	46.4	-	-
5	***ZnO/Silicalite-1***	46.2	1.1	33.8 ± 2.0

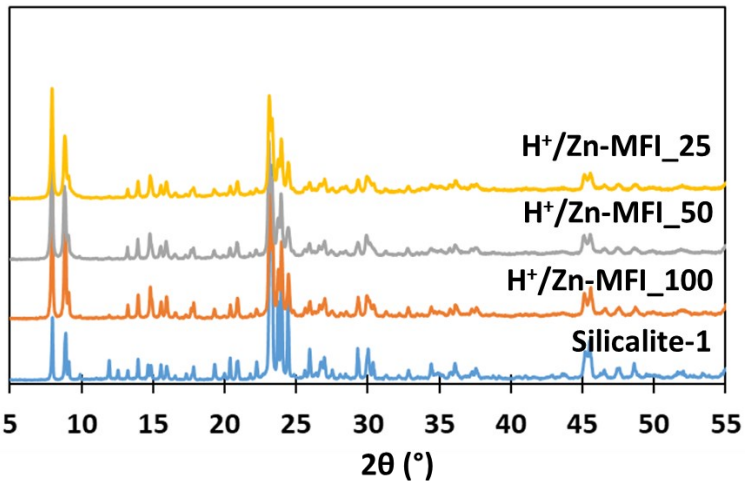

Figure 64: Powder-XRD patterns of Zn-MFI and Silicalite-1 samples used for CH_4 activation reactions.

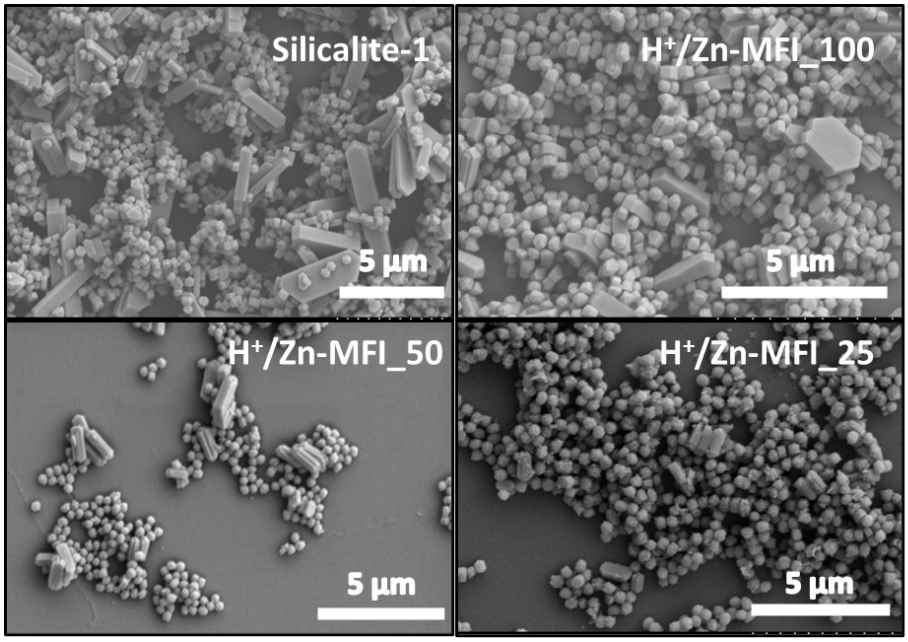

Figure 65: SEM images of Zn-MFI and Silicalite-1 samples used for CH_4 activation reactions acquired with a voltage 5 kV.

6.2.2. CH_4 activation over ZnVD/Zn-MFI Zeotypes

The samples were placed in a quartz u-tube and dehydrated under reduced pressure overnight prior to Zn^0 insertion in the u-tube and its vapourisation into Zn^{2+} extra-framework cations. This procedure was applied following the method developed and optimised in the group by Shah et al.[25] and reported in detail in Section 3.1.2.3. The H^+/Zn-MFI sample (*fresh* ZnVD/Zn-MFI_100) was used for the reaction making sure that only a short amount of time (approximately 1 day) would pass between the calcination and the dehydration steps, in order to limit the amount of moisture absorbed in the material. For this sample, ^{13}C labelled methane was used in order to enhance the signal intensity in the

^{13}C NMR spectrum. The reaction with methane was carried out at 250 °C, however instead of a continuous exposure to methane for 15 minutes, the u-tube was exposed to the $^{13}CH_4$ cylinder for brief intervals of 5 seconds, repeated three times. After the last exposure, the tube was left for 15 minutes under static conditions. Subsequently, the u-tube was sealed and transferred into an Ar-filled glovebox, where the NMR rotor was packed with the sample and sealed, then transferred to the spectrometer to be analysed. The spectrum obtained is reported in Figure 66. Despite the low signal to noise ratio, a signal centred at -20 ppm could be detected. The splitting of the signal could be due to the low S/N ratio; however, the chemical shift of the signal is in agreement with literature data which assign [Zn^{II}-CH_3] species to a -19 ppm peak. The shift to slightly lower chemical shifts could be due to the different framework environment provided by the presence of Zn instead of Al in framework positions. The experiment showed that a zincosilicate MFI material undergoing the same treatment and reaction conditions as the ones applied to aluminosilicate ZSM-5 samples would deliver the same reactivity to CH_4. However, these results could not be confirmed by repetition of the same experiment. Specifically, no reactivity towards CH_4 could be observed again for a *fresh* ZnVD/Zn-MFI_100 or *aged* ZnVD/Zn-MFI_100 sample.

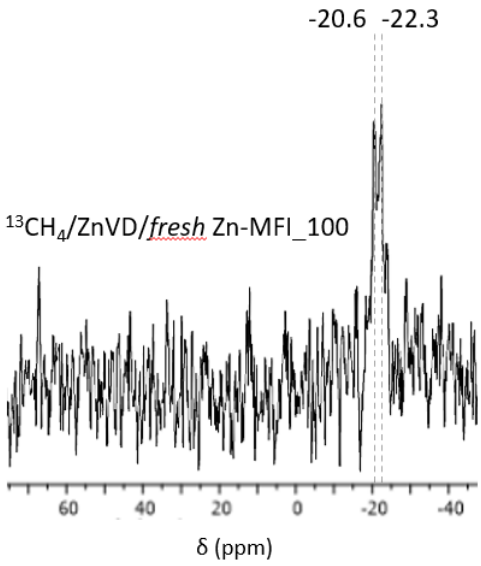

Figure 66: ^{1}H – ^{13}C CP MAS NMR spectrum of $^{13}CH_4$/ZnVD/*fresh* Zn-MFI_100 that shows the presence of a -20 ppm peak, attributable to [Zn^{II}-CH_3] species.

The methane activation reaction was carried out using non-labelled CH_4 over *fresh* Zn-MFI materials with different Si:Zn ratios (50 and 25) following Zn vapour deposition. The ^{13}C MAS NMR analysis was carried out using the same parameters described above and the results obtained are reported in Figure 67, compared to the spectra obtained from the *fresh* ZnVD/Zn-MFI_100 and a ZnVD/ZSM-5 sample (aluminosilicate, Si:Al = 12.5). No detectable signal at -20 ppm was observed; however, three new signals were found at -2.9, 127 and 149 ppm. The peak detected at -2.9 ppm was

assigned to physisorbed methane, interacting with a stronger Zn Lewis acid site.[13] Similar results were observed by Kolyagin et al. for $^{13}CH_4$ activation experiments performed over a ZnVD/ZSM-5 (ammonium form, Si:Al = 40) samples using different methane loadings per unit cell.[13] At the lowest loading level (0.3 molecule/unit cell) they detected the presence of a peak at -3 ppm and interpreted it as a downfield shift of the signal of adsorbed methane on $Zn^{\delta+}$ - $O^{\delta-}$ pairs. In fact, at higher loadings such as 1 molecule/unit cell and 3 molecule/unit cell, the signal shifted to -4.5 ppm and -6.5 ppm, respectively. They attributed the shift to the fact that methane molecules would preferably adsorb onto strongly polarised $Zn^{\delta+}$-$O^{\delta-}$ pairs when only few CH_4 molecules are present. Based on this interpretation, we can conclude that the presence of a -2.9 peak in our samples suggests adsorption of methane on strongly polarised $Zn^{\delta+}$-$O^{\delta-}$ sites. The other two signals observed in the ^{1}H–^{13}C CP spectrum could not be unequivocally identified, however, their chemical shifts appear to be in the characteristic range of alkene and/or aromatic species. Other organo-zinc species reported to be formed by reaction of methane with a Zn-modified zeolite do not show chemical shifts similar to those observed in our experiments.[27]

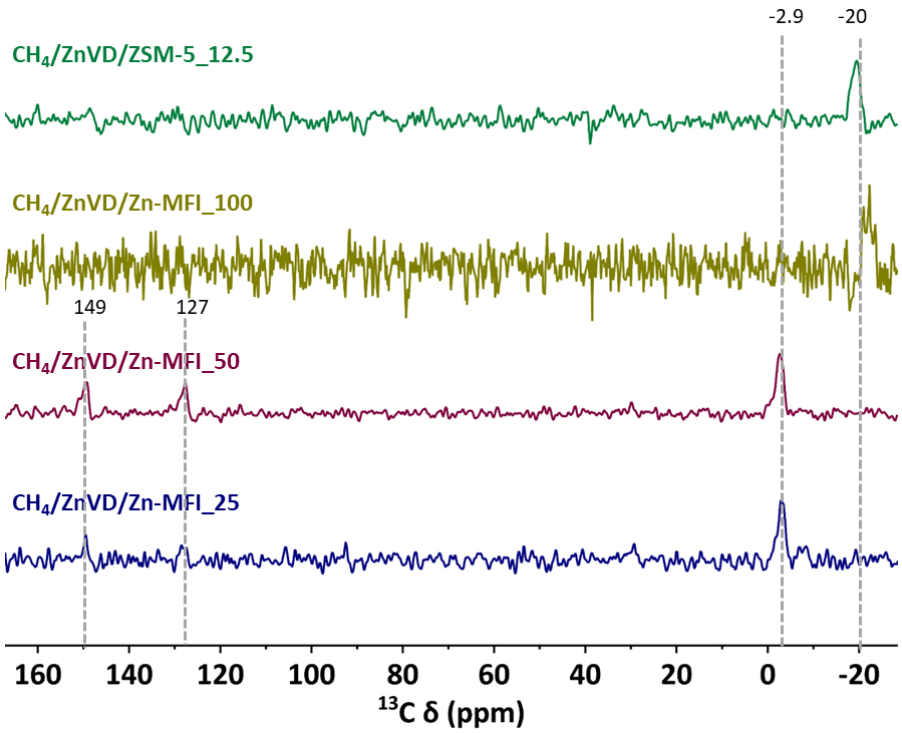

Figure 67: ^{1}H – ^{13}C CP MAS NMR spectra of CH_4/ZnVD/Zn-MFI_25, CH_4/ZnVD/Zn-MFI_50, *fresh* ZnVD/Zn-MFI_100 and ZnVD/ZSM-5_12.5: the first two show a -2.9 ppm peak due to physisorption of CH_4 onto strongly polarised $Zn^{\delta+}$ - $O^{\delta-}$ pairs and high-frequency peaks at 149 and 127 ppm whilst the latter show the -19 ppm peak typical of Zn-CH_3 species.

In order to shed some light on the active species responsible for the formation of products with such high-frequency signals, the same methane activation reaction was carried out using ZnVD/Silicalite-1, ZnO impregnated Silicalite-1 and ZnVD/ZnO impregnated Silicalite-1 samples. The

results obtained from $^{1}H - ^{13}C$ CP MAS NMR analyses are reported in the Appendix. The $^{1}H - ^{13}C$ CP spectrum of the ZnO/Silicalite sample does not show any signals, indicating the absence of reactivity with methane under such reaction conditions. On the other hand, when zinc vapour deposition was carried out on the same Silicalite-1 sample, the products formed upon the reaction with CH_4 were the same as the one observed in Figure 67 for CH_4/ZnVD/Zn-MFI_25 and 50. Slightly different results were obtained from the reaction between CH_4 and a zinc vapour deposited-ZnO impregnated Silicalite-1 sample, with the peak assigned to strongly adsorbed methane showing a downfield shift of 1 ppm.

Further ^{1}H NMR analyses were carried out on the samples after CH_4 activation experiments. The results are shown in Figure 68. The proton spectra of zincosilicate samples and the ZSM-5 (Si:Al=12.5) sample after zinc vapour deposition and methane activation are reported in Figure 68(a). The spectra show the presence of a 0.3 ppm peak, common to all samples, and corresponding to methane molecules adsorbed into the zeotype pores.[18] The peaks observed between 1.5 ppm and 2.2 ppm can be assigned to SiOH protons,[15], [18] which are independent from the interaction with methane. The higher frequency peaks at 7.8 ppm and 8.6 ppm are only observed in the Zn-MFI_25 and Zn-MFI_50 samples, and to a smaller extent in the Zn-MFI_100 sample. The interaction with methane in these samples produced two high frequency signals in the $^{1}H - ^{13}C$ CP MAS NMR spectra (see Figure 67), therefore it is reasonable to assume that the protons giving rise to the higher-frequency signals in the protons belong to these species. Similar features were observed for the ZnVD/Silicalite-1 sample (Figure 68(b)), which also shows the two high frequency peaks in the $^{1}H - ^{13}C$ CP spectrum (Figure 67). These signals, however, are not visible in the ZnO/Silicalite-1 and the ZnVD/ZSM-5 samples, in agreement with the results of the $^{1}H–^{13}C$ CP analyses.

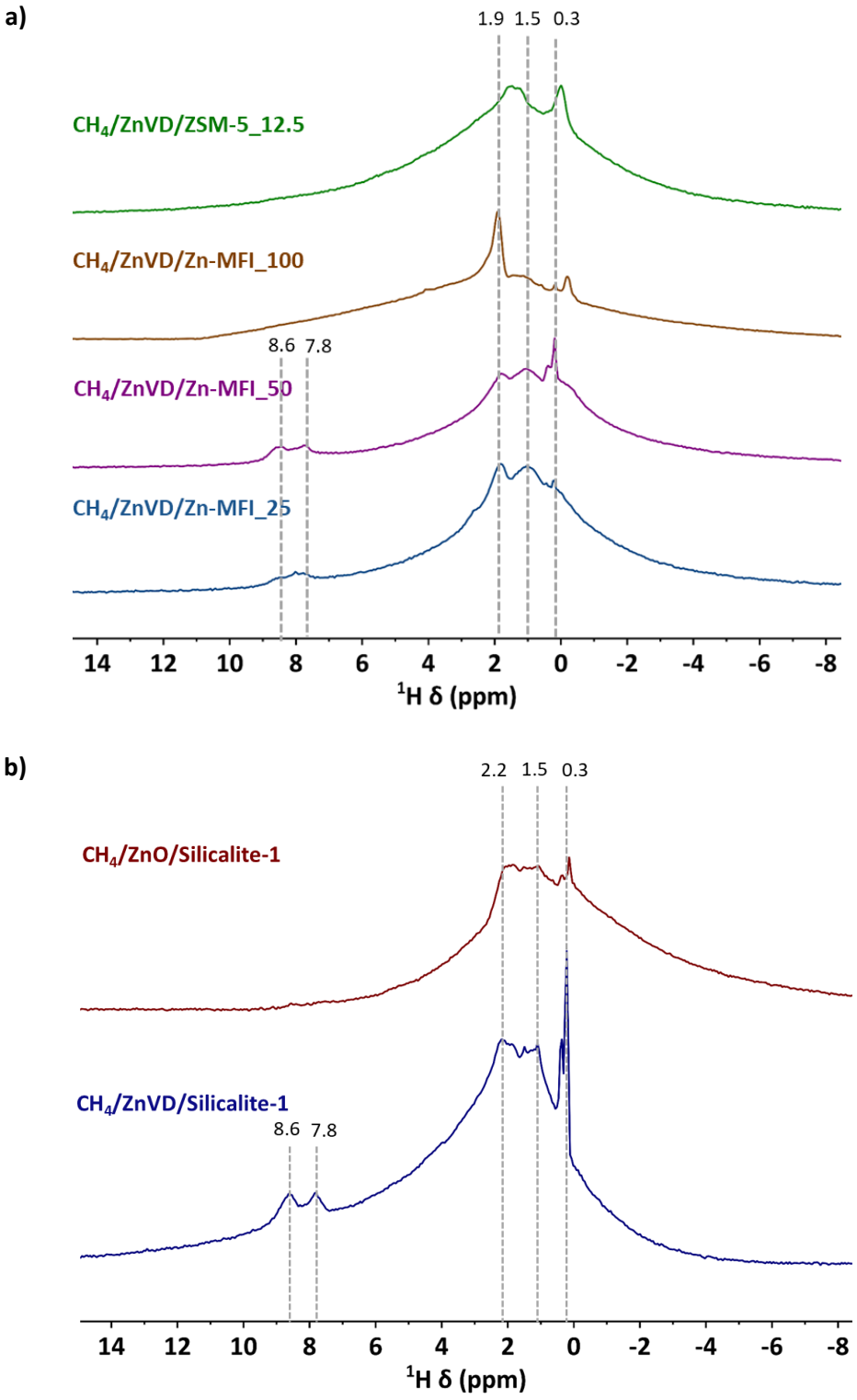

Figure 68: ^{1}H spectra of samples acquired after Zn vapour deposition and methane activation, carried out at 250 °C with 15 minutes of exposure, on zincosilicate and aluminosilicate ZSM-5 samples (a) and ZnVD or ZnO-impregnated Silicalite-1 samples (b).

In order to rule out the possibility that residual SDA molecules trapped in the channels after the calcination step were responsible for the formation of residual organic species, generating the high-frequency peaks in the $^{1}H - {}^{13}C$ CP spectra, TGA and elemental microanalysis (CHN) were carried out on the samples. In Table 20 the results of CHN analysis are reported, which show that no carbon residues could be detected in the samples after calcination at 550 °C. In order to corroborate this observation, TGA analyses were carried out on as made and calcined samples (Silicalite-1 and H^+/Zn-MFI_100) and the results are reported in Figure 69. Figure 69(a) shows the weight loss curves of Silicalite-1 as made and calcined, heated up from room temperature to 800 °C with a ramp rate of 10 °C/min under a N_2 atmosphere. It can be seen that the as made sample exhibits a substantial weight loss (> 10 %) between 350 and 500 °C, related to the decomposition of the SDA. On the other hand, the weight of the calcined sample does not show any remarkable change, except for the loss of water at low temperature. Additionally, at a constant temperature of 550 °C maintained for 10 hours (Figure 69(b)), the as made sample only shows weight loss during the first hour, whilst the weight remains practically constant for the remaining time. Very similar results can be observed for the H^+/Zn-MFI_100 sample (Figure 69(a) and (b)), with significant weight loss only observed when the as made sample was heated up to temperatures > 350 °C. These observations suggest that the calcination step carried out at 550 °C for 5 hours is effective for the removal of SDA species; therefore, it can be concluded that the high-frequency ^{13}C NMR signals at 127 and 149 ppm detected in the samples following the reaction with CH_4 are not attributable to residues from decomposition of theSDA in the materials.

Table 20: Elemental microanalysis (CHN) results Zn-MFI and Silicalite-1 samples in the as made and calcined forms. Typical values of uncertainty affecting the measurements are around 1% of the measured values.

		C (wt%)		***H (wt%)***		***N (wt%)***	
Entry	**Sample**	**As made**	**Calcined**	**As made**	**Calcined**	**As made**	**Calcined**
1	***H^+/Zn-MFI_25***	8.99	0.02	1.99	0.41	0.88	0.22
2	***H^+/Zn-MFI_50***	9.11	0	1.96	0.17	0.88	0
3	***H^+/Zn-MFI_100***	9.20	0	1.99	0.41	0.88	0.25
4	***Silicalite-1***	9.21	0	1.95	0.11	0.88	0

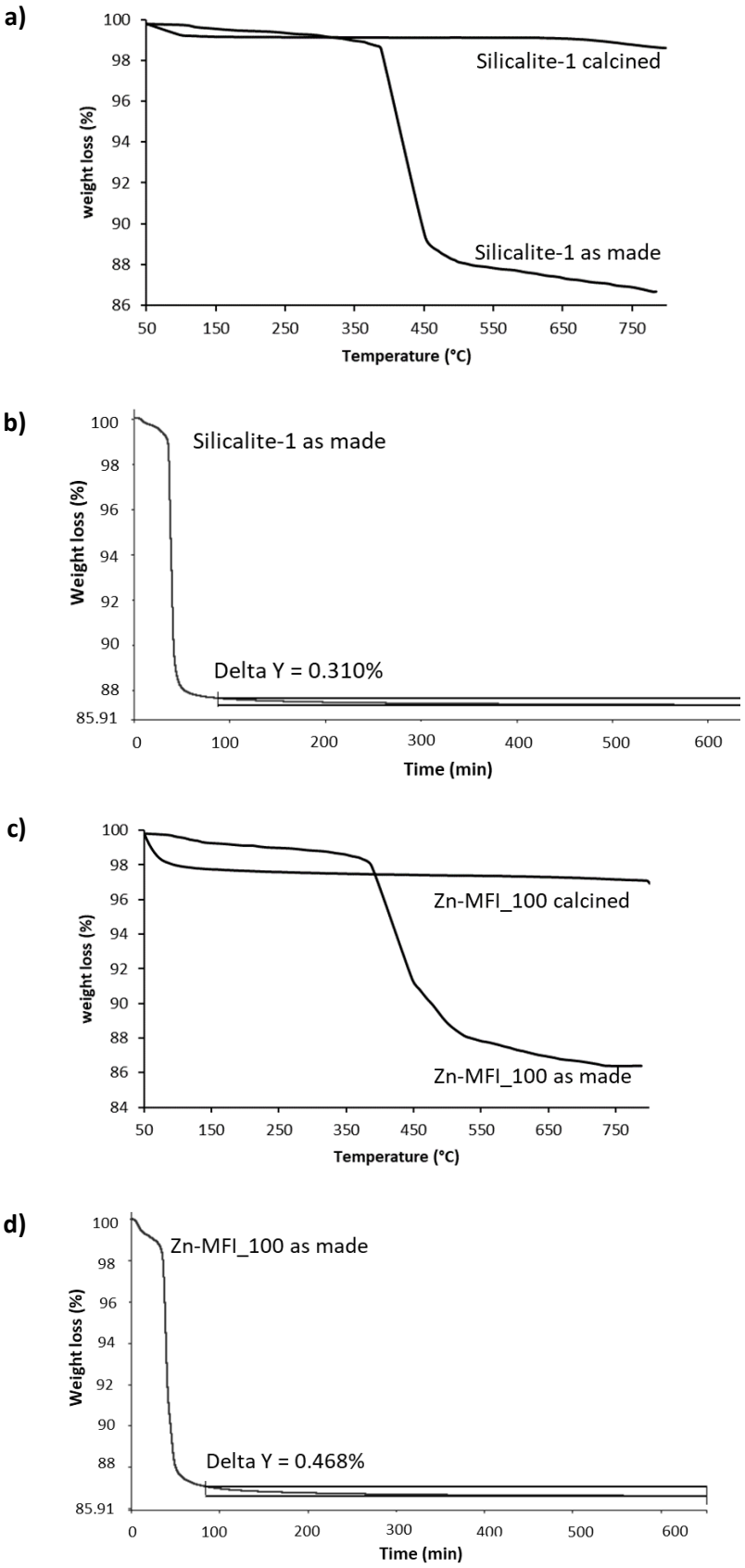

Figure 69: TGA curves obtained between room temperature and 800 °C for Silicalite-1 (a) and Zn-MFI_100 (c); curves that represent the weight loss of the samples at a constant temperature of 550 °C for 10 hours acquired for Silicalite-1 (b) and Zn-MFI_100 (d).

Further attempts to activate methane were carried out over aluminosilicate zeolites ion-exchanged with Ni^{2+} and Cu^{2+} before undergoing Zn vapour deposition. The aim was to generate a bi-metallic active site, however CH_4 activation experiments performed over these materials revealed the same activity of Zn^{2+}/Zeolites, therefore Ni and Cu species were acting as spectators. The results of these experiments are reported in Section 9.4 of the Appendix.

6.2.3. Post-Reaction Characterisation of Samples

The zincosilicate and Silicalite-1 samples used for methane activation reactions were analysed by means of p-XRD and electron microscopy in order to assess the framework integrity after being exposed to high temperature under reduced pressure conditions, zinc-vapour deposited and reacted with CH_4. Powder-XRD analyses were carried out using silicon wafer-topped slides, on which a thin layer of vaseline was applied. The results are reported in Figure 70. In Figure 70(a) the p-XRD patterns obtained from zincosilicate and Silicalite-1 samples after methane activation are shown. The signal-to-noise ratio and therefore the crystallinity of the samples appears to be lower than the one observed for the parent materials; however, the typical features of the MFI framework type can still be clearly recognised, without the appearance of ZnO or Zn^0 features. The low signal-to-noise ratio could also be due to the use of the Vaseline setup for the p-XRD analysis. In order to confirm this, the parent H^+/Zn-MFI_100 and the material after the reaction were analysed through p-XRD using the Vaseline setup and compared (Figure 70(b)). Despite both showing low signal-to-noise ratio due to the use of Vaseline, the loss of crystallinity in the "spent" sample due to the reaction conditions is still noticeable, as the signal-to-noise ratio is lower than in the parent material. The use of Vaseline, and therefore of a very thin layer of sample powder, causes a lower signal to noise ratio due to the smaller amount of sample analysed.

SEM analyses were carried out in order to confirm whether the sample crystals were still intact or if the effects of the loss of crystallinity could be visibly detected. The images acquired are shown in Figure 71. The crystallites do not show any sign of damage; their shape and integrity appear to be the same as those observed in Figure 65 of the parent materials.

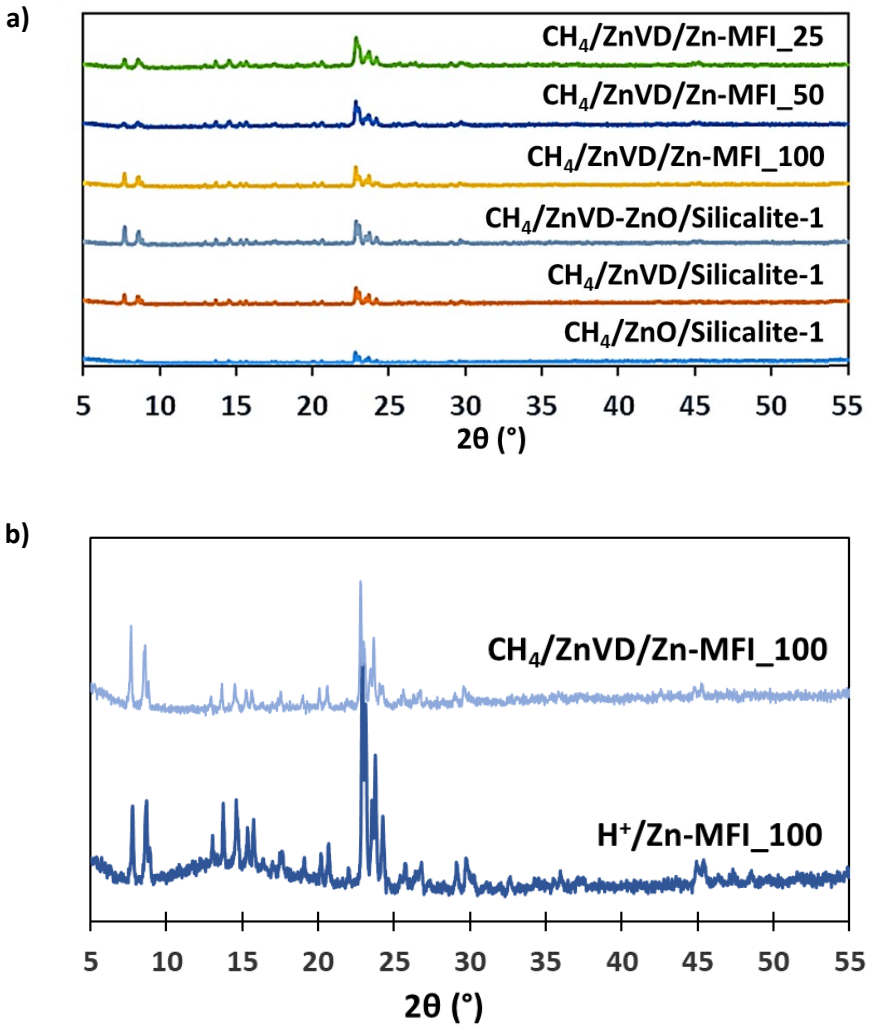

Figure 70: Powder-XRD patterns of spent samples after Zn vapour deposition and methane activation reactions (a); comparison of spent ZnVD/Zn-MFI_100 sample and parent H^+/Zn-MFI_100 (b).

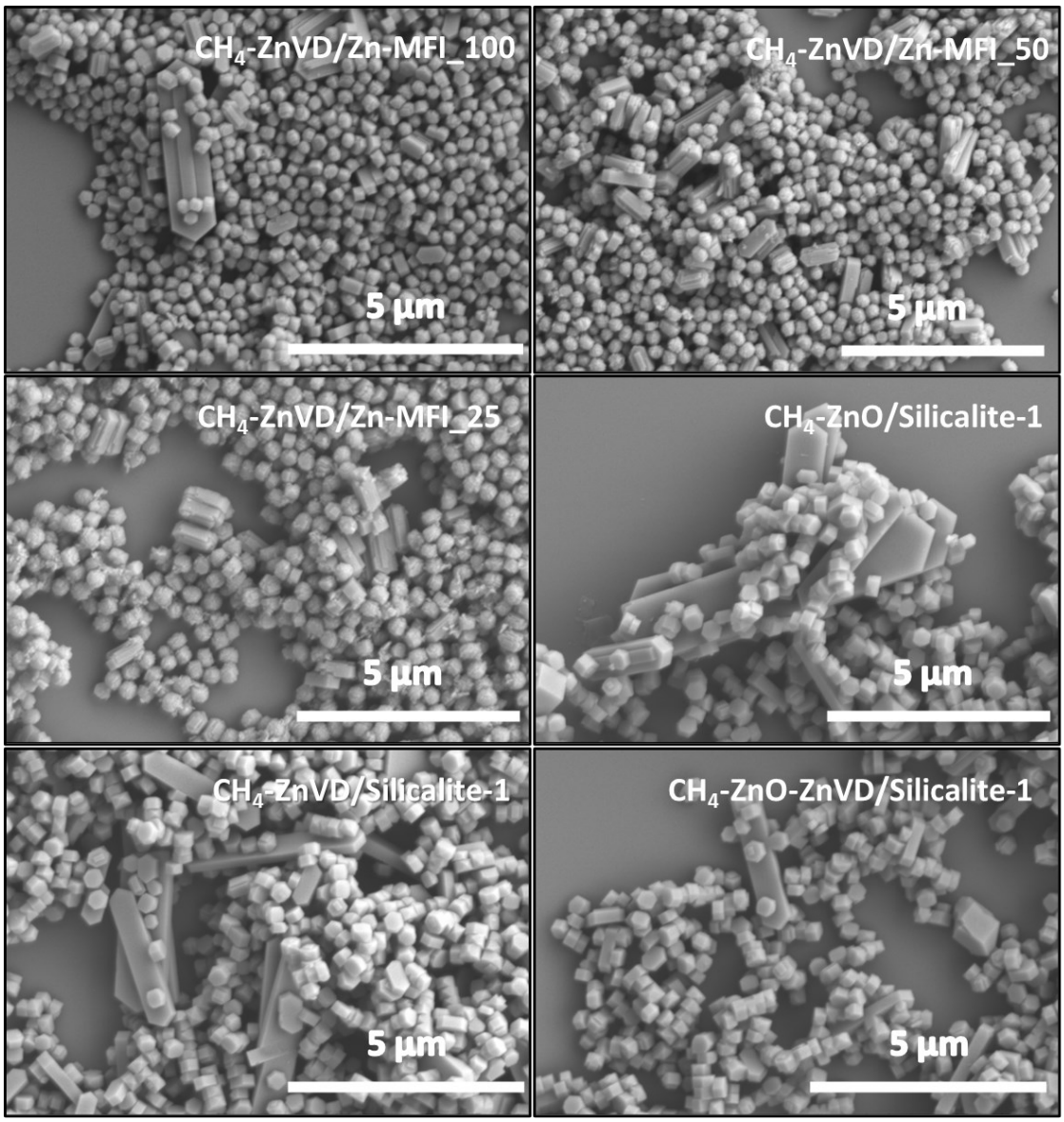

Figure 71 SEM images of Zn-MFI and Silicalite-1 samples after CH_4 activation reactions acquired with a voltage 5 kV.

6.3. Chapter 6 Conclusions

Methane activation reactions were carried out on a series of Zn-MFI samples with a range of Si:Zn ratios: 100, 50 and 25. The reactions were performed on the samples after post-synthetic zinc vapour deposition (ZnVD) using Zn^0 powder, vapourised at 500 °C under reduced pressure, according to an established procedure generally applied to aluminosilicate zeolites.[25] The resulting materials were then exposed to methane at 250 °C and analysed by means of ^{13}C NMR. The results obtained from Zn-MFI samples were compared to ZnO-impregnated Silicalite-1, zinc vapour deposited Silicalite-1, zinc vapour deposited/ZnO impregnated Silicalite-1 and aluminosilicate ZSM-5 samples, in order to understand which Zn species were interacting with methane during the reactions.

The outcome of the experiments revealed that the *fresh* ZnVD/Zn-MFI sample with Si:Zn ratio of 100, used for the reaction only two days after its synthesis, showed a ^{13}C NMR signal at -20 ppm, corresponding to Zn – CH_3 species.[14], [16], [27], [28] However, this result could not be replicated with the same material.

Methane activation reactions carried out under the same reaction conditions using *fresh* Zn-MFI samples with Si:Zn ratios of 50 and 25 resulted in strongly adsorbed methane (- 3 ppm signal), [14] and two high-frequency signals at 149 and 127 ppm, which have not been reported before and whose nature remains unclear. Analogously, the ^{1}H NMR spectra of these samples showed higher-frequency peaks at 7.8 and 8.6 ppm, alongside the 0.3 ppm signal corresponding to adsorbed methane. The experiments were repeated using Silicalite-1 as a support for ZnO, Zn^{2+} introduced through ZnVD and a combination of the two. ^{13}C NMR analyses revealed the absence of peaks for the ZnO-impregnated Silicalite-1 sample after exposure to CH_4. On the other hand, the Silicalite-1 samples that underwent to the ZnVD procedure showed the presence of strongly physisorbed methane (-3 ppm) and of the species producing the high-frequency signals, with ^{13}C NMR spectra very similar to those obtained from Zn-MFI samples with Si:Zn ratios of 50 and 25.

The different reactivity of the zincosilicate samples could be explained considering the different environment around the heteroatoms. The presence of Zn^{II} instead of Al^{III} in tetrahedral framework positions causes profound differences in the chemical properties of the materials. A certain degree of Lewis acidity is introduced in the framework, alongside a change in the strength of the Brønsted acid sites (see Appendix 9.5.1). These factors may cause variations in the strength of the interaction between Zn^{2+} sites and CH_4 molecules, especially at higher Zn loadings. Additionally, the activation of methane would result in the Zn – CH_3 species and a BAS being in very close proximity, which could cause the reverse reaction to take place. This would also explain the presence of physisorbed methane on ZnVD/Silicalite-1, as the reaction of Si – OH groups in the material with Zn^0 at high temperature may lead to the formation of framework Zn species in Silicalite-1.[29] The results obtained confirmed that ZnO species are unreactive towards methane under these experimental conditions, and therefore the activation of the C – H bond of CH_4 takes place over extra-framework Zn^{2+} sites.

Chapter 6 Bibliography

[1] M. Ravi, M. Ranocchiari, and J. A. van Bokhoven, "The Direct Catalytic Oxidation of Methane to Methanol—A Critical Assessment," *Angew. Chemie Int. Ed.*, 56, 52, pp. 16464–16483, **2017**, doi: 10.1002/ANIE.201702550.

[2] E. M. Turan, E. van Steen, and K. P. Möller, "Comparison of mechanisms for the direct, gas phase, partial oxidation of methane to methanol," *Chem. Eng. Sci.*, 241, p. 116718, **2021**, doi: 10.1016/J.CES.2021.116718.

[3] B. Han, Y. Yang, Y. Xu, U. J. Etim, K. Qiao, B. Xu, Z. Yan, "A review of the direct oxidation of methane to methanol," *Chinese J. Catal.*, 37, 8, pp. 1206–1215, **2016**, doi: 10.1016/S1872-2067(15)61097-X.

[4] M. B. Park, E. D. Park, and W. S. Ahn, "Recent progress in direct conversion of methane to methanol over copper-exchanged zeolites," *Front. Chem.*, 7, pp. 1–7, **2019**, doi: 10.3389/FCHEM.2019.00514/BIBTEX.

[5] M. Ravi, V. L. Sushkevich, A. J. Knorpp, M. A. Newton, D. Palagin, A. B. Pinar, M. Ranocchiari, J. A. van Bokhoven "Misconceptions and challenges in methane-to-methanol over transition-metal-exchanged zeolites," *Nat. Catal.*, 2, June, pp. 485–494, **2019**, doi: 10.1038/s41929-019-0273-z.

[6] S. Raynes, M. A. Shah, and R. A. Taylor, "Direct conversion of methane to methanol with zeolites : towards understanding the role framework type," *Dalt. Trans.*, 48, 28, pp. 10364–10384, **2019**, doi: 10.1039/c9dt00922a.

[7] B. E. R. Snyder, M. L. Bols, R. A. Schoonheydt, B. F. Sels, and E. I. Solomon, "Iron and Copper Active Sites in Zeolites and Their Correlation to Metalloenzymes," *Chem. Rev.*, 118, 5, pp. 2718–2768, **2017**, doi: 10.1021/ACS.CHEMREV.7B00344.

[8] M. A. Newton, A. J. Knorpp, V. L. Sushkevich, D. Palagin, and J. A. Van Bokhoven, "Active sites and mechanisms in the direct conversion of methane to methanol using Cu in zeolitic hosts: a critical examination," *Chem. Soc. Rev.*, 49, 5, pp. 1449–1486, **2020**, doi: 10.1039/C7CS00709D.

[9] L. Sun, Y. Wang, C. Wang, Z. Xie, N. Guan, and L. Li, "Water-involved methane-selective catalytic oxidation by dioxygen over copper zeolites," *Chem*, 7, 6, pp. 1557–1568, **2021**, doi: 10.1016/J.CHEMPR.2021.02.026/ATTACHMENT/836D862B-CDB5-4129-9686-A7FA1B391EA2/MMC1.PDF.

[10] A. de Klerk, "Engineering evaluation of direct methane to methanol conversion," *Energy Sci. Eng.*, 3, 1, pp. 60–70, **2015**, doi: 10.1002/ESE3.51.

[11] Z. R. Jovanovic, J. P. Lange, M. Ravi, A. Knorpp, V. L. Sushkevich, M. A. Newton, D. Palagin, J. A. van Bokhoven, "Oxidation of methane to methanol over Cu-exchanged zeolites: Scientia gratia scientiae or paradigm shift in natural gas valorization?," *J. Catal.*, 385, pp. 238–245, **2020**, doi: 10.1016/J.JCAT.2020.02.001.

[12] V. B. Kazansky and A. I. Serykh, "Unusual localization of zinc cations in MFI zeolites modified by different ways of preparation," *Phys. Chem. Chem. Phys.*, 6, 13, pp. 3760–3764, **2004**, doi: 10.1039/B401853B.

[13] Y. G. Kolyagin, I. I. Ivanova, V. V. Ordomsky, A. Gedeon, and Y. A. Pirogov, "Methane Activation over Zn-Modified MFI Zeolite: NMR Evidence for Zn−Methyl Surface Species Formation," *J. Phys. Chem. C*, 112, 50, pp. 20065–20069, **2008**, doi: 10.1021/JP8067766.

[14] Y. G. Kolyagin, I. I. Ivanova, V. V Ordomsky, A. Gedeon, and Y. A. Pirogov, “Methane Activation over Zn-Modified MFI Zeolite : NMR Evidence for Zn - Methyl Surface Species Formation,” *J. Phys. Chem. C*, 112, pp. 20065–20069, **2008**, doi: 10.1021/jp8067766.

[15] A. A. Gabrienko, S. S. Arzumanov, M. V Luzgin, A. G. Stepanov, and V. N. Parmon, “Methane Activation on Zn2+-Exchanged ZSM - 5 Zeolites . The Effect of Molecular Oxygen Addition,” *J. Phys. Chem. C*, 119, p. 24910−24918, **2015**, doi: 10.1021/acs.jpcc.5b08759.

[16] Y. G. Kolyagin, I. I. Ivanova, and Y. A. Pirogov, “1H and 13C MAS NMR studies of light alkanes activation over MFI zeolite modified by Zn vapour,” *Solid State Nucl. Magn. Reson.*, 35, 2, pp. 104–112, **2009**, doi: 10.1016/J.SSNMR.2009.01.005.

[17] E. A. P. and and R. A. van Santen, “Activation of Light Alkanes over Zinc Species Stabilized in ZSM-5 Zeolite: A Comprehensive DFT Study,” *J. Phys. Chem. C*, 111, 6, pp. 2643–2655, **2007**, doi: 10.1021/JP065911V.

[18] M. V. Luzgin, D. Freude, J. Haase, and A. G. Stepanov, “Methane interaction with Zn2+-exchanged zeolite H-ZSM-5: Study of adsorption and mobility by one- and two-dimensional variable-temperature 1H solid-state NMR,” *J. Phys. Chem. C*, 119, 25, pp. 14255–14261, **2015**, doi: 10.1021/acs.jpcc.5b04028.

[19] V. B. Kazansky, V. Y. Borovkov, A. I. Serikh, R. A. van Santen, and B. G. Anderson, “Nature of the sites of dissociative adsorption of dihydrogen and light paraffins in ZnHZSM-5 zeolite prepared by incipient wetness impregnation,” *Catal. Lett. 2000 661*, 66, 1, pp. 39–47, **2000**, doi: 10.1023/A:1019031119325.

[20] S. M. T. Almutairi, B. Mezari, P. C. M. M. Magusin, E. A. Pidko, and E. J. M. Hensen, “Structure and Reactivity of Zn-Modified ZSM-5 Zeolites: The Importance of Clustered Cationic Zn Complexes,” *ACS Catal.*, 2, 1, pp. 71–83, **2011**, doi: 10.1021/CS200441E.

[21] N. Koike, W. Chaikittisilp, K. Iyoki, Y. Yanaba, T. Yoshikawa, S. P. Elangovan, K. Itabashi, T. Okubo “Organic-free synthesis of zincoaluminosilicate zeolites from homogeneous gels prepared by a co-precipitation method,” *Dalt. Trans.*, 46, 33, pp. 10837–10846, **2017**, doi: 10.1039/c7dt02001e.

[22] N. Koike, K. Iyoki, S. H. Keoh, W. Chaikittisilp, and T. Okubo, “Synthesis of New Microporous Zincosilicates with CHA Zeolite Topology as Efficient Platforms for Ion-Exchange of Divalent Cations,” *Chem. - A Eur. J.*, 24, 4, pp. 808–812, **2018**, doi: 10.1002/chem.201705277.

[23] N. Koike, K. Iyoki, B. Wang, Y. Yanaba, S. P. Elangovan, K. Itabashi, W. Chaikittisilp, T. Okubo “Increasing the ion-exchange capacity of MFI zeolites by introducing Zn to aluminosilicate frameworks,” *Dalt. Trans.*, 47, 28, pp. 9546–9553, **2018**, doi: 10.1039/C8DT01391H.

[24] M. A. Deimund, J. Labinger, and M. E. Davis, “Nickel-exchanged zincosilicate catalysts for the oligomerization of propylene,” *ACS Catal.*, 4, 11, pp. 4189–4195, **2014**, doi: 10.1021/cs501313z.

[25] M. A. Shah, S. Raynes, D. C. Apperley, and R. A. Taylor, “Framework Effects on Activation and Functionalisation of Methane in Zinc-Exchanged Zeolites,” *ChemPhysChem*, 21, pp. 673–679, **2020**, doi: 10.1002/cphc.201900973.

[26] Elmar Hecht, “Über chirale Methylzinkaminoalkoxide,” *Zeitschrift fur Anorg. und Allg. Chemie*, 626, pp. 2223–2227, **2000**, doi: 10.1002/1521-3749.

[27] J. F. Wu, W. D. Wang, J. Xu, F. Deng, and W. Wei, “Reactivity of C 1 Surface Species Formed in Methane Activation on Zn-Modified H-ZSM-5 Zeolite,” *Chem. - A Eur. J.*, 16, pp. 14016–14025, **2010**, doi: 10.1002/chem.201002258.

[28] A. G. Stepanov, S. S. Arzumanov, A. A. Gabrienko, V. N. Parmon, I. I. Ivanova, and D. Freude,

"Significant Influence of Zn on Activation of the C-H Bonds of Small Alkanes by Brønsted Acid Sites of Zeolite **," *ChemPhysChem*, 9, pp. 2559–2563, **2008**, doi: 10.1002/cphc.200800569.

[29] D. Zhao, X. Tian, D. E. Doronkin, S. Han, V. A. Kondratenko, J. D. Grunwaldt, A. Perechodjuk, T. H. Vuong, J. Rabeah, R. Eckelt, U. Rodemerck, D. Linke, G. Jiang, H. Jiao, E. V. Kondratenko "In situ formation of ZnOx species for efficient propane dehydrogenation," *Nat. 2021 5997884*, 599, 7884, pp. 234–238, **2021**, doi: 10.1038/s41586-021-03923-3.

7. Chapter 7: Lewis Acid-catalysed Reactions over Zn-substituted Zeotypes

7.1. Introduction to Lewis Acid-catalysed Reactions

The potential of Lewis-acidic zeolites in catalysis was discovered with the introduction of titanosilicate MFI zeotype (TS-1) in 1983, which was observed to be highly efficient in activating peroxide species, thanks to the Lewis acidity of the Ti framework sites.[1] One important application that benefits from the properties of this material is the oxidation of propylene with hydrogen peroxide to produce propylene oxide, already used in industrial plants.[2] Since the 1980s, several other metals have been studied as Lewis-acid species in zeolite catalysts, such as Sn, Zr, Hf and Nb.[3]–[5] Zeolite and zeotype materials prepared using these species have been shown to be promising catalysts for oxidations,[6]–[8] isomerisations,[6], [9]–[12] dehydrations,[13], [14] aldol condensations,[15] and Diels-Alder[16] reactions (among others) of biomass-derived substrates.

Zinc-substituted zeotypes started to be considered as promising catalysts during the early 2000s thanks to the work on zincosilicate MFI carried out by Kowalak et al.[17], [18]; however, it is only during recent years that the interest in this class of catalysts has been increasing. Orazov and Davis selected a series of reactions (glucose isomerisation, Meerwein-Ponndorf-Verley-Oppenauer (MPVO) and Diels-Alder cycloaddition-dehydration) and reported the performance of zincosilicate zeotypes such as CIT-6 (BEA), VPI-8 (VET), Zn ZSM-5 (MFI) and the mesoporous Zn-MCM-41 for these reactions, and compared them to aluminosilicate or zinco-aluminosilicate analogues.[19] Their results showed that CIT-6 was the most active and adaptable catalyst, thanks to strong interactions between reactant molecules and zinc Lewis acid sites at low temperature and the stabilisation effect provided by the BEA framework.[19] Yan et al. studied the potential of Zn MWW catalysts for ethanol conversion to butadiene, for which the zincosilicate catalyst showed the highest selectivity (40 %), compared to ZnO-impregnated aluminosilicate (18 %) and pure-silica (22 %) counterparts, and the lowest production of ethylene.[20] Given the Lewis-acidic nature of framework zinc species, and considering that counter-balancing protons are only weak Brønsted acids, product selectivity is often very different than that obtained from strong Brønsted acid sites in zeolites.[20]

A remarkable advantage of metal-substituted zeotypes used as Lewis-acid catalysts is the possibility of tuning the catalysts for specific applications by selecting the types of metals to be substituted in the framework.[19], [21], [22] This opens the possibility of designing and preparing highly-performing catalysts and even bifunctional materials. An example of the latter was recently provided by Qi et al. with the preparation of a Zn-Y BEA zeotype by post-synthetic metal insertion in de-aluminated BEA. The catalyst allowed for the direct conversion of ethanol to butadiene, with the Zn sites being responsible of the dehydrogenation of ethanol to acetaldehyde, and the consequent conversion to butadiene taking place on Y sites.[23] De-aluminated BEA was also employed by Dou et al. for the preparation of a Zn-Cu BEA bifunctional catalysts by mechanical grinding. The materials were

then applied to the de-polymerisation of lignin to liquid fuels, showing a remarkable yield of 81 % petroleum ether, the highest reported for this application.[24], [25]

7.2. Results and Discussion

A series of zincosilicate and other heteroatom-substituted zeotypes with the MFI framework type were prepared according to the TEOS-synthesis method using $Zn(NO_3)_2$ as Zn precursorand used as Lewis-acid catalysts in different chemical reactions. The reactions considered were (i) the epoxidation of 1-hexene to 1-epoxyhexane using H_2O_2 as oxidising agent (Scheme 5(a)), (ii) the Prins condensation reaction of β-pinene and paraformaldehyde to obtain Nopol® (Scheme 5(b)), and (iii) the dehydrogenation of ethanol to acetaldehyde (Scheme 5(c)). While the first two were carried out as batch reactions, with analysis of the products performed by GC-MS, the latter was carried out in a flow reactor (HEL FlowCat) with on-line GC-MS analysis.

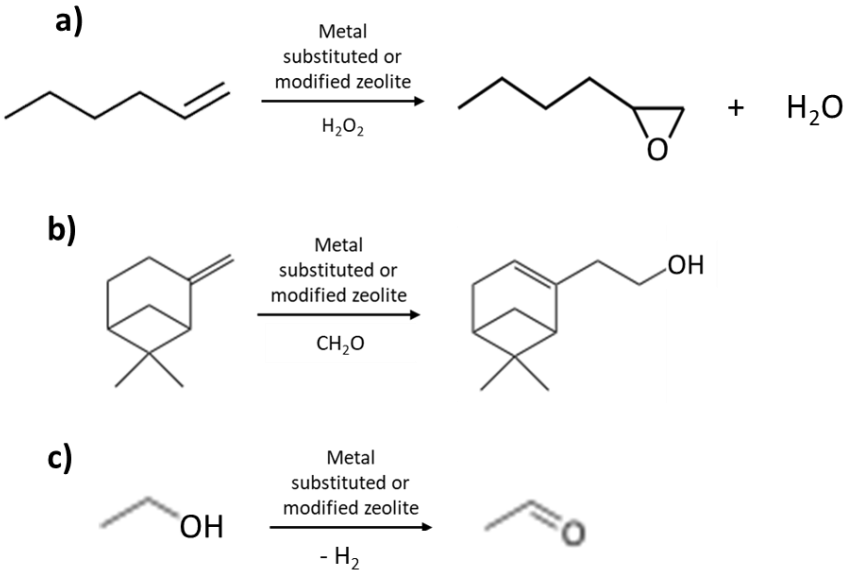

Scheme 5: Reactions carried out over zincosilicate zeotypes presented in this Chapter; epoxidation of 1-hexene to 1-epoxyhexane (a), Prins condensation of β-pinene and paraformaldehyde to nopol (b) and dehydrogenation of ethanol to acetaldehyde (c).

7.2.1. Epoxidation Reactions over Lewis-acid Heterogeneous Catalysts

The epoxidation of alkenes is a crucial step in the process of functionalisation of hydrocarbons, with H_2O_2-based epoxidation being the "cleanest" way to perform this reaction.[29] To date, Ti-containing microporous (or mesoporous) and even amorphous catalysts are the most efficient heterogeneous materials for the epoxidation of alkenes.[30] The reason for this is the ability of the Ti sites to activate hydrogen peroxide species, which become the active oxidants in the reaction.[29], [31] The final step of the reaction mechanism proposed by Clerici and Ingallina involves the formation of a

five-member-ring transition state between the solvent, H_2O_2 and framework Ti species.[32] The usual description of the TS-1 active site and mechanism has been recently challenged by Copéret et al. who suggested that the TS-1 catalyst actually contains non-isolated dinuclear Ti sites.[37] TS-1 is undoubtedly the most studied system for this application; however, due to the limited size of its pore openings (10 MR, 0.51 x 0.55 nm), its performances in the epoxidation of bulky or branched alkenes are poor.[33] For this reason, other Ti-substituted systems have been studied, such as Ti-BEA, Ti-MOR and Ti-MWW.[34] Sastre and Corma have demonstrated that Ti-BEA may be a more optimal epoxidation catalyst thanks to the higher Lewis acidity of its Ti sites, which is related to the position of the Ti sites and the geometry of the Ti – O – Si angles.[35] Recently, a bifunctional Ti-Sn BEA catalyst has been prepared for the direct conversion of alkenes to diols, with the Ti sites catalysing the epoxidation step of the reaction and the Sn sites being responsible for the epoxide hydration to form the diol.[36]

The design and synthesis of new, optimised microporous epoxidation catalysts is limited by the scarce literature about alternative metal-substituted zeotypes and their perfomance in epoxidation reactions, compared to titanosilicate zeotypes.[38] Bregante and Flaherty have conducted a series of experiments using group IV and V metal-substituted BEA zeotypes, showing that the catalytic activity of the materials in the epoxidation of cyclohexene with H_2O_2 improved with increasing Lewis acidity of the metals.[38] Other supported transition metals have been tested as epoxidation catalysts. A series of zeolite frameworks ion-exchanged with Mn^{II}, were tested for the epoxidation of styrene with H_2O_2 in the presence of a sodium hydrocarbonate buffer.[39] The buffer was suggested to play a major role in the reaction mechanism by reactiong with hydrogen peroxide to form proxymonocarbonate. Ni^{II} has also been also considered as an active species, for example as a Ni^{II}-complex supported on a MCM-41 catalyst and used for the epoxidation of olefins using tert-BuOOH[40] or directly as framework Ni^{II} species, as in the case of the nanoporous nickel phosphate VSB-5, used for the epoxidation of cyclic olefins with H_2O_2.[41] However, the reaction mechanisms involving this kind of active species are still uncertain and under debate.

Zn heteroatoms have not received much attention for this kind of application, however they show good potential for other Lewis-acid catalysed reactions. To the best of our knowledge, the only example of epoxidation carried out with a framework Zn^{II} species was given for a ZIF-8 sample, which was successfully used for the epoxidation of menadione with hydrogen peroxide.[42] However, the authors do not provide any information regarding the reaction mechanism or the role of the Zn^{II} species. In order to explore the potential of zincosilicates for this application, part of this work was dedicated to finding suitable reaction conditions for Zn-modified zeolites or Zn-substituted zeotypes to be able to catalyse the epoxidation of 1-hexene, using H_2O_2 as the oxidising species.

7.2.1.1. Epoxidation of 1-hexene to 1-epoxyhexane over Zn-substituted/modified Zeolites

The epoxidation reactions involving 1-hexene and hydrogen peroxide were carried out in a round bottom flask using methanol as a solvent and analysing the reaction products by GC-MS. Different catalysts, listed in Table 21**,** were screened for this reaction, which underwent various post-synthetic treatments. Silicalite-1 was prepared using the TEOS-based synthesis without the addition of heteroatoms, whilst TS-1 and H^+/Ni-MFI were prepared according to the procedure described in Section 4.2.1.1 and used after calcination at 550 °C for 6 hours. K^+/Zn-MFI and H^+/Zn-MFI were prepared using the TEOS-based synthesis with and without the addition of KOH, respectively, and calcined. K^+/Zn-MFI was prepared with a TPA:K ratio of 3. Zn^{2+}/ZSM-5 was the result of the ion-exchange of a commercial NH_4^+/ZSM-5 zeolite (Si:Al = 12.5) with $Zn(NO_3)_2$

Table 21: Elemental analysis results obtained from XRF characterisation of samples used for 1-hexene epoxidation reactions. The uncertainty on the measurements is the 6% of the values (only reported for Si:T and M:T ratios).

Entry	***Name***	***M[a] and T[b] content (wt %)***	***Si:T***	***M:T***
1	***Silicalite-1***	-	-	-
2	***TS-1***	0.8 (Ti)	84.2 ± 5.1 (Si:Ti)	-
3	***K^+/Zn-MFI_TPA:K=3***	2.3 (K); 1.4 (Zn)	86.7 ± 5.2 (Si:Zn)	2.8 ± 0.2 (K:Zn)
4	***Zn^{2+}/ZSM-5***	3.9 (Zn); 3.7 (Al)	10.0 ± 0.6 (Si:Al)	0.4 ± 0.02 (Zn:Al)
5	***H^+/Zn-MFI_TPA:K=∞***	0.8 (Zn)	82.0 ± 4.9 (SiZn)	-
6	***H^+/Ni-MFI***	0.6 (Ni)	162.4 ± 9.7 (Si:Ni)	-

[a] M = Zn or K
[b] T = Al, Zn or Ti

The outcome of the reactions is reported in Figure 72 as the selectivity to 1-epoxyhexane (%), obtained using the calibration curve reported in Section 9.7 of the Appendix. It is immediately noticeable that the TS-1 catalyst shows superior properties (90 % selectivity to the target product) compared to the other catalysts tested. Among the latter, the only active materials were the K^+-containing Zn-MFI catalyst and, to a slightly greater extent, the H^+/Zn-MFI catalyst. This suggests that Zn^{II} species incorporated in the framework of a zeotype can act as active species for epoxidation reactions. This conclusion is supported by the fact that no products were observed during control experiments carried out without the use of a catalyst. On the other hand, the experiments revealed that Zn^{2+} extra-framework species are not able to activate the epoxidation of 1-hexene under the same reaction conditions.

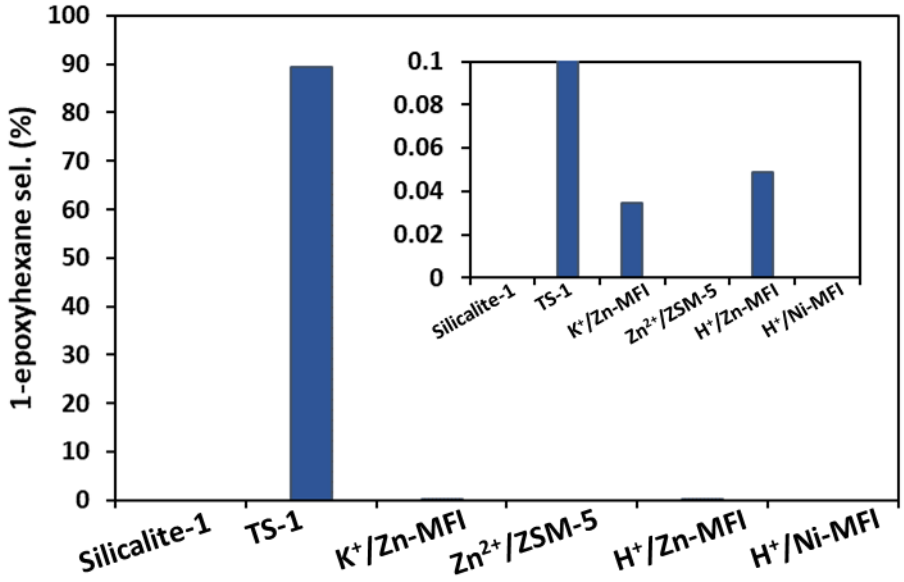

Figure 72: Results from 1-hexene epoxidation reactions represented in terms of 1-epoxyhexane selectivity. The experiments were performed only once, therefore the uncertainty on the values could not be evaluated.

7.2.2. Prins Condensation Reactions over Lewis-acid Heterogeneous Catalysts

The Prins reaction was described for the first time in 1919 by H. J. Prins[43] and it refers to the acid catalysed process of addition of formaldehyde to olefins. Currently, the industrial processes that involve Prins reactions use homogeneous catalysts (such as sulfuric acid, acetic acid, $ZnCl_2$, $SnCl_4$ or other aprotic Lewis acids), which bring major disadvantages related to reusability, wastewater production, low selectivity and difficult purification of the products.[44] These issues could be resolved by switching to heterogeneous catalysts. Zeolites are among the solid catalysts that have been considered for this application[45]–[49] and it was observed that the products of the Prins reaction depended on the zeolite topology. Vasiliadou et al. used H^+/ZSM-5 catalysts for the condensation of isobutene with formaldehyde and showed that tuning the acidity and the reaction conditions would enable to increase the selectivity of the desired product (isoprene) as opposed to 3-methyl-3-buten-1-ol (3MBO).[50] The same reaction was carried out by Bedenko et al., who demonstrated that changing the nature of the acid sites of the catalysts (from Brønsted to Lewis by ion-exchanging the zeolites with Mg^{2+}) would cause a substantial change in the product distribution for zeolites with the BEA topology, with isoprene being the primary product in H^+/BEA (47.7 % selectivity) and 3MBO being the main product in Mg^{2+}/BEA (36.9 % selectivity). The authors also observed that a change in Brønsted/Lewis acidity did not affect the product distribution for catalysts with the MFI topology (approx. 97 % selectivity to 3MBO). This was attributed to strong topology- and channel size-related effects in the MFI framework.[51]

Another relevant Prins reaction is the addition of formaldehyde to β-pinene to produce nopol.[52] An issue related to the use of zeolites for this application is the undesired production of β-pinene isomers instead of the desired product in the presence of Brønsted acid sites.[53] It was demonstrated that the use of ion-exchanged or impregnated zeolites or heteroatom-substituted zeotypes, and therefore the presence of Lewis acidity and a substantial reduction of Brønsted acidity, would increase the selectivity of the target product.[27], [44], [53]–[57] Marakatti et al. studied the performance of Zn and other metal-exchanged zeolites with different topologies (BEA, MFI, MOR, Y and X) for the β-pinene/paraformaldehyde Prins reaction and they reported the highest activity and selectivity to nopol for Zn^{2+}/BEA, Zn^{2+}/X and Zn^{2+}/Y due to the presence of large pores. Generally, materials with low Brønsted/Lewis acid ratios showed good performance in their study.[27]

The use of zeotype catalysts for the Prins reaction in which Lewis acidity is provided by isomorphous substitution has only been reported for Sn[55] and Zr-substituted[56] zeotypes and Zn-substituted mesoporous Zn-Al MCM-41.[52] However, as shown by Marakatti et al., Zn-exchanged zeolites were also able to promote the condensation between β-pinene and paraformaldehyde and deliver nopol with high selectivity. The reaction mechanism (Scheme 6) proposed by the authors explains the interaction between β-pinene and paraformaldehyde with the Lewis acidic nature of the Zn^{2+} species interacting with the lone pair on the O atom of the carbonyl groups. The subsequent polarisaiton of the C=O bond of paraformaldehyde allows for an attack by β-pinene on the electrophilic centre. The final proton transfer on the oxygen and formation of a double bond produces nopol.[27] The use of a Zn-substituted rather than a Zn-exchanged catalyst could potentially bring advantages in terms of stability and preventing leaching of the metal species. Therefore, part of this work was dedicated to β-pinene/paraformaldehyde condensation reactions carried out on Zn-ZSM-5 catalysts and the study of their performance.

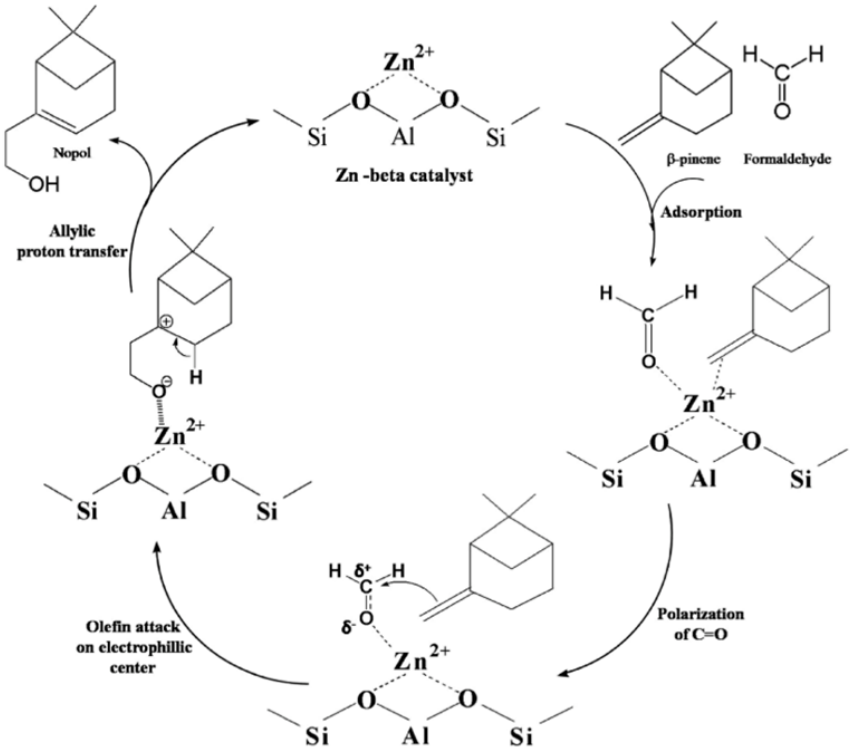

Scheme 6: Reaction mechanism proposed for the Prins condensation reaction between β-pinene and paraformaldehyde over a Zn^{2+}-exchanged zeolite to form nopol. Adapted with permission from ref [27].

7.2.2.1. β-pinene/paraformaldehyde Condensation to Nopol over Zn-substituted Zeotypes

The Prins condensation reactions were carried out in a batch reactor (round bottom flask) equipped with a condenser and placed in an oil bath on a hotplate stirrer. The reaction conditions were adapted from Marakatti et al.,[47] as described in the experimental details section. B-pinene and paraformaldehyde were added to the solvent (acetonitrile) and the reaction was stirred at 90 °C for 6 hours. The products were analysed by GC-MS. The reaction was carried out using K^+/Zn-MFI and H^+-K^+/Zn-MFI catalysts, compared to a Zn^{2+}-Cu^{2+}/ZSM-5 catalyst, prepared *via* ion exchange of the parent ZSM-5 zeolite using a 0.3 M solution of $Zn(NO_3)_2$ and $Cu(NO_3)_2$. The samples used and their elemental compositions before and after the reactions are listed in Table 22. From the results obtained it appears that the reaction conditions did not affect the composition of the catalysts, except for the K^+/Zn-MFI catalyst (Table 22, entry 1) which shows a decrease in the K^+ content in the spent sample. The same behaviour, however to a considerably lower extent, can be also observed for the H^+-K^+/Zn-MFI catalyst (Table 22, entry 2). The crystallinity of the samples after the reactions was checked as well by means of pXRD analysis, and the results are shown in Figure 73. The catalysts appear crystalline and they show the characteristic features of the MFI framework type.

Table 22: Catalysts used and their elemental composition obtained by XRF analysis. The uncertainty on the measurements is the 6% of the values (only reported for Si:T and M:T ratios).

Entry	Name		M[a] and T[b] content (wt %)	Si:T	M:T
1	K^+/Zn-MFI	***Parent***	2.4 (K); 1.7 (Zn)	73.6 ± 4.4 (Si:Zn)	2.4 ± 0.1 (K:Zn)
		Spent	0.8 (K); 1.3 (Zn)	85.5 ± 5.1 (Si:Zn)	1.0 ± 0.1 (K:Zn)
2	H^+-K^+/Zn-MFI	***Parent***	0.2 (K); 1.3 (Zn)	94.7 ± 5.7 (Si:Zn)	0.3 ± 0.02 (K:Zn)
		Spent	0.12 (K); 1.5 (Zn)	85.7 ± 5.1 (Si:Zn)	0.1 ± 0.01 (K:Zn)
3	Zn^{2+}-Cu^{2+}/ZSM-5	***Parent***	3.1 (Zn); 0.7 (Cu); 3.0 (Al)	11.0 ± 0.7 (Si:Al)	0.4 ± 0.02 (Zn:Al) 0.1 ± 0.01 (Cu:Al)
		Spent	3.5 (Zn); 0.8 (Cu); 4.0 (Al)	10.2 ± 0.6 (Si:Al)	0.4 ± 0.02 (Zn:Al) 0.1 ± 0.01 (Cu:Al)

[a] M = Zn, K or Cu
[b] T = Al or Zn

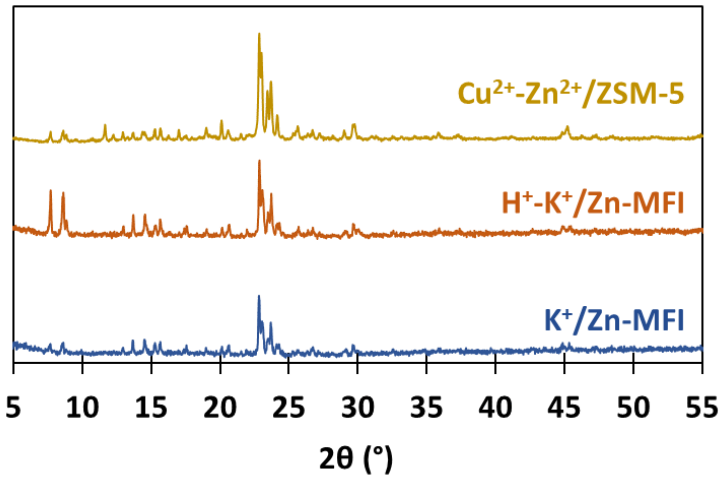

Figure 73: P-XRD patterns of the spent catalysts applied in Prins condensation reactions.

The outcome of Prins condensation reactions is reported in Figure 74. The results are reported as peak area values obtained by MS analysis, as the system was not calibrated. The selectivity to nopol was low for all the catalysts tested, with values of 0.27 % for K^+/Zn-MFI, 0.23 % for H^+-K^+/Zn-MFI and 1.01 % for Zn^{2+}-Cu^{2+}/ZSM-5. The reactions also produced a range of cyclic species (see Section 9.8 of the Appendix for full MS traces), including isomers of β-pinene, especially when H^+-K^+/Zn-MFI and Zn^{2+}-

Cu^{2+}/ZSM-5 were used. The highest nopol selectivity was observed with the Zn^{2+}-Cu^{2+}/ZSM-5 catalyst, probably due to a combination of Brønsted acidity provided by the zeolite framework and the presence of Zn^{2+} ad Cu^{2+} extra-framework cations. The outcome of the reactions could be explained considering the features of the MFI-type framework: the openings of the 10-MR channels have a width of approximately 0.55 nm. This size is probably too small to ensure high selectivity to nopol. A highly efficient condensation of β-pinene to nopol could potentially be obtained using frameworks with wider channels or mesoporous materials, such as Zn-Al MCM-41, which was recently reported to deliver 100% selectivity to nopol with 83.8 % conversion thanks to its mesoporous nature. [44], [52]

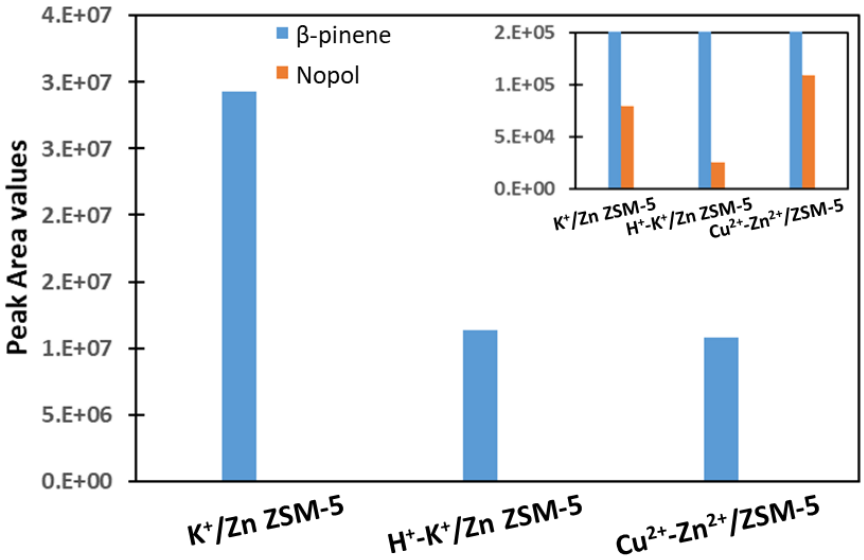

Figure 74: Results of Prins condensation reactions carried out over zeolite and zincosilicate samples as peak area values of β-pinene and nopol, obtained from GC-MS analysis. The experiments were performed only once, therefore the uncertainty on the values could not be evaluated.

7.2.3. Ethanol Conversion Reactions over Lewis-acid Heterogeneous Catalysts

Biomass-derived ethanol, or bio-ethanol, is an attractive feedstock option for the production of commodity chemicals because it can be easily converted to widely used basic chemicals such as ethylene, acetaldehyde, butenes and n-butanol. Moreover, it is available in large quantities at reasonable prices and therefore represents a sustainable feedstock for the chemical industry.[58], [59] Some of the most relevant products obtainable from ethanol are represented in Scheme 7.

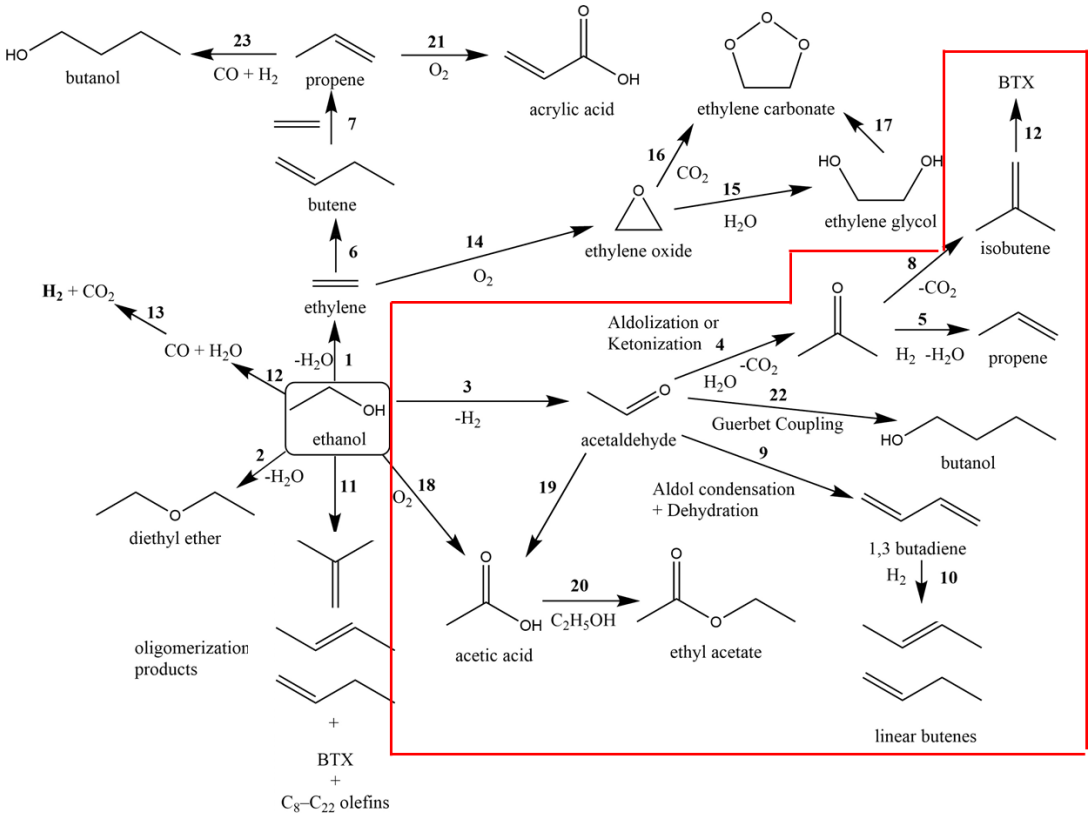

Scheme 7: Representation of upgraded chemicals obtainable from ethanol through different reaction mechanism. The highlighted area shows products of interest that can be obtained from the dehydrogenation of ethanol to form acetaldehyde. Adapted with permission from ref [59].

Brønsted acid zeolites and γ-Al_2O_3 are among the most efficient catalysts for ethanol dehydration to ethylene,[60] an important starting material for the fabrication of several products, such as polyethylene-based products.[58] Zeolites provide the advantage of being more selective thanks to their structural and chemical properties, and can convert ethanol to ethylene even at temperatures < 200 °C.[61] Generally, the product distribution obtained from ethanol conversion over zeolites depends on the acidity of the framework (Si/Al ratio, modifications of the zeolite) and on the reaction conditions (mainly temperature).[62] Higher reaction temperatures are particularly useful to form longer chain hydrocarbons from ethylene with Brønsted acid zeolites. The products obtained are usually ethylene, C_3-C_4 olefins and higher C_{5+} hydrocarbons. However, these conditions also lead to quick coking and catalyst deactivation.[58]

One industrially relevant process based on ethanol feedstock is the conversion to acetaldehyde, a versatile starting material for the fabrication of other commodity products (see highlighted area in Scheme 7). The dehydrogenation of ethanol to acetaldehyde can take place in oxidative and non-oxidative conditions, with the latter having the advantage of co-producing hydrogen as well.[63] Metal-modified zeolite catalysts exhibit high efficiency in terms of selectivity and conversion for this process; remarkable results were recently obtained with Cu-modified silicalite-1,[64] ZnO-impregnated MOR zeolites,[28] and Zn-grafted onto de-aluminated BEA

zeolite.[65] The latter is of great importance for the present work, as it represents one of the few examples of the ability of isomorphously substituted Zn to catalyse this reaction, following the reaction mechanism proposed in Scheme 8. Another earlier example of framework-substituted Zn species functioning as active sites for the conversion of ethanol to acetaldehyde was provided in 2018 by Yan et al. for a Zn-substituted MWW zeotype.[20]

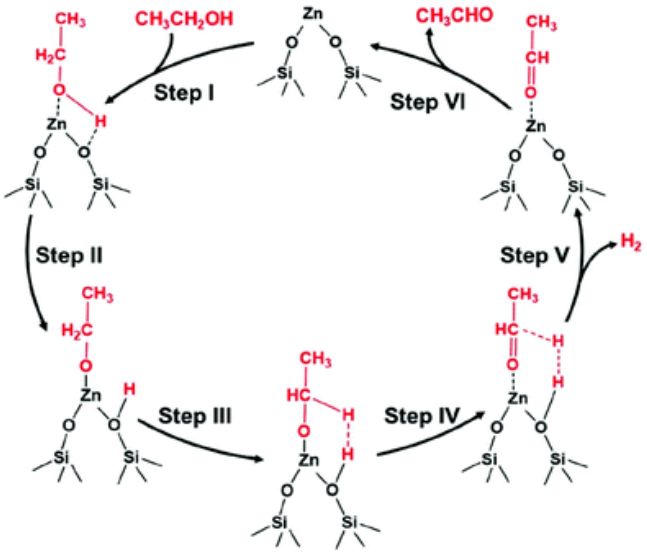

Scheme 8: Proposed reaction mechanism for the conversion of ethanol into acetaldehyde taking place over Lewis acid sites in a Zn-substituted zeolite. Adapted with permission from ref [65].

Favouring the production of acetaldehyde from ethanol, as opposed to other products such as ethylene or diethyl ether, is a direct consequence of the substitution of Zn heteroatoms in the framework. This causes a partial or total loss of Brønsted acidity in the materials and the presence of Lewis acid sites, which plays a major role in steering the product selectivity towards acetaldehyde.[20], [65] Qi et al. showed by means of FT-IR analysis that their Zn-substituted de-aluminated BEA catalyst exhibited no evidence of Brønsted acidity, with the loss of the band at 3610 cm^{-1}.[23] Yan et al. carried out FT-IR measurements after pyridine adsorption on their Zn-MWW material, compared to the aluminosilicate counterpart. They demonstrated that in the zincosilicate material the band assigned to Brønsted acid sites (1545 cm^{-1}) could not be detected, whilst a considerably intense band at 1455 cm^{-1}, corresponding to Lewis acid sites, was observed.[20]

In this work, ethanol conversion reactions were carried out in flow with on-line GC-MS analysis over Zn-substituted zeotypes with the MFI framework type. The product distribution was investigated for the Zn-MFI zeotypes in their protic form or containing extra-framework cations. The effect of the reaction temperature and the flow rate of ethanol were also studied and, finally, the catalysts' lifetime were investigated.

7.2.3.1. *Carbon Balance and Reproducibility*

The results of ethanol conversion experiments were reported considering selectivity to products and conversion of ethanol. The latter was calculated from the amount of ethanol injected in the reactor. However, test reaction performed to assess the consistency of the ethanol feed showed conflicting results. The test reactions were carried out using ethanol only as feed, in the absence of catalyst (i.e. only through the reactor packed with SiC). The tests were conducted at a constant temperature of 400 °C, with on-line analysis performed every 5 minutes. The results obtained are reported in Figure 75. The measured flow rate and the ethanol output found in both tests are lower than the expected ones by approximately 50 %. This could be due to technical issues related to the functioning of the pumping system. In order to solve this issue, the ethanol flow rate used to calculate the conversion values was worked out considering a carbon balance of 95 % in each run. The carbon balance is a quantity defined as:

$$C_{balance}(\%) = \frac{\sum_i x_{C,i}}{x_{C,EtOH(In)}} \cdot 100 \qquad \text{Equation 20}$$

Where $x_{C,i}$ and $x_{C,EtOH(in)}$ are the concentration (mmol/min) of the species *i* and the concentration of the ethanol feed, multiplied by the number of carbon atoms they contain. An estimated value of carbon balance equal to 95 % was chosen considering (i) the absence of other products (e.g. aromatics) and (i) a low coking level in the catalysts (see Table 23), suggesting that there is no substantial loss of carbon species between the input and the output in the reactions. The values of ethanol feed obtained using the estimated carbon balance were then used to calculate the conversion and yield of the products.

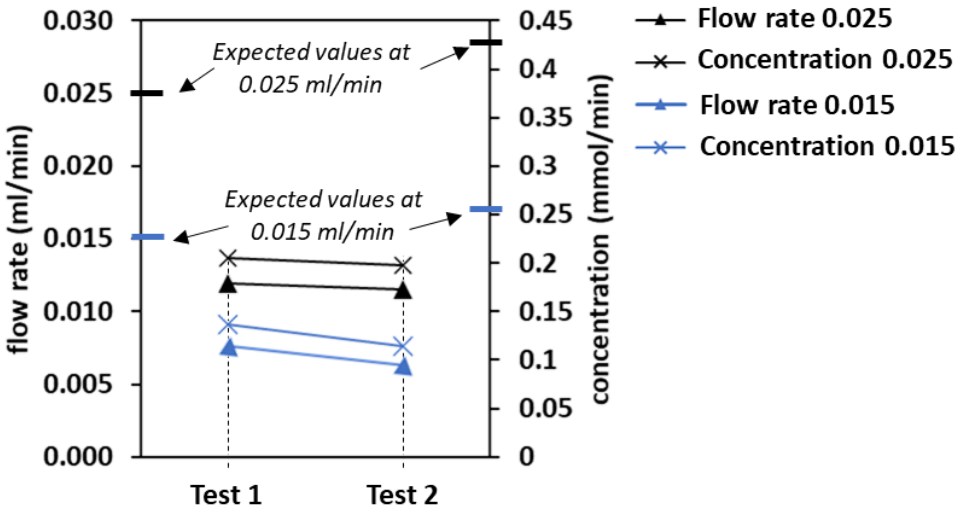

Figure 75: Results for tests carried out on input flow rate (ml/min) and output (mmol/min) of ethanol over two runs in the absence of catalyst at 400 °C.

Table 23: Coking levels in the catalysts after ethanol conversion reactions carried out at 350 °C for 5 hours and 400 °C for 50 hours. Carbon content was obtained through CHN elemental microanalysis.

Entry	Catalyst	Reaction temperature (°C)	Reaction time (h)	Carbon content (wt %)
1	***K^+/Zn-MFI***	350	5	0.92
2	***K^+/Zn-MFI***	400	50	0.15
3	***H^+-K^+/Zn-MFI***	350	5	0.62
4	***H^+-K^+/Zn-MFI***	400	50	1.72
5	***H^+/Zn-MFI***	350	5	1.90
6	***H^+/Zn-MFI***	400	50	3.28
7	***ZnO/ZSM-5***	400	50	4.75

In order to ensure the reproducibility of the results, some experiments were repeated under the same reaction conditions. The conversion and acetaldehyde selectivity values obtained from K^+/Zn-MFI, H^+-K^+/Zn-MFI and H^+/Zn-MFI catalysts at 400 °C with an ethanol flow rate of 0.025 ml/min over three different runs are reported in Table 24 and plotted in Figure 76. The values are reported as the average and standard error evaluated over the three runs for each sample. The standard error was around 2% of the experimental values.

Table 24: Ethanol conversion (%) and acetaldehyde selectivity (%) values obtained from three runs carried out under the same conditions (400 °C and 0.025 ml/min flow rate). The values are reported as the average ± the uncertainty on the measurements (approximately 2%).

Samples		Ethanol Conversion (%)	Average	Acetaldehyde Selectivity (%)	Average
K^+/Zn-MFI	Test 1	26.8	27.6 ± 0.7	52.2	54.2 ± 1.7
	Test 2	22.7		48.5	
	Test 3	33.5		61.7	
H^+-K^+/Zn-MFI	Test 1	62.4	63.1 ± 1.7	42.0	38.3 ± 0.6
	Test 2	69.1		35.4	
	Test 3	57.8		37.5	
H^+/Zn-MFI	Test 1	67.6	68.5 ± 0.5	35.4	33.7 ± 0.3
	Test 2	70.4		31.4	
	Test 3	67.6		34.4	

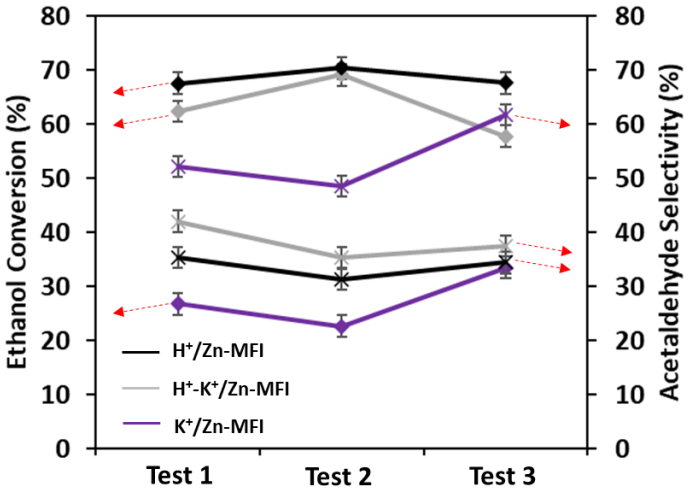

Figure 76: Conversion (%) and acetaldehyde selectivity (%) values plotted for K^+/Zn-MFI, $H^{+-}K^+$/Zn-MFI and H^+/Zn-MFI catalysts under the same reaction conditions (400 °C and 0.025 ml/min flow rate) over three runs.

7.2.3.2. Suppression of Brønsted Acidity by Heteroatom Substitution

The activity and product distribution of Brønsted and Lewis acid zeolites (and zeotypes) was investigated. The fixed-bed reactor was packed with approximately 300 mg of catalyst in a SiC bed (see experimental section for details) and the reaction was carried out at 350 °C for 5 hours, following 1 hour of activation carried out at 400 °C under flowing N_2 (40 ml/min). The ethanol flow rate was maintained at 0.025 ml/min throughout the experiment. Products were analysed via on-line GC-MS-BID, with samples automatically taken by the two 6-port VICI sample valves every 30 minutes. The materials used for this series of experiments are listed in Table 25.

Table 25: Catalysts used and their elemental composition obtained by XRF analysis. The uncertainty on the measurements is the 6% of the values (only reported for Si:T and M:T ratios).

Entry	Name	M[a] and T[b] content (wt %)	Si:T	M:T
1	***ZnO-K⁺/ZSM-5***	0.8 (Zn); 1.0 (Al)	44.0 ± 0.9 (Si:Al)	1.0 ± 0.02 (K:Al); 0.3 ± 0.01 (Zn:Al)
2	***H⁺-K⁺/Zn-MFI***	0.4 (K); 1.2 (Zn)	91.8 ± 1.8 (Si:Zn)	0.5 ± 0.01 (K:Zn)
3	***H⁺/Ni-MFI***	1.1 (Ni)	93.3 ± 1.9 (Si:Ni)	-
4	***Ni²⁺/Zn-MFI***	1.0 (Ni); 0.9 (Zn)	128.1 ± 2.6 (Si:Zn)	1.3 ± 0.03 (Ni:Zn)
5	***Silicalite-1***	-	-	-

[a] M = Zn, K or Ni
[b] T = Al, Zn or Ni

The crystallinity of the catalysts was analysed by p-XRD before and after the reaction, to confirm that the framework was not damaged by the reaction conditions. The results obtained are reported in Figure 77 and show that the samples maintain their crystallinity after the reactions. However, a minor formation of NiO nanoparticles can be observed for the spent Ni^{2+}/Zn-ZSM-5 catalyst (Figure 77(b)).

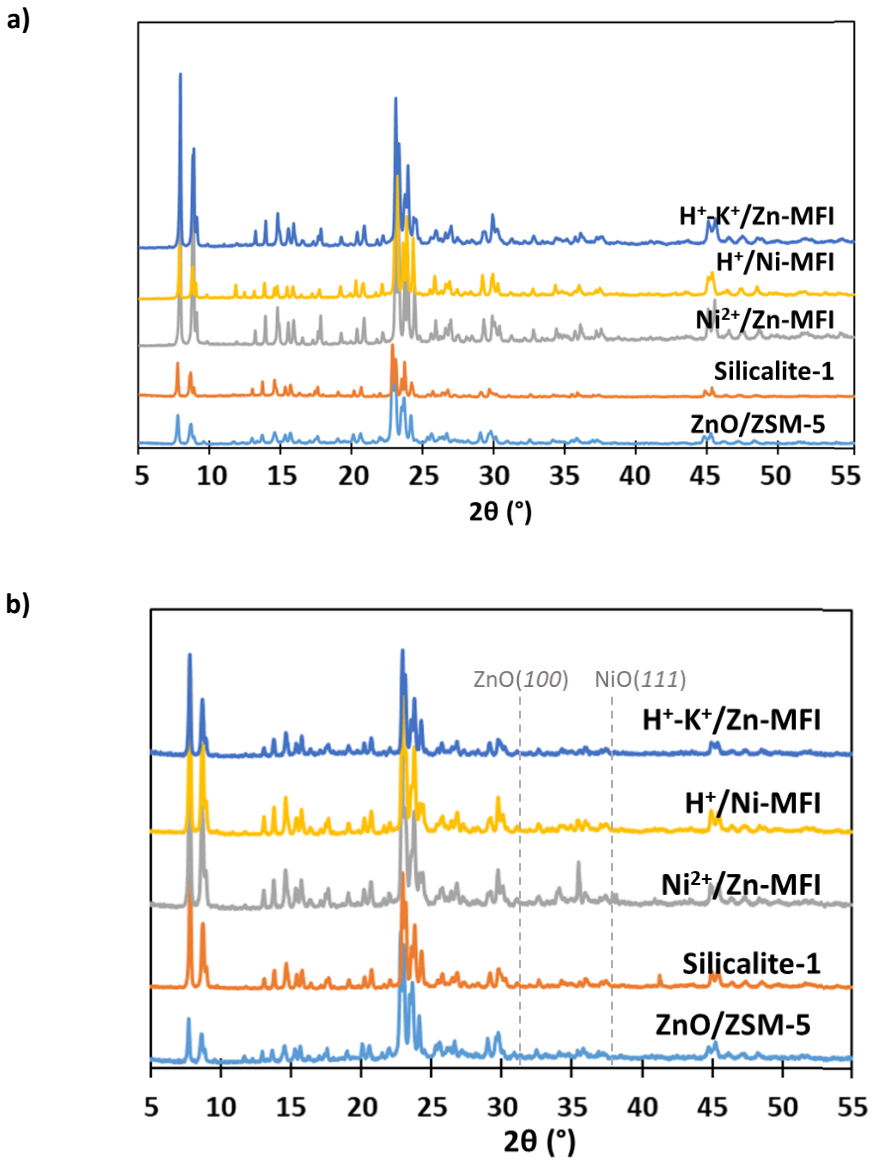

Figure 77: Powder-XRD patterns of parent (a) and spent (b) catalysts after in-flow ethanol conversion reactions carried out at 350 °C with 0.025 ml/min ethanol flow.

In Section 9.5.1 of the Appendix the results of ^{31}P NMR analysis carried out after deposition of tetramethyl phosphine oxide (TMPO) over Silicalite-1, ZSM-5 and Zn-MFI are reported. The outcome of the experiments confirmed that Zn-MFI materials do not show any sign of Brønsted acidity, similarly to Silicalite-1, and a prominent Lewis-acid character.

All the zeolites and zeotypes used for this series of experiments showed an off-white colour prior to being used for the reactions. Changes of colour after the reaction can be indicative of formation of metal nano particles or presence of coke deposits in the spent catalysts, which are shown in Figure 78. From the pictures, it can be observed that a visible change of colour from off-white is evident in the ZnO-K^+/ZSM-5 catalyst and, to a lower extent, in the Ni^{2+}/Zn-MFI catalyst. For the latter, it could be due to the formation of Ni nano particles.

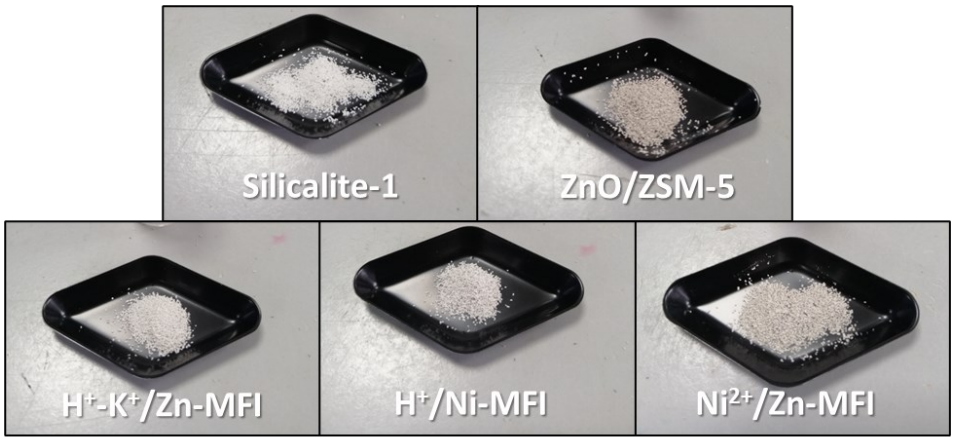

Figure 78: Pictures showing the spent Silicalite-1, ZnO-K^+/ZSM-5, H^+-K^+/Zn-MFI, H^+/Ni-MFI and Ni^{2+}/Zn-MFI catalysts after ethanol conversion experiments at 350 °C with 0.025 ml/min ethanol flow.

The products obtained were reported in terms of their selectivity (%); the conversion of ethanol (%) was also calculated, according to:

$$S_i(\%) = \frac{x_i}{x_{total}} \cdot 100 \quad \text{Equation 21}$$

$$C_{EtOH}(\%) = \frac{x_{EtOH(In)} - x_{EtOH(Out)}}{x_{EtOH(In)}} \cdot 100 \quad \text{Equation 22}$$

Where S_i and x_i are respectively the selectivity (%) and the concentration (mmol/min) for the product *i* and x_{total} is the sum of the concentrations (mmol/min) of all the products detected. The term C_{EtOH} refers to the conversion of ethanol (%), $x_{EtOH(In)}$ and $x_{EtOH(Out)}$ are the concentrations (mmol/min) of the ethanol feed and the residual ethanol detected, respectively. The results of the ethanol conversion experiments are reported in the plots in Figure 79.

a) Silicalite-1

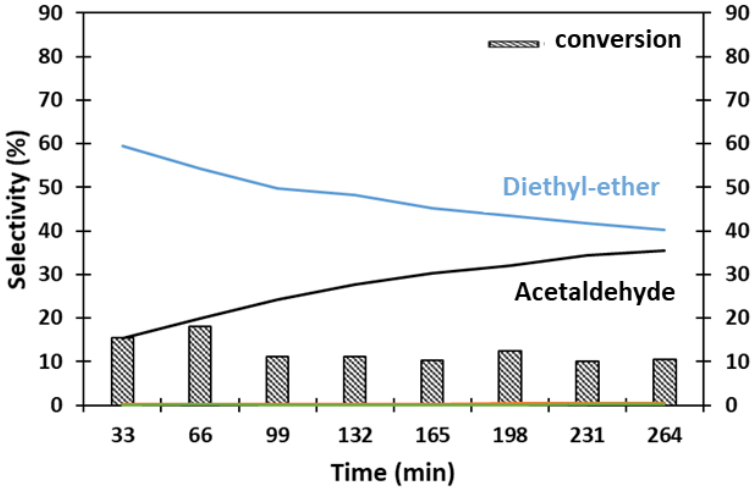

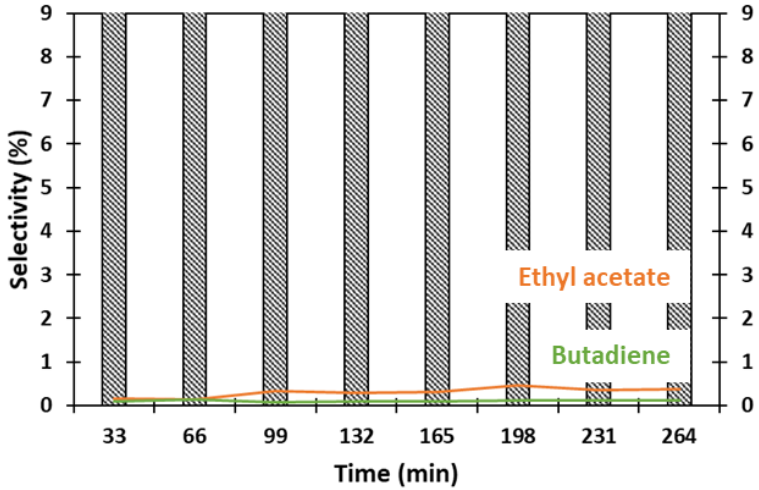

b) ZnO-K^+/ZSM-5

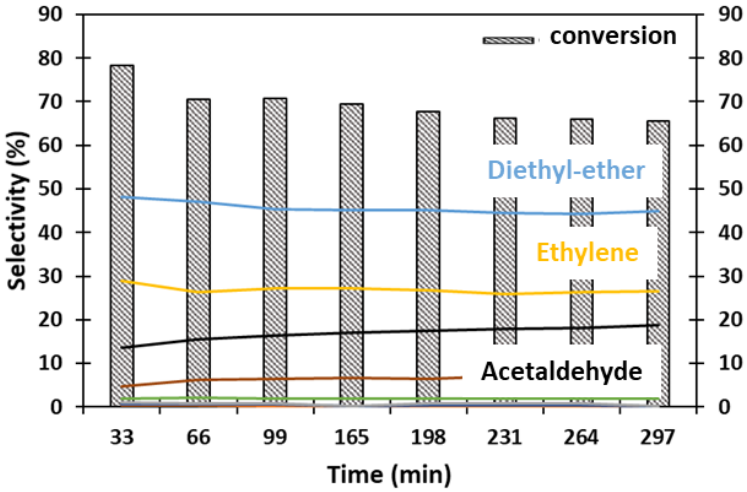

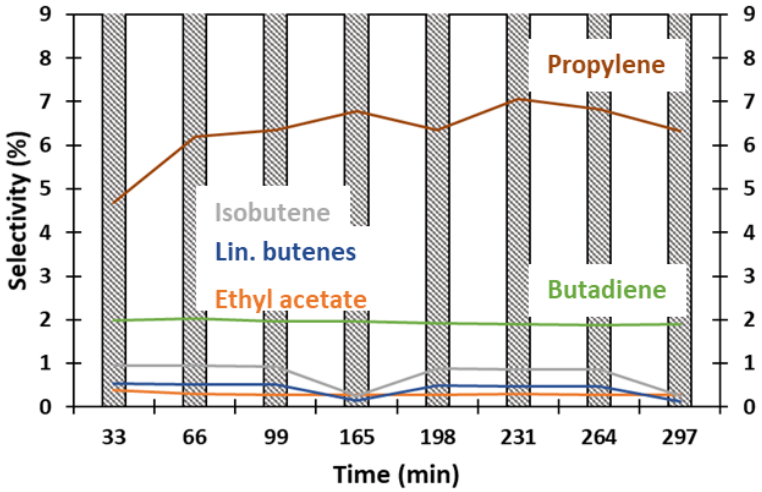

c) H^+-K^+/Zn-MFI

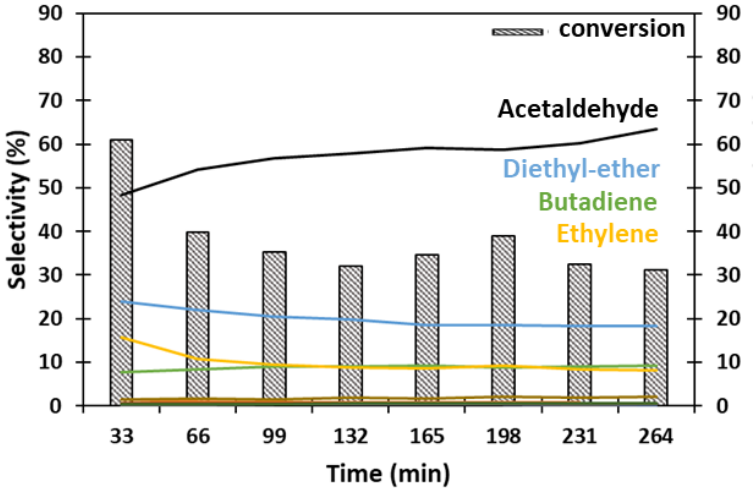

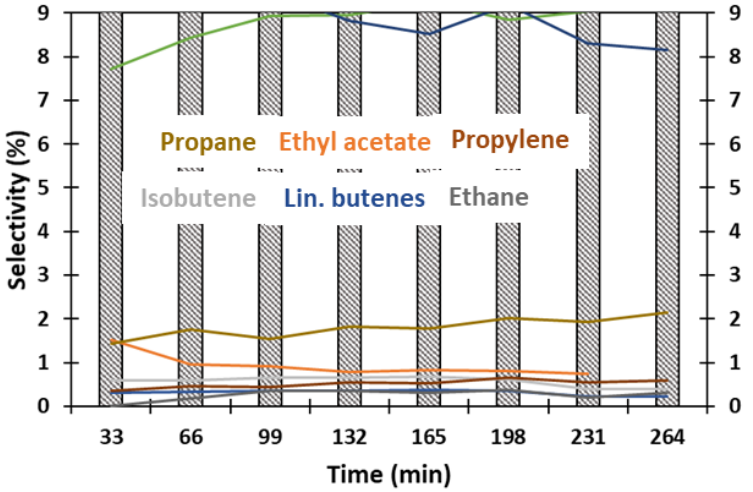

d) H^+/Ni-MFI

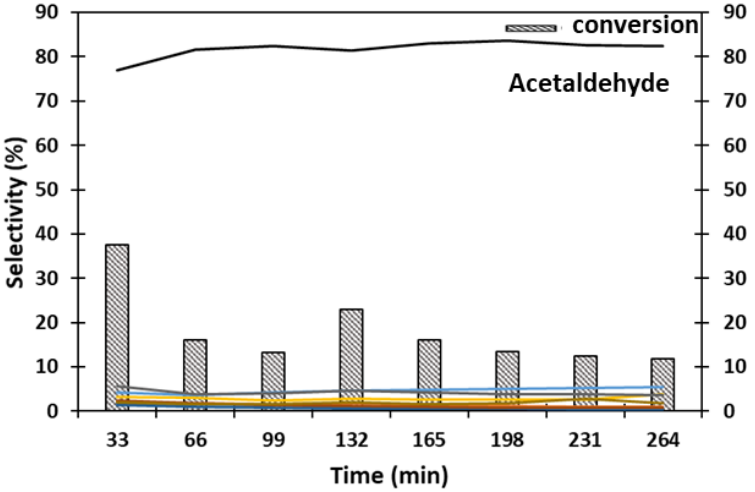

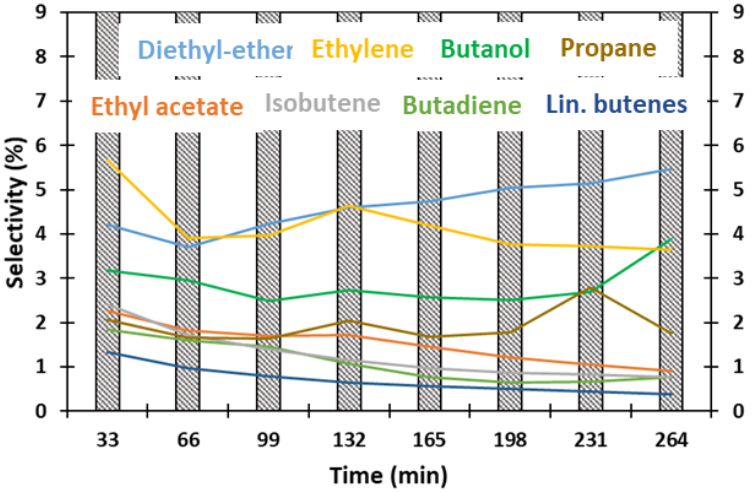

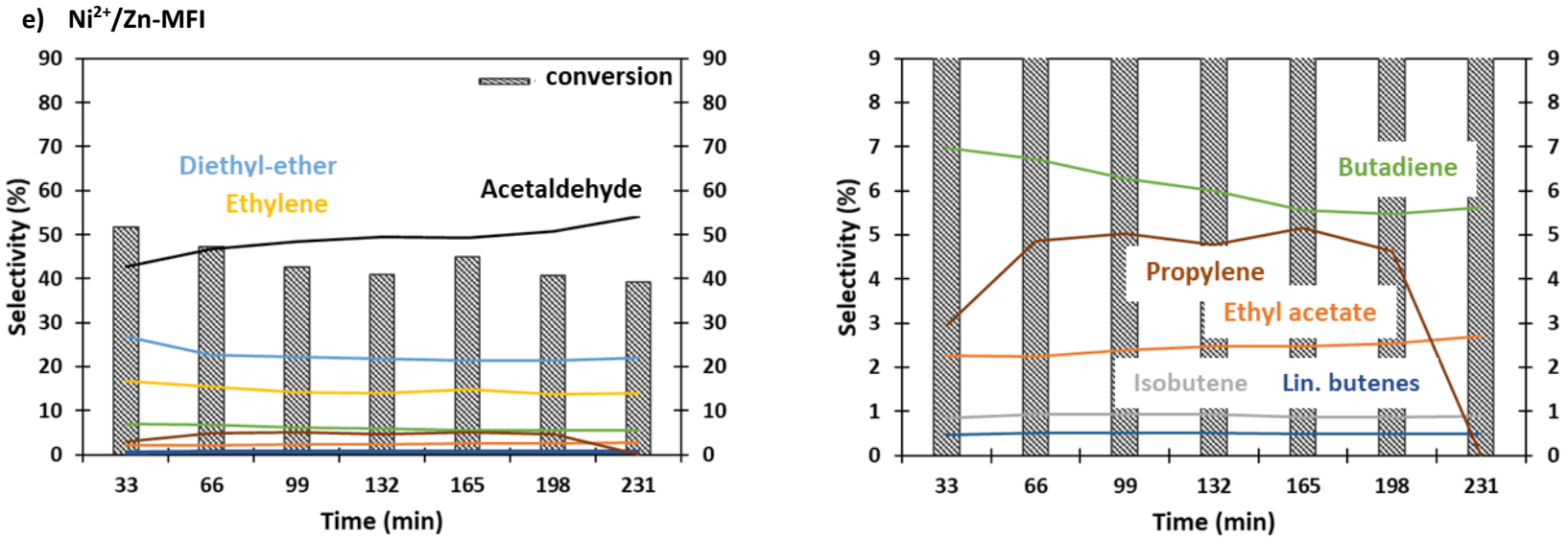

Figure 79: Product selectivity and ethanol conversion obtained from experiments carried out at 350 °C for 5 hours with a flow rate of ethanol of 0.025 ml/min and 300 mg of catalyst.

The plots showing the product selectivity and ethanol conversion percentages of the samples highlight the difference in the reactivity of the catalysts based on their acid character. Using silicalite-1, the formation of diethyl ether, starting with 60% selectivity, gradually decreases while the production of acetaldehyde increases. A considerably smaller selectivity to butadiene and ethyl acetate is also observed (< 0.5 %), with a conversion of approximately 12 %. The acidity of the silicalite-1 catalyst derives from silanol nest protons, which show a weak Brønsted acid character;[66]–[68] this explains the product distribution observed for this material. The low activity of the catalyst (conversion) is due to the absence of Lewis acid species and/or strong Brønsted acidity. The ZnO-impregnated ZSM-5 catalyst, ZnO-K^+/Zn-MFI, showed considerably different results. The main product observed was diethyl ether (50 % selectivity), followed by ethylene (30 % selectivity) and acetaldehyde (20 % selectivity). Propylene was also produced with approximately 5 % selectivity. Other minor products were also detected, with selectivity < 2 %, such as butadiene, butenes and ethyl acetate. The conversion rate is approximately 65 % after 5 hours. ZnO is a well-known material for ethanol dehydrogenation [69] and ZSM-5 has been identified as a good microporous support for the conversion of ethanol to hydrocarbons at high temperatures (> 400 °C).[70] ZnO-impregnated Rb^+/MOR was recently observed to deliver acetaldehyde with high selectivity (> 90 %) and conversion rates (> 80 %) at 400 °C.[28] The same study showed that changing the extra-framework cation to Rb^+ also played a significant role in the reduction of ethylene selectivity. The results observed for our ZnO-K^+/ZSM-5 catalyst, and especially the lower acetaldehyde selectivity, could be due to a series of factors, such as (i) lower reaction temperature, (ii) ZSM-5 framework effects and (iii) residual Brønsted acidity.

The use of a Zn-MFI zeotype (H^+-K^+/Zn-MFI) significantly enhanced the selectivity to acetaldehyde (60 % after 5 hours) and lowered the selectivity to ethylene and diethyl ether (< 20 % and < 30 %, respectively), both of which continuously decreased throughout the experiment. The selectivity to butadiene also increased to approximately 10 %, becoming higher than the selectivity of ethylene after less than 4 hours. Other minor products (< 2 % selectivity) include propane, ethyl acetate, propylene, butenes and ethane. The ethanol conversion decreases from a value of 60 % detected during the first 30 minutes to around 35 %, and remains stable for the rest of the experiment. The effect of the weaker Brønsted acid character of the catalyst is clearly visible in the product distribution: the presence of Lewis acid Zn species promotes the dehydrogenation of ethanol to acetaldehyde, whilst the dehydration to ethylene and diethyl ether is limited by the absence of strong Brønsted acidity.

A different Lewis-acid zeotype containing Ni^{II} in tetrahedral framework positions (H^+/Ni-MFI) was also tested under the same conditions. For this catalyst, the product selectivity to acetaldehyde was over 80 %, with all the other products showing a selectivity < 10 % (approx. 5 % for ethylene and diethyl ether). Evidently, the Brønsted acid character of this catalyst was even lower than the Zn-substituted MFI catalyst. A noteworthy aspect of the product distribution observed for the H^+/Ni-MFI

catalyst is the presence of 1-butanol, which was not detected for the other catalysts. This was reported for other Ni-containing catalysts, which showed a high selectivity to 1-butanol.[70] The conversion of ethanol followed the trend observed for H^+-K^+/Zn-MFI, i.e. a higher conversion rate at the initial stage of the reaction (over 35 %), which then decreased and remained stable over time (approximately 15 %).

The product distribution exhibited by the Ni^{2+}-exchanged zincosilicate (Ni^{2+}/Zn-MFI) is very similar to the one observed for the H^+-K^+/Zn-MFI catalyst. The selectivity to acetaldehyde was approximately 40 % at the start of the reaction and increased with time (55 % after 4 hours), following the same trend as the one observed in the experiment carried out with the H^+-K^+/Zn-MFI catalyst. Similarly, diethyl ether, ethylene and butadiene were detected as well (with approx. 20 %, 15 % and < 10 % selectivities, respectively). Other products (propylene, ethyl acetate and butenes) were produced with < 5 % selectivity, with an overall ethanol conversion of 45 %. These results suggest that the activity of the Ni^{2+}/Zn-ZSM-5 catalyst is mainly controlled by the framework-Zn species and the extra-framework Ni species are not playing a major role, unlike the Ni in the framework catalyst (H^+/Ni-MFI). This can be also confirmed by the absence of 1-butanol in the reaction products.

Results of ^{1}H NMR analysis carried out on the spent materials after EtOH conversion experiments are reported in Section 9.5.2.

7.2.3.3. Product Distribution in K^+-containing Samples

The activity and product distribution of Zn-MFI samples was further investigated. The samples tested were prepared in their fully-exchanged K^+ form (K^+/Zn-MFI), partially exchanged K^+ form (H^+-K^+/Zn-MFI) and fully protic form (H^+/Zn-MFI). The results obtained with zincosilicate samples were compared to a ZnO-impregnated K^+/ZSM-5 zeolite (ZnO/ZSM-5). The catalyst mass used for this set of experiments was between 60 and 70 mg, as opposed to 300 mg used for the experiments described in the previous section (7.3.3.1). This choice was made with the aim of assessing if a reduction of the catalyst mass would compromise its performance. The elemental composition of the materials used for this series of experiments are listed in Table 26 and their p-XRD patterns are shown in Figure 80**.** The elemental analysis of the catalysts revealed that the Zn content is the highest in the K^+/Zn-MFI material (1.69 wt %) and it decreases to 1.26 wt % in the material exchanged with NH_4^+ and calcined (H^+-K^+/Zn-MFI), The latter also shows the presence of residual K^+ (0.2 wt %). The ZnO-impregnated catalyst was prepared using a K^+-exchanged ZSM-5 zeolite with a Zn content close to that found in the other catalysts. The final material (ZnO-K^+/ZSM-5) shows a 0.97 K:Al ratio and a 0.33 Zn:Al ratio, suggesting the absence of Brønsted acid sites. From the p-XRD patterns of the materials appear to be highly crystalline and no peaks attributable to ZnO are observed in the ZnO-K^+/ZSM-5 material, indicating a good dispersion of ZnO in the catalyst.

Table 26: Catalysts used and their elemental composition obtained by XRF analysis. The uncertainty on the measurements is the 6% of the values (only reported for Si:T and M:T ratios).

Entry	Name	M[a] and T[b] content (wt %)	Si:T	M:T
1	***K⁺/Zn-MFI***	2.4 (K); 1.7 (Zn)	73.6 ± 1.5 (Si:Zn)	2.4 ± 0.1 (K:Zn)
2	***H⁺-K⁺/Zn-MFI***	0.2 (K); 1.3 (Zn)	94.7 ± 1.9 (Si:Zn)	0.3 ± 0.01 (K:Zn)
3	***H⁺/Zn-MFI***	1.0 (Zn)	71.6 ± 1.4 (Si:Zn)	-
4	***ZnO-K⁺/ZSM-5***	0.8 (Zn); 1.0 (Al)	44.0 ± 0.9 (Si:Al)	1.0 ± 0.02 (K:Al); 0.3 ± 0.01 (Zn:Al)

[a] M = K or Zn
[b] T = Zn or Al

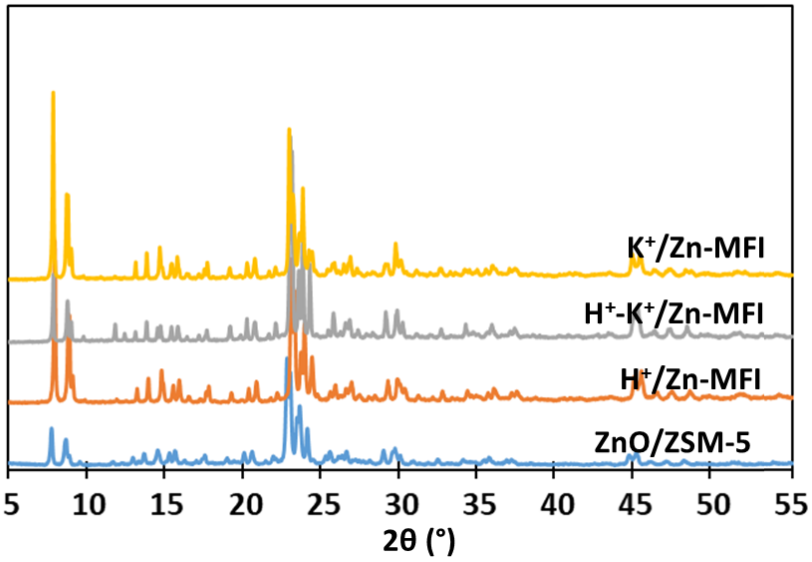

Figure 80: Powder-XRD patterns of the parent samples used for ethanol conversion reactions at 350 °C or 400 °C with ethanol flow rates of 0.015 ml/min or 0.025 ml/min.

The products obtained from ethanol conversion reactions were reported in terms of product selectivity distribution (%), product yield distribution (%) and productivity ($mmol_{product}/mmol_{Zn} \cdot min$). The selectivity and yield distribution and the productivity were calculated according to:

$$S_{i\,(AVG)}(\%) = \frac{x_{i\,(AVG)}}{x_{total}} \cdot 100 \qquad \text{Equation 23}$$

$$Y_{i\,(AVG)}(\%) = \frac{\left(S_{i\,(AVG)} \cdot C_{i\,(AVG)}\right)}{100} \qquad \text{Equation 24}$$

$$P_i\left({}^{mmol}/_{mmol_{Zn} \cdot min}\right) = \frac{x_{i\,(AVG)}}{n_{Zn}} \qquad \text{Equation 25}$$

Where S_i is the selectivity (%), Y_i is the yield (%) and P_i is the productivity ($mmol_{product}/mmol_{Zn} \cdot min$) for the product *i*, and n_{Zn} is the amount of Zn in the catalyst, expressed in mmols. The yield,

selectivity, conversion and concentration of the products are considered as the average values from all the injections in one experiment. The results obtained are reported in Figure 82 and Figure 83 and tabulated in Table 27 and Table 28(a) and (b). Table 27 shows the ethanol conversion (%) obtained with the four catalysts at 350 °C and 400 °C using different EtOH flow rates, whilst in Table 28(a) and (b) the average product selectivity (%), yield (%) and catalyst productivity ($mmol_{prod}/mmol_{Zn} \cdot min$) are reported for each product at 350 °C and 400 °C using different EtOH flow rates.

Table 27: Zn content (mmol) in the catalysts and ethanol conversion (%) values obtained with different experimental conditions. The uncertainty on the measurements was evaluated as the 2%.

			EtOH Conversion (%)			
			350 °C		400 °C	
Entry	Catalyst	x_{Zn} (mmol)	0.015 $ml_{(EtOH)}/min$	0.025 $ml_{(EtOH)}/min$	0.015 $ml_{(EtOH)}/min$	0.025 $ml_{(EtOH)}/min$
1	***K^+/Zn-MFI***	0.023	13.93	12.34	31.96	26.83
2	***H^+-K^+/Zn-MFI***	0.014	31.33	19.30	73.49	62.39
3	***H^+/Zn-MFI***	0.012	39.19	24.25	80.45	67.56
4	***ZnO-K^+/ZSM-5***	0.01	36.32	32.69	90.75	77.70

The performance of the catalysts at different conditions of temperature and ethanol flow rate for the production of acetaldehyde is reported in Figure 81. Figure 81(a) shows the conversion (%) of ethanol at different temperatures and different flow rates for the studied catalysts. At 400 °C, the highest conversion is detected for ZnO/ZSM-5, with 91 % conversion at 0.015 ml/min EtOH flow rate. This value decreases following ZnO/ZSM-5 > H^+/Zn-MFI > H^+- K^+/Zn-MFI >> K^+/Zn-MFI, with a conversion of 31 % in the latter. The conversion values recorded with 0.015 ml/min flow rate are on average 10 % higher than the ones recorded at 0.025 ml/min. This could be due to a longer residence time of ethanol (i.e. more time to react) in the catalysts at a slower flow rate. A similar trend can be observed for the ethanol conversion at 350 °C; generally, the conversion values are approximately half of those recorded at higher temperatures and they decrease with the introduction of K^+ extra-framework species in the zincosilicate catalysts, with K^+/Zn-MFI showing the lowest conversion (approx. 12 %). The highest conversion at 350 °C is found for the H^+/Zn-MFI catalyst (39 %), close to that of ZnO/ZSM-5 (36 %).

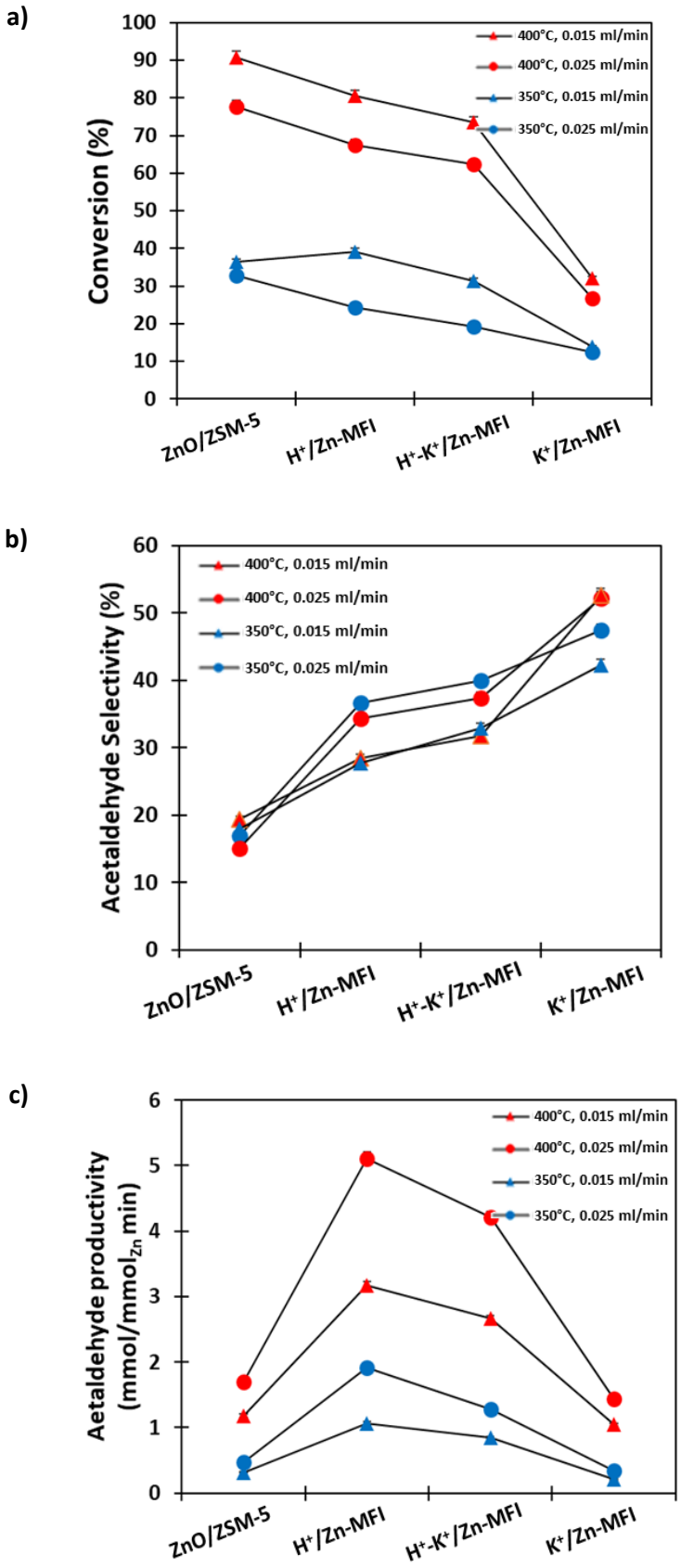

Figure 81: Average ethanol conversion (%) (a), acetaldehyde selectivity (%) (b) and productivity for acetaldehyde ($mmol_{acetaldehyde}/mmol_{Zn} \cdot min$) (c) at different experimental conditions. The uncertainty on the measurements was evaluated as the 2%.

The trend for the acetaldehyde selectivity (Figure 81(b)) is the opposite of the one observed for the conversion. The ZnO/ZSM-5 catalyst shows the lowest selectivity (< 20 %), most likely due to the presence of residual Brønsted acidity, which causes the formation of other products such as diethyl ether and ethylene. The selectivity to acetaldehyde increases gradually with the presence of exchanged K^+ species in the Zn-MFI catalysts, with 52 % selectivity recorded at 400 °C for the K^+/Zn-MFI catalyst, independent of the ethanol flow rate. A difference of approximately 10 % can be noticed between the selectivity values obtained at 0.025 and 0.015 ml/min EtOH, at both temperatures for H^+/Zn-MFI and H^+-K^+/Zn-MFI. The selectivity appears higher at 0.025 ml/min, suggesting that the formation of acetaldehyde takes place faster and a longer residence time of ethanol in the catalyst (corresponding to a slower flow rate) causes the formation of other products instead. In particular, the production of ethylene is higher at 0.015 ml/min.

Finally, the productivity of acetaldehyde, expressed as $mmol_{Acetaldehyde}/mmol_{Zn}\cdot min$ was analysed and the results reported in Figure 81(c). The H^+/Zn-MFI catalyst produces the highest amount of acetaldehyde at 400 °C and 0.025 ml/min EtOH, with almost double the amount recorded for the same sample at a temperature of 350 °C (1.9 $mmol/mmol_{Zn}\cdot min$ in the latter and 5.1 $mmol/mmol_{Zn}\cdot min$ in the first). The H^+- K^+/Zn-MFI catalyst exhibits the second-highest productivity, whilst ZnO/ZSM-5 and K^+/Zn-MFI show very similar results at the same reaction conditions.

Table 28(a): Average product selectivity (%), yield (%) and catalyst productivity ($mmol_{prod}/mmol_{Zn} \cdot min$) obtained at 350 and 400 °C with an ethanol flow rate of 0.015 ml/min. The uncertainty on the measurement was evaluated as the 2%.

	K⁺/Zn-MFI						***H⁺-K⁺/Zn-MFI***						***H⁺/Zn-MFI***						***ZnO-K⁺/ZSM-5***					
	S (%)		**Y (%)**		**P[a]**		**S (%)**		**Y (%)**		**P[a]**		**S (%)**		**Y (%)**		**P[a]**		**S (%)**		**Y (%)**		**P[a]**	
	350[b]	**400[b]**	**350**	**400**	**350**	**400**	**350**	**400**	**350**	**400**	**350**	**400**	**350**	**400**	**350**	**400**	**350**	**400**	**350**	**400**	**350**	**400**	**350**	**400**
Diethyl Ether	2.2	0.6	0.3	0.2	0.01	0.01	13.8	4.9	4.3	3.6	0.2	0.2	18.6	5.4	7.3	4.3	0.4	0.3	45.2	8.9	16.4	8.0	0.6	0.4
Ethyl Acetate	0.5	0.4	0.1	0.1	0.00	0.00	0.3	0.3	0.1	0.2	0.00	0.01	0.7	0.3	0.3	0.3	0.01	0.02	0.2	0.1	0.1	0.1	0.00	0.01
Butanol	4.2	1.4	0.6	0.5	0.01	0.01	-	-	-	-	-	-	-	-	-	-	-	-	-	-	-	-	-	-
Acetaldehyde	42.4	52.6	5.9	16.8	0.2	1.1	33.0	31.8	10.3	23.4	0.9	2.7	27.7	28.5	10.9	22.9	1.1	3.17	18.0	19.5	6.5	17.7	0.3	1.2
Butadiene	-	0.2	-	0.1	-	0.00	1.7	1.2	0.5	0.9	0.02	0.1	1.8	1.3	0.7	1.1	0.03	0.1	1.3	0.6	0.5	0.6	0.02	0.03
Isobutane	-	-	-	-	-	-	-	6.2	-	4.6	-	0.3	-	5.5	-	4.5	-	0.3	-	2.5	-	2.3	-	0.1
Lin. Butenes	-	0.1	-	0.02	-	0.00	0.1	0.1	0.02	0.1	0.00	0.00	0.1	0.2	0.02	0.1	0.00	0.01	0.2	0.1	0.1	0.1	0.00	0.01
Isobutene	-	0.1	-	0.03	-	0.00	0.1	0.2	0.03	0.1	0.00	0.01	0.1	0.3	0.1	0.2	0.00	0.02	0.4	0.3	0.2	0.2	0.01	0.01
Ethylene	4.7	8.4	0.7	2.7	0.02	0.2	21.5	39.1	6.7	28.7	0.6	3.3	27.2	44.1	10.6	35.4	1.0	4.9	20.0	58.3	7.3	52.9	0.5	5.3
Ethane	13.4	10.8	1.9	3.4	0.1	0.2	3.3	3.0	1.03	2.2	0.1	0.3	2.3	2.5	0.9	2.0	0.1	0.3	1.9	1.8	0.7	1.7	0.1	0.2
Propylene	-	-	-	-	-	-	-	0.4	-	0.3	-	0.02	-	0.4	-	0.3	-	0.03	1.7	0.5	0.6	0.5	0.03	0.03
Propane	32.7	25.4	4.6	8.1	0.1	0.4	25.9	12.9	8.1	9.4	0.4	0.7	21.4	11.6	8.4	9.3	0.6	0.9	11.1	7.4	4.0	6.7	0.2	0.5

Table 29(b): Average product selectivity (%), yield (%) and catalyst productivity ($mmol_{prod}/mmol_{Zn} \cdot min$) obtained at 350 and 400 °C with an ethanol flow rate of 0.025ml/min. The uncertainty on the measurement was evaluated as the 2%.

	K⁺/Zn-MFI						***H⁺-K⁺/Zn-MFI***						***H⁺/Zn-MFI***						***ZnO-K⁺/ZSM-5***					
	S (%)		**Y (%)**		**P[a]**		**S (%)**		**Y (%)**		**P[a]**		**S (%)**		**Y (%)**		**P[a]**		**S (%)**		**Y (%)**		**P[a]**	
	350[b]	**400[b]**	**350**	**400**	**350**	**400**	**350**	**400**	**350**	**400**	**350**	**400**	**350**	**400**	**350**	**400**	**350**	**400**	**350**	**400**	**350**	**400**	**350**	**400**
Diethyl Ether	5.6	1.5	0.7	0.4	0.0	0.0	18.4	7.6	3.6	4.8	0.3	0.4	22.1	9.0	5.4	6.1	0.6	0.7	47.2	24.4	15.4	19.0	1.0	1.4
Ethyl Acetate	0.5	0.4	0.1	0.1	0.0	0.0	0.4	0.3	0.1	0.2	0.0	0.0	0.6	0.4	0.2	0.3	0.0	0.0	0.2	0.1	0.1	0.1	0.0	0.0
Butanol	-	-	-	-	-	-	-	-	-	-	-	-	-	-	-	-	-	-	-	-	-	-	-	-
Acetaldehyde	47.5	52.2	5.9	14.0	0.3	1.4	40.0	37.5	7.7	23.4	1.3	4.2	36.7	34.4	8.9	23.3	1.9	5.1	17.0	15.1	5.6	11.7	1.9	1.7
Butadiene	0.0	0.1	0.0	0.0	0.0	0.0	1.4	1.5	0.3	0.9	0.0	0.1	1.5	1.6	0.4	1.1	0.0	0.1	1.1	0.8	0.4	0.6	0.0	0.0
Isobutane	-	-	-	-	-	-	-	7.3	-	4.5	-	0.4	-	6.7	-	4.5	-	0.5	-	0.6	-	0.5	-	0.2
Lin. Butenes	-	0.0	-	0.0	-	0.0	0.1	0.1	0.0	0.1	0.0	0.0	0.1	0.1	0.0	0.1	0.0	0.0	0.2	0.2	0.0	0.1	0.0	0.0
Isobutene	-	0.1	-	0.0	-	0.0	0.1	0.2	0.0	0.1	0.0	0.0	0.1	0.3	0.0	0.2	0.0	0.0	0.3	0.3	0.1	0.2	0.0	0.0
Ethylene	11.2	16.2	1.4	4.3	0.1	0.5	20.7	29.8	4.0	18.6	0.7	3.2	21.9	34.4	5.3	23.3	1.2	5.1	17.2	46.3	5.6	36.0	0.7	5.3
Ethane	13.8	8.2	1.7	2.2	0.1	0.2	3.5	2.7	0.7	1.7	0.1	0.3	2.8	1.4	0.7	0.9	0.2	0.2	2.6	1.6	0.9	1.2	0.1	0.2
Propylene	-	-	-	-	-	-	-	0.6	-	0.4	-	0.0	-	0.5	-	0.3	-	0.0	2.1	0.9	0.7	0.7	0.1	0.1
Propane	20.9	20.9	2.6	5.6	0.1	0.4	15.5	12.6	3.0	7.9	0.3	1.0	14.2	11.7	3.5	7.9	0.5	1.2	12.1	9.8	4.0	7.6	0.3	0.7

[a] P is expressed as $mmol_{product}/mmol_{Zn} \cdot min$

[b] 350 and 400 are the reaction temperatures, expressed as °C

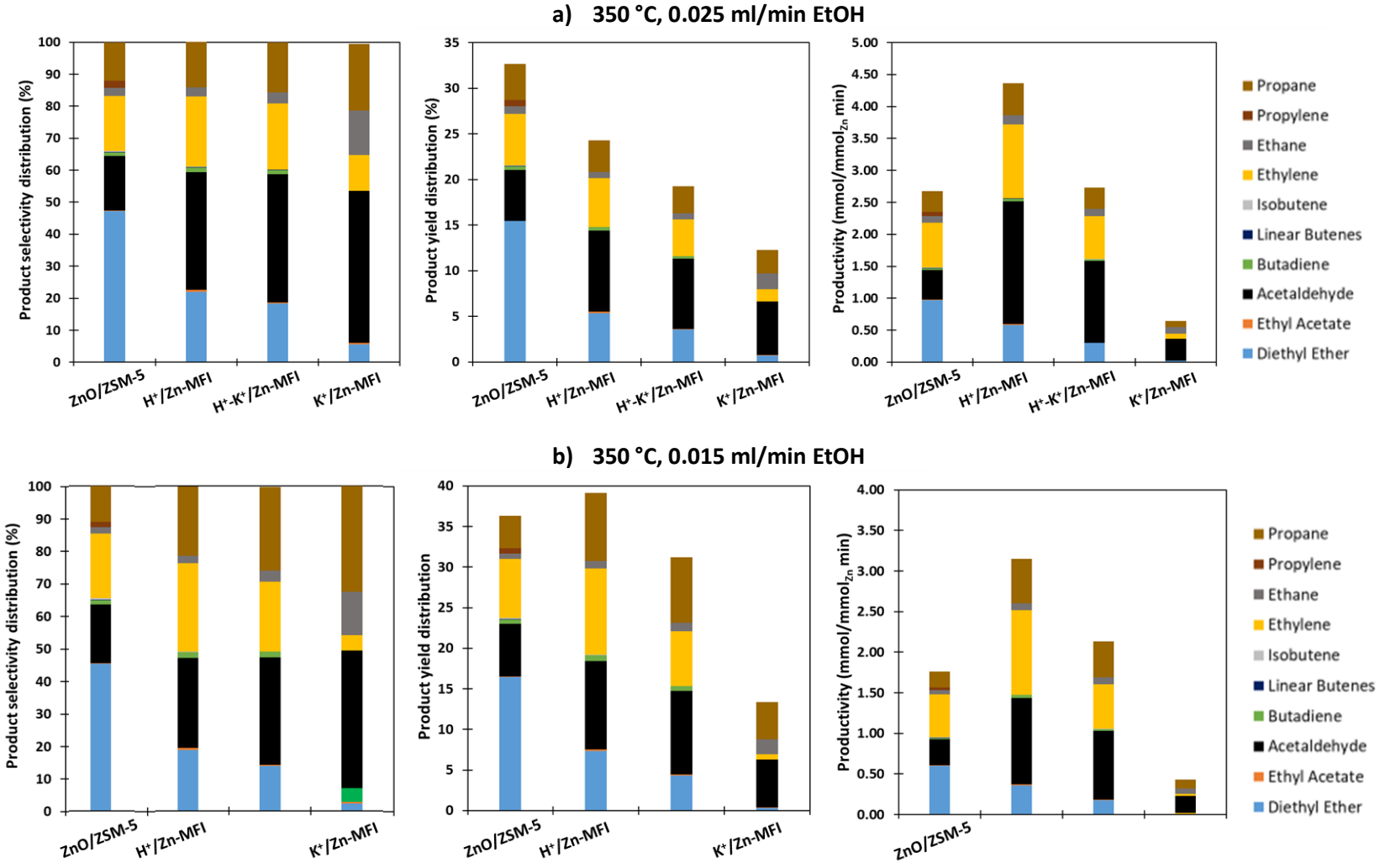

Figure 82: Average product selectivity (%), yield (%) and catalyst productivity ($mmol_{prod}/mmol_{Zn} \cdot min$) plotted for each catalyst tested at 350 °C and different EtOH flow rates, with approximately 70 mg of catalyst for each reaction.

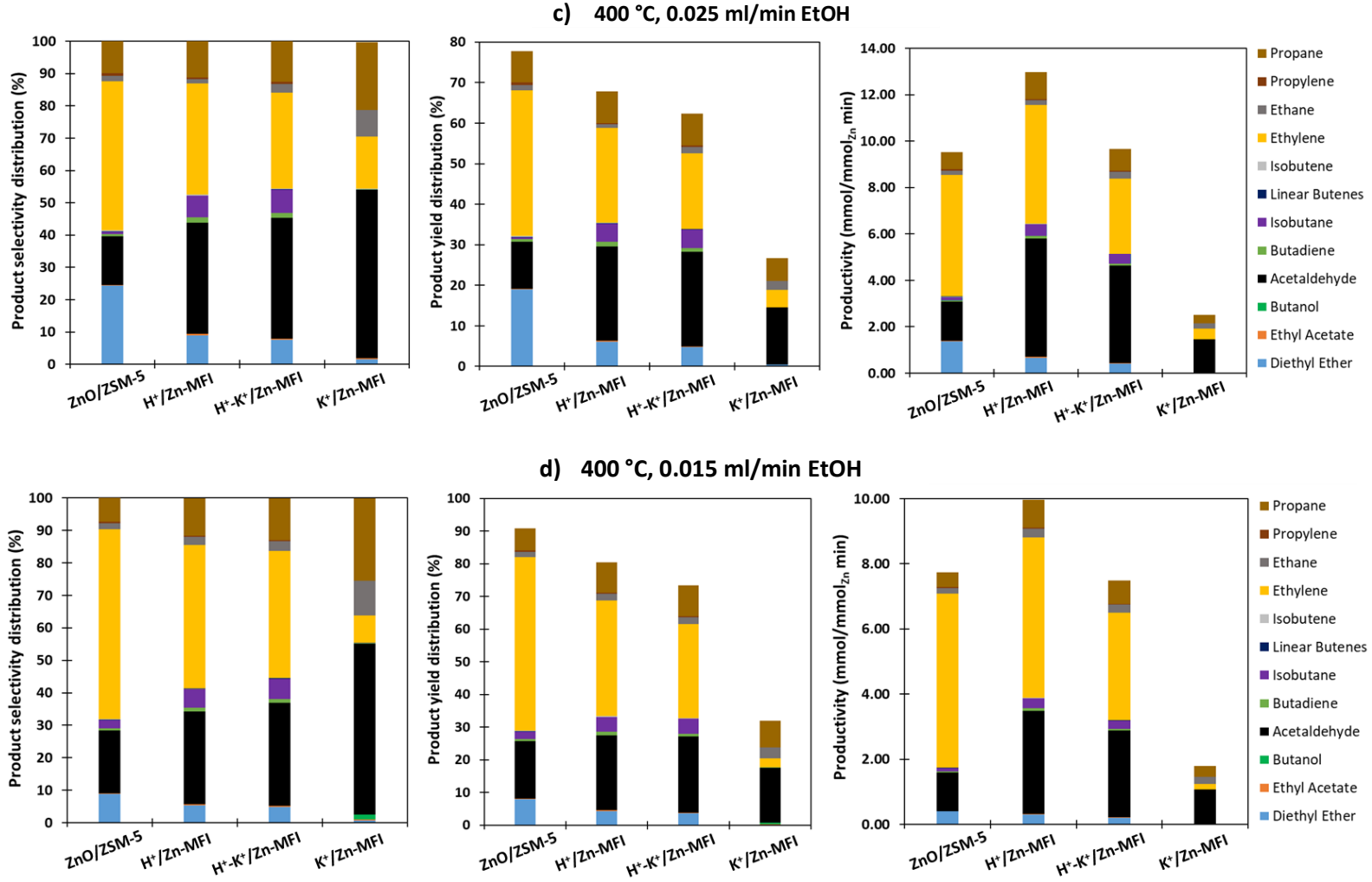

Figure 83: Average product selectivity (%), yield (%) and catalyst productivity ($mmol_{prod}/mmol_{Zn} \cdot min$) plotted for each catalyst tested at 400 °C and different EtOH flow rates, with approximately 70 mg of catalyst for each reaction.

The effects of the reaction temperature and EtOH flow rate on the product distribution and productivity of the catalysts were investigated. At 350 °C a remarkable difference can be noticed between the selectivity of the ZnO/ZSM-5 catalyst and the zincosilicate catalysts. In the ZnO/ZSM-5 material, the main product detected is diethyl ether, (48% selectivity). However, for the zincosilicate materials, the major product is acetaldehyde, with diethyl ether being a minor product. By reducing the concentration of Brønsted acid sites on the zincosilicates, the selectivity to diethyl ether drops from 15-20% for H^+/Zn-MFI to < 5% for K^+/Zn-MFI. This trend is observed at both 0.025 and 0.015 ml/min EtOH flow rates; additionally, at 0.015 ml/min and 350 °C the selectivity to diethyl ether is the lowest in the K^+/Zn-MFI catalyst, with the production of a small amount of butadiene. On the other hand, the selectivity to acetaldehyde follows the opposite trend: ZnO/ZSM-5 shows the lowest acetaldehyde selectivity whilst Zn-MFI samples are more selective, especially K^+-containing Zn-MFI, with over double the selectivity to acetaldehyde obtained with K^+/Zn-MFI compared to ZnO/ZSM-5 and no remarkable differences when the EtOH flow rate is changed. Two noteworthy aspects are: (i) the decrease of selectivity to ethylene in the presence of extra-framework K^+ cations, which is especially evident at 0.015 ml/min EtOH flow rate, and (ii) an increase in the production of propane following the same trend. The product yield is affected by the different temperature and flow rate due to the significant changes in EtOH conversion values recorded at the different conditions. The ethanol conversion values recorded at 400 °C are in fact two times higher than the ones recorded at 350 °C (Table 27). The H^+/Zn-MFI catalyst shows the highest overall product yield at 350 °C and 0.015 ml/min EtOH flow rate, whilst the fully-exchanged K^+/Zn-MFI catalyst exhibits the lowest yield. However, the acetaldehyde yield obtained from K^+/Zn-MFI and ZnO/ZSM-5 are comparable, with the absence of ethylene and diethyl ether by-products in K^+/Zn-ZSM-5, due to the lack of Brønsted acidity. The highest acetaldehyde productivity is detected for the H^+/Zn-MFI catalyst, with over 5 $mmol_{Acetaldehyde}/mmol_{Zn}$·min recorded at 400 °C and 0.025 ml/min EtOH, corresponding to 300 $mmol_{Acetaldehyde}/mmol_{Zn}$·h.

7.2.3.4. Studies on the Catalysts' Lifetime

The catalysts' durability and lifetime were tested through a 50 h run at 400 °C using 0.025 ml/min EtOH flow and a 20 h run with 350 °C and 400 °C temperature ramps at 0.015 ml/min and 0.025 ml/min. The fixed-bed reactor was packed with approximately 100 mg of catalyst.

The samples used for this set of experiments were the same catalysts presented in the previous section: K^+/Zn-MFI, H^+-K^+/Zn-MFI, H^+/Zn-MFI, ZnO/ZSM-5 listed in detail in Table 26. The spent catalysts were analysed by means of pXRD in order to confirm the integrity of the framework after the reactions (Figure 84) and they exhibit a high degree of crystallinity, without the loss of any features in the patterns, suggesting that the materials are robust and can endure at least 50 h reactions at 400°C. No evidence of ZnO reflections was detected in the pXRD patterns, indicating a good dispersion of ZnO on

the ZSM-5 support and that the experimental conditions did not affect the framework zinc species in the zincosilicates. The physical appearance of the spent catalysts is shown in Figure 85. The fully exchanged K^+/Zn-MFI catalyst remains white even after the reaction, whilst where the K^+ exchange is partial (H^+-K^+/Zn-MFI) or absent (H^+/Zn-MFI) the colour of the catalysts changes to grey-brown. This suggests the presence of a certain degree of coke deposition in these catalysts. Based on these observations, it could be hypothesised that the presence of residual or weak Brønsted acidity causes the acceleration of the coking phenomenon in the catalysts.

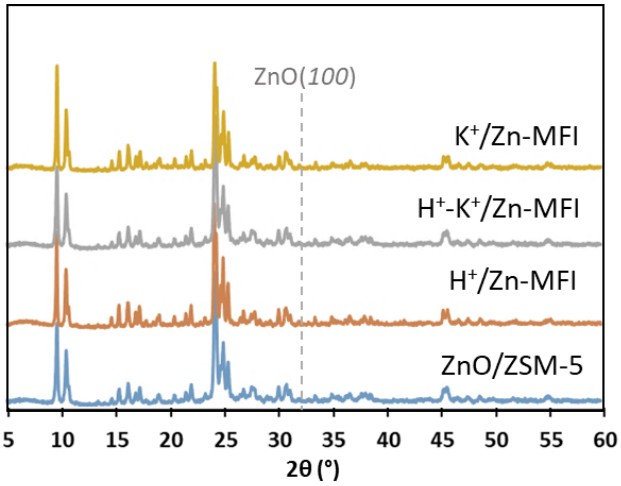

Figure 84: Powder-XRD patterns of the spent catalysts used for ethanol conversion reactions carried out at 400 °C for 50 h with an ethanol flow rate of 0.025 ml/min.

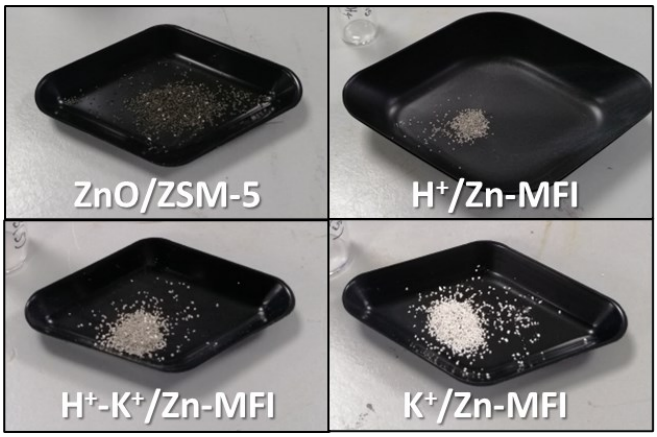

Figure 85: Pictures representing the spent catalysts after ethanol conversion reactions carried out at 400 °C for 50 h with an ethanol flow rate of 0.025 ml/min.

The spent catalysts were also studied by electron microscopy (SEM), in order to detect any changes caused by the reaction conditions on their structure integrity. The images acquired are reported in Figure 86. The materials appear to be undamaged, however the K^+-containing Zn-MFI catalysts (Figure 86(c) and (d)) show the presence of agglomerates of crystals. This is most likely due to the pre-treatment applied to the catalysts, which includes pressing the powders into a pellet prior to being sieved.

The results in product selectivity and ethanol conversion obtained from the 50 h-long runs at 400 °C using 0.025 ml/min EtOH flow are shown in

Figure 87.

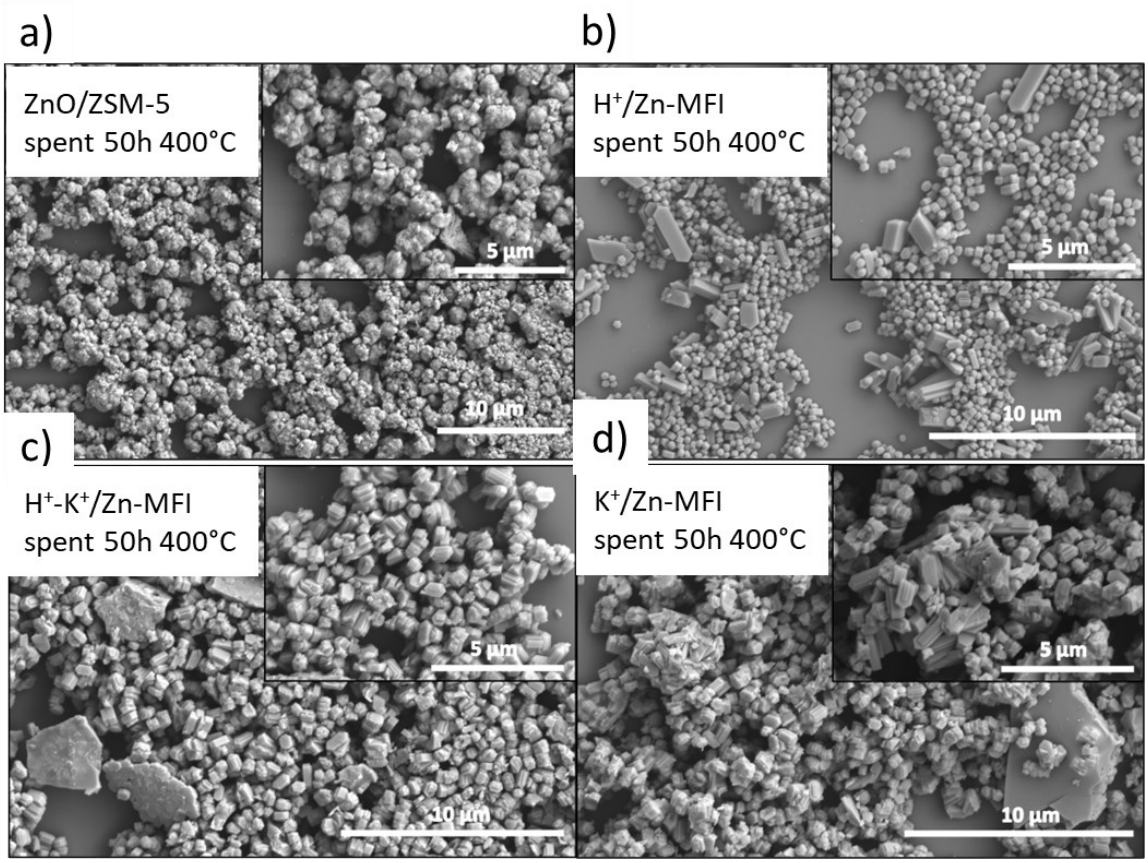

Figure 86: SEM images of spent samples used for ethanol conversion reactions at 400 °C for 50 h and 0.025 ml/min ethanol flow, acquired at 5 kV.

a)

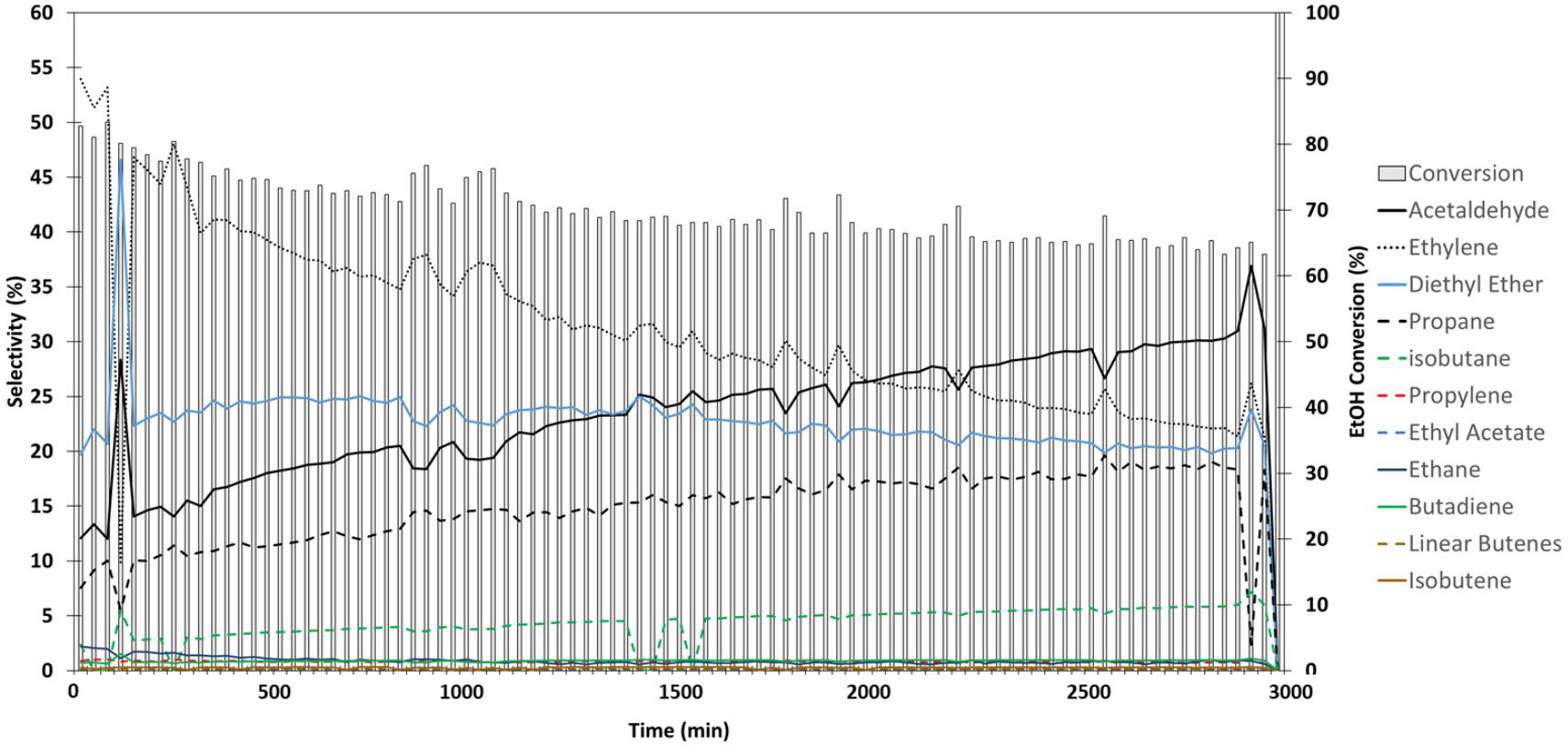
Selectivity (%)
EtOH Conversion (%)
Time (min)
0
500
1000
1500
2000
2500
3000
Conversion
Acetaldehyde
Ethylene
Diethyl Ether
Propane
isobutane
Propylene
Ethyl Acetate
Ethane
Butadiene
Linear Butenes
Isobutene

b)

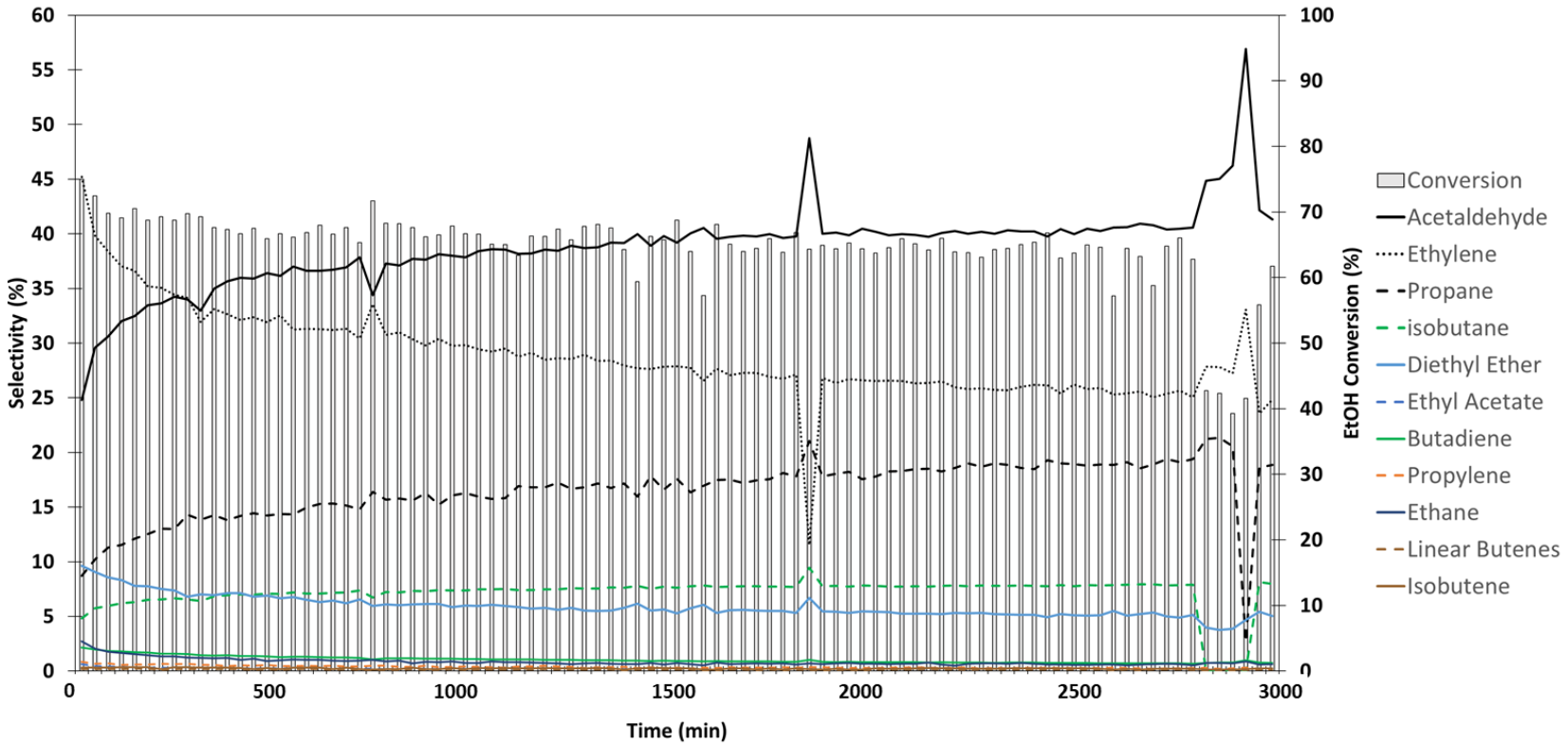
Selectivity (%)
EtOH Conversion (%)
Time (min)
0
500
1000
1500
2000
2500
3000
Conversion
Acetaldehyde
Ethylene
Propane
isobutane
Diethyl Ether
Ethyl Acetate
Butadiene
Propylene
Ethane
Linear Butenes
Isobutene

c)

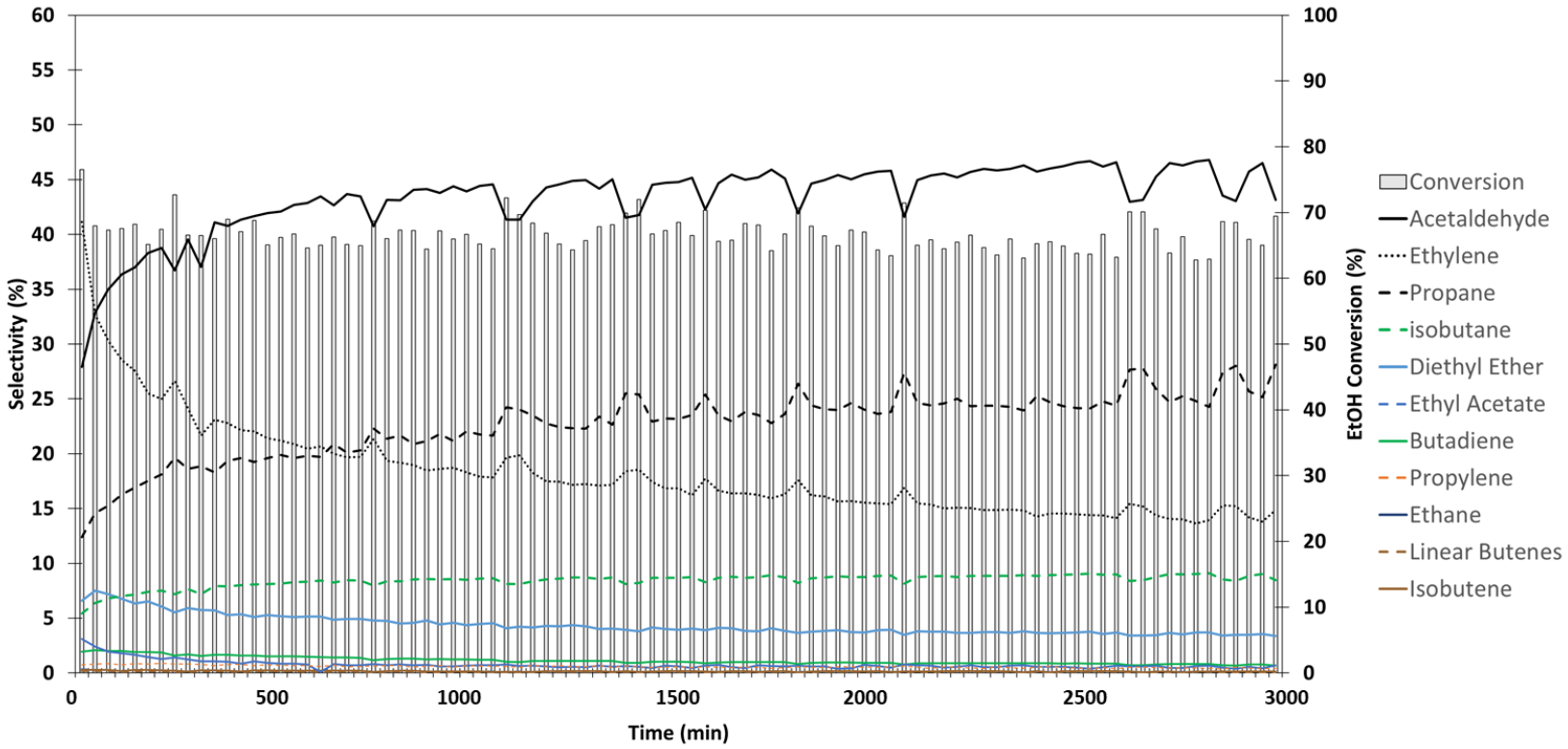
Selectivity (%)
EtOH Conversion (%)
Time (min)
0
500
1000
1500
2000
2500
3000
Conversion
Acetaldehyde
Ethylene
Propane
isobutane
Diethyl Ether
Ethyl Acetate
Butadiene
Propylene
Ethane
Linear Butenes
Isobutene

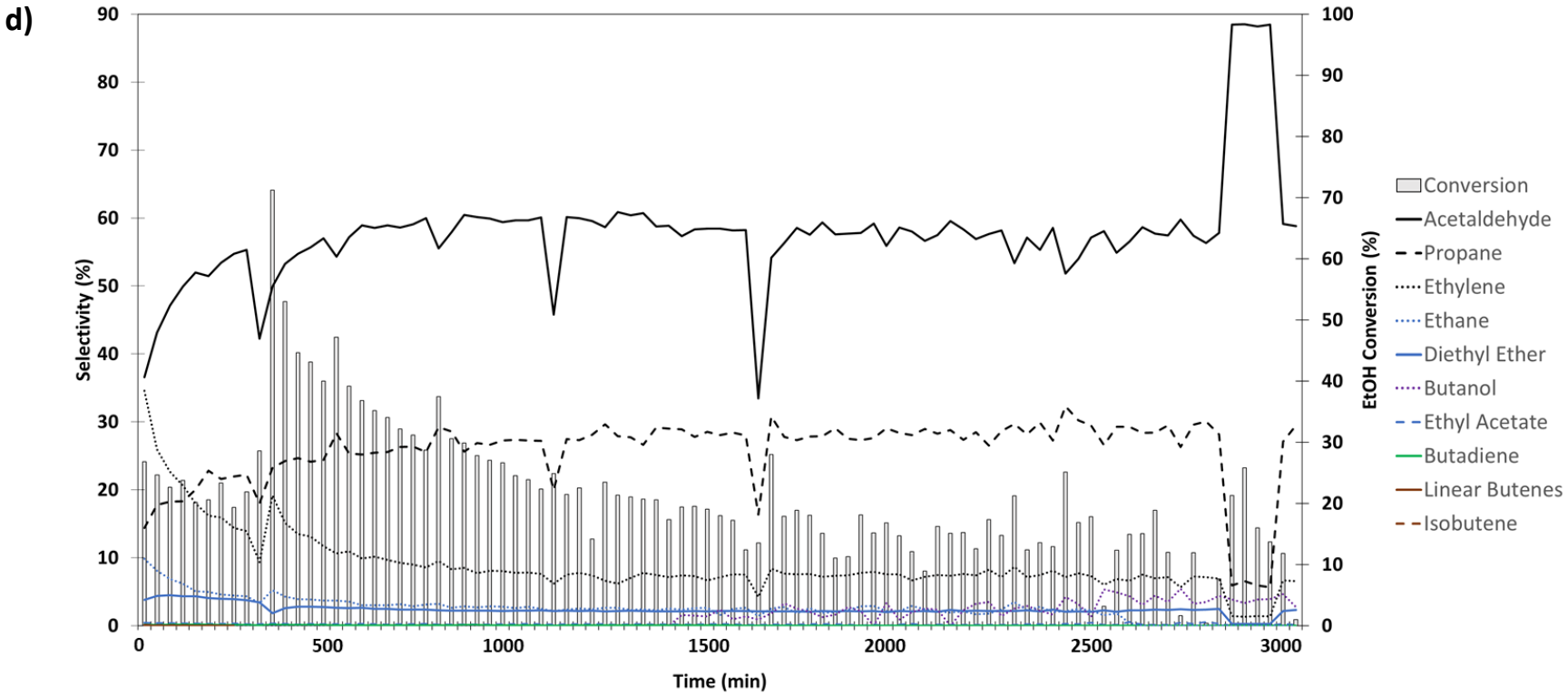

Figure 87: Product selectivity (%) and ethanol conversion (%) plotted as a function of time for ZnO/ZSM-5 (a), H^+/Zn-MFI (b), H^+-K^+/Zn-MFI and K^+/Zn-MFI (d), obtained from reactions carried out at 400 °C for 50 h with an ethanol flow rate of 0.025 ml/min and approximately 100 mg of catalyst. The points that diverge abruptly from the data are generated by technical issues related to the pumping system.

Figure 87(a) shows the values of selectivity and conversion for the ZnO/ZSM-5 catalyst. A striking feature that can be observed for this catalyst is the change of selectivity trend between acetaldehyde and ethylene: at the initial stage of the experiment, ethylene was the main product formed, with over 50 % selectivity. The corresponding acetaldehyde selectivity was low as 15 %. The production of ethylene decreases steadily, while acetaldehyde increases. At the end of the experiment, the selectivity to acetaldehyde has more than doubled (over 30 %), whilst the selectivity to ethylene is around 20 %. The third and fourth main products are diethyl ether and propane (approx. 20%), with the production of the latter steadily increasing over time. A constantly increasing formation of isobutane (around 5 % selectivity) could also be detected. Another noteworthy aspect is that values of ethanol conversion slowly decrease, losing approximately 10 % throughout the entire run (50 h). This could be related to the formation of coke deposits in the catalyst, as suggested by the colour of the spent sample (Figure 85), which could prevent the ethanol interacting with the active sites. Additionally, given the decrease in the production of ethylene, another factor to be considered is the poisoning of the active sites for the production of ethylene.

A constant conversion is instead observed for the H^+/Zn-MFI catalyst, stable at values around 40 % (

Figure 87(b)). For this material, the trend between acetaldehyde and ethylene reverses considerably earlier, after only 4 hours, with acetaldehyde reaching a selectivity of over 40 % and ethylene decreasing to 20 % at the end of the experiment. An increasing formation of propane, reaching up to 20% selectivity, can be observed as well, alongside the production of isobutane and diethyl ether (< 10%). A similar behaviour can also be observed for the partially K^+-exchanged catalyst, shown in

Figure 87(c): the conversion values remain mostly constant around 40 % and a change of trend between acetaldehyde and ethylene is detected. However, the latter takes place even earlier, after approximately 1 hour, with the selectivity to ethylene decreasing quickly and reaching even lower values than the ones observed for the H^+/Zn-MFI catalyst. Additionally, for H^+-K^+/Zn-MFI the selectivity to propane exceeds the selectivity to ethylene after 12 hours. This feature was not observed in the reactions carried out over the previous catalysts. The propane selectivity reaches values up to 25 %, becoming the second main product of the reaction. The fully exchanged zincosilicate catalyst (K^+/Zn-MFI,

Figure 87(d)) shows remarkably different values of conversion, alongside a different product distribution. The conversion is not constant and shows an abrupt jump from 20 % to 60 % after 6 hours, followed by a gradual decrease until values around 20 % are reached again, and maintained more or less constantly until the end of the experiment. The selectivity to acetaldehyde reaches a plateau of 60 % after 4 hours, whilst the production of ethylene decreases quickly to values < 10 %, which is the lowest selectivity to ethylene among all the experiments. The change of trend between propane and

ethylene, already detected for the H^+-K^+/Zn-MFI catalyst, takes place after only 2 hours using K^+/Zn-MFI. The selectivity to propane reaches values right below 30 %, with propane being the second most selective product for this catalyst.

These observations show the profound effect of the presence of K^+ cations in extra-framework positions of the zincosilicate catalysts. The materials result to be considerably less selective to ethylene, thanks to the absence of strong Brønsted acid sites, but the production of propane becomes non-negligible, especially for H^+-K^+/Zn-MFI and K^+/Zn-MFI.

Figure 88 represents the temperature ramp profile used for the series of experiments carried out to investigate the effects of the temperature and ethanol flow rate on the productivity of the catalysts. The run started at 350 °C with an ethanol flow rate of 0.015 ml/min. After the first 200 minutes, the temperature was increased to 400 °C and maintained for further 200 minutes before being lowered to 350 °C again. This last step was carried out in order to make sure that the performance of the catalyst al lower temperature would remain the same without being affected by the high temperature step. The same three 200-minute steps were repeated at a flow rate of 0.025 ml/min of ethanol and the results compared for H^+/Zn-MFI, H^+-K^+/Zn-MFI and K^+/Zn-MFI catalysts. The data are reported in Figure 89.

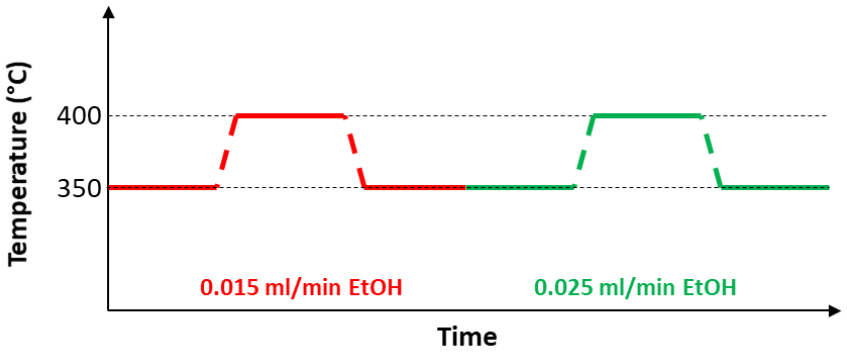

Figure 88: Temperature profile used for ethanol conversion reactions carried out with different flow rates and temperature ramps (350 °C – 400 °C – 350 °C) with heating ramps of 10 °C/min and a total reaction time of approximately 20 hours.

Figure 89(a) shows the performance of H^+/Zn-MFI. The ethanol conversion is highly affected by the temperature, as the values measured at 400 °C are two times higher than the ones measured at 350 °C. Additionally, they appear to be slightly higher at lower ethanol flow rate. Whilst the selectivity to acetaldehyde is only mildly affected by the change of temperature, and keeps increasing over both ethanol flow rates, other products such as ethylene, diethyl ether and propane appear to be substantially dependent on the temperature. On the one hand, the selectivity to ethylene almost doubles at 400 °C, despite decreasing gradually with time, and on the other hand the selectivities of propane and diethyl ether decrease at 400 °C. Finally, despite not being one of the main products, the

selectivity to isobutane also shows an increase from approx. 1 % at 350 °C to over 5 % at 400 °C. A similar trend was observed for H^+-K^+/Zn-MFI (Figure 89(b)), with higher and increasing selectivity to acetaldehyde and propane and lower selectivity to ethylene and diethyl ether. Similarly to the trend observed for H^+/Zn-MFI, the ethanol conversion remained nearly the same at 350 °C and 0.015 or 0.025 ml/min; however, it increased up to three times its initial value at 400 °C, with slightly higher conversion at 0.015 ml/min. The results obtained from this experiment were considerably different for the K^+/Zn-MFI catalyst (Figure 89(c)) to the ones described so far. The conversion drops down to around 30 % at 400 °C and 10 % at 350 °C and its values appear to be not as regular and stable as the ones measured for the other catalysts. The effect of the temperature on the selectivity to acetaldehyde, however, is remarkable, with values 2 times higher at 400 °C compared to the ones detected at 350 °C. Propane is the second major product, as observed in the previous 50 h experiment, with values of selectivity oscillating around 40 %, the highest measured in this set of experiments. However, the selectivity is not stable as it was in H^+/Zn-MFI and H^+-K^+/Zn-MFI, probably due to the low and unstable conversion trend. Ethylene is almost absent throughout the reaction.

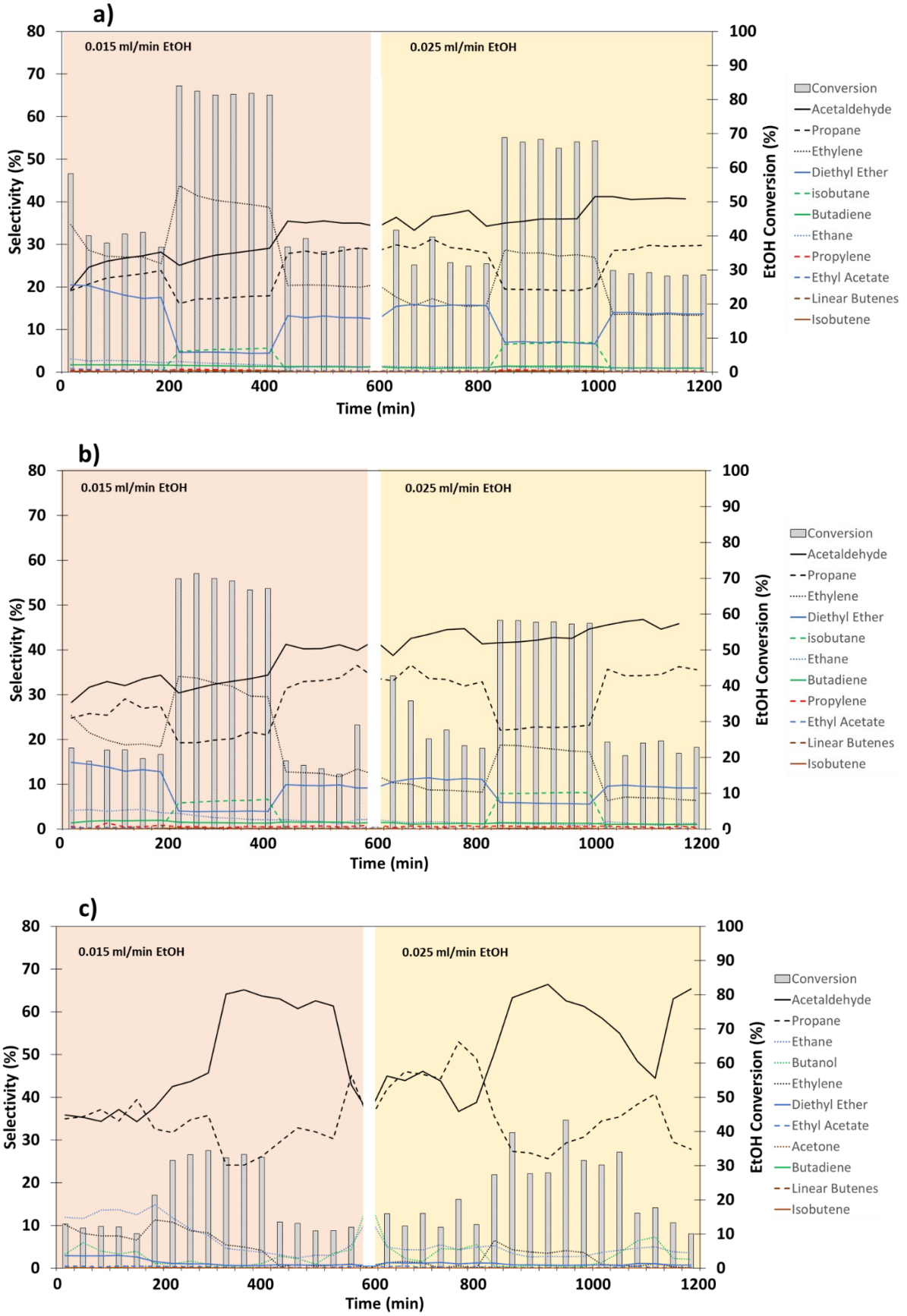

Figure 89: Product selectivity (%) and ethanol conversion (%) as a function of the reaction time for H^+/Zn-MFI (a), H^+-K^+/Zn-MFI (b) and K^+/Zn-MFI (c), obtained from reactions carried out over temperature ramps (350-400-350 °C) at 0.015 and 0.025 ml/min flow rate and using approx. 100 mg of catalyst.

7.2.3.5. Discussion on the Reaction Pathways

Based on the results obtained from the experiments, it can be concluded that the zincosilicate catalysts provide a more selective and efficient way to produce acetaldehyde from ethanol dehydrogenation, compared to a ZnO-impregnated zeolite catalyst. It was observed that the Zn-MFI catalysts became more selective to acetaldehyde with increasing K^+ exchange level, most likely due to the loss of Brønsted acid sites. The latter is instead responsible for the formation of ethylene (and diethyl ether).[72], [73] The reaction mechanisms that take place on the active sites of the catalyst during ethylene and acetaldehyde formation are represented in Scheme 9. Scheme 9(a) shows the conversion of ethanol into ethylene over a Brønsted acid site. This reaction is generally accepted to proceed through the intermediacy of a surface-bound ethoxide species, followed by elimination of ethylene and the reformation of the BAS.[74] As the Brønsted acid sites present in the zincosilicate catalysts are not as strong as they would be in an aluminosilicate framework,[19], [20], [75], [76] zincosilicates produce ethylene to a lower extent. Additionally, Brønsted acidity could also derive from silanol species (e.g. defect sites in the zeotypes). The latter have been observed by Qi et al. to catalyse the dehydration of ethanol to ethylene with 97 % selectivity.[65] The conversion to acetaldehyde (Scheme 9(b)) is proposed to occur on the Lewis acid sites[77] through the formation of a zinc-ethoxide. Subsequently, one of the hydrogen atoms of the CH_2 group reacts with the hydroxyl proton, and the reaction proceeds with the elimination of H_2 and the formation of acetaldehyde.[78] The suppression of the Brønsted acidity and the defect-healing effect provided by extra-framework K^+ species is thought to be responsible for the change in product selectivity distribution between H^+/Zn ZSM-5, H^+-K^+/Zn-MFI and K^+/Zn-MFI.

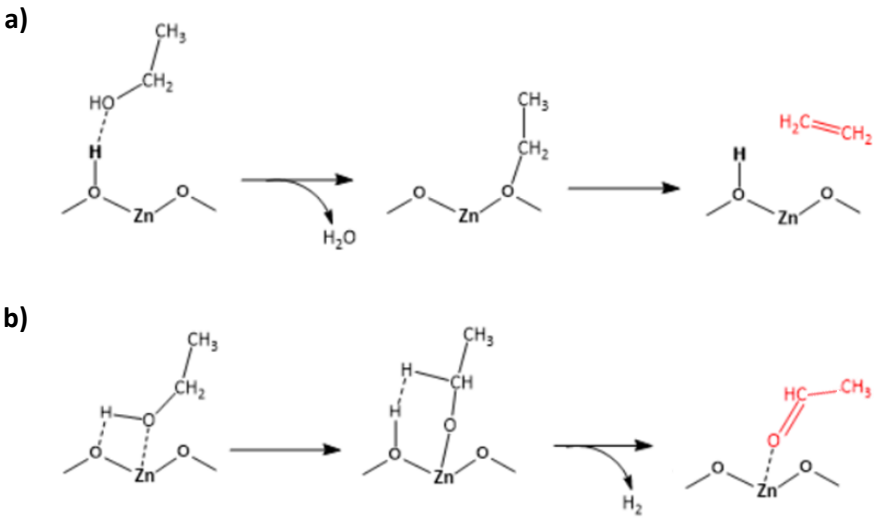

Scheme 9: Mechanisms for the conversion of ethanol to ethylene over a Brønsted acid site (a) or to acetaldehyde over a Lewis acid site (b).

The reactions carried out for 20 and 50 hours highlighted that, in addition to the production of ethylene and acetaldehyde, propane could also be formed and even become the second main product for K^+/Zn-MFI and H^+-K^+/Zn-MFI. Usually, the production of short-chain paraffins from ethanol over zeolites can be achieved with low selectivity, as a secondary by-product from the conversion of ethanol into ethylene or higher hydrocarbons.[79]–[81] In particular, H^+/ZSM-5 and transition metal-exchanged ZSM-5 catalysts were observed to produce propane at 350 °C; however, the selectivity to propane was always lower compared to ethylene, olefins or longer-chain paraffins.[79], [81] From our experiments, the production of propane was favoured by lower temperature (350 °C), as its selectivity decreased at 400 °C (Figure 89). Moreover, the catalyst containing a higher amount of K^+ showed an increase in selectivity to propane up to 40%. The production of propane from ethanol was not reported by Qi et al. for their Zn-substituted BEA catalyst[23] and was reported with only very low selectivity (< 5 %) by Yan et al. for their Zn-MWW catalyst.[20] We hypothesise that the high production of propane that was observed for our zincosilicate catalysts is due to the presence of Zn species in framework positions, and enhanced by the extra-framework K^+ cations. A reaction mechanism for the production of propane from ethanol is proposed in Scheme 10. Two different reaction pathways are suggested: one starting from the dehydrogenation of ethanol to acetaldehyde (represented in green) and its decomposition to form -CH_3 adsorbed onto the catalyst, which then reacts with another ethanol molecule to form propane. Further dehydrogenation of the latter could also lead to the formation of propylene. Alternatively, ethanol could be converted to ethyl acetate and subsequently acetone by ketonisation (represented in red). The hydrogenation of acetone forms isopropyl alcohol, which could undergo dehydration to propylene and, finally, hydrogenation to propane.[82] However, another reaction that can take place from ethyl acetate is its decomposition into ethylene, CO_2, H_2, and CH_3 species[83] adsorbed onto the catalyst, which then would follow the reaction pathway represented in green. The likelihood of the two different reaction pathways was evaluated qualitatively considering the products detected by GC-MS.

Figure 87 and Figure 89 show that acetaldehyde and propane follow the same trend, with both products' selectivity increasing with time. Additionally, a decrease in both acetaldehyde and propane is observed at high temperature (400 °C). This could suggest that the formation of propane derives from acetaldehyde decomposition (mechanism reported in green) and it is therefore dependent on the amount of acetaldehyde produced during the reaction. On the other hand, ethyl acetate is only detected in low amounts in H^+/Zn-MFI and acetone and isopropyl alcohol are not detected at all. However, a very fast consumption of these products during the reaction could be hypothesised to explain their absence in the product distribution.

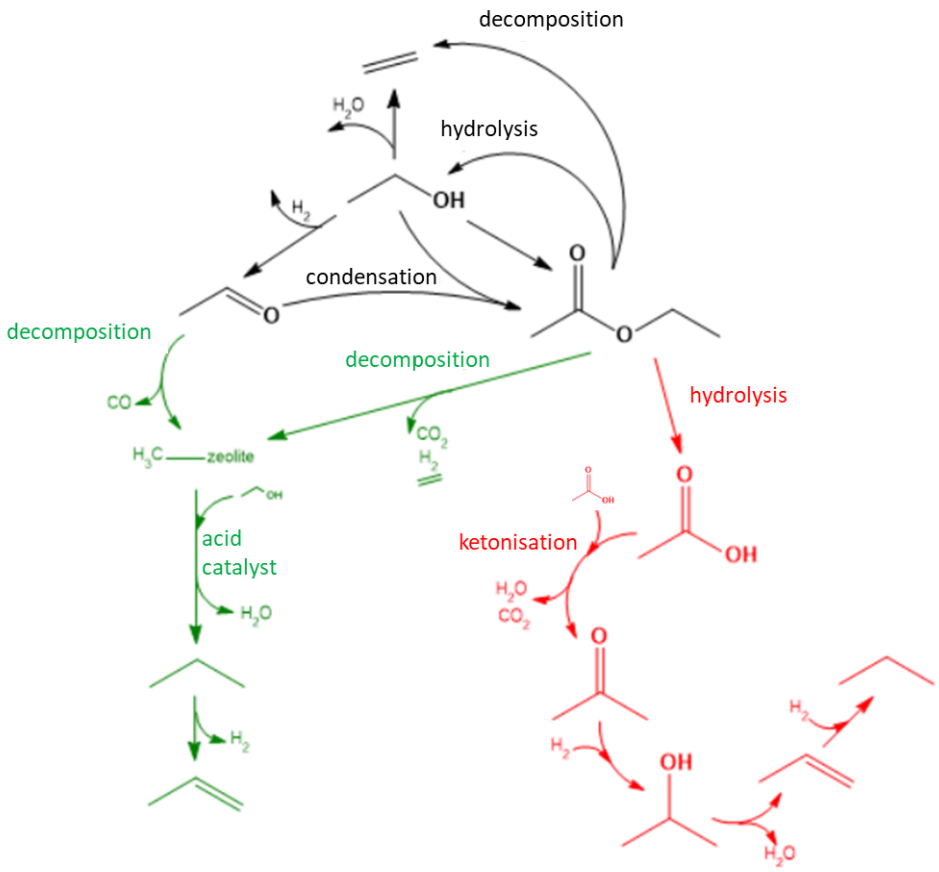

Scheme 10: Proposed reaction pathways for the conversion of ethanol to propene starting from acetaldehyde decomposition (green) or ethyl acetate decomposition (red).

The product distribution for the ethanol conversion reaction observed for our zincosilicate catalysts shows similarities with other results reported in the literature. A decrease in the formation of ethylene and diethyl ether with time was observed by Qi et al. for the ethanol conversion reaction carried out at 320 °C using Zn-substituted de-aluminated BEA catalysts.[23] The authors also report that the formation of acetaldehyde steadily increases throughout the experiment, until it reaches a plateau at approximately 60% of acetaldehyde selectivity. The time necessary to obtain the plateau was observed to decrease with the Zn loading of the catalysts.[23] Our results follow a very similar trend, with acetaldehyde becoming the favoured product, more rapidly when a lower number of silanol/Brønsted acid sites are available. The results obtained by Yan et al. for ethanol conversion performed over Zn-MWW (at 400 °C) are also in line with these observations. In particular, a steady increase in the production of acetaldehyde (up to 51% selectivity) and decrease in the formation of ethylene (13% selectivity) was reported for the zincosilicate catalyst.[20]

In Section 9.6 of the Appendix the results of an EtOH conversion experiments carried out using CH_4 as carrier gas instead of N_2 are reported. This “co-processing” experiment was attempted to see if the production of acetaldehyde would increase by adding another C1 source to the feed. However, the results showed a higher production of diethyl ether instead.

7.3. Chapter 7 Conclusions

The study of zincosilicate zeotypes as Lewis acid catalysts revealed that these materials can efficiently promote reactions such as the dehydrogenation of ethanol to acetaldehyde at 350 °C or 400 °C. The conversion of ethanol was highly selective for Zn-MFI samples containing K^+ cations in extra-framework positions. It was observed that the selectivity to acetaldehyde was nearly double in the K^+/Zn-MFI catalyst compared to H^+/Zn-MFI, under certain reaction conditions. However, the ethanol conversion in the latter could reach values up to three times higher than the K^+-exchanged counterpart and, conseqently, showed superior productivity values. In the K^+/Zn-MFI catalyst the effect of the exchanged K^+ species is the suppression of Brønsted acidity. Consequently, only the reactions activated by the framework-Zn Lewis acid sites can take place. The substantially lower conversion values could be due to the presence of spectator K^+ species which occupy the space in the framework channels and pores, making it more difficult for ethanol molecules to reach the active sites. The best trade-off behaviour between the high activity of a ZnO-impregnated ZSM-5 zeolite and the remarkable selectivity of a K^+/Zn-MFI catalyst was observed for the H^+-K^+/Zn-MFI catalyst, with an acetaldehyde productivity of 4.2 $mmol_{AcH}/mmol_{Zn} \cdot min$ at 400 °C and 0.025 ml/min ethanol flow rate. The ethanol conversion for this material is considerably higher than K^+/Zn-MFI and the second most selective to acetaldehyde in the series of catalysts studied. Different reaction conditions were explored in order to find the best ones to ensure the highest performance of the materials. From the experiments it emerged that acetaldehyde benefits from a faster flow of ethanol; this may be due to the fact that acetaldehyde forms quickly and therefore does not require high residence time of ethanol in the catalyst. On the other hand, the formation of propane is promoted by a slower ethanol flow rate.[82] The production of propane is also favoured by lower reaction temperatures (350 °C).

The Prins condensation reaction between β-pinene and paraformaldehyde to produce nopol and the epoxidation reaction of 1-hexene with H_2O_2 to produce 1-epoxyhexane were also carried out in order to assess the potential of zincosilicate MFI zeotypes to promote Lewis-acid catalysed reactions. The results obtained showed low selectivity to the target products for both reactions. In the case of the β-pinene/paraformaldehyde condensation, the low activity of the catalysts, also observed for a metal-exchanged ZSM-5 zeolite, could be due to the structural properties of the MFI framework type, with channels too small to enable the efficient formation of nopol. Nevertheless, the results obtained provide the evidence of the potential of Zn-substituted zeotypes for this application, so far only reported for the mesoporous Zn-Al MCM-41,[52] showing that framework Zn^{II} sites are active and their incorporation into a framework containing larger channels could deliver promising results in this application.

The epoxidation of 1-hexene using H_2O_2 was successfully performed using TS-1, an already well-established catalyst for this reaction.[31] Under the same reaction conditions, Zn-substituted MFI catalysts exhibited considerably lower selectivity values. Ti^{IV}-based catalysts are d^0 Lewis acids in their highest oxidation state, therefore they easily bond to ligands and facilitate the heterolysis of hydrogen peroxide. This makes them optimal alkene epoxidation catalysts.[84] On the other hand, Zn^{II} is a d^{10} species, making the bond to the alkene and interaction with hydrogen peroxide more challenging.

Chapter 7 Bibliography

[1] M. Taramasso, G. Perego, and B. Notari, “Preparation of porous crystalline synthetic material comprised of silicon and titanium oxides,” 4410501A, 1983.

[2] V. Russo, R. Tesser, E. Santacesaria, and M. Di Serio, “Chemical and Technical Aspects of Propene Oxide Production via Hydrogen Peroxide (HPPO Process),” *Ind. Eng. Chem. Res.*, 52, 3, pp. 1168–1178, **2013**, doi: 10.1021/IE3023862.

[3] H. Y. Luo, J. D. Lewis, and Y. Román-Leshkov, “Lewis Acid Zeolites for Biomass Conversion: Perspectives and Challenges on Reactivity, Synthesis, and Stability,” *Annu. Rev. Chem. Biomol. Eng.*, 7, 1, pp. 663–692, **2016**, doi: 10.1146/annurev-chembioeng-080615-034551.

[4] M. Moliner, “State of the art of Lewis acid-containing zeolites: Lessons from fine chemistry to new biomass transformation processes,” *Dalton Transactions*, 43, 11. Royal Society of Chemistry, pp. 4197–4208, Mar. 21, 2014, doi: 10.1039/c3dt52293h.

[5] P. Y. Dapsens, C. Mondelli, and J. Pérez-Ramírez, “Design of Lewis-acid centres in zeolitic matrices for the conversion of renewables,” *Chemical Society Reviews*, 44, 20. Royal Society of Chemistry, pp. 7025–7043, Oct. 21, 2015, doi: 10.1039/c5cs00028a.

[6] M. Boronat, A. Corma, M. Renz, and P. M. Viruela, “Predicting the Activity of Single Isolated Lewis Acid Sites in Solid Catalysts,” *Chem. – A Eur. J.*, 12, 27, pp. 7067–7077, **2006**, doi: 10.1002/CHEM.200600478.

[7] H. Y. Luo, L. Bui, W. R. Gunther, E. Min, and Y. Román-Leshkov, “Synthesis and catalytic activity of Sn-MFI nanosheets for the baeyer-villiger oxidation of cyclic ketones,” *ACS Catal.*, 2, 12, pp. 2695–2699, **2012**, doi: 10.1021/cs300543z.

[8] E. Peeters, G. Pomalaza, I. Khalil, A. Detaille, D. P. Debecker, A. P. Douvalis, M. Dusselier, B. F. Sels, “Highly Dispersed Sn-beta Zeolites as Active Catalysts for Baeyer–Villiger Oxidation: The Role of Mobile, In Situ Sn(II)O Species in Solid-State Stannation,” *ACS Catal.*, 11, 10, pp. 5984–5998, **2021**, doi: 10.1021/ACSCATAL.1C00435.

[9] M. Moliner, Y. Román-Leshkov, and M. E. Davis, “Tin-containing zeolites are highly active catalysts for the isomerization of glucose in water,” *Proc. Natl. Acad. Sci.*, 107, 14, pp. 6164–6168, **2010**, doi: 10.1073/PNAS.1002358107.

[10] P. Wolf, M. Valla, A. J. Rossini, A. Comas-Vives, F. Núñez-Zarur, B. Malaman, A. Lesage, L. Emsley, C. Copéret, I. Hermans, “NMR Signatures of the Active Sites in Sn-β Zeolite,” *Angew. Chemie*, 126, 38, pp. 10343–10347, **2014**, doi: 10.1002/ange.201403905.

[11] R. Gounder and M. E. Davis, “Monosaccharide and disaccharide isomerization over Lewis acid sites in hydrophobic and hydrophilic molecular sieves,” *J. Catal.*, 308, pp. 176–188, **2013**, doi: 10.1016/J.JCAT.2013.06.016.

[12] Mercedes Boronat, Avelino Corma, M. Renz, “Mechanism of the Meerwein−Ponndorf−Verley−Oppenauer (MPVO) Redox Equilibrium on Sn− and Zr−Beta Zeolite Catalysts,” *J. Phys. Chem. B*, 110, 42, pp. 21168–21174, **2006**, doi: 10.1021/JP063249X.

[13] C. M. Osmundsen, M. S. Holm, S. Dahl, and E. Taarning, “Tin-containing silicates: structure–activity relations,” *Proc. R. Soc. A*, 468, pp. 2000–2016, **2012**, doi: 10.1098/rspa.2012.0047.

[14] C. M. Lew, N. Rajabbeigi, and M. Tsapatsis, “Tin-containing zeolite for the isomerization of cellulosic sugars,” *Microporous Mesoporous Mater.*, 153, pp. 55–58, **2012**, doi: 10.1016/J.MICROMESO.2011.12.020.

[15] J. D. Lewis, S. Van de Vyver, and Y. Román-Leshkov, “Acid–Base Pairs in Lewis Acidic Zeolites

Promote Direct Aldol Reactions by Soft Enolization," *Angew. Chemie*, 127, 34, pp. 9973–9976, **2015**, doi: 10.1002/ANGE.201502939.

[16] J. J. Pacheco and M. E. Davis, "Synthesis of terephthalic acid via Diels-Alder reactions with ethylene and oxidized variants of 5-hydroxymethylfurfural," *Proc. Natl. Acad. Sci. U. S. A.*, 111, 23, pp. 8363–8367, **2014**, doi: 10.1073/pnas.1408345111.

[17] S. Kowalak, E. Szymkowiak, I. Lehmann, and G. Giordano, "Catalytic properties of MFI zincosilicates," in *Studies in Surface Science and Catalysis*, **2001**, 135, p. 311, doi: 10.1016/S0167-2991(01)81700-6.

[18] S. Kowalak, E. Janiszewska, M. Gierczyliska, V. l. Dolata, N. Evmiridis, T. Katranas, A. Vlessidis, V. Tsiatouras, F. Roessner, E. Schneider "Catalytic activity of zincosilicate MFI for the dehydrogenation of hydrocarbons," *Stud. Surf. Sci. Catal.*, 154, pp. 2200–2207, **2004**, doi: 10.1016/S0167-2991(04)80477-4.

[19] M. Orazov and M. Davis, "Catalysis by framework zinc in silica-based molecular sieves," *Chem. Sci.*, 7, pp. 2264–2274, **2016**, doi: 10.1039/C5SC03889H.

[20] W. Yan, X. Shibo, D. Yonghua, M. K. Schreyer, T. S. Xing, L. Yan, A. Borgna "Heteroatomic Zn-MWW Zeolite Developed for Catalytic Dehydrogenation Reactions: A Combined Experimental and DFT Study," *ChemCatChem*, 10, 14, pp. 3078–3085, **2018**, doi: 10.1002/cctc.201800199.

[21] J. W. Harris, J. S. Bates, B. C. Bukowski, J. Greeley, and R. Gounder, "Opportunities in Catalysis over Metal-Zeotypes Enabled by Descriptions of Active Centers Beyond Their Binding Site," *ACS Catal.*, 10, 16, pp. 9476–9495, **2020**, doi: 10.1021/ACSCATAL.0C02102.

[22] B. A. Johnson, J. R. Di Iorio, and Y. Román-Leshkov, "Tailoring Distinct Reactive Environments in Lewis Acid Zeolites for Liquid Phase Catalysis," *Accounts Mater. Res.*, 2, 11, pp. 1033–1046, **2021**, doi: 10.1021/ACCOUNTSMR.1C00146.

[23] L. Qi, Y. Zhang, M. A. Conrad, C. K. Russell, J. Miller, and A. T. Bell, "Ethanol Conversion to Butadiene over Isolated Zinc and Yttrium Sites Grafted onto Dealuminated Beta Zeolite," *J. Am. Chem. Soc.*, 142, 34, pp. 14674–14687, **2020**, doi: 10.1021/jacs.0c06906.

[24] X. Dou, W. Li, C. Zhu, X. Jiang, H. M. Chang, and H. Jameel, "Cleavage of aryl-ether bonds in lignin model compounds using a Co-Zn-beta catalyst," *RSC Adv.*, 10, 71, pp. 43599–43606, **2020**, doi: 10.1039/d0ra08121c.

[25] X. Dou, X. Jiangb, W. Lia, C. Zhua, Q. Liuc, Q. Lud, X. Zhenge, H. Changb, H. Jameel "Highly efficient conversion of Kraft lignin into liquid fuels with a Co-Zn-beta zeolite catalyst," *Appl. Catal. B Environ.*, 268, p. 118429, **2020**, doi: 10.1016/j.apcatb.2019.118429.

[26] H. Li, B. Xu, B. Deng, X. Yan, and Y. Zheng, "Epoxidation of 1-hexene with hydrogen peroxide over nitrogen-incorporated TS-1 zeolite," *Catal. Commun.*, 46, pp. 224–227, **2014**, doi: 10.1016/j.catcom.2013.12.023.

[27] V. S. Marakatti, A. B. Halgeri, and G. V. Shanbhag, "Metal ion-exchanged zeolites as solid acid catalysts for the green synthesis of nopol from Prins reaction," *Catal. Sci. Technol.*, 4, 11, pp. 4065–4074, **2014**, doi: 10.1039/c4cy00596a.

[28] S. J. Raynes and R. A. Taylor, "Zinc oxide-modified mordenite as an effective catalyst for the dehydrogenation of (bio)ethanol to acetaldehyde," *Sustain. Energy Fuels*, 5, 7, pp. 2136–2148, **2021**, doi: 10.1039/d1se00091h.

[29] G. Grigoropoulou, J. H. Clark, and J. A. Elings, "Recent developments on the epoxidation of alkenes using hydrogen peroxide as an oxidant," *Green Chem.*, 5, 1, pp. 1–7, **2003**, doi: 10.1039/b208925b.

[30] V. Smeets, E. M. Gaigneaux, and D. P. Debecker, "Titanosilicate Epoxidation Catalysts: A

Review of Challenges and Opportunities," *ChemCatChem*, **2021**, doi: 10.1002/CCTC.202101132.

[31] G. Bellussi, A. Carati, M. Clerici, G. Maddinelli, and R. Millini, "Reactions of titanium silicalite with protic molecules and hydrogen peroxide," *J. Catal.*, 333, 1, pp. 220–230, **1992**.

[32] M. G. Clerici and P. Ingallina, "Epoxidation of Lower Olefins with Hydrogen Peroxide and Titanium Silicalite," *J. Catal.*, 140, 1, pp. 71–83, **1993**.

[33] W. Wu, D. T. Tran, S. Cheng, Y. Zhang, N. Li, H. Chen, Y. H. Chin, L. Yao, D. Liu, "Local environment and catalytic property of External Lewis acid sites in hierarchical lamellar titanium Silicalite-1 zeolites," *Microporous Mesoporous Mater.*, 311, p. 110710, **2021**, doi: 10.1016/J.MICROMESO.2020.110710.

[34] Y. Huo, Y. Zhang, W. Xu, K. Tang, X. Lu, R. Ma, Y. Fu, W. Zhu "Acid-Modulated Synthesis of Ti-MWW Zeolites with Rich Framework Ti Species for Efficient Epoxidation," *Ind. Eng. Chem. Res.*, 59, 45, pp. 19929–19937, **2020**, doi: 10.1021/ACS.IECR.0C03518.

[35] G. Sastre and A. Corma, "Relation between structure and Lewis acidity of Ti-Beta and TS-1 zeolites A quantum-chemical study," *Chem. Phys. Lett.*, 302, 5–6, pp. 447–453, **1999**.

[36] Q. Lei "Tandem Lewis acid catalysis for the conversion of alkenes to 1,2-diols in the confined space of bifunctional TiSn-Beta zeolite," *Chinese J. Catal.*, 42, 7, pp. 1176–1184, **2021**, doi: 10.1016/S1872-2067(20)63734-2.

[37] C. P. Gordon, H. Engler, A. S. Tragl, M. Plodinec, T. Lunkenbein, A. Berkessel, J. H. Teles, A. Parvulescu, C. Copéret "Efficient epoxidation over dinuclear sites in titanium silicalite-1," *Nature*, 586, 7831, pp. 708–713, **2020**, doi: 10.1038/s41586-020-2826-3.

[38] D. T. Bregante and D. W. Flaherty, "Periodic Trends in Olefin Epoxidation over Group IV and v Framework-Substituted Zeolite Catalysts: A Kinetic and Spectroscopic Study," *J. Am. Chem. Soc.*, 139, 20, pp. 6888–6898, **2017**, doi: 10.1021/jacs.7b01422.

[39] B. Qi "Catalytic epoxidation of alkenes with 30% H2O2 over Mn2+ -exchanged zeolites," *J. Mol. Catal. A. Chem.*, 322, 1–2, pp. 73–79, **2010**, doi: 10.1016/j.molcata.2010.02.019.

[40] S. Bhunia and S. Koner, "Tethering of nickel (II) Schiff-base complex onto mesoporous silica : An efficient heterogeneous catalyst for epoxidation of olefins," *Polyhedron*, 30, 11, pp. 1857–1864, **2011**, doi: 10.1016/j.poly.2011.04.040.

[41] S. H. Jhung, J. H. Lee, A. K. Cheetham, G. Férey, and J. S. Chang, "A shape-selective catalyst for epoxidation of cyclic olefins: The nanoporous nickel phosphate VSB-5," *J. Catal.*, 239, 1, pp. 97–104, **2006**, doi: 10.1016/J.JCAT.2006.01.020.

[42] I. D. D. Ivanchikova, V. Y. Evtushok, O. V. Zalomaeva, D. I. Kolokolov, A. G. Stepanov, and O. Kholdeeva, "Heterogeneous epoxidation of menadione with hydrogen peroxide over zeolite imidazolate framework ZIF-8.," *Dalt. Trans.*, **2020**, doi: 10.1039/D0DT02658A.

[43] H J Prins, "On the Condensarion of Formaldehyde with some Unsaturated Compounds," *KNAW, Proc.*, 22, pp. 51–56, **1919**.

[44] S. P. Bedenko, K. I. Dement'ev, V. F. Tret'yakov, and A. L. Maksimov, "The Prins Reaction over Heterogeneous Catalysts (a Review)," *Pet. Chem.*, 60, 7, pp. 723–730, **2020**, doi: 10.1134/S0965544120070026.

[45] P. B. Venuto and P. S. Landis, "Organic Catalysis over Crystalline Aluminosilicates," *Adv. Catal.*, 18, C, pp. 259–371, **1968**, doi: 10.1016/S0360-0564(08)60430-7.

[46] E. Dumitriu, D. Gongescu, and V. Hulea, "Contribution to The Study of Isobutene Condensation With Formaldehyde Catalyzed By Zeolites," *Stud. Surf. Sci. Catal.*, 78, C, pp. 669–676, **1993**,

doi: 10.1016/S0167-2991(08)63381-9.

[47] E. Dumitriu, V. Hulea, T. Hulea, C. Chelaru, and S. Kaliaguine, “Selective Synthesis of Isoprene by Prins Condensation Using Molecular Sieves,” *Stud. Surf. Sci. Catal.*, 84, C, pp. 1997–2004, **1994**, doi: 10.1016/S0167-2991(08)63760-X.

[48] E. Dumitriu, D. Trong On, and S. Kaliaguine, “Isoprene by Prins Condensation over Acidic Molecular Sieves,” *J. Catal.*, 170, 1, pp. 150–160, **1997**, doi: 10.1006/JCAT.1997.1745.

[49] E. Dumitriu, V. Hulea, I. Fechete, C. Catrinescu, A. Auroux, J. F. Lacaze, C. Guimon, “Prins condensation of isobutylene and formaldehyde over Fe-silicates of MFI structure,” *Appl. Catal. A Gen.*, 181, 1, pp. 15–28, **1999**, doi: 10.1016/S0926-860X(98)00366-4.

[50] E. S. Vasiliadou, S. Li, S. Caratzoulas, and R. F. Lobo, “Formaldehyde-isobutene Prins condensation over MFI-type zeolites,” *Catal. Sci. Technol.*, 8, 22, pp. 5794–5806, **2018**, doi: 10.1039/c8cy01667d.

[51] S. P. Bedenko, A. A. Kozhevnikov, K. I. Dement’ev, V. F. Tret’yakov, and A. L. Maximov, “The Prins condensation between i-butene and formaldehyde over modified BEA and MFI zeolites in liquid phase,” *Catal. Commun.*, 138, p. 105965, **2020**, doi: 10.1016/j.catcom.2020.105965.

[52] M. Selvaraj and S. Kawi, “Highly selective synthesis of nopol over mesoporous and microporous solid acid catalysts,” *J. Mol. Catal. A Chem.*, 246, 1–2, pp. 218–222, **2006**, doi: 10.1016/J.MOLCATA.2005.10.033.

[53] J. Wang, S. Jaenicke, G. K. Chuah, W. Hua, Y. Yue, and Z. Gao, “Acidity and porosity modulation of MWW type zeolites for Nopol production by Prins condensation,” *Catal. Commun.*, 12, 12, pp. 1131–1135, **2011**, doi: 10.1016/j.catcom.2011.03.034.

[54] A. Corma, S. Iborra, M. Mifsud, and M. Renz, “Mesoporous molecular sieve Sn-MCM-41 as Baeyer-Villiger oxidation catalyst for sterically demanding aromatic and α,β-unsaturated aldehydes,” *ARKIVOC*, 9, pp. 124–132, **2005**.

[55] E. A. Alarcón, L. Correa, C. Montes, and A. L. Villa, “Nopol production over Sn-MCM-41 synthesized by different procedures – Solvent effects,” *Microporous Mesoporous Mater.*, 136, 1–3, pp. 59–67, **2010**, doi: 10.1016/J.MICROMESO.2010.07.021.

[56] D. M. Do, S. Jaenicke, and G. K. Chuah, “Mesoporous Zr-SBA-15 as a green solid acid catalyst for the Prins reaction,” *Catal. Sci. Technol.*, 2, 7, pp. 1417–1424, **2012**, doi: 10.1039/c2cy20084h.

[57] M. K. Yadav and R. V. Jasra, “Synthesis of nopol from β-pinene using ZnCl2 impregnated Indian Montmorillonite,” *Catal. Commun.*, 7, 11, pp. 889–895, **2006**, doi: 10.1016/J.CATCOM.2006.04.002.

[58] J. Sun and Y. Wang, “Recent Advances in Catalytic Conversion of Ethanol to Chemicals,” *ACS Catal.*, 4, 4, pp. 1078–1090, **2014**, doi: 10.1021/CS4011343.

[59] R. A. Dagle, A. D. Winkelman, K. K. Ramasamy, V. L. Dagle, and R. S. Weber, “Ethanol as a Renewable Building Block for Fuels and Chemicals,” *Ind. Eng. Chem. Res.*, 59, 11, pp. 4843–4853, **2020**, doi: 10.1021/ACS.IECR.9B05729.

[60] I. Takahara, M. Saito, M. Inaba, and K. Murata, “Dehydration of Ethanol into Ethylene over Solid Acid Catalysts,” *Catal. Letters*, 105, 3, pp. 249–252, **2005**, doi: 10.1007/S10562-005-8698-1.

[61] R. Le Van Mao, P. Levesque, G. McLaughlin, and L. H. Dao, “Ethylene from ethanol over zeolite catalysts,” *Appl. Catal.*, 34, C, pp. 163–179, **1987**, doi: 10.1016/S0166-9834(00)82453-7.

[62] Z. Song, A. Takahashi, N. Mimura, and T. Fujitani, “Production of Propylene from Ethanol Over

ZSM-5 Zeolites," *Catal. Lett. 2009 1313*, 131, 3, pp. 364–369, **2009**, doi: 10.1007/S10562-009-0071-3.

[63] Jifeng Pang *et al.*, "Advances in catalytic dehydrogenation of ethanol to acetaldehyde," *Green Chem.*, **2021**, doi: 10.1039/D1GC02799A.

[64] J. Pang, M. Zheng, C. Wang, X. Yang, H. Liu, X. Hua, J. Sun, Y. Wang, T. Zhang "Hierarchical Echinus-like Cu-MFI Catalysts for Ethanol Dehydrogenation," *ACS Catal.*, 10, 22, pp. 13624–13629, **2020**, doi: 10.1021/ACSCATAL.0C03860.

[65] L. Qi, Y. Zhang, M. A. Conrad, C. K. Russell, J. Miller, and A. T. Bell, "Ethanol Conversion to Butadiene over Isolated Zinc and Yttrium Sites Grafted onto Dealuminated Beta Zeolite," *J. Am. Chem. Soc.*, 142, 34, pp. 14674–14687, **2020**, doi: 10.1021/jacs.0c06906.

[66] P. Lanzafame, K. Barbera, S. Perathoner, G. Centi, A. Aloise, M. Migliori, A. MacArio, J. B. Nagy, G. Giordano "The role of acid sites induced by defects in the etherification of HMF on Silicalite-1 catalysts," *J. Catal.*, 330, pp. 558–568, **2015**, doi: 10.1016/J.JCAT.2015.07.028.

[67] J. Zhang, X. Zhu, G. Wang, P. Wang, Z. Meng, and C. Li, "The origin of the activity and selectivity of silicalite-1 zeolite for toluene methylation to para-xylene," *Chem. Eng. J.*, 327, pp. 278–285, **2017**, doi: 10.1016/J.CEJ.2017.06.114.

[68] I. C. Medeiros-Costa, E. Dib, N. Nesterenko, J. P. Dath, J. P. Gilson, and S. Mintova, "Silanol defect engineering and healing in zeolites: opportunities to fine-tune their properties and performances," *Chem. Soc. Rev.*, 50, 19, pp. 11156–11179, **2021**, doi: 10.1039/D1CS00395J.

[69] W. A. Lazier and H. Adkins, "DEHYDROGENATION AND DEHYDRATION OF ALCOHOLS OVER A ZINC OXIDE CATALYST," *J. Am. Chem. Soeciety*, 47, p. 2295, **1925**, Accessed: Oct. 15, 2021. [Online]. Available: https://pubs.acs.org/sharingguidelines.

[70] R. Barthos, A. Széchenyi, and F. Solymosi, "Decomposition and Aromatization of Ethanol on ZSM-Based Catalysts," *J. Phys. Chem. B*, 110, 43, pp. 21816–21825, **2006**, doi: 10.1021/jp063522v.

[71] T. Riittonen, E. Toukoniitty, D. K. Madnani, A. Leino, K. Kordas, M. Szabo, A. Sapi, K. Arve, J. Wärnå, J. Mikkola "One-Pot Liquid-Phase Catalytic Conversion of Ethanol to 1-Butanol over Aluminium Oxide—The Effect of the Active Metal on the Selectivity," *Catal. 2012, Vol. 2, Pages 68-84*, 2, 1, pp. 68–84, **2012**, doi: 10.3390/CATAL2010068.

[72] T. K. Phung, L. Proietti Hernández, A. Lagazzo, and G. Busca, "Dehydration of ethanol over zeolites, silica alumina and alumina: Lewis acidity, Brønsted acidity and confinement effects," *Appl. Catal. A Gen.*, 493, pp. 77–89, **2015**, doi: 10.1016/j.apcata.2014.12.047.

[73] F. F. Madeira, N. S. Gnep, P. Magnoux, S. Maury, and N. Cadran, "Ethanol transformation over HFAU, HBEA and HMFI zeolites presenting similar Brønsted acidity," *Appl. Catal. A Gen.*, 367, 1–2, pp. 39–46, **2009**, doi: 10.1016/J.APCATA.2009.07.033.

[74] S. Zeng, J. Li, N. Wang, W. Zhang, Y. Wei, Z. Liu, S. Xu "Investigation of Ethanol Conversion on H-ZSM-5 Zeolite by in Situ Solid-State NMR," *Energy & Fuels*, 35, 15, pp. 12319–12328, **2021**, doi: 10.1021/ACS.ENERGYFUELS.1C02151.

[75] E. H. Yuan, K. Zhang, G. Lu, Z. Mo, and Z. Tang "Structural and Textural Characteristics of Zn-Containing ZSM-5 Zeolites and Application for the Selective Catalytic Reduction of NOx with NH3 at High Temperatures," *Catal. Surv. from Asia*, 20, 1, pp. 41–52, **2016**, doi: 10.1007/s10563-015-9205-3.

[76] N. Koike, K. Iyoki, S. H. Keoh, W. Chaikittisilp, and T. Okubo, "Synthesis of New Microporous Zincosilicates with CHA Zeolite Topology as Efficient Platforms for Ion-Exchange of Divalent Cations," *Chem. - A Eur. J.*, 24, 4, pp. 808–812, **2018**, doi: 10.1002/chem.201705277.

[77] Y. Huang, B. Wang, H. Yuan, Y. Sun, D. Yang, X. Cui, F. Shi "The catalytic dehydrogenation of ethanol by heterogeneous catalysts," *Catalysis Science and Technology*, 11, 5. Royal Society of Chemistry, pp. 1652–1664, Mar. 07, 2021, doi: 10.1039/d0cy02479a.

[78] L. Qi, Y. Zhang, M. A. Conrad, C. K. Russell, J. Miller, and A. T. Bell, "Ethanol Conversion to Butadiene over Isolated Zinc and Yttrium Sites Grafted onto Dealuminated Beta Zeolite," *Cite This J. Am. Chem. Soc*, 142, pp. 14674–14687, **2020**, doi: 10.1021/jacs.0c06906.

[79] J. Schulz and F. Bandermann, "Conversion of ethanol over metal-exchanged zeolites," *Chem. Eng. Technol.*, 16, 5, pp. 332–337, **1993**, doi: 10.1002/CEAT.270160509.

[80] W. Xia, K. Chen, A. Takahashi, X. Li, X. Mu, L. Liu, I. Nakamura, T. Fujitani "Effects of particle size on catalytic conversion of ethanol to propylene over H-ZSM-5 catalysts—Smaller is better," *Catal. Commun.*, 73, pp. 27–33, **2016**, doi: 10.1016/J.CATCOM.2015.10.008.

[81] R. H. Gil-Horán, J. C. Chavarría-Hernández, P. Quintana-Owen, and · Aída Gutiérrez-Alejandre, "Ethanol Conversion to Short-Chain Olefins Over ZSM-5 Zeolite Catalysts Enhanced with P, Fe, and Ni," *Top. Catal.*, 63, pp. 414–427, **2020**, doi: 10.1007/s11244-020-01229-8.

[82] M. Iwamoto, "Selective catalytic conversion of bio-ethanol to propene: A review of catalysts and reaction pathways," *Catal. Today*, 242, PB, pp. 243–248, **2015**, doi: 10.1016/J.CATTOD.2014.06.031.

[83] T. K. Phung, L. Proietti Hernández, A. Lagazzo, and G. Busca, "Dehydration of ethanol over zeolites, silica alumina and alumina: Lewis acidity, Brønsted acidity and confinement effects," *Appl. Catal. A Gen.*, 493, pp. 77–89, **2015**, doi: 10.1016/J.APCATA.2014.12.047.

[84] K. A. Joergensen, "Transition-metal-catalyzed epoxidations," *Chem. Rev.*, 89, 3, pp. 431–458, **1989**.

8. Chapter 8: Outlook and Conclusions

8.1. Outlook and Conclusions

A simple synthesis strategy was adopted and optimised for the preparation of zinc-substituted MFI samples. The controlled addition of KOH as an inorganic mineralising agent during the preparation of the synthesis gel was beneficial in preventing the formation of structural defects in the form of Si – OH sites and ensure a predominantly closed framework enviroment around the Zn^{II} heteroatoms. This was confirmed by ion-exchange experiments using divalent cations (Ni^{2+}) and ssNMR analyses. A thorough characterisation of the Zn-MFI samples synthesised was carried out using several analysis techniques, and the substitution of Zn^{II} in tetrahedral framework sites was further confirmed. The reactivity of Zn-MFI samples was tested for a range of chemical reactions: methane activation, ethanol dehydrogenation, 1-hexene epoxidation and β-pinene/paraformaldehyde condensation.

Synthesis

The first attempts at the synthesis of Zn-MFI zeotypes using a synthesis method involving pyrrolidine as OSDA[1] delivered poor results in terms of sample purity. A new synthesis strategy was therefore adapted,[2], [3] which allowed for the preparation of highly crystalline and pure Zn-MFI samples. In order to improve the structural properties of the materials, KOH was added during the synthesis. The mineralising agent contributed to a better incorporation of the Zn^{II} heteroatoms and their stabilisation in tetrahedral framework sites. The result of this was a higher ion exchange capacity towards Ni^{2+} (100 %).

The study carried out through ^{1}H - ^{29}Si ssNMR revealed that the Zn-MFI samples prepared using KOH showed a lower amount of defect sites, evaluated as the ratio between Q_4 and Q_3 silicon environments. After calcination, the amount of defects was even lower, with percentages of Q_4 sites close to 100%, whilst the Zn-MFI sample prepared without the addition of KOH contained defects even after calcination. The correlation between the presence of OSDA molecules and the presence of defect sites was revealed through 2D ssNMR studies. Similarly to what was reported by Dib et al.[4], [5] OSDA molecules were observed to interact with framework silicon species. In particular, ^{1}H- ^{29}Si HETCOR analysis showed correlation between Q_3 silicon sites and proton signals assigned to hydrogen bonded $SiOH\cdots^{-}OSi$ species.[6], [7] Interestingly, the intensity of the correlation signals was observed to decrease with the increasing of K^{+} content in the samples. Proton DQ/SQ experiments revealed the presence of correlation between protons belonging to the $SiOH\cdots^{-}OSi$ species and to the OSDA, suggesting that interactions of framework species with TPA^{+} cations are taking place. The presence of TPA^{+} cations requires negatively charged framework sites, which is likely to be the cause of the formation of framework defect sites, in which the $Si\text{-}O^{-}$ sites would charge balance TPA^{+} species. Terminal CH_3 groups of the OSDA were also observed to interact with Q_3 Si sites. Additionally, after calcination, ^{1}H ssNMR analysis on the samples did not show any evidence of $SiOH\cdots^{-}OSi$ signals, due to

elimination of OSDA molecules and subsequent healing effect of the defects during the calcination procedure.

A correlation between the amount of KOH, the presence of OSDA molecules and the formation of structural defects was observed for the first time for Zn-MFI samples. The interaction of the organic molecules with the framework promotes the formation of Si–OH defects, whilst the presence of K^+ hinders it. A competitive behaviour between TPA^+ and K^+ cations as charge-balancing species was observed by means of TGA analysis on uncalcined samples. The studies carried out in this work helped shed some light on the structural characteristics as-synthesised and calcined Zn-MFI samples, alongside the introduction of strategies to optimise the materials. Ultimately, it was shown that microwave-assisted synthesis methods can be applied for the preparation of Zn-MFI zeotypes and drastically reduce the synthesis time.

Characterisation

In addition to routine characterisation techniques such as p-XRD and elemental analysis, which confirmed the crystallinity and composition of the materials, spectroscopic techniques were also applied to the study of Zn-MFI samples. X-ray Absorption Spectroscopy analyses were carried out at the Diamond Light Source Synchrotron facility in Oxfordshire, in order to probe the chemical environment of Zn heteroatoms in the framework. The study elucidated the coordination environment of Zn heteroatoms in the framework in dehydrated and hydrated conditions. The XANES spectra of the two Zn-MFI materials showed minor differences but indicated the presence of coordination with water in the hydrated H^+/Zn-MFI sample. However, no evidence was detected of the formation of fully hydrated extra-framework $[Zn(H_2O)_6]^{2+}$ species. This was confirmed by EXAFS analysis, which revealed that a better fit could be obtained for the hydrated H^+/Zn-MFI sample with the inclusion of 1.75 water molecules, whilst the dehydrated H^+/Zn-MFI material could be satisfactorily fitted without the inclusion of water. As a result of of water coordination, an increase in the bond length of the first Zn-O coordination shell could also be detected. Further work on the data fit would be beneficial to improve the degree of confidence of this conclusion, as the bond length values for hydrated and dehydrated Zn-MFI materials showed some overlap due to the uncertainty on the values.

UV-vis spectroscopy corroborated the results found by XAS, which suggested a tetrahedral coordination for (most of) the Zn^{II} sites. The Zn-MFI samples (prepared without KOH and with different Si:Zn ratios) exhibited an absorption band centred at 210 nm, which corresponds to charge transfer transitions between framework Zn and lattice oxygen species.[9]Diffuse-Reflectance IR spectroscopy studies were able to corroborate that (i) Zn heteroatoms were successfully substituted in the framework, through the observation of a shift towards lower wavenumbers of the bands associated with asymmetrical Si–O–T stretching mode, and (ii) that the zincosilicate materials show the presence of hydrogen-bonding silanol defects, especially in Zn-MFI materials containing lower amounts of K^+

cations.

The morphology, shape and size distribution of the Zn-MFI samples was analysed by means of SEM. From the study it emerged that the crystals of the samples prepared without the addition of KOH have different sizes: among small (500 nm) hexagonal button-like shaped crystals, elongated crystals were present, with sizes one order of magnitude greater. Zn-MFI samples prepared with different amounts of KOH, on the other hand, exhibited a much narrower particle size distribution and the shape of the crystals appeared to be only slightly elongated over one dimension.

Applications

The synthesised Zn-MFI samples were used in various applications to test their reactivity. Initially, they were used as a support for divalent extra-framework Zn^{2+} cations, in order to promote the direct conversion of methane to methanol.[10]–[13] The results of the experiments showed that it was possible to activate methane over ZnVD/Zn-MFI (Si:Zn = 100), however, this result was not reproducible. It also emerged that the higher Lewis acid character of the samples, related to the presence of a higher amount of framework Zn (Si:Zn = 50 and Si:Zn = 25), could not promote the cleavage of a C–H bond of methane. In fact, the results of the experiments carried out using these samples showed strongly physisorbed methane species, alongside unidentified carbon-containing species.

Other applications aimed at the exploitation of the Lewis-acid character induced by the subsitution of Zn^{II} heteroatoms in the framework, such as the epoxidation of 1-hexene with H_2O_2 to 1-epoxyhexane and the Prins condensation reaction of β-pinene and paraformaldehyde to nopol, were studied. For the first, Zn-MFI samples were not particularly active, probably due to the different electronic configuration of Zn^{II} and Ti^{IV} species, generally playing a key role interacting with H_2O_2 and leading to the epoxidation. The β-pinene/paraformaldehyde condensation reaction appeared to take place, however to a low extent in Zn-MFI, with the formation of some by-products. The reason for this was attributed to structural properties of the MFI framework, in particular to the size of the pore openings, perhaps too small to accommodate nopol molecules or transition states of the reaction. Further studies could focus on the use of different Zn-substituted frameworks with bigger pore openings (e.g. CIT-6) to promote this or other Prins condensation reactions.

More promising results were obtained for ethanol conversion experiments. Zinc has already been identified as an active species for the conversion of ethanol to acetaldehyde, in the form of extra-framework ZnO,[14] or as a framework-substituted species.[15], [16] The results of the experiments reported in this work showed that H^+/Zn-MFI and H^+-K^+/Zn-MFI catalysts could deliver good selectivity to acetaldehyde (around 40 %) and high ethanol conversion (> 70 %) at 400 °C. The highest productivity was recorded for the H^+/Zn-MFI catalyst, with 5.1 $mmol_{AcH}/mmol_{Zn}$·min at 400 °C with an ethanol flow rate of 0.025 ml/min. Moreover, the Zn-MFI catalysts appeared to be robust and able to maintain the

same perfomance for 50 hours at 400 °C, as opposed to a ZnO/ZSM-5 catalyst, which showed slowly decreasing conversion with time. Additionally, ethylene and diethyl ether showed the highest selectivity values for ZnO/ZSM-5, with a higher acetaldehyde selectivity observed only after 30 hours. On the contrary, acetaldehyde was the main product from the start of the reaction for the Zn-MFI catalysts. This striking difference was attributed to the combined effects of the presence of residual Brønsted acidity in the ZnO/ZSM-5 catalyst and the absence of it in the Zn-MFI samples. Another aspect that was investigated was the change in reactivity due to the presence of K^+ extra-framework cations. In particular, it was observed that the ethanol conversion decreased with the increasing K^+ content, to approximately 1/3 of the conversion value recorded for the H^+/Zn-MFI catalyst. This behaviour is most likely due to the fact that K^+ cations are not active species in the reaction and their presence prevents the ethanol molecules reaching the active framework-Zn sites. However, the K^+/Zn-MFI catalyst showed the highest selectivity to acetaldehyde (> 60 %) and the lowest to ethylene. The best trade-off between acetaldehyde selectivity, ethanol conversion and catalyst durability was observed for the H^+-K^+/Zn-MFI catalyst. The acetaldehyde productivity for this material was 4.2 $mmol_{AcH}/mmol_{Zn}$ min, corresponding to 250 $mmol_{AcH}/mmol_{Zn}$ h, a value more than 3 times higher than the highest one reported by Raynes et al. for a ZnO/Rb-MOR catalyst at the same temperature of 400 °C (67 $mmol_{AcH}/mmol_{Zn}$ h [14]). The stability and high acetaldehyde productivity of the Zn-MFI catalysts reported in this thesis make them desirable alternatives to commercial copper chromite catalysts, which bear the risk of producing toxic Cr^{6+} species on disposal.[17],[18] Finally, among the products, propane appeared to be formed with non-negligible selectivity (between 20 and 30 %). It was suggested that the decomposition of acetaldehyde could be the reason of the formation of propane, however further studies are required in order to identify a reaction pathway.

Overall, the Zn-MFI catalysts appeared to be significantly active for the conversion of ethanol to acetaldehyde. Further modifications, such as the insertion of other heteroatoms in the framework or in extra-framework positions could improve their performance and enhance their selectivity and/or conversion properties. Additionally, the propane produced could be further dehydrogenated to propene, a highly useful chemical, by introduction of other active sites in the catalysts, creating a bi-functional material. Further studies are also needed in order to better understand the reactivity of the materials in the methane-to-methanol reactions. DFT analysis could be the ideal choice to achieve this and identify the organic species that generate the high-frequency signals in the ^{13}C NMR spectra. The Zn-MFI samples show the potential of promoting Lewis acid-catalysed reactions; therefore, more applications should be screened in order to exploit their properties. As reported by Serrano et al., Lewis acid sites promote the catalytic transfer hydrogenation *via* Meerwein–Ponndorf–Verley reactions.[19] This property has successfully been exploited in Zr-substituted Beta catalysts for the reduction of levulinic acid into γ-valerolactone (GVL) with high yield (99 %).[20] Finally, the preparation of these Zn-substituted zeotypes could be further optimised and extended to different zeolite topologies by

applying novel synthesis methods, such as microwave-assisted synthesis,[21] mechanochemical procedures[22], [23] or disassembly/re-assembly methods.[24], [25]

Chapter 8 Bibliography

[1] Z. Göğebakan and H. Yu, "Crystallization Field and Rate Study for the Synthesis of Ferrierite," *Ind. Eng. Chem. Res.*, 46, 7, pp. 2006–2012, **2007**, doi: 10.1021/IE061013.

[2] N. K. Mal, V. Ramaswamy, P. R. Rajamohanan, and A. V Ramaswamy, "Sn-MFI molecular sieves : synthesis methods , 29Si liquid and solid MAS-NMR , 119Sn static and MAS NMR studies," *Microporous Mater.*, 12, pp. 331–340, **1997**.

[3] Y. G. Kolyagin, A. V. Yakimov, S. Tolborg, P. N. R. Vennestrøm, and I. I. Ivanova, "Application of 119Sn CPMG MAS NMR for Fast Characterization of Sn Sites in Zeolites with Natural 119Sn Isotope Abundance," *J. Phys. Chem. Lett.*, 7, 7, pp. 1249–1253, **2016**, doi: 10.1021/ACS.JPCLETT.6B00249.

[4] E. Dib, J. Grand, A. Gedeon, S. Mintova, and C. Fernandez, "Control the position of framework defects in zeolites by changing the symmetry of organic structure directing agents," *Microporous Mesoporous Mater.*, p. 110899, **2021**, doi: 10.1016/j.micromeso.2021.110899.

[5] E. Dib, J. Grand, S. Mintova, and C. Fernandez, "Structure-Directing Agent Governs the Location of Silanol Defects in Zeolites," *Chem. Mater.*, 27, 22, pp. 7577–7579, **2015**, doi: 10.1021/acs.chemmater.5b03668.

[6] G. Brunklaus, H. Koller, and S. I. Zones, "Defect Models of As-Made High-Silica Zeolites: Clusters of Hydrogen-Bonds and Their Interaction with the Organic Structure-Directing Agents Determined from 1 H Double and Triple Quantum NMR Spectroscopy," *Angew. Chemie Int. Ed.*, 55, 46, pp. 14459–14463, **2016**, doi: 10.1002/anie.201607428.

[7] H. Koller, R. F. Lobo, S. L. Burkett, and M. E. Davis, "SiO ** * *HOSi Hydrogen Bonds in As-Synthesized High-Silica Zeolites," **1995**. Accessed: Nov. 24, 2020. [Online]. Available: https://pubs.acs.org/sharingguidelines.

[8] A. Hagen, K. Hallmeier, C. Hennig, R. Szargan, T. Inui, and F. Roessner, "State of Zn in MFI type zeolites characterized by XANES and EXAFS," in *Studies in Surface Science and Catalysis*, H. K. Beyer, J. B. Nagy, H. G. Karge, and I. Kiricsi, Eds. Elsevier, **1995**, pp. 195–202.

[9] L. Wang, S. Sang, S. Meng, Y. Zhang, Y. Qi, and Z. Liu, "Direct synthesis of Zn-ZSM-5 with novel morphology," *Mater. Lett.*, 61, pp. 1675–1678, **2007**, doi: 10.1016/j.matlet.2006.07.097.

[10] M. A. Shah, S. Raynes, D. C. Apperley, and R. A. Taylor, "Framework Effects on Activation and Functionalisation of Methane in Zinc-Exchanged Zeolites," *ChemPhysChem*, 21, pp. 673–679, **2020**, doi: 10.1002/cphc.201900973.

[11] Y. G. Kolyagin, I. I. Ivanova, V. V. Ordomsky, A. Gedeon, and Y. A. Pirogov, "Methane Activation over Zn-Modified MFI Zeolite: NMR Evidence for Zn−Methyl Surface Species Formation," *J. Phys. Chem. C*, 112, 50, pp. 20065–20069, **2008**, doi: 10.1021/JP8067766.

[12] Y. G. Kolyagin, I. I. Ivanova, and Y. A. Pirogov, "1H and 13C MAS NMR studies of light alkanes activation over MFI zeolite modified by Zn vapour," *Solid State Nucl. Magn. Reson.*, 35, 2, pp. 104–112, **2009**, doi: 10.1016/J.SSNMR.2009.01.005.

[13] A. A. Gabrienko, S. S. Arzumanov, M. V Luzgin, A. G. Stepanov, and V. N. Parmon, "Methane Activation on Zn2+-Exchanged ZSM - 5 Zeolites . The Effect of Molecular Oxygen Addition," *J. Phys. Chem. C*, 119, p. 24910−24918, **2015**, doi: 10.1021/acs.jpcc.5b08759.

[14] S. J. Raynes and R. A. Taylor, “Zinc oxide-modified mordenite as an effective catalyst for the dehydrogenation of (bio)ethanol to acetaldehyde,” *Sustain. Energy Fuels*, 5, 7, pp. 2136–2148, **2021**, doi: 10.1039/d1se00091h.

[15] W. Yan, X. Shibo, D. Yonghua, M. K. Schreyer, T. S. Xing, L. Yan, A. Borgna “Heteroatomic Zn-MWW Zeolite Developed for Catalytic Dehydrogenation Reactions: A Combined Experimental and DFT Study,” *ChemCatChem*, 10, 14, pp. 3078–3085, **2018**, doi: 10.1002/cctc.201800199.

[16] L. Qi, Y. Zhang, M. A. Conrad, C. K. Russell, J. Miller, and A. T. Bell, “Ethanol Conversion to Butadiene over Isolated Zinc and Yttrium Sites Grafted onto Dealuminated Beta Zeolite,” *J. Am. Chem. Soc.*, 142, 34, pp. 14674–14687, **2020**, doi: 10.1021/jacs.0c06906.

[17] E. Santacesaria, G. Carotenuto, R. Tesser, and M. di Serio, “Ethanol dehydrogenation to ethyl acetate by using copper and copper chromite catalysts,” Chemical Engineering Journal, vol. 179, pp. 209–220, Jan. 2012, doi: 10.1016/J.CEJ.2011.10.043.

[18] A. Segawa, A. Nakashima, R. Nojima, N. Yoshida, and M. Okamoto, “Acetaldehyde Production from Ethanol by Eco-Friendly Non-Chromium Catalysts Consisting of Copper and Calcium Silicate,” Industrial and Engineering Chemistry Research, vol. 57, no. 35, pp. 11852–11857, Sep. 2018

[19] D. P. Serrano, J. A. Melero, G. Morales, J. Iglesias, and P. Pizarro, “Progress in the design of zeolite catalysts for biomass conversion into biofuels and bio-based chemicals,” *https://doi.org/10.1080/01614940.2017.1389109*, 60, 1, pp. 1–70, **2017**, doi: 10.1080/01614940.2017.1389109.

[20] J. Wang, S. Jaenicke, and G. K. Chuah, “Zirconium–Beta zeolite as a robust catalyst for the transformation of levulinic acid to γ-valerolactone via Meerwein–Ponndorf–Verley reduction,” *RSC Adv.*, 4, 26, pp. 13481–13489, **2014**, doi: 10.1039/C4RA01120A.

[21] Z. Sun, Y. Yan, G. Li, Y. Zhang, and Y. Tang, “Microwave Influence on Different M − O Bonds During MFI-Type Heteroatom (M) Zeolite Preparation,” *Ind. Eng. Chem. Res.*, 56, 39, pp. 11167–11174, **2017**, doi: 10.1021/acs.iecr.7b03072.

[22] P. Hu, K. Iyoki, H.i Yamada, Y. Yanaba, K. Oharac, N. Katadad, T. Wakihara “Synthesis and characterization of MFI-type zincosilicate zeolites with high zinc content using mechanochemically treated Si–Zn oxide composite,” *Microporous Mesoporous Mater.*, 288, p. 109594, **2019**, doi: 10.1016/J.MICROMESO.2019.109594.

[23] M. H. Nada, E. G. Gillan, and S. C. Larsen, “Mechanochemical reaction pathways in solvent-free synthesis of ZSM-5,” *Microporous Mesoporous Mater.*, 276, September 2018, pp. 23–28, **2019**, doi: 10.1016/j.micromeso.2018.09.009.

[24] P. Elia, M. Opanasenko, P. S. Wheatley, M. Shamzhy, M. Mazur, P. Nachtigall, W. J. Roth, R. E. Morris J. Cejka “The ADOR mechanism for the synthesis of new zeolites,” *Chem. Soc. Rev.*, 44, 20, pp. 7177–7206, **2015**, doi: 10.1039/C5CS00045A.

[25] M. Mazur, V. Kasneryk, J. Přech, F. Brivio, C. Ochoa-Hernández, A. Mayoral, M. Kubů, J. Čejka “Zeolite framework functionalisation by tuneable incorporation of various metals into the IPC-2 zeolite,” *Inorg. Chem. Front.*, 5, 11, pp. 2746–2755, **2018**, doi: 10.1039/c8qi00732b.

9. Appendix

9.1. Synthesis and Characterisation of Zn-TON

The synthesis of Zn-TON was adapted from one of the methods described by Barri and Young.[1] Ludox AS-40 was used as SiO_2 source and was initially mixed with the OSDA, diethylenetriamine (DETA). Subsequently, this mixure was poured into a solution of $Zn(OH)_2$ and NaOH in H_2O and stirred at room temperature. ZSM-22 seeds (0.2 wt% with respect to the amount of SiO_2) were added to the synthesis gel before being transferred into a stainless-steel autoclave. The hydrothermal synthesis was carried out at 175 °C for 2 days under static conditions. After 2 days the autoclave containing the synthesis products was quenched in ice and the products washed with de-ionised water and centrifuged until the pH of the washing water was lower than 8. The products were finally dried at 100 °C overnight. The molar ratios of the synthesis gel were: SiO_2:$Zn(OH)_2$:DETA:NaOH:H_2O=1:0.04:0.82:0.07:14. The products were analysed using pXRD, SEM and ^{29}Si SSNMR.

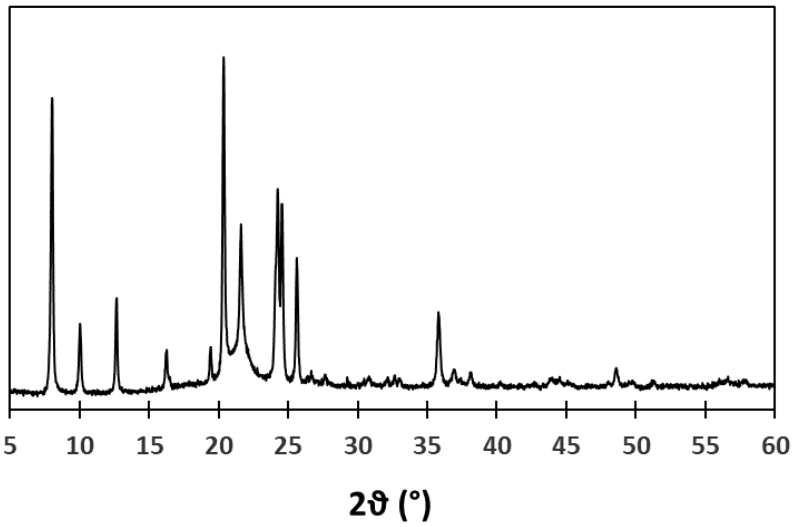

Figure 90: Powder-XRD pattern of Zn-TON, showing the characteristic features of the TON framework type, except for the particularly intense peak at 20 °, belonging to an unidentified impurity.

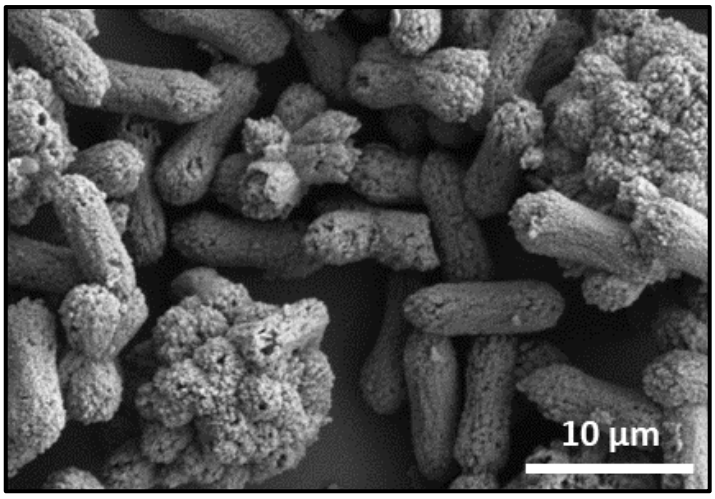

Figure 91: SEM image acquired at 5 kV of Zn-TON crystals, showing elongated structures of approximately 10 µm, made up of smaller particles.

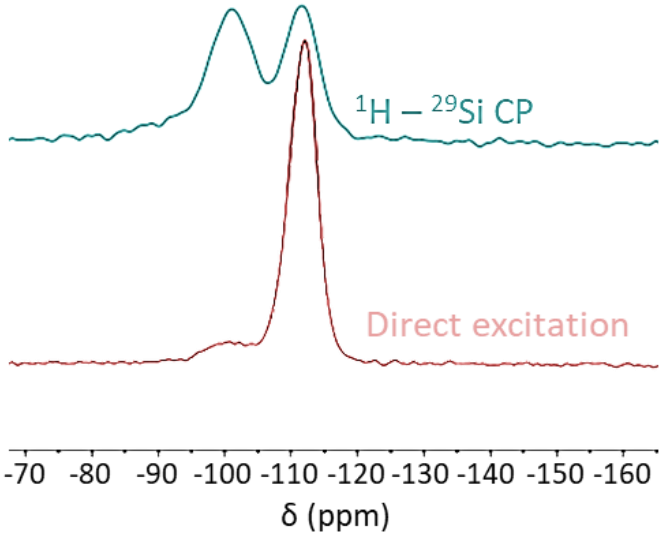

Figure 92: NMR spectra of Zn-TON acquired in ^{1}H – ^{29}Si Cross Polarisation and ^{29}Si Direct Excitation modes, showing Q_4 (-112 ppm) and Q_3 (- 102 ppm) environments around the Si atoms in the framework. The CP signals indicate the presence of Si atoms in close proximity with H atoms, suggesting the presence of a considerable amount of defects.

9.2. Further SEM Analysis of Heteroatom-substituted MFI

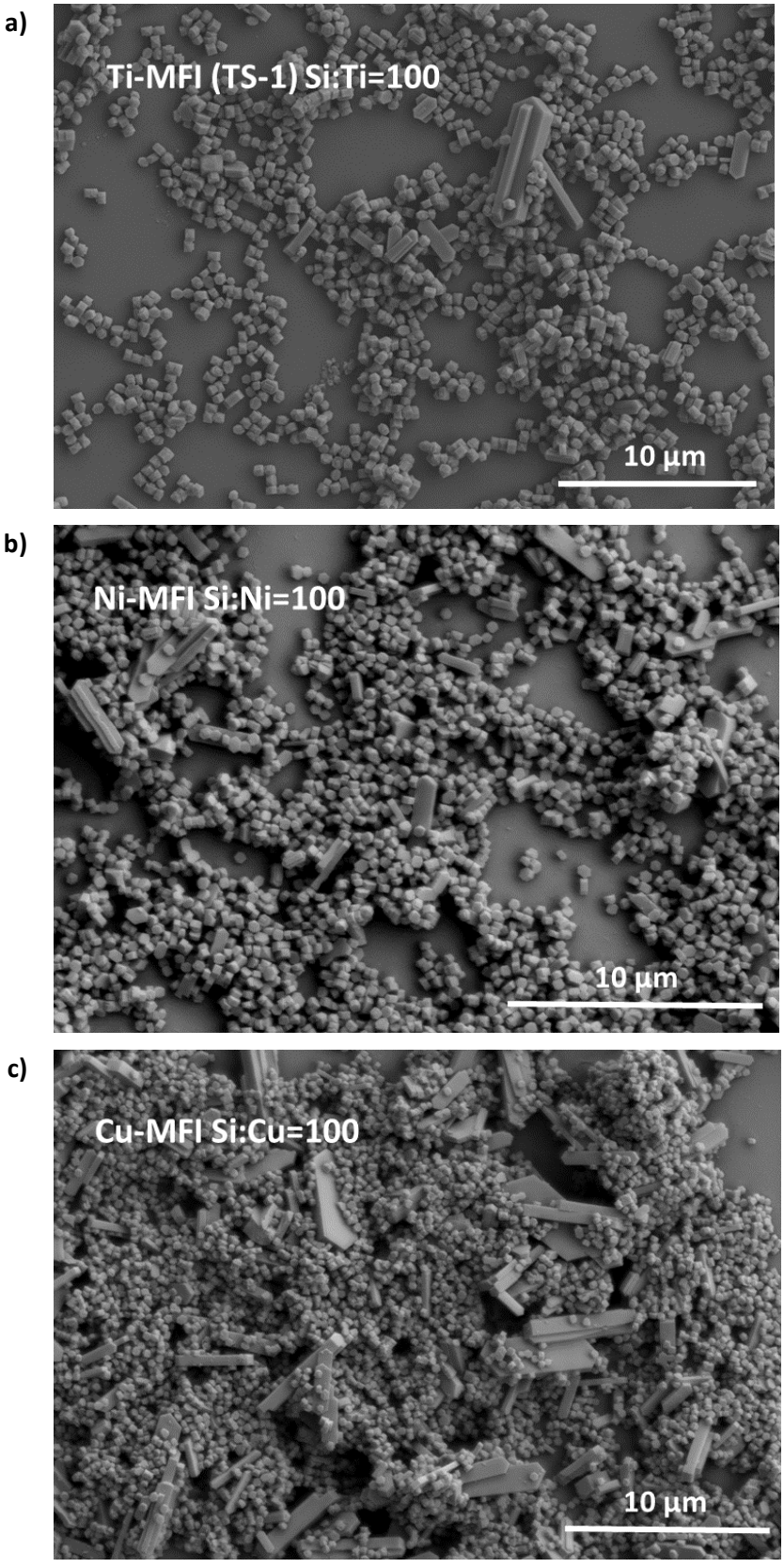

Figure 93: SEM images acquired at 5 kV of heteroatom-substituted MFI materials prepared with Si:T ratios of 100 using Ti (a), Ni (b) and Cu (c), showing the presence of small, hexagonal-shaped crystals alongside elongated particles reaching sizes of approximately 10 µm.

9.3. Further ^{29}Si ssNMR Analysis on Zn-MFI Samples

9.3.1. Zn-MFI Analysed through ^{1}H-^{29}Si CP and ^{29}Si Direct Excitation NMR Experiments

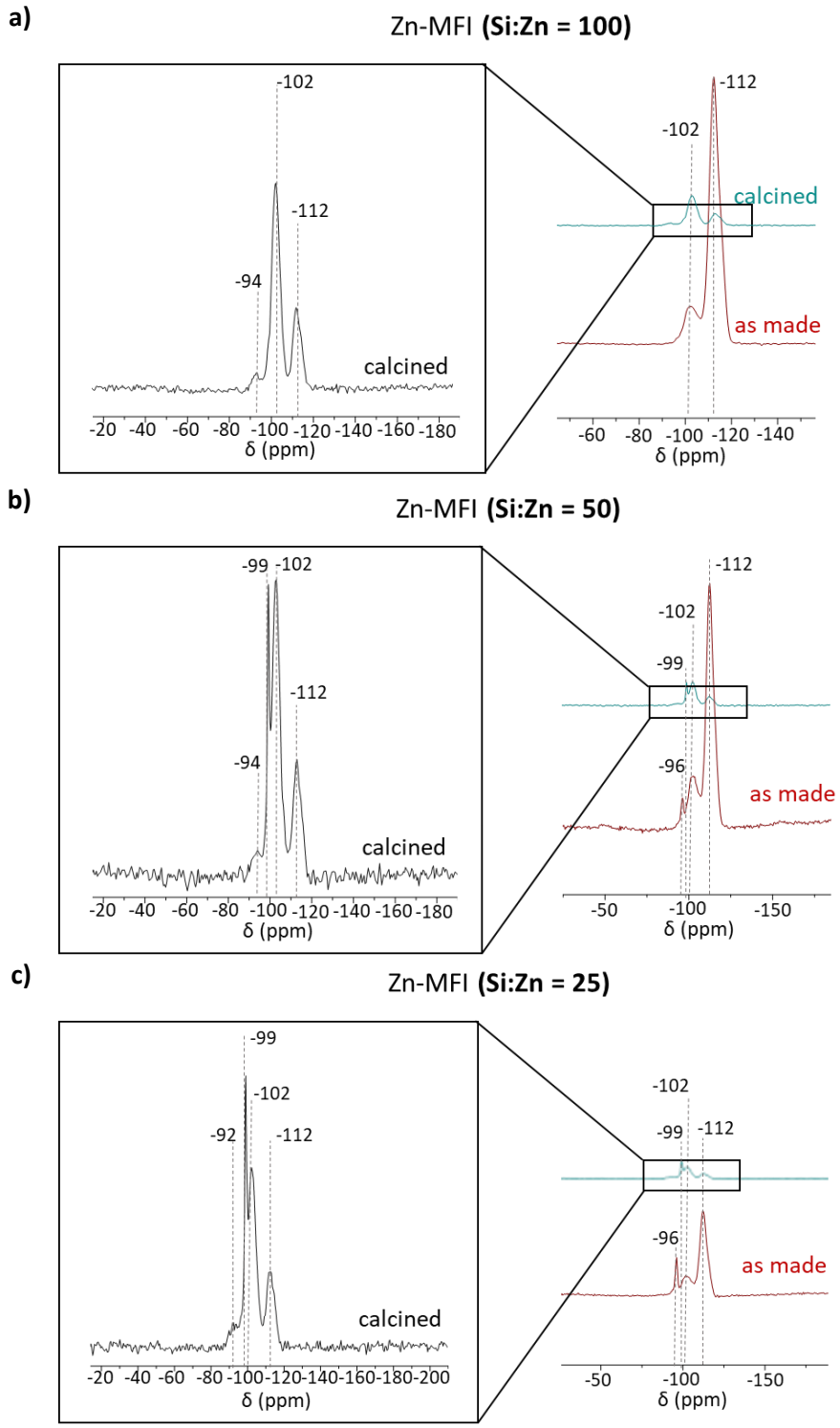

Figure 94: Spectra acquired through ^{1}H-^{29}Si Cross Polarisation analysis of Zn-MFI materials (prepared using the TEOS synthesis, no KOH and $ZnCl_2$ as Zn source) in the as-made and calcined forms with Si:Zn ratios of 100 (a), 50 (b) and 25 (c). The intensity of the peak at – 99 ppm in the calcined samples increases with the increasing of the Zn content in the samples.

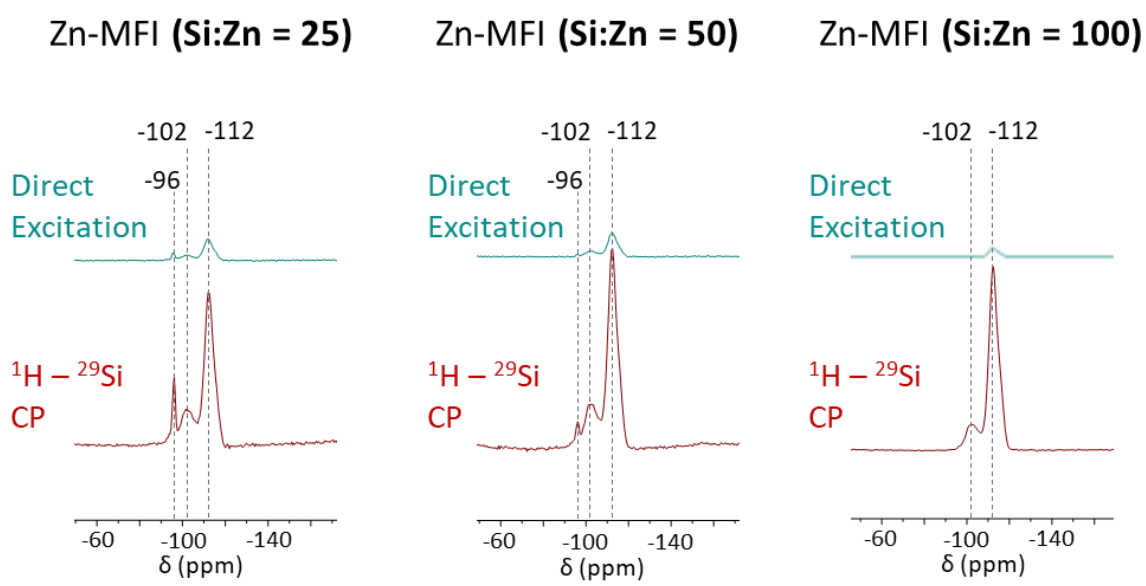

Figure 95: Spectra acquired through ^{1}H-^{29}Si Cross Polarisation and ^{29}Si Direct Excitation analysis of as-made Zn-MFI materials (prepared using the TEOS synthesis, no KOH and $ZnCl_2$ as Zn source) with Si:Zn ratios of 25, 50 and 100. The intensity of the peak at – 96 ppm decreases with the decreasing of the Zn content in the samples.

Table 30: Percentage of Q_4 and Q_3 sites obtained from ^{29}Si Direct Excitation experiments carried out on Zn-MFI samples prepared using different K^+ contents.

Sample	TPA:K	Treatment	Q_3 (%)	Q_4 (%)	Q_4/Q_3
H^+/Zn-MFI	***∞***	*As made*	19	81	4.3
		Calcined	6	94	14.6
		Dehydrated	9	91	10.1
		Re-hydrated	8	92	11.5
K^+/Zn-MFI	***6.5***	*As made*	20	80	4.0
		Calcined	2	98	49.0
		Dehydrated	4	96	22.3
		Re-hydrated	7	93	13.3
K^+/Zn-MFI	***5.65***	*As made*	19	81	4.3
		Calcined	3	97	32.3
		Dehydrated	3	97	32.3
		Re-hydrated	3	97	32.3
K^+/Zn-MFI	***3***	*As made*	22	78	3.5
		Calcined	6	94	15.6
		Dehydrated	4	96	24.0
		Re-hydrated	4	96	24.0

9.3.2. Silicalite-1 Analysed trough ^{1}H-^{29}Si CP NMR Experiments

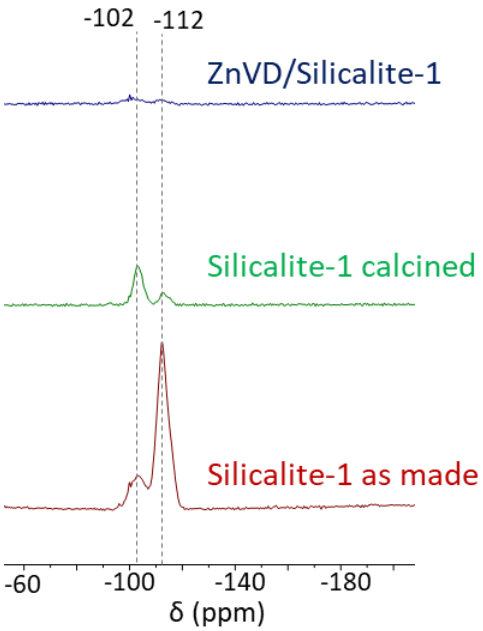

Figure 96: Spectra acquired through ^{1}H-^{29}Si CP analysis of Silicalite-1 in the as-made, calcined and Zn vapour deposited forms. The signal intensity, related to the proximity of H atoms to Si atoms, decreases after the calcination process and it is almost absent after the ZnVD process.

9.4. Methane Activaton over Bi-metallic Sites

9.4.1. Methane Activation over ZnVD/Ni^{2+}/ZSM-5

Ni^{2+}-exchanged ZSM-5 samples (Ni:Al = 0.45) were prepared using the method described in Section 3.1.1 and underwent Zn vapour deposition. Methane activation was then carried out following the procedure described in Section 3.1.2.3. A colour change was observed between the Ni^{2+}-exchanged sample and the sample after ZnVD from pale green to black, most likely due to the reduction of Ni^{2+} to metallic Ni^{0} particles, as revealed by pXRD. The outcome of the methane activation reaction was the production of Zn-CH_3 species, with the presence of a limited amount of oxygenated species, such as Zn-OCH_3 and Zn-COOH. Therefore, the reactivity of the materials was identical to that of Zn vapour deposited zeolites.[2]

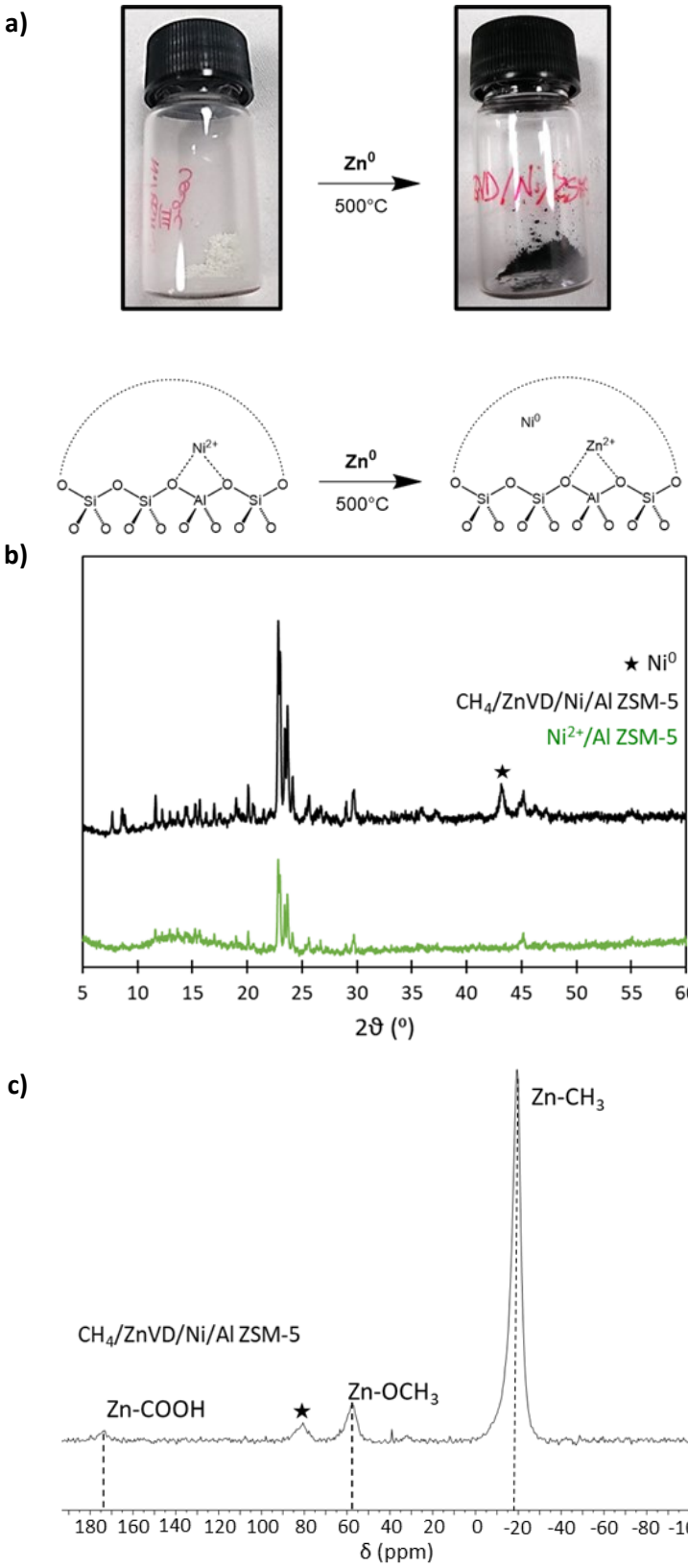

Figure 97: Representation of Ni^{2+}/ZSM-5 before and after the ZnVD treatment (a), pXRD patterns highlighting the presence of Ni^0 species in the ZnVD/Ni^{2+}/ZSM-5 sample (b) and ^{13}C NMR spectrum of the product post-methane activation reaction (c). In the latter, the signals belonging to Zn-CH_3 (-19 ppm), Zn-OCH_3 (58 ppm) and Zn-COOH (173 ppm) are highlighted. The stars denote spinning sidebands.

9.4.2. Methane Activation over ZnVD/Cu^{2+}/ZSM-5

Cu^{2+}-exchanged ZSM-5 samples (Cu:Al = 0.49) were prepared using the method described in Section 3.1.1 and underwent Zn vapour deposition using amounts of Zn^0 powder corresponding to Zn:Cu ratios of 100:1, 10:1 and 1:1. Methane activation was then carried out following the procedure described in Section 3.1.2.3 . A change of colour was observed between the samples before and after ZnVD, from pale blue to pink/red, indicating a change of oxidation state of Cu^{2+} to Cu^+ and/or Cu^0. The outcome of the methane activation reactions was the production of Zn-CH3 species for the samples prepared with Zn:Cu ratios of 100 and 10; however, no signals were observed for the sample with Zn:Cu = 1.

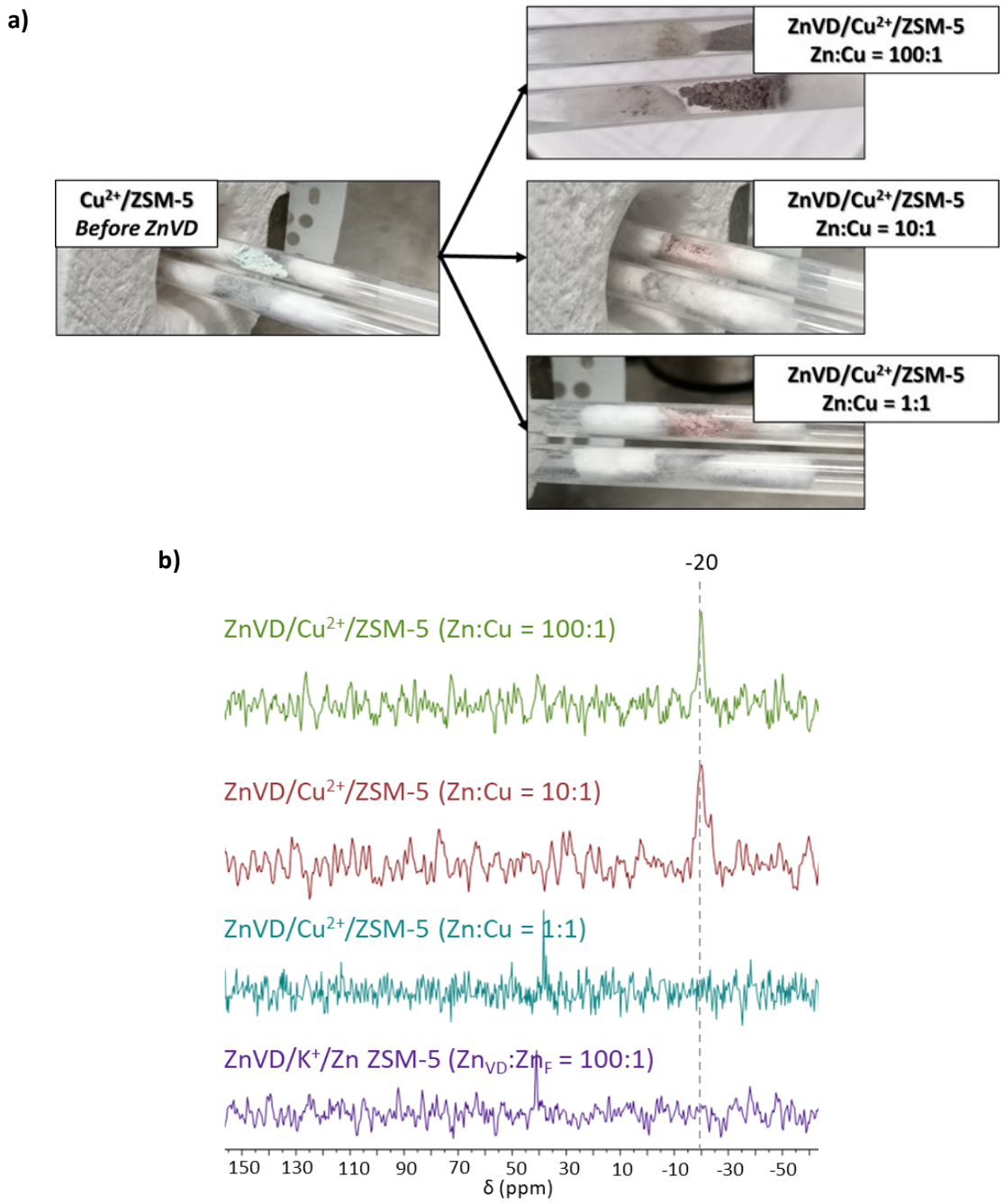

Figure 98: Images of Cu^{2+}/ZSM-5 before and after the ZnVD treatment (a) and ^{13}C NMR spectrum of the products post-methane activation reaction (b). A signal at -20 ppm can be observed for ZnVD/Cu^{2+}/ZSM-5 samples with Zn:Cu ratios of 100 and 10, whilst the sample with Zn:Cu = 1 showed no ability to activate methane. The 13C obtained from methane activation carried out over a K^+/Zn-MFI sample, showing the absence of signals, is reported for comparison.

9.5. Characterisation of the Acidity of Samples used for EtOH Conversion Reactions

9.5.1. Zeolites and zeotypes Analysed through ^{31}P NMR Experiments

^{31}P SSNMR spectroscopy of adsorbed trimethylphosphine oxide (TMPO) was carried out over Zn-MFI and Silicalite-1 samples and the results compared to Al-ZSM-5 in order to show the different acid character of the samples. The adsorption of TMPO was carried out under inert conditions and the samples analysed to detect changes in ^{31}P chemical shift of the P = O species due to interactions with Brønsted or Lewis acid sites. When the P = O bond of TMPO interacts with Brønsted acid sites higher chemical shifts (around δ = 86–53 ppm) are produced than those observed for binding of TMPO to a Lewis acid site (around δ = 60–55 ppm).[3] ^{31}P NMR spectra were acquired on a Bruker Avance III 400 MHz spectrometer in the ^{1}H - ^{31}P high-power decoupling (hpdec) cross-polarisation mode with a 10 s recycle delay, 161.99 MHz frequency and 10 kHz spin rate.

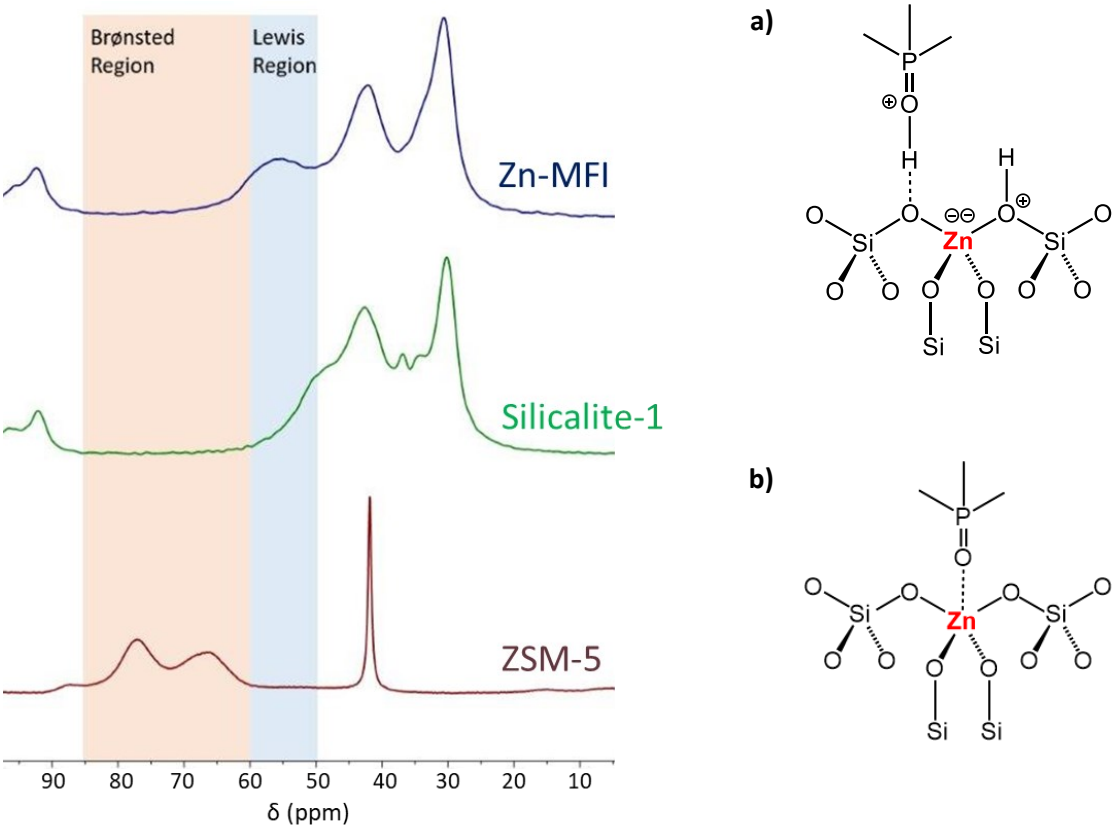

Figure 99: NMR spectra showing ^{31}P signals of TMPO adsorbed onto Zn-MFI, Silicalite-1 and ZSM-5 showing signals in the Brønsted (a) and Lewis (b) acid regions.

9.5.2. Materials used for EtOH Conversion Analysed through ^{1}H NMR Experiments

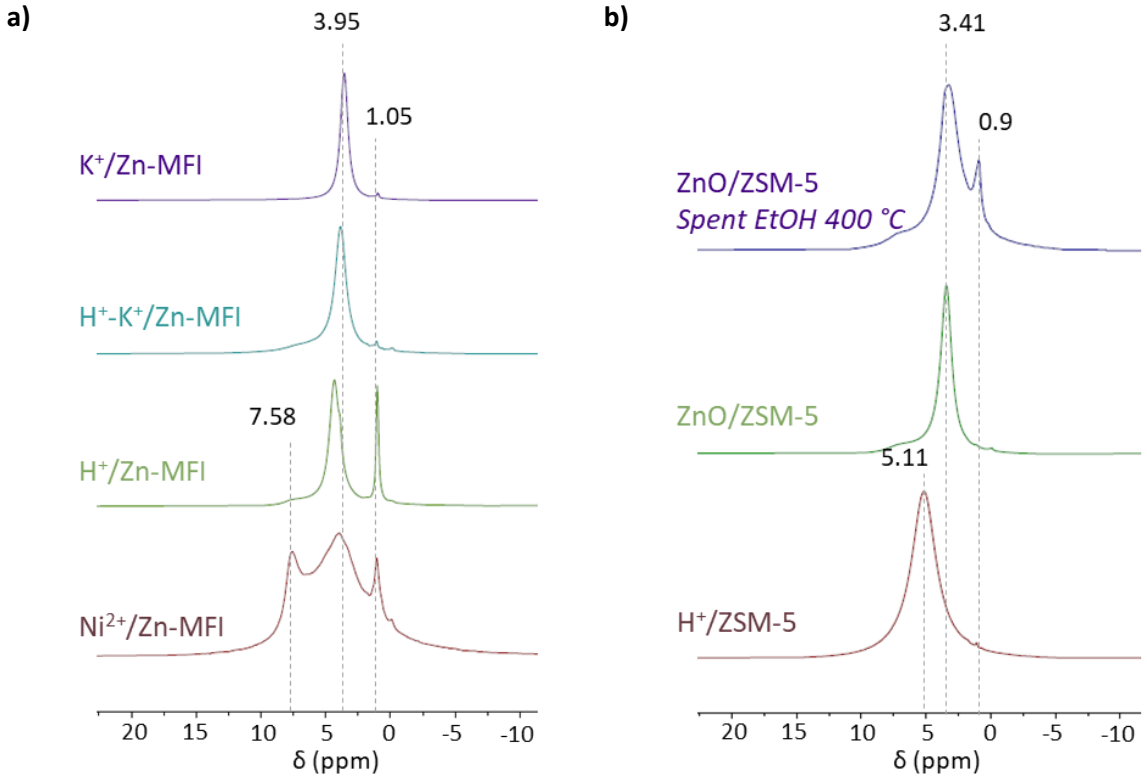

Figure 100: NMR spectra showing ^{1}H proton signals acquired on a Bruker Avance III HD spectrometer at 400.17 MHz using a pulse-acquire experiment with DEPTH background suppression for spent Zn-MFI samples used in EtOH conversion reactions carried out at 350 °C (a) and for ZnO/ZSM-5 before and after the reaction carried out at 400 °C and compared to a H^{+}/ZSM-5 sample (b).

9.6. EtOH/CH_4 Co-processing Reactions

A co-processing reaction was carried out using EtOH and CH_4 over a ZnO/ZSM-5 sample at 350 °C with 40 ml/min methane flow rate.

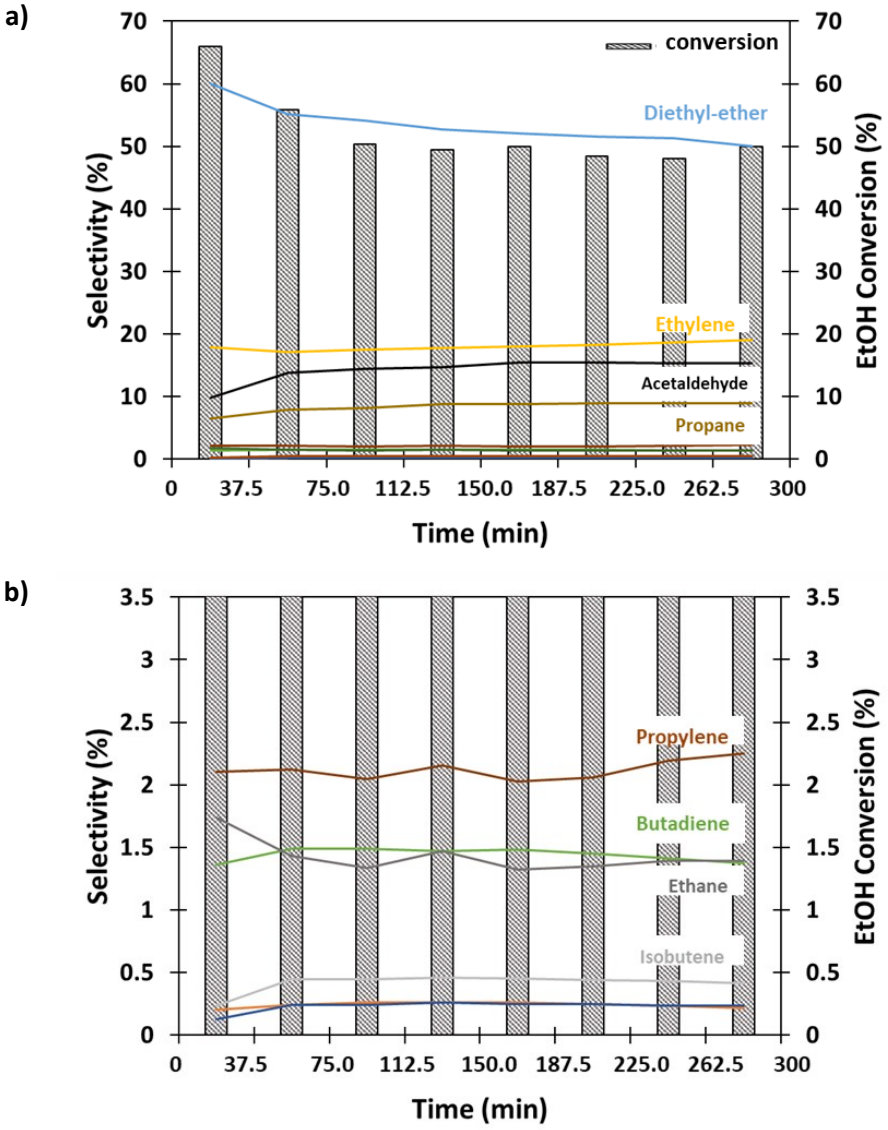

Figure 101: Product selectivity (%) and EtOH conversion (%) obtained from EtOH/CH4 co-processing reaction carried out at 350 °C with 100 mg ZnO/ZSM-5 catalyst and 40 ml/min methanol (a); close-up section of the upper figure (b).

9.7. Calibration curves for 1-hexene epoxidation

a)

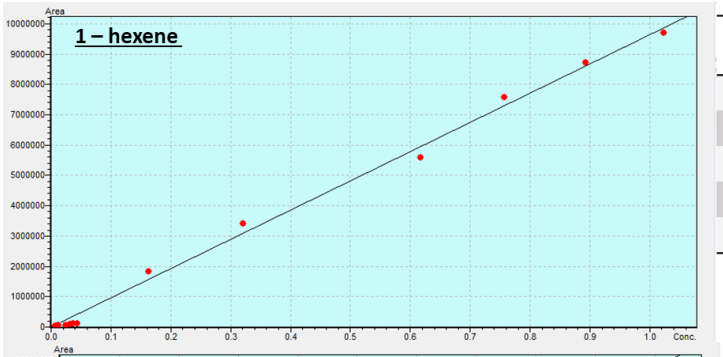

Concentration (mmol/ml)	Peak Area
0.1634	1821190
0.3205	3407241
0.6172	5575583
0.7574	7571656
0.8927	8706066

y = 9642065x
R = 0.99813

b)

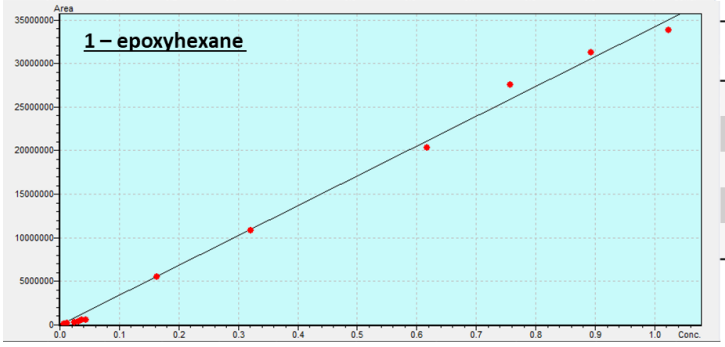

Concentration (mmol/ml)	Peak Area
0.1634	5506168
0.3205	10816480
0.6172	20294931
0.7574	27556501
0.8927	31244748

y = 34215660x
R = 0.99849

Figure 102: GC-MS calibration curves obtained for 1-hexene (a) and 1-hepoxyhexane (b).

9.8. MS Traces from β-pinene/paraformaldehyde Condensation Reactions

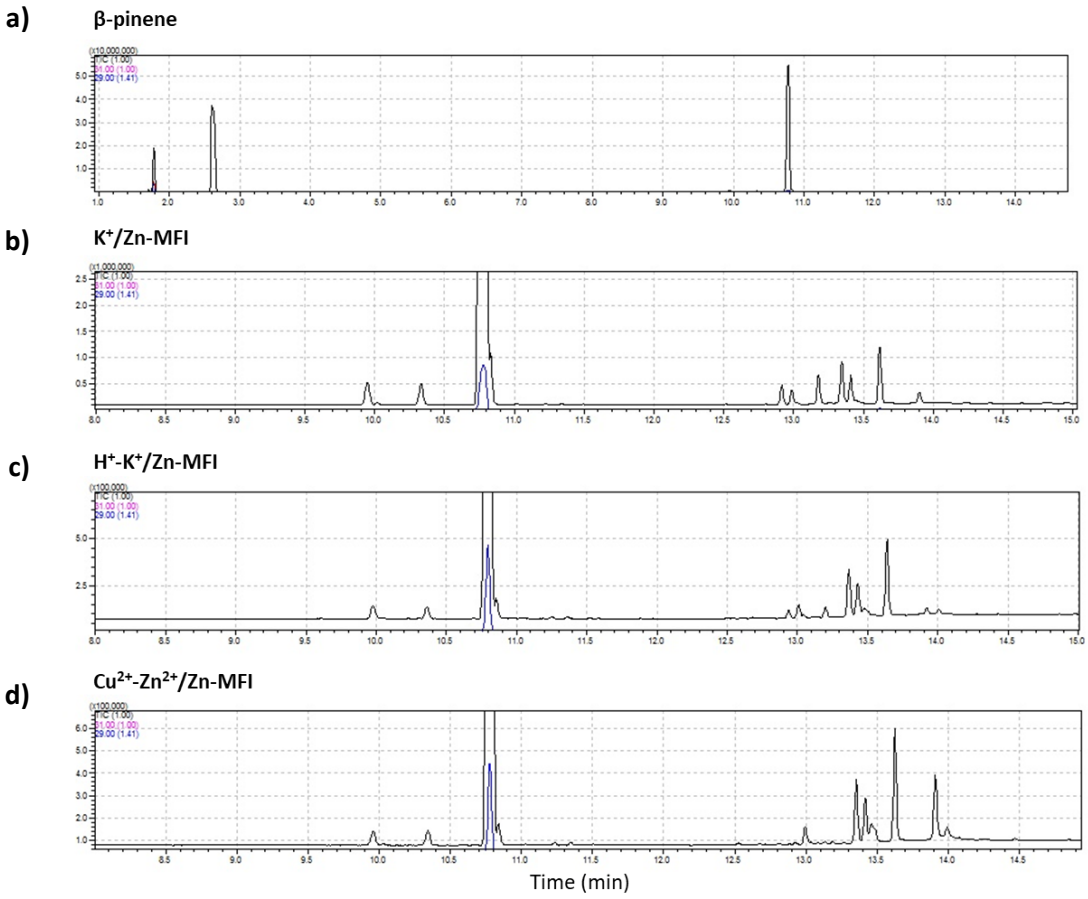

Figure 103: MS traces obtained from β-pinene only (a) showing its characteristic peaks and K^+/Zn-MFI (b), H^+-K^+/Zn-MFI (c) and Cu^{2+}-Zn^{2+}/ZSM-5 (c) showing the peaks corresponding to the reaction products.

9.9. Evaluation of the Experimental Errors on XRF Results

Table 31: Average and standard deviation over 10 XRF measurements on a commercial zeolite BEA sample (Si:Al = 12.5).

Si/Al molar ratio	
11.7	
19.9	
11.4	
11.7	
11.6	
11.7	
11.8	
11.6	
11.6	
11.8	
AVERAGE	12.5

STANDARD DEVIATION	2.5

The standard error (*SE*) on the measurements was calculated using the formula:

$$SE = \frac{\sigma}{\sqrt{n}}$$

Where σ is the standard deviation (2.5) and n is the sample size (10). The resulting standard error was equal to 0.8, corresponding to the 6% of the average value.

Appendix Bibliography

[1] S. A. I. Barri and D. Young, “Crystalline zincosilicate.,” EP 0124998 A2, 1983.

[2] M. A. Shah, S. Raynes, D. C. Apperley, and R. A. Taylor, “Framework Effects on Activation and Functionalisation of Methane in Zinc-Exchanged Zeolites,” *ChemPhysChem*, 21, pp. 673–679, **2020**, doi: 10.1002/cphc.201900973.

[3] Y. Wang, S. Xin, Y. Chu, J. Xu, G. Qi, Q. Wang, Q. Xia, F. Deng “Influence of trimethylphosphine oxide loading on the measurement of zeolite acidity by solid-state nmr spectroscopy,” *J. Phys. Chem. C*, 125, 17, pp. 9497–9506, **2021**, doi: 10.1021/ACS.JPCC.1C01789/SUPPL_FILE/JP1C01789_SI_001.PDF.